Victor Valentinovich Eremenko (On His 70th Birthday)

This issue of *Low Temperature Physics* honors a remarkable event—the 70th birthday of Victor Valentinovich Eremenko, a Full Member of the National Academy of Sciences of Ukraine, an outstanding scientist and a gifted organizer.

He was born on August 26, 1932 in Kharkov to a family of well-known physicists. In his childhood and later on he absorbed the special atmosphere of scientific creative power that was characteristic of the physics community known as the Kharkov school of physics. After graduating from Kharkov State University in 1955, Eremenko continued his education as a post-graduate and worked at the Institute of Physics in Kiev. In this period his scientific interest was concentrated on the optical properties of semiconductors and molecular crystals. Eremenko defended his PhD thesis in 1959. In 1961 he was invited to Kharkov to head a department at the newly established Institute for Low Temperature Physics and Engineering. He was among those who contributed greatly to the advancement of the Institute and displayed to a full degree his natural endowments as a researcher and an organizer of the scientific process.

During his first years at the Institute he initiated a new scientific field—optical spectroscopy of antiferromagnets. For many years this field of research has been progressing successfully owing to the efforts of V. V. Eremenko and his disciples. His scientific achievements in this field, as well as in magnetism, magnetooptics, high-temperature superconductivity, and the physics of strongly correlated systems, have won world recognition. The best known results include the detection of the intermediate and mixed states in antiferromagnets, the discovery of new magnetooptical effects in antiferromagnetic crystals, the detection of photoinduced phenomena in magnetic insulators and high-T_c superconductors, and the observation of quantum oscillations of the magnetostriction in mixed-state superconductors. The results obtained by V. V. Eremenko have been the subject of nearly 400 publications and summarized in monographs, such as the *Introduction to Spectroscopy of Magnets* and *Magnetooptics and Spectroscopy of Antiferromagnets*.

Professor Eremenko is a winner of the State Prizes of Ukraine and Azerbaijan and prizes awarded by the Academy of Sciences of Ukraine, USSR, and Polish Academies of Sciences. He has been elected a fellow member of the American Physical Society and a foreign member of the Russian Academy of Natural Sciences.

Professor Eremenko shares generously his profound knowledge and ample scientific experience with young scientists. He has formed a remarkable scientific school including three Associate Members of the National Academy of Sciences of Ukraine, and fourteen Doctors and over fifty Candidates of Physics and Mathematics. His disciples and followers work successfully in many scientific institutions and universities in Ukraine and abroad.

As the Director of the Institute for Low Temperature Physics and Engineering of the National Academy of Sciences of Ukraine, V. V. Eremenko has been doing a lot to support and keep up the scientific potential of the Institute in these hard times for Ukrainian science.

Professor Eremenko applies a great deal of effort and energy to the Journal *Fizika Nizkikh Temperatur* (*Low Temperature Physics*). To a considerable extent, it is due to his effort that this journal can boast of the highest impact factor among the scientific journals in Ukraine.

The charm, democratic spirit, and good will inherent in the personality of V. V. Eremenko invariably attract the true respect and love of his colleagues, friends, followers, and the employees of the Institute and the Journal.

Professor Eremenko comes to his 70th birthday full of creative power and energy to accomplish his extensive plans.

The Editorial Board of *Fizika Nizkikh Temperatur* give their Editor-in-Chief Victor Valentinovich Eremenko best wishes for strong health and new achievements in his versatile creative activity as a scientist and an organizer.

This special issue presents the works of the colleagues, friends, and followers of Victor Valentinovich Eremenko. The response of physicists, eager to acknowledge their regard for this event, was so immense that we were unable to include here all the manuscripts that arrived from all over the world. The Editorial Board sincerely apologizes for our inability to publish all of the numerous papers in this issue. They will appear in the next issues of *Low Temperature Physics*. All of the contributions are concerned with scientific fields strongly influenced by the activity of V. V. Eremenko and demonstrate the latest achievements in these fields.

Editorial Board

Recent progress in magneto-optics and research on its application (Review)

N. Kojima*

Graduate School of Arts and Sciences, The University of Komaba 3-8-1, Meguro-ku, Tokyo 153-8902, Japan

K. Tsushima

Kyushu Institute of Information Sciences, saifu 6-3-1, Dazaifu, Fukuoka 818-0117, Japan
(Submitted April 10, 2002)
Fiz. Nizk. Temp. **28**, 677–690 (July 2002)

Various kinds of magneto-optical properties are investigated in rare earth orthochromites. From an analysis of Cr^{3+} exciton absorption in $RCrO_3$ (R=Tb, Dy, and Ho), it is unferred that these compounds exhibit an anomalous spin-reorientation in a magnetic field along the *b* axis, where the weak ferromagnetic moment of the Cr^{3+} spins rotates in the *ac* plane perpendicular to the *b* axis. In these compounds, when the R^{3+} spin configuration is disordered, an anomalous satellite band appears on the lower-energy side of the Cr^{3+} exciton absorption, which is associated with the breakdown of the $\mathbf{k}=0$ selection rule due to the disorder of the R^{3+} spin configuration. In $YbCrO_3$, various kinds of cooperative excitations, such as a Cr^{3+} exciton coupled with an Yb^{3+} magnon and a $Cr^{3+}-Yb^{3+}$ exciton molecule, which are induced by the antisymmetric exchange interaction between the Cr^{3+} and Yb^{3+} spins, appear in the visible region. The propagation of these cooperative excitations depends strongly on the spin structure and the external magnetic field. In $ErCrO_3$, a photo-induced spin-reorientation takes place within 50 μs after the photo-irradiation corresponding to the ${}^4A_{2g}\rightarrow{}^2E_g$ transition of Cr^{3+}, and it returns to the initial spin configuration in about 400 ms. This phenomenon is detected in the time-resolved Er^{3+} absorption spectra corresponding to the ${}^4I_{15/2}\rightarrow{}^4I_{9/2}$ transition. Finally, we briefly review the recent frontier research on applications developed mainly in Japan. © *2002 American Institute of Physics.* [DOI: 10.1063/1.1496656]

1. INTRODUCTION

It is our very great honor and a great pleasure to submit our special review paper to this issue dedicated to Prof. V. V. Eremenko on his 70th birthday. One of the authors (K.T.) has known him since the 1960s, and soon after, we had an opportunity to meet and talk, for instance, at the time of the First and Second International Symposiums on Magneto-Optics, each as an organizer: in Kyoto, 1987,[1] and in Kharkov, 1991.[2] We had also frequent communications over the years, including his visit to Japan with his son. Every communication we have had with each other is an unforgettable remembrance.

More than 150 years ago, M. Faraday discovered that when linearly polarized light propagates through flint glass under an applied magnetic field, its plane of polarization is rotated. Since Faraday's original discovery, magneto-optics has become a highly fascinating field of research, which is of great importance from the standpoints of basic science and application. Especially, the magneto-optics and spectroscopy of magnetically ordered materials have been actively developing since the 1960s. Recently, Eremenko *et al.*,[3] Zvezdin and Kotov,[4] and Sugano and Kojima[5] have edited books in which recent fascinating topics of magneto-optical properties are described.

In magnetically ordered materials, various kinds of magneto-optical properties appear as a result of a synergistic effect between optical properties and magnetic properties. The magnetic interaction between elementary excitations such as excitons and magnons enables them to combine with one another, forming new and more complex excitations such as exciton–magnon transitions, which are observed in the visible region. Moreover, both the magnetic interaction and spin structure have effects on the propagation, the energy position and the shape of elementary excitations. Therefore, analysis of the magneto-optical properties is one of the most powerful tools for investigating the spin configurations and magnetic phase transitions.

In this paper, we describe various kinds of magneto-optical properties of rare earth orthochromites and review the recent frontier research on application. In Sec. 2, we report an anomalous field-induced spin-reorientation in $RCrO_3$ (R=Tb, Dy, and Ho) by the analysis of Cr^{3+} exciton absorption. Moreover, we describe the breakdown of the $k=0$ selection rule for the Cr^{3+} exciton absorption in $RCrO_3$ (R=Dy and Ho) induced by the disorder of the R^{3+} spin configuration. In Sec. 3, we describe various types of cooperative excitations in $YbCrO_3$ induced by the $Cr^{3+}-Yb^{3+}$ exchange interaction. Moreover, we describe how the $Cr^{3+}-Yb^{3+}$ antisymmetric exchange interaction depends on the dynamics of their cooperative excitations. In Sec. 4, after a survey of the recent progress of photo-induced magnetism, we describe our pioneering work of the photo-induced spin-reorientation in $ErCrO_3$. In Sec. 5, we survey the recent frontier research on applications especially those developed in Japan.

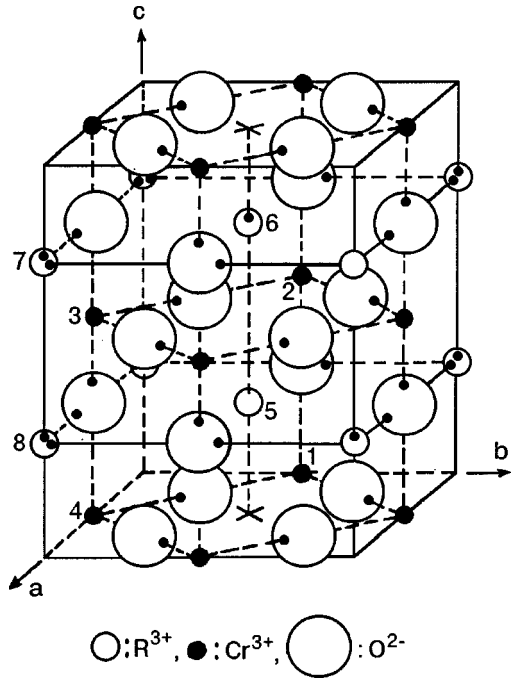

FIG. 1. Unit cell of $RCrO_3$. The Cr^{3+} and R^{3+} positions are indicated with numbers *1–4* and *5–8*, respectively.

2. OPTICAL INVESTIGATION OF VARIOUS MAGNETIC PHASE TRANSITIONS

It is well known that electronic excitations of several electron-volts in magnetic insulators can be regarded as transitions within an incomplete *d* or *f* shell of a single magnetic ion. Such a localized excitation cannot, however, be an eigenstate of the crystal, and the excitation migrates on magnetic ions as an excitation wave called a Frenkel exciton. This property is reflected in the energy dispersion and the Davydov splitting. In magnetically ordered state, analysis of the Frenkel exciton is one of the most powerful methods of elucidating the spin configuration and magnetic phase transitions, because the magnetic symmetry change associated with phase transition is directly reflected in the selection rule for the polarized exciton lines.

In this Section, we elucidate an anomalous type of spin-reorientation in rare earth orthochromites, $RCrO_3$ (R=Ho, Dy, and Tb), by the analysis of Cr^{3+} exciton lines.

$RCrO_3$ has an orthorhombically distorted perovskite structure belonging to the space group P_{bnm} (D_{2h}^{16}) [Ref. 6]. The unit cell contains four molecules as shown in Fig. 1. The Cr^{3+} spins order spontaneously at the Néel temperature T_{N1}, and these compounds generally exhibit a weak ferromagnetic moment. At the second Néel temperature T_{N2}, the R^{3+} spins begin to reorder antiferromagnetically. The allowed spin configurations for the Cr^{3+} and R^{3+} sites at $T_{N1}<T<T_{N2}$ are shown in Fig. 2. The allowed spin configurations are denoted as $\Gamma_1(A_xG_yC_z;C_z^R)$, $\Gamma_2(F_xC_yG_z;F_x^RC_y^R)$, and $\Gamma_4(G_xA_yF_z;F_z^R)$ in the Bertaut notation.[7]

2.1. Field induced spin reorientation in $HoCrO_3$

It is well known that $RCrO_3$ and $RFeO_3$ exhibit various types of field induced spin reorientation wherein the weak ferromagnetic moment becomes parallel to the direction of the applied magnetic field. In the cases $H_0\|a$ and *c*, the spin

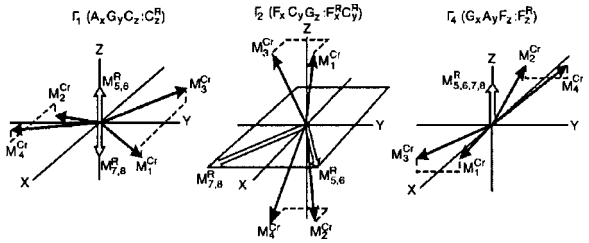

FIG. 2. Spin configuration of $RCrO_3$ at $T_{N2}<T<T_{N1}$.

reorientations of $(\Gamma_1,\Gamma_4)\rightarrow\Gamma_2$ and $(\Gamma_1,\Gamma_2)\rightarrow\Gamma_4$ have been reported for various $RCrO_3$ and $FeCrO_3$. In the case of $H_0\|b$, on the other hand, no spin reorientation is expected, because any spin configuration with a weak ferromagnetic moment of the Cr^{3+} spins along the *b* axis cannot be allowed in the absence of an external magnetic field. However, Courths *et al.* and we have observed an abrupt spectral change in $HoCrO_3$ at 1.8 K in a magnetic field $H_0 \approx 20$ kOe along the *b* axis, and they have suggested that this spectral change at 20 kOe be interpreted as a spin reorientation wherein the weak ferromagnetic moment of the Cr^{3+} spins rotates in the *ac* plane perpendicular to the *b* axis.[8,9]

In $HoCrO_3$, the Cr^{3+} spins are antiferromagnetically ordered below $T_{N1}=140$ K, with a weak ferromagnetic moment, as $\Gamma_2(F_xC_yG_z;F_x^RC_y^R)$ [Ref. 10]. No additional transition has been observed down to 1.5 K. As shown in Fig. 2, in the case of Γ_2 spin configuration, the Cr^{3+} sublattice magnetic moments and the Cr^{3+} net magnetic moment lie along the *c* axis and the *a* axis, respectively. The anisotropy axes of the Ho^{3+} ions lie in the *ab* plane at about $\pm 65°$ from the *a* axis,[10] and the *g* values along the *a*, *b*, and *c* axes are 7.3, 15.7, and 0, respectively,[8] where the magnitude of the effective spin of Ho^{3+} is 1/2. Therefore, the Ho^{3+} spins are strictly confined in the *ab* plane.

Figure 3 shows the behavior of the energies of the absorption spectra around 13700 cm^{-1} for $HoCrO_3$ in a magnetic field $H_0\|b$ at 1.5 K. In this energy region, four sharp lines (R_1, R_2, R_3, and R_4) of magnetic dipole character are observed. The four magnetic dipole lines are assigned to the Davydov-split components of the Cr^{3+} exciton corresponding to the transition from the lowest substate of $^4A_{2g}$ to the lowest substate of ^2E_g. As shown in Fig. 3, when the magnetic field is applied along the *b* axis, the R_{1-4} lines split into two pairs, R_1, R_2 and R_3, R_4, in the range of 10 to 20 kOe, and an abrupt spectral change occurs at about 20 kOe. As the magnetic field increases from 19.5 to 20.5 kOe, the *R* lines for the lower-magnetic-field phase vanish, while those for the higher-magnetic-field phase grow. The discontinuous variation of the energies of the *R* lines and the existence of both phases in a small field region ($\sim$1 kOe) around the critical field H_c ($\sim$20 kOe) indicate that this phase transition is of first order. The energies, polarizations, and intensities of the *R* lines show notable changes at this phase transition, which suggest the occurrence of a spin reorientation of Cr^{3+}. Above 20 kOe, the energies of the *R* lines remain unchanged, indicating that the antiferromagnetic axis in the higher-magnetic-field phase is perpendicular to the *b* axis. Therefore, it is obvious that the spin configurations of the Cr^{3+}

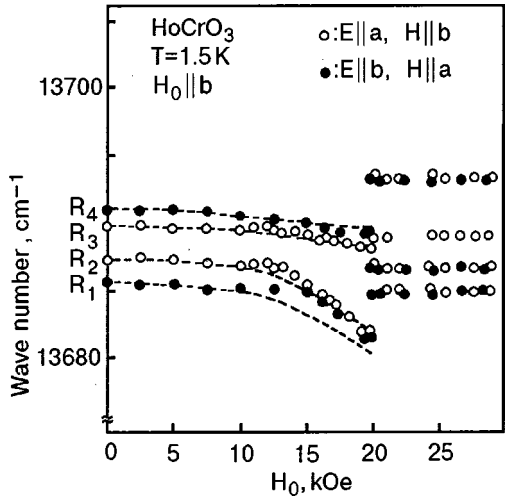

FIG. 3. Magnetic field dependence of the lowest energy region of the ${}^4A_{2g}\rightarrow{}^2E_g$ transition of Cr^{3+} in $HoCrO_3$. E and H denote the electric and magnetic vectors of the incident light, respectively. Solid and open circles: experimental points. Dashed lines: calculated energy shifts of the R lines corresponding to the transition from the lowest substate of ${}^4A_{2g}$ to the lowest substate of ${}^2E_g$ of Cr^{3+} by setting $\tilde{D}_x=\tilde{D}'_x=1.2\ \mathrm{cm}^{-1}$ and $\tilde{D}_y=\tilde{D}'_y=1.2\ \mathrm{cm}^{-1}$.

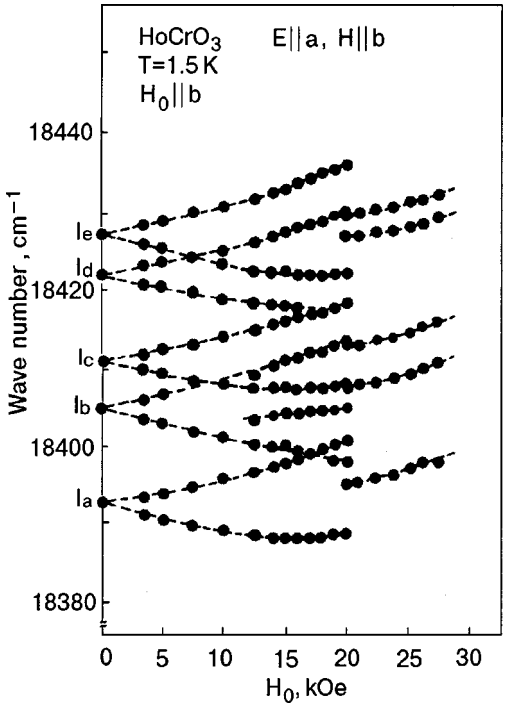

FIG. 4. Magnetic field dependence of the ${}^5I_8\rightarrow{}^5S_2$ transition of Ho^{3+} in $HoCrO_3$.

spins below and above H_c are $\Gamma_2(F_xC_yG_z)$ and $\Gamma_4(G_xA_yF_z)$, respectively.

The remarkable splitting of the R lines in the external magnetic field region between 10 kOe and 20 kOe are explained as follows. The molecular field H_B ($\|c$) induced by the $Cr^{3+}-Ho^{3+}$ exchange interaction at the $S^{\mathrm{Cr}}_{i=1}$ spin is expressed as

$$g_c^{\mathrm{Cr}}\beta H_B=4(\tilde{D}_y\langle S^{\mathrm{Ho}}_{5x}\rangle+\tilde{D}'_y\langle S^{\mathrm{Ho}}_{7x}\rangle)-4(\tilde{D}_x\langle S^{\mathrm{Ho}}_{5y}\rangle-\tilde{D}'_x\langle S^{\mathrm{Ho}}_{7y}\rangle) \tag{1}$$

and that at the $S^{\mathrm{Cr}}_{i=3}$ spin as

$$g_c^{\mathrm{Cr}}\beta H_B=4(\tilde{D}_y\langle S^{\mathrm{Ho}}_{5x}\rangle+\tilde{D}'_y\langle S^{\mathrm{Ho}}_{7x}\rangle)+4(\tilde{D}_x\langle S^{\mathrm{Ho}}_{5y}\rangle-\tilde{D}'_x\langle S^{\mathrm{Ho}}_{7y}\rangle), \tag{2}$$

where $\tilde{D}_x$, $\tilde{D}'_x$, $\tilde{D}_y$, and $\tilde{D}'_y$ denote the antisymmetric exchange interaction constants between Cr^{3+} and Ho^{3+}. In the absence of external magnetic field, the molecular fields H_B due to the $Cr^{3+}-Ho^{3+}$ interaction at the four inequivalent Cr^{3+} spins are equal because $\langle S^{\mathrm{Ho}}_{jx}(j=5,6)\rangle=\langle S^{\mathrm{Ho}}_{jx}(j=7,8)\rangle$ and $\langle S^{\mathrm{Ho}}_{jy}(j=5,6)\rangle=-\langle S^{\mathrm{Ho}}_{jy}(j=7,8)\rangle$. However, when the magnetic field is applied along the b axis the values of $\langle S^{\mathrm{Ho}}_j(j=7,8)\rangle$ change, and then the molecular fields due to the $Cr^{3+}-Ho^{3+}$ interation at the $S^{\mathrm{Cr}}_{i=1,2}$ spins become different from those at the $S^{\mathrm{Cr}}_{i=3,4}$ spins, and this causes the remarkable splitting of the R lines in the magnetic field region between 10 and 20 kOe. The broken lines in Fig. 3 show the energy shifts of the R lines for $H_0\|b$, calculated by setting $\tilde{D}_x=\tilde{D}'_x=1.2\ \mathrm{cm}^{-1}$ and $\tilde{D}_y=\tilde{D}'_y=1.2\ \mathrm{cm}^{-1}$. In this calculation we assumed that the molecular field for the ${}^2E_g$ state is equal to that for the ground state. As can be seen in Fig. 3, the behavior of the R lines in the magnetic field region $H_0<H_c$ is well reproduced by the calculation.

In order to confirm the above-mentioned result, we have investigated the behavior of the ${}^5I_8\rightarrow{}^5S_2$ transition of Ho^{3+} in a magnetic field $H_0\|b$ at $T=1.5$ K (see Fig. 4). At $T=1.5$ K, only the transitions from the lowest energy level I of the ground multiplet (${}^5I_8$) to the five singlet states of ${}^5S_2$, labeled as I_a, I_b, I_c, I_d, and I_e in order of increasing energy, can be observed. As shown in Fig. 4, when an external magnetic field is applied up to H_c, the I_a-I_e lines split, and the splitting increases with increasing magnetic field. However, the splitting vanishes at H_c. If the spin configuration of Cr^{3+} is $\Gamma_2(F_xC_yG_z)$, the effective field on the Ho^{3+} site with $S^{\mathrm{Ho}}_y=S$ is different from that with $S^{\mathrm{Ho}}_y=-S$ when the external field is applied along the b axis, and this causes the so-called sublattice splitting. Then, the splitting of I_a-I_e lines in the magnetic field region $H_0<H_c$ is interpreted as the sublattice splitting of the ${}^5I_8\rightarrow{}^5S_2$ transition.

In the case $H>H_c$, from the analysis of Cr^{3+} exciton lines, the spin configuration is considered to be $\Gamma_4(G_xA_yF_z)$, where the molecular field at the Ho^{3+} spin becomes parallel to the c axis and its value should be nearly zero because g_c^{Ho} is negligibly small. Therefore, in the higher-magnetic-field phase ($H_0>H_c$), the Ho^{3+} spins are arrayed only by the external magnetic field ($H_0\|b$), and the Zeeman energies on the four Ho^{3+} sites are equal. Thus, the sublattice splitting of I_a-I_e lines corresponding to the ${}^5I_8\rightarrow{}^5S_2$ transition of Ho^{3+} vanish above H_c (=20 kOe). Thus, we can determine the spin configurations of $HoCrO_3$ in various magnetic fields $H_0\|b$, which are shown schematically in Fig. 5.

2.2. Field-induced spin reorientation in $TbCrO_3$

The Cr^{3+} spins in $TbCrO_3$ are antiferromagnetically ordered below $T_{N1}=167$ K, with a weak ferromagnetic moment, as $\Gamma_2(F_xC_yG_z;F^{\mathrm{R}}_xC^{\mathrm{R}}_y)$ [Ref. 11]. The Tb^{3+} spins are antiferromagnetically ordered below $T_{N2}=3.1$ K, and the spin configuration below T_{N2} is denoted as $\Gamma_{25}(F_xC_yG_z:F^{\mathrm{R}}_xC^{\mathrm{R}}_y;G^{\mathrm{R}}_xA^{\mathrm{R}}_y)$ [Ref. 11]. The easy axes of the Tb^{3+} spins lie in the ab plane at about $\pm45°$ from the a axis.

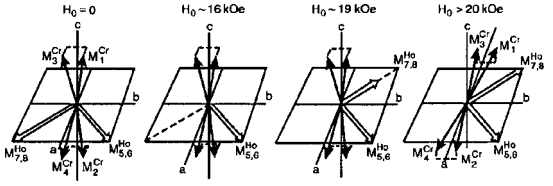

FIG. 5. Spin configurations of $HoCrO_3$ in various magnetic fields at 1.5 K. The magnetic field $H_0 \| b$.

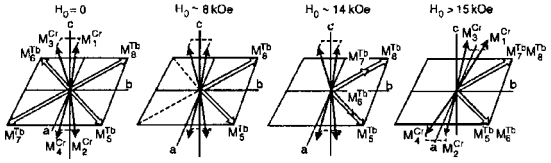

FIG. 7. Spin configurations of $TbCrO_3$ in various magnetic fields at 1.5 K. The magnetic field $H_0 \| b$.

The g values along the a, b, and c axes are 12.6, 12.6, and 0, respectively,[12] where the magnitude of the effective spin of Tb^{3+} is 1/2. Therefore, the Tb^{3+} spins are strictly confined to the ab plane.

Figure 6 shows the behavior of the Davydov-split components of the Cr^{3+} exciton line corresponding to the ${}^4A_{2g} \rightarrow {}^2E_g$ transition in $TbCrO_3$. As is seen in Fig. 6, when the magnetic field is applied along the b axis, the R_{1-4} lines split into two pairs, R_1, R_2 and R_3, R_4, in the magnetic field region between 8 and 15 kOe. At about 15 kOe, the energies, polarizations, and intensities of the R lines show notable changes, which resemble closely the behavior of the R lines in $HoCrO_3$ at the spin reorientation from Γ_2 to Γ_4. Therefore, it is obvious that the spin configurations of the Cr^{3+} spins in $TbCrO_3$ below and above $H_c(=15\,\text{kOe})$ are Γ_2 $(F_xC_yG_z)$ and Γ_4 $(G_xA_yF_z)$, respectively.

In the magnetic field region below H_c, with increasing external field, the energy gravity of the R lines drops around 8 kOe and then it remains unchanged. The drop in the energy of the R lines at about 8 kOe is attributed to the spin flip of the Tb_6^{3+} and Tb_7^{3+} sites. Thus, we can determine the spin configurations of $TbCrO_3$ in various magnetic fields of $H_0 \| b$, which are shown schematically in Fig. 7.

2.3. Field induced spin reorientation in $DyCrO_3$

The Cr^{3+} spins in $DyCrO_3$ are antiferromagnetically ordered below $T_{N1}=146$ K, with a weak ferromagnetic moment, as $\Gamma_2(F_xC_yG_z;\ F_x^RC_y^R)$ [Ref. 13]. The Dy^{3+} spins are antiferromagnetically ordered below $T_{N2}=2.0$ K, and the spin configuration below T_{N2} is denoted as $\Gamma_{25}(F_xC_yG_z:\ F_x^RC_y^R;G_x^RA_y^R)$ [Ref. 13]. The easy axes of the Dy^{3+} spins lie in the ab plane at about $\pm 60°$ from the a axis. The g values along the a, b, and c axes are 6.0, 17.0, and 0, respectively,[14] where the magnitude of the effective spin of Dy^{3+} is 1/2. Therefore, the Dy^{3+} spins are strictly confined to the ab plane.

Figure 8 shows the behavior of the Davydov-split components of the Cr^{3+} exciton line corresponding to the ${}^4A_{2g} \rightarrow {}^2E_g$ transition in $DyCrO_3$. When the magnetic field is applied along the b axis, the energies, polarizations, and intensities of the R lines change dramatically at about 2 kOe. Above 3 kOe, these properties of the R lines remain unchanged. From the analogy of the behavior of the R lines in $HoCrO_3$ and $TbCrO_3$, we conclude that $DyCrO_3$ exhibits a field-induced spin reorientation from $\Gamma_2(F_xC_yG_z)$ to $\Gamma_4(G_xA_yF_z)$ at $H_0(\|b)=2$ kOe.

2.4. Breakdown of the k=0 selection rule of Frenkel exciton

In the optical absorption corresponding to the pure Frenkel exciton, only the zone-center exciton is observable, because the magnitude of the propagation vector of visible light is of the order of 10^{-3} reciprocal lattice vectors, which is usually called the $\mathbf{k}=0$ selection rule. However, in the cases of mixed crystals or amorphous materials, it is predicted that the deviation from a periodic structure causes a breakdown of the $\mathbf{k}=0$ selection rule for the exciton transition. Impuri-

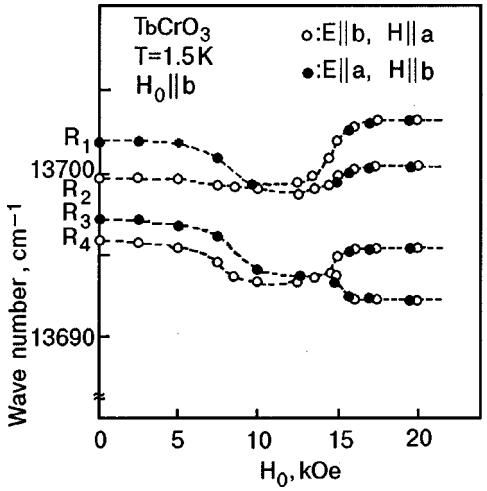

FIG. 6. Magnetic field dependence of the R lines of $TbCrO_3$. The dashed lines are a guide for the eye.

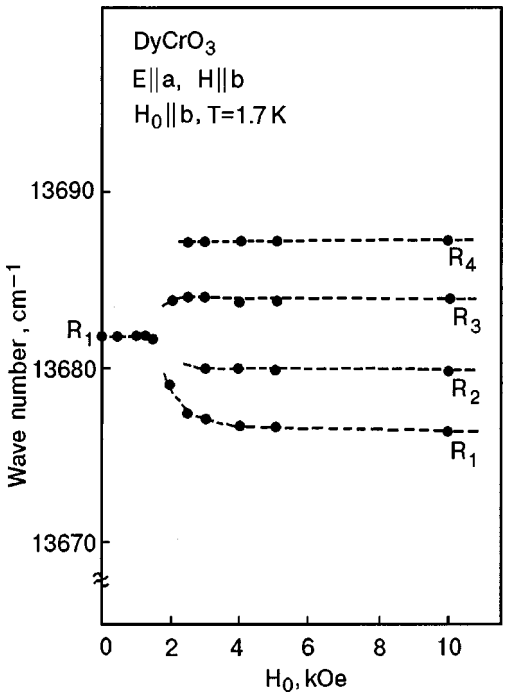

FIG. 8. Magnetic field dependence of the R lines of $DyCrO_3$. The dashed lines are a guide for the eye.

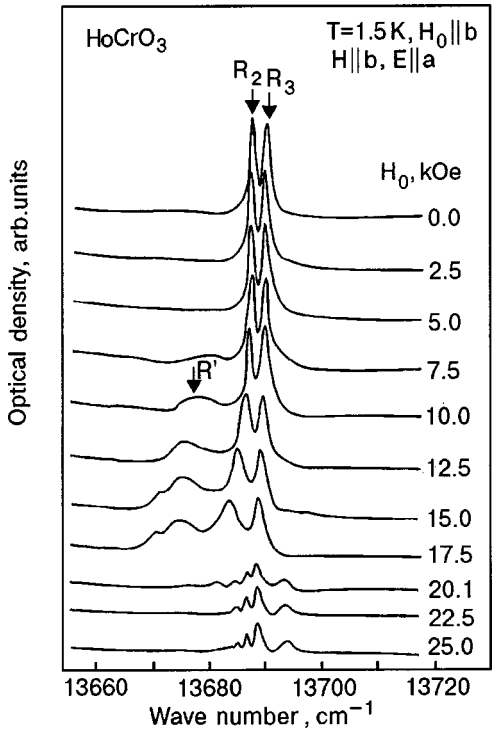

FIG. 9. Behavior of the R lines and the R' band of $HoCrO_3$ in magnetic fields along the b axis.

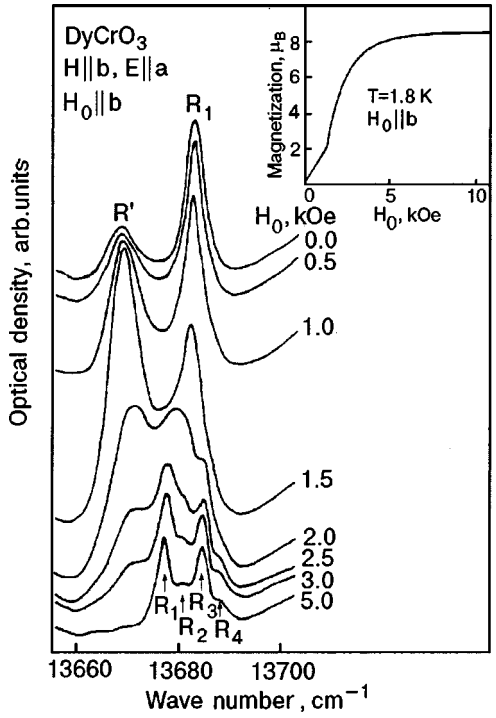

FIG. 10. Behavior of the R lines and the R' band of $DyCrO_3$ in magnetic fields along the b axis at 1.8 K. The inset shows the magnetization curve.

ties, alloy nonuniformities, and interface roughness occurring on a unit-cell length scale of are the best-known examples which provide an appropriate momentum of elastic scattering. Thus, the deviation from the virtual crystal leads to a $\mathbf{k}\neq 0$ (nonvertical) transition through the medium of the momentum of elastic scattering. In fact, the disorder-induced optical transitions for mixed crystals such as $AgCl_{1-x}Br_x$ [Ref. 15], $GaAs_{1-x}P_x$ [Ref. 16] and $Al_xGa_{1-x}As$ [Ref. 17] have characteristics which can be associated with the breakdown of the $\mathbf{k}$ selection rule for a periodic structure.

However, the breakdown of the $\mathbf{k}=0$ selection rule induced by the spin-configuration disorder has not yet been elucidated. In this Section, we report the breakdown of the $\mathbf{k}=0$ selection rule for the Cr^{3+} exciton absorption in $RCrO_3$ (R=Ho and Dy) induced by the disorder of the R^{3+} spin configuration.

Figure 9 shows the field dependence of the optical absorption spectra corresponding to the lowest-energy region of the ${}^4A_{2g}\rightarrow{}^2E_g$ transition of Cr^{3+} in $HoCrO_3$ [Ref. 18]. The R_2 and R_3 lines are the Davydov-split components of the pure Cr^{3+} exciton. When an external magnetic field is applied along the b axis at 1.5 K, an anomalous satellite band R' appears on the lower-energy side of the R lines at about 7.5 kOe, and its intensity passes through a maximum at 16 kOe and then disappears at $H_c=20$ kOe. As we have said, when the external magnetic field is increased along the b axis of $HoCrO_3$, the sublattice magnetic moments, $\mathbf{M}_7^{\mathrm{Ho}}$ and $\mathbf{M}_8^{\mathrm{Ho}}$ due to the S_7^{Ho} and S_8^{Ho} spins decrease and vanish at about 16 kOe, and above 16 kOe they grow gradually toward the direction of the applied magnetic field. On the other hand, $\mathbf{M}_5^{\mathrm{Ho}}$ and $\mathbf{M}_6^{\mathrm{Ho}}$ are saturated in the whole field range. From the behavior of the R' band and the spin configuration of $HoCrO_3$ in magnetic field along the b axis, it is obvious that the transition responsible for the R' satellite band in $HoCrO_3$ is allowed when the spin configuration of the Ho^{3+} sites is disordered.

Figure 10 shows the field dependence of the optical absorption spectra corresponding to the lowest-energy region of the ${}^4A_{2g}\rightarrow{}^2E_g$ transition of Cr^{3+} in $DyCrO_3$. The R_1 line is the Davydov-split component of the pure Cr^{3+} exciton. When an external magnetic field is applied along the b axis at 1.7 K, the intensity of the R' satellite band increases abruptly at 1.5 kOe and then decreases rapidly. As can be seen in the inset of Fig. 10, when the external magnetic field is applied along the b axis at 1.8 K, the metamagnetic transition takes place at 1.5 kOe, where the magnetic moments due to the S_6^{Dy} and S_7^{Dy} spins reverse their directions, from antiparallel to the external magnetic field to parallel. Therefore, it is obvious that the transition responsible for the R' satellite band in $DyCrO_3$ is allowed when the spin configuration of the Dy^{3+} sites is disordered.

The characteristic properties of the R' satellite band in $RCrO_3$ (R=Ho and Dy) may be summarized as follows. 1. The energy of the R' band is lower by about 16 cm^{-1} than the average energy of the pure Cr^{3+} exciton lines. 2. The dipole nature of the R' band is poorly characterized, while that of the pure Cr^{3+} exciton lines is explicitly magnetic. 3. The field-induced energy shift of the R' band disagrees with the sum of the energy shift of the Cr^{3+} exciton and the R^{3+} spin flip, which implies that the R' band does not correspond to the Cr^{3+} exciton coupled with R^{3+} spin flip. 4. The transition responsible for the R' band is allowed when the R^{3+} spin configuration is disordered by temperature or external magnetic field. 5. As the magnetic moment of the R^{3+} spins approach saturation, the R' band disappears.

Let us now discuss the transition mechanism responsible for the R' band in $RCrO_3$ (R=Ho and Dy). The Cr^{3+} exci-

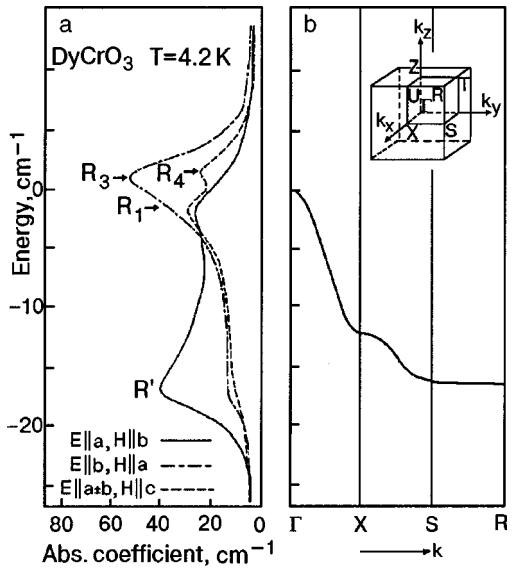

FIG. 11. (a) R lines and R' band of $DyCrO_3$, (b) Cr^{3+} exciton dispersion in $YbCrO_3$. The origin of the energy is fixed at the average energy of the free Cr^{3+} exciton lines.

ton dispersion due to the spin allowed transfer is expressed as

$$E(k)=E_0+2V_{11}^a\cos(ak_x)+2V_{11}^b\cos(bk_y)$$
$$\pm 8V_{13}\cos(ak_x/2)\cos(bk_y/2)\cos(ck_z/2), \qquad (3)$$

where E_0 is the relevant excitation energy for the single Cr^{3+} ion, V_{11}^a and V_{11}^b represent the intra-sublattice transfers along the a and b axes, respectively, and V_{13} the spin-allowed intersublattice transfer. From an analysis of the absorption spectra corresponding to the Cr^{3+} exciton coupled with the R^{3+} magnon in $RCrO_3$ (R=Tm and Yb), the Cr^{3+} exciton due to the ${}^4A_{2g}\rightarrow{}^2E_g$ transition has a large negative dispersion whose values for $TmCrO_3$ and $YbCrO_3$ are estimated at -14 cm^{-1} and -16 cm^{-1} [Refs. 19 and 20], respectively. Therefore, it is plausible that the sign and the magnitude of the Cr^{3+} exciton dispersion in $HoCrO_3$ and $DyCrO_3$ are almost the same as those of the Cr^{3+} exciton dispersion in $TmCrO_3$ and $YbCrO_3$. Figure 11b shows the energy dispersion of the Cr^{3+} exciton due to the ${}^4A_{2g}\rightarrow{}^2E_g$ transition in $YbCrO_3$, where $V_{11}^a=3.0$ cm^{-1} and $V_{11}^b=1.0$ cm^{-1}. As is seen in Fig. 11, the energy position of the R' band in $RCrO_3$ (R=Ho and Dy) agrees very closely with that of the Cr^{3+} exciton at the Brillouin zone boundary, which implies that the R' band is assigned to the excitation of the pure Cr^{3+} exciton at the zone boundary, which is caused by the disorder of the R^{3+} spin configuration. However, in general, the optical excitation of the pure Cr^{3+} exciton at the zone boundary cannot be observed without the breakdown of the $\mathbf{k}=0$ selection rule.

Thus, we arrive at the following conclusion. The magneto-elastic effect due to the R^{3+} (R=Ho and Dy) ion is extraordinarily large because of the strong spin–orbit interaction. When the R^{3+} spins fluctuate on account of temperature or external magnetic field, the disorder of the R^{3+} spin configuration deforms the periodic lattice potential. Through the medium of the strong magneto-elastic effect, the disorder of the R^{3+} spin configuration causes the breakdown of the $\mathbf{k}=0$ selection rule of the Cr^{3+} exciton absorption, and this is reflected in the appearance of the R' satellite band in the lower energy side of the free Cr^{3+} exciton.

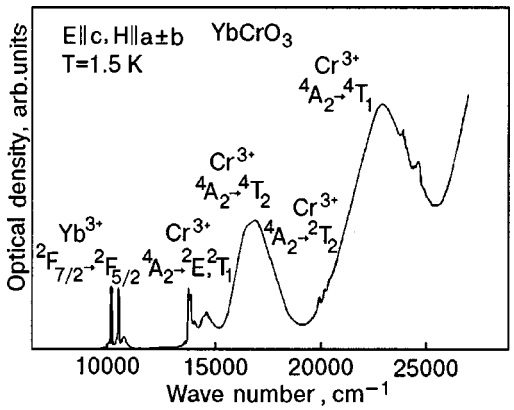

FIG. 12. Optical absorption spectra of $YbCrO_3$ in the energy region from visible to near-infrared.

3. VARIOUS COOPERATIVE EXCITATIONS

In magnetically ordered materials, various types of elementary excitations such as excitons and magnons exist. The magnetic interaction between these elementary excitations enables them to combine with one another, forming cooperative excitations such as exciton–magnon transitions,[21] which are observed in the visible region. In this Section, we describe two kinds of cooperative excitations induced by $3d-4f$ exchange interaction in $YbCrO_3$. Figure 12 shows the optical absorption spectra of $YbCrO_3$ in the energy region from visible to near-infrared at 1.5 K. The absorption spectra of $YbCrO_3$ in the energy region between 10000 cm^{-1} and 25000 cm^{-1} are assigned as shown in Fig. 12. In this energy region, besides the elementary excitations due to d–d and f–f transition and the cooperative excitations induced by the $3d-3d$ and $4f-4f$ exchange interactions, various kinds of cooperative excitations induced by the $3d-4f$ exchange interaction are observed. The Yb^{3+} exciton–Cr^{3+} magnon excitation is observed in the ${}^2F_{7/2}\rightarrow{}^2F_{5/2}$ transition of Yb^{3+} [Ref. 22], and the Cr^{3+} exciton – Yb^{3+} magnon excitation is observed in the ${}^4A_{2g}\rightarrow{}^2E_g$ transition of Cr^{3+} [Ref. 20]. Moreover, the Cr^{3+} exciton–Yb^{3+} exciton excitation is observed on the higher energy side of the ${}^4A_{2g}\rightarrow{}^4T_{1g}$ transition of Cr^{3+} [Ref. 23].

Let us briefly summarize the magnetic properties of $YbCrO_3$. In $YbCrO_3$, there are three types of magnetic interactions, $Cr^{3+}-Cr^{3+}$, $Cr^{3+}-Yb^{3+}$, and $Yb^{3+}-Yb^{3+}$, each of which generally consists of the isotropic and the symmetric and antisymmetric anisotropic exchange interactions. Among various $RCrO_3$ compounds, $YbCrO_3$ is an interesting one with a strong anisotropic exchange interaction between the Cr^{3+} and Yb^{3+} ions.[24] In the case of the Yb^{3+} ion, which has only one $4f$ hole, the $4f$ orbital is widely spread, leading to a strong $3d-4f$ exchange interaction in $YbCrO_3$. The strong anisotropic exchange interaction between the Cr^{3+} and Yb^{3+} spins in $YbCrO_3$ is able to induce various kinds of cooperative excitations. The Cr^{3+} spins in $YbCrO_3$ are antiferromagnetically ordered below $T_{N1}=118$ K, with a weak ferromagnetic moment, as

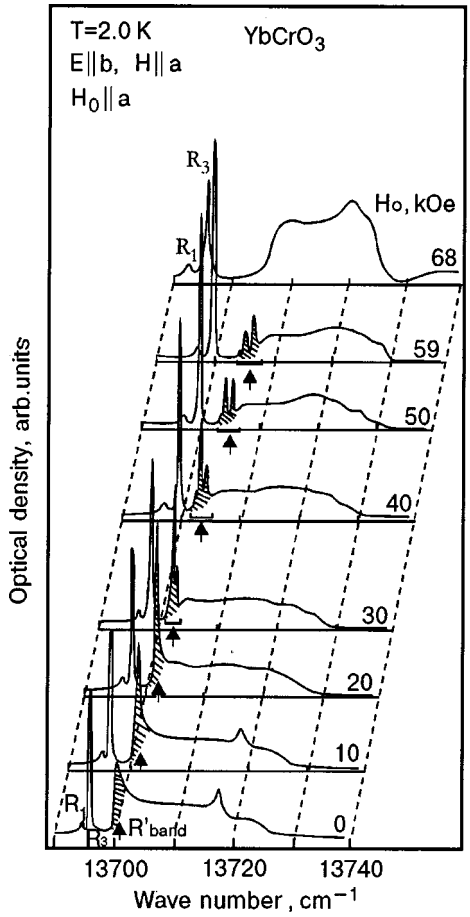

FIG. 13. Behavior of the R lines and the R' band of $YbCrO_3$ under magnetic fields along the a axis at 2.0 K. The arrows show the bound state of the R' band.

$\Gamma_2(F_xC_yG_z;F_x^{\mathrm{R}}C_y^{\mathrm{R}})$.[25] The spontaneous magnetic moment of $YbCrO_3$ crosses zero at 16.5 K, which reveals that the induced magnetic moment of the Yb^{3+} spins is antiparallel to the weak ferromagnetic moment of the Cr^{3+} spins.[25]

3.1. Cooperative excitation between the Cr^{3+} exciton and Yb^{3+} magnon

Figure 13 shows the absorption spectra corresponding to the lowest energy region of the ${}^4A_{2g}\rightarrow{}^2E_g$ transition of Cr^{3+} in $YbCrO_3$. The R_1 and R_3 lines with magnetic dipole character are assigned to the Davydov-split components of the pure Cr^{3+} exciton. In the neighborhood of the Cr^{3+} exciton lines, an electric dipole band (R' band) appears, which has an anomalous band shape with a sharp cutoff on the lower-energy side and fine structure. The R' band corresponds to the cooperative excitation of a Cr^{3+} exciton and Yb^{3+} magnon. The bandwidth and the cutoff profile on the lower- energy side of the R' band could be reproduced quantitatively by taking into account a negative exciton dispersion of -16 cm^{-1} [Ref. 20].

As is seen in Fig. 13, when the external magnetic field is applied along the a axis of $YbCrO_3$ at 2.0 K, a sharp and strong peak (arrow in Fig. 13) typical of a bound state appears on the lower-energy side of the R' band. At about 25 kOe, the bound state grows most strongly. Above 30 kOe, the bound state splits into several peaks and their intensity decreases significantly. At about 68 kOe, a dramatic spectral change occurs. The discontinuous spectral change between 59 kOe and 68 kOe is due to the metamagnetic phase transition (H_c) where the weak ferromagnetic moment of the Cr^{3+} spins reverses its direction from being antiparallel to parallel to the net magnetic moment of the Yb^{3+} spins. At this metamagnetic transition [26] the profile of the R' band changes drastically and its bound state disappears completely.

From the appearance of the bound state on the lower-energy side of the R' band, we arrive at the following concept. The Cr^{3+} exciton coupled with the Yb^{3+} magnon at the Brillouin zone edge is localized in an external magnetic field $H_0\|a$, while the Cr^{3+} exciton coupled with an Yb^{3+} magnon at any point of the Brillouin zone except the zone edge is delocalized. At 25 kOe, the Cr^{3+} exciton coupled with the Yb^{3+} magnon at the Brillouin zone edge is most strongly localized, which is reflected in the field-dependent energy shift of the R' band. Since the R' band is assigned to the cooperative excitation between a Cr^{3+} exciton and Yb^{3+} magnon, the magnetic field-dependent shift of the energy separation $\Delta E(H_0)$ between the R' band and the Cr^{3+} exciton lines should be expressed as

$$\Delta E(H_0)=\Delta E_{R'}(H_0)-\Delta E_R(H_0)=\Delta E_{\mathrm{Yb}}(H_0), \tag{4}$$

with

$$\begin{aligned}&\Delta E_{R'}(H_0)=E_{R'}(H_0)-E_{R'}(H_0=0),\\ &\Delta E_R(H_0)=E_R(H_0)-E_R(H_0=0),\\ &\Delta E_{\mathrm{Yb}}(H_0)=E_{\mathrm{Yb}}(H_0)-E_{\mathrm{Yb}}(H_0=0),\end{aligned} \tag{5}$$

where $E_{R'}(H_0)$ and $E_R(H_0)$ denote the energy position of the lower-energy side of the R' band and that of the average energy of the R lines in an external magnetic field $H_0\|a$, respectively, and $E_{\mathrm{Yb}}(H_0)$ denotes the energy of the Yb^{3+} magnon in an external magnetic field $H_0\|a$, which is estimated from an analysis of the Yb^{3+} exciton–Yb^{3+} magnon excitation appearing in the ${}^2F_{7/2}\rightarrow{}^2F_{5/2}$ transition of Yb^{3+} [Ref. 24].

Figure 14 shows the magnetic field dependence of $\Delta E_{R'}(H_0)-\Delta E_R(H_0)$ and $\Delta E_{\mathrm{Yb}}(H_0)$. The negative deviation of $\Delta E_{R'}(H_0)-\Delta E_R(H_0)$ from $\Delta E_{\mathrm{Yb}}(H_0)$ is caused by the attractive force between the Cr^{3+} exciton and the Yb^{3+} magnon. As can be seen in Fig. 14, the attractive force becomes strongest at 25 kOe, where the Cr^{3+} exciton–Yb^{3+} magnon at the Brillouin zone boundary is most strongly localized. Therefore, the bound state of the R' band grows most strongly at 25 kOe.

In the case that the bound state begins to migrate, the bound state distinguishes four Cr^{3+} sites in the unit cell. Therefore, in the process of delocalization of the bound state, the bound state exhibits Davydov splitting. In fact, as is seen in Fig. 13, the bound state of the R' band splits above 30 kOe. Therefore, we arrived at the following conclusion. In the magnetic field region above 30 kOe, the zone–edge Cr^{3+} exciton coupled with the Yb^{3+} magnon begins to migrate, which reflects upon the splitting of the bound state and the significant decrease in its intensity.

At the metamagnetic transition ($H_c=67$ kOe), the weak ferromagnetic moment of the Cr^{3+} spins reverses its direction, where the antisymmetric exchange interaction between

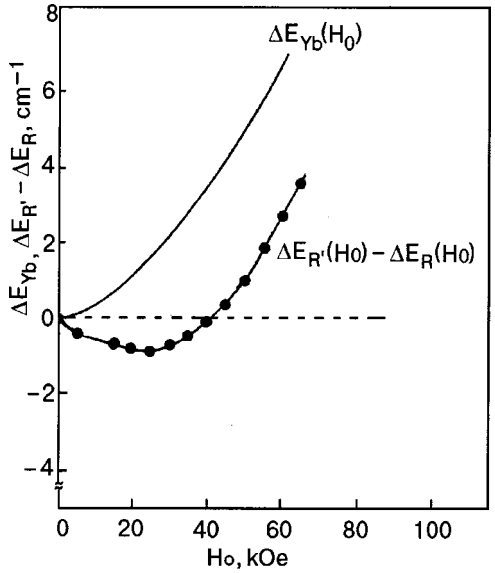

FIG. 14. Comparison between the experimentally obtained values of $\Delta E_{Yb}(H_0)$ and $\Delta E_{R'}(H_0) - \Delta E_R(H_0)$. The descriptions of $\Delta E_{Yb}(H_0)$, $\Delta E_{R'}(H_0)$ and $\Delta E_R(H_0)$ are given in the text.

the Cr^{3+} and Yb^{3+} spins, $\mathbf{D}(\mathbf{S}^{Cr} \times \mathbf{S}^{Yb})$, changes discontinuously in its sign and intensity. The change of the antisymmetric exchange interaction between the Cr^{3+} and Yb^{3+} spins at H_c should cause a drastic change of the R' band. Above H_c, the shape of the R' band resembles closely the density of states of the Cr^{3+} exciton coupled with the Yb^{3+} magnon, which implies that the cooperative excitation behaves as a two-particle continuous state above H_c. Therefore, it is concluded that the $Cr^{3+}-Yb^{3+}$ antisymmetric exchange interaction between the Cr^{3+} exciton and the Yb^{3+} magnon is attractive below H_c. On the contrary, its attractive force vanishes above H_c.

3.2. Cooperative excitation between Cr^{3+} exciton and Yb^{3+} exciton

Figure 15 shows the absorption spectra in the energy region between 23800 cm^{-1} and 24000 cm^{-1}. These spectra correspond to the cooperative transition consisting of the $^4A_{2g} \rightarrow {}^2E_g$ transition of Cr^{3+} and the $^2F_{7/2} \rightarrow {}^2F_{5/2}$ transition

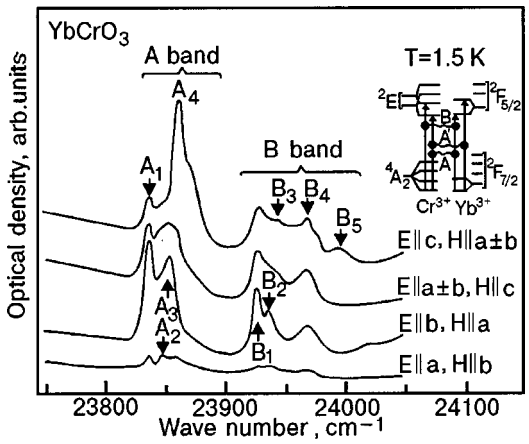

FIG. 15. Optical absorption spectra of $YbCrO_3$ at 1.5 K. *E* and *H* denote the electric and magnetic vectors of the incident light, respectively.

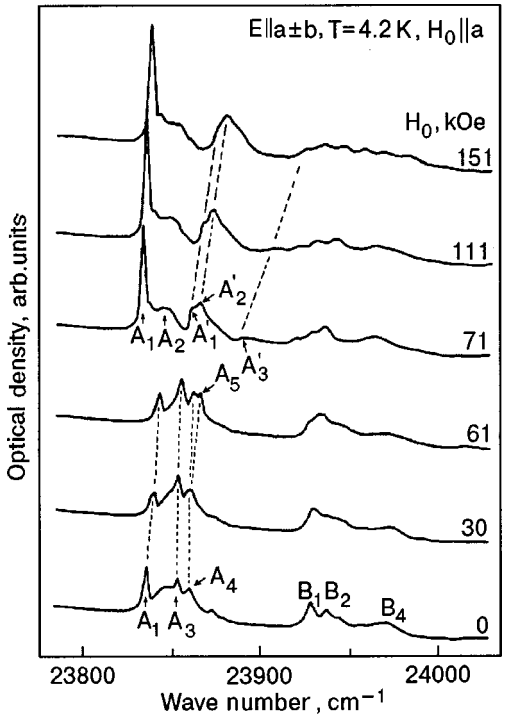

FIG. 16. Magnetic field dependence of the *A* and *B* bands of $YbCrO_3$ at 4.2 K.

of Yb^{3+} in $YbCrO_3$. The average energy of the *R* lines is 13695.6 cm^{-1}. Since this Cr^{3+} exciton has a negative energy dispersion of -16 cm^{-1}, the energy of the Cr^{3+} exciton at the Brillouin zone boundary is estimated at 13679.6 cm^{-1}. On the other hand, the lowest energy of the $^2F_{7/2} \rightarrow {}^2F_{5/2}$ transition of Yb^{3+} is 10164.6 cm^{-1} [Ref. 24]. The sum of the energies of the Cr^{3+} exciton and the Yb^{3+} exciton at the Brillouin zone boundary is estimated at 23844.2 cm^{-1}, which is almost equal to the energy of the A_1 line (23836.0 cm^{-1}) in Fig. 15. The *A* and *B* bands are assigned as shown in the inset of Fig. 15.

Figure 16 shows the behavior of the *A* and *B* bands in a the magnetic field along the *a* axis. As is shown in Fig. 16, at the metamagnetic transition $H_c(=67$ kOe) the profile of the *A* band changes drastically. In particular, above H_c, a sharp and strong peak typical of a bound state appears on the low-frequency edge of the *A* band. Since the energy dispersion of the Cr^{3+} exciton corresponding to the $^4A_{2g} \rightarrow {}^2E_g$ transition is -16 cm^{-1}, the low-frequency edge of the *A* band corresponds to the $Cr^{3+}-Yb^{3+}$ exciton molecule at the Brillouin zone boundary. From the appearance of the bound state on the low-frequency edge of the *A* band above H_c, it is considered that the $Cr^{3+}-Yb^{3+}$ exciton molecule at the Brillouin zone boundary is strongly localized above H_c.

As we have said, the $Cr^{3+}-Yb^{3+}$ antisymmetric exchange interaction, $\mathbf{D}(\mathbf{S}^{Cr} \times \mathbf{S}^{Yb})$, in $YbCrO_3$ creates various cooperative excitations between the Cr^{3+} and Yb^{3+} elementary excitations. In the case of Cr^{3+} exciton–Yb^{3+} exciton system, the $Cr^{3+}-Yb^{3+}$ antisymmetric exchange interaction acts as a strong attractive force above H_c. Contrary to this, it acts on the Cr^{3+} exciton–Yb^{3+} magnon system as a strong attractive force below H_c. From this result, the sign of the antisymmetric exchange interaction between the Cr^{3+} exciton (^2E_g) and the Yb^{3+} exciton ($^2F_{5/2}$) is presumed to be

different from that between the Cr^{3+} exciton (^2E_g) and the Yb^{3+} magnon ($^2F_{7/2}$).

4. PHOTOINDUCED MAGNETISM

One of the recent topics of solid state physics is the photoinduced transformation of the electronic and magnetic state of matter. The magnetic states of several compounds such as $[Fe(ptz)_6](BF_4)_2$ (ptz=1-propyl-tetrazole),[27] $K_{0.4}Co_{1.3}[Fe(CN)_6]\cdot 5H_2O$ (Ref. 28), (In, Mn)As/GaSb (Ref. 29), have been revealed to be transformed to another state by photoirradiation. In the case of $[Fe(ptz)_6](BF_4)_2$, the ground state of Fe(II) is converted between the low-spin state ($t_2^6, S=0$) and the high-spin state ($t_2^4e^2, S=2$) by photoirradiation corresponding to the d–d transition.[27,30] In the case of $K_{0.4}Co_{1.3}[Fe(CN)_6]\cdot 5H_2O$ [Ref. 28], this compound can be switched reversibly back and forth between ferrimagnetism and paramagnetism by photoirradiation corresponding to the charge transfer transition between the Co and Fe sites. In a novel III–V-based magnetic semiconductor heterostructure p-(In, Mn)As/GaSb grown by molecular beam epitaxy, the ferromagnetic order is induced by photogenerated carriers.[29]

These studies on photoinduced magnetism are creating a new field of solid state physics. In connection with photoinduced magnetism, pioneering works have been done by Tsushima *et al.*,[31,32] Kovalenko *et al.*,[33,34] and Golovenchitz *et al.*[35] For instance, Kovalenko *et al.* have found that the linearly polarized illumination of yttrium iron garnet, $Y_3Fe_{5-x}Si_xO_{12}$, results in a spin-reorientation transition as a result of the photoinduced change of the crystalline magnetic anisotropy.[33,34] On the other hand, Tsushima *et al.* have observed a photoinduced spin-reorientation transition from the antiferromagnetic to the weak-ferromagnetic spin structure of $ErCrO_3$ by using a time-resolved spectroscopic method.[31,32] In this Section, we describe the photoinduced spin reorientation from $\Gamma_1(A_xG_yC_z;C_z^R)$ to $\Gamma_4(G_xA_yF_z;F_z^R)$ for $ErCrO_3$.

Let us briefly summarize the magnetic properties of $ErCrO_3$. $ErCrO_3$ is magnetically ordered below $T_{N1}=133$ K with a weak-ferromagnetic structure denoted as $\Gamma_4(G_xA_yF_z;F_z^R)$.[36] At 9.8 K, $ErCrO_3$ exhibits the temperature induced spin reorientation from $\Gamma_4(G_xA_yF_z;F_z^R)$ to $\Gamma_1(A_xG_yC_z;C_z^R)$, where the ferromagnetic moment disappears. Below 9.8 K, the Γ_4 phase can be recovered by applying a small external magnetic field ($H_0<1.5$ kOe) along the c axis.[37,38]

In order to generate the photoinduced spin reorientation, we used a Q-switched ruby laser (6943 Å, 25 ns in half-width, and with an output power of a few mJ) as a photo irradiation source. The absorption spectrum of Er^{3+} in $ErCrO_3$ was observed at 1.8 K to detect the photoinduced spin-reorientation transition from $\Gamma_1(A_xG_yC_z;C_z^R)$ to $\Gamma_4(G_xA_yF_z;F_z^R)$. Figure 17a shows the energy levels and the selection rule for the electric dipole transitions between the $^4I_{15/2}$ (denoted I' and I'') ground state and the $^4I_{9/2}$ (denoted b' and b'') excited state of Er^{3+} in $ErCrO_3$. As can be seen in the figure, the absorption spectrum for this transition is composed of four lines, which we label $I'b'$, $I'b''$, $I''b'$ and $I''b''$. In the $\Gamma_1(A_xG_yC_z;C_z^R)$ spin configuration, the $I'b'$ and $I''b''$ absorption lines are superimposed because

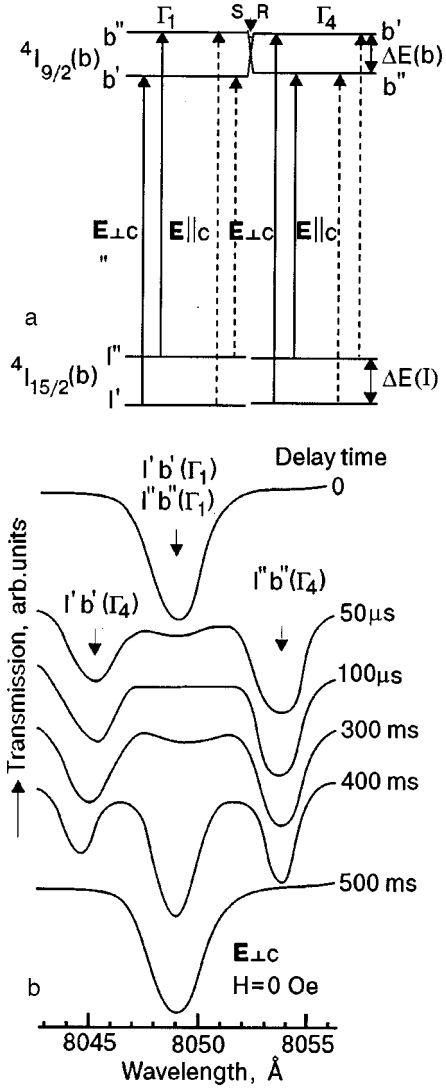

FIG. 17. (a) Schematic energy level diagram for the $^4I_{15/2}(I)\rightarrow{}^4I_{9/2}$ (b) transitions of $ErCrO_3$. Also shown are optical transitions and their polarization. (b) Time-resolved *Ib* absorption spectra after initial laser excitation.

$\Delta E(I)\sim\Delta E(b)\sim 10$ K. The four lines, however, are well resolved in the $\Gamma_4(G_xA_yF_z;F_z^R)$ spin configuration. For the case of $E\perp c$, the absorption lines $I'b'$ and $I''b''$ observed at 8049 Å are associated with the $\Gamma_1(A_xG_yC_z;C_z^R)$ spin configuration. In the $\Gamma_4(G_xA_yF_z;F_z^R)$ spin configuration, these absorption lines are observed at 8045 and 8054 Å. Figure 17b shows the time-resolved *Ib* absorption spectra after initial laser excitation at 7 K. It can be seen that $ErCrO_3$ undergoes a phase transition from $\Gamma_1(A_xG_yC_z;C_z^R)$ to $\Gamma_4(G_xA_yF_z;F_z^R)$ within 50 μs after the photoirradiation, and that it returns to the $\Gamma_1(A_xG_yC_z;C_z^R)$ phase in about 400 ms after the irradiation.

The idea of a photoinduced spin-reorientation transition is based on the following argument. In many $RCrO_3$ compounds and $RFeO_3$, the direction of the easy axis of magnetization changes easily as the temperature changes or an external magnetic field is applied. It is expected that the critical temperature of spin reorientation is changed when some of the magnetic ions are substituted by magnetic impurities. For example, $YFe_{1-x}Co_{x/2}Ti_{x/2}O_3$ ($x=0.003$) undergoes the spin

reorientation from $\Gamma_2(F_xC_yG_z)$ to $\Gamma_4(G_xA_yF_z)$ at 247 K, while $YFeO_3$ does not show any spin reorientation.[39] The magnetic anisotropy of $YFeO_3$ influenced by a small amount of Co^{2+} is responsible for the appearance of spin reorientation in $YFe_{1-x}Co_{x/2}Ti_{x/2}O_3$ ($x=0.003$).[40] Therefore, the photoirradiation is regarded as a transient substitution of the magnetic ions by magnetic impurities, which presumably induces the phase transition when the sample is kept near the critical temperature. However, in general, both of thermomagnetic effect and transient impurity effect are induced by laser irradiation. The transient impurity effect is justified if the phase transition is induced before any nonradiative and radiative decay of the photoexcited state occurs. Since the lifetime of the ^2E_g state of Cr^{3+} is quite long (several ms), photoirradiation corresponding to the $^4A_{2g}\rightarrow{}^2E_g$ transition of Cr^{3+} in $ErCrO_3$ is the most effective way to bring about the photoinduced spin-reorientation transition. In order to further prove the transient impurity effect, the time-resolved spectroscopic measurement by using an ultrashort (femtosecond) laser will be indispensable.

Finally, in connection with photoinduced magnetism, it should be noted that in some crystals of the family of antiferromagnetic garnets $Ca_3Mn_2Ge_3O_{12}$, etc., photoinduced phenomena have been discovered by Eremenko, Gnatchenko, *et al.*[41–44] Photoirradiation with visible light gives rise to long-lived changes: linear birefringence, magnetic moment in the antiferromagnetic state, and augmentation of optical absorption coefficient. The observed photoinduced changes of the optical and magnetic properties in antiferromagnetic garnets persist for a long time after the illumination is switched off. The discovery of sufficiently great photoinduced changes of the refractive index and absorption coefficient in antiferromagnetic garnets will create a new field of optical and magneto-optical recording.

5. RECENT FRONTIER RESEARCH ON APPLICATION

We shall describe briefly the recent research on the application of magneto-optical materials using their unique magneto-optical nonreciprocity. The most advantageous peculiarity of magneto-optical materials lies in the fact that the propagation of light in those magnetic materials is antisymmetric (nonreciprocal) with respect to time inversion.

One such application is the use of highly bismuth-substituted rare-earth iron garnets for optical isolators and circulators in a near-infrared wavelength region.[45,46] Another is the use of diluted magnetic semiconductors such as CdMnTe for integrated magneto-optical waveguides in a shorter-wavelength region.[47] A schematic figure of an integrated magneto-optical guide on a GaAs substrate, achieved by Zaets and Ando, is shown in Fig. 18.[48]

Finally, in addition to the above so-called magneto-optical recording has been implemented in a real device for a rewritable high-density nonvolatile memory. It shows more development year by year. The most recent progress in higher-density magneto-optical recording, including super-resolution limiting recording densities smaller than a domain size, has been reviewed in a recent book by Kaneko.[49]

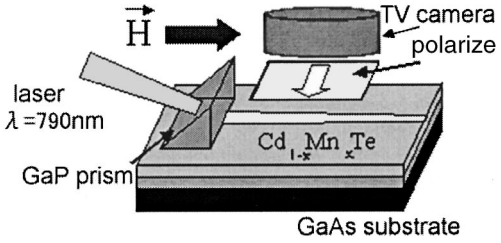

FIG. 18. Magneto-optical waveguide of $Cd_{1-x}Mn_xTe$ on GaAs substrate. The TE mode of light scattered from the surface of the waveguide is observed by illuminating with a TM-mode laser with $\lambda=790$ nm (Ref. 48).

6. CONCLUSION

We have investigated various kinds of magneto-optical properties for rare earth orthochromites. In $RCrO_3$ (R=Tb, Dy and Ho), from the analysis of Cr^{3+} exciton absorption, we have inferred that these compounds exhibit an anomalous spin reorientation in a magnetic field along the *b* axis, where the weak ferromagnetic moment of the Cr^{3+} spins rotates in the *ac* plane perpendicular to the *b* axis. It is quite difficult to elucidate the microscopic mechanism of this phase transition by means of magnetization measurements.

In $RCrO_3$ (R=Dy and Ho), we have elucidated the breakdown of the $\mathbf{k}=0$ selection rule for the Cr^{3+} exciton absorption induced by the disorder of the R^{3+} spin configuration. The magneto-elastic effect due to the R^{3+} (R=Dy and Ho) ion is extraordinarily large because of the strong spin–orbit interaction. Through the medium of this strong magneto-elastic effect, the disorder of the R^{3+} spin configuration causes the breakdown of the $\mathbf{k}=0$ selection rule of the Cr^{3+} exciton absorption, which is reflected in the appearance of the anomalous satellite band R' on the lower-energy side of the free Cr^{3+} exciton absorption.

In $YbCrO_3$, we have observed various kinds of cooperative excitations such as a Cr^{3+} exciton coupled with an Yb^{3+} magnon, and a $Cr^{3+}-Yb^{3+}$ exciton molecule in the visible region, which are induced by the antisymmetric exchange interaction between the Cr^{3+} and Yb^{3+} spins. In these cooperative excitations, the $Cr^{3+}-Yb^{3+}$ antisymmetric exchange interaction acts as a strong attractive force, which is responsible for the appearance of the bound state at the lower frequency edge in the cooperative excitations.

In $ErCrO_3$, a photoinduced spin reorientation from Γ_1 to Γ_4 takes place within 50 μs after photoirradiation corresponding to the $^4A_{2g}\rightarrow{}^2E_g$ transition of Cr^{3+}, and it returns to the initial spin configuration in about 400 ms. This phenomenon was detected by the time-resolved Er^{3+} absorption spectra corresponding to the $^4I_{15/2}\rightarrow{}^4I_{9/2}$ transition. The photoirradiation is regarded as a transient substitution of the magnetic ions by magnetic impurities, which presumably induces the phase transition. In order to further prove the transient impurity effect, time-resolved spectroscopic measurements by using an ultrashort laser will be indispensable.

Finally, in connection with the recent topics of magneto-optics such as optical isolator, integrated magneto-optical waveguide, and magneto-optical recording, we briefly reviewed the recent frontier research on application mainly developed in Japan.

The authors would like to thank the many scientists over

the years who have given us the opportunity to collaborate with them on our recent work. Some of them are S. Sugano, I. Tsujikawa, K. Aoyagi, H. Kamimura, W. M. Yen, T. Tamaki, N. Watanabe, J. Dillon, Jr., K. V. Rao, P. L. Richards, M. Pardavi-Horvath, and H. Szymczak.

V. V. Eremenko should undoubtedly be specially cited as an exceptionally eminent physicist among those. The authors also would like to thank many other younger research colleagues for pleasant collaboration in many subjects on many occasions.

This work was partly supported by the Science and Technical Research Laboratories of the Japan Broadcasting Corporation, and a Grant-in-Aid for Science Research from the Ministry of Education, Science, Sports and Culture.

*E-mail: cnori@mail.ecc.u-tokyo.ac.jp

[1] *Advance in Magneto-Optics*, in *Proceedings of the International Symposium in Magneto-Optics*, J. Magn. Soc. Jpn. **11**, Supplement, S1 (1987).
[2] *Advance in Magneto-Optics*, in *Proceedings of the 2nd International Symposium in Magneto-Optics*, Fiz. Nizk. Temp. **18**, Supplement, No. S1, (1992).
[3] V. V. Eremenko, N. F. Kharchenko, Yu. G. Litvinenko, and V. M. Naumenko, *Magneto-Optics and Spectroscopy of Antiferromagnets*, Springer-Verlag (1992).
[4] A. K. Zvezdin and V. A. Kotov, *Modern Magnetooptics and Magnetooptical Materials*, Institute of Physics Publishing (1997).
[5] S. Sugano and N. Kojima (Ed.), *Magneto-Optics*, Springer (2000).
[6] S. Quezel-Ambrunaz and M. Mareschal, Bull. Soc. Fr. Mineral. Crystallogr. **LXXXVI**, 204 (1963).
[7] E. F. Bertaut, in *Magnetism III*, G. T. Rado and H. Suhl (Eds.), Academic, New York (1963), p. 149.
[8] R. Courths and S. Hüfner, Z. Phys. **B24**, 193 (1976).
[9] N. Kojima, I. Tsujikawa, and K. Tsushima, *Proc. Int. Conf. Ferrites*, Kyoto (1980), p. 769.
[10] R. M. Hornreich, B. M. Wanklyn, and I. Yaeger, Int. J. Magn. **2**, 77 (1972).
[11] E. F. Bertaut, J. Mareschal, and G. F. de Vries, J. Phys. Chem. Solids **28**, 2143 (1967).
[12] J. D. Gordon, R. M. Hornreich, S. Shtrikman, and B. M. Wanklyn, Phys. Rev. B **13**, 3012 (1976).
[13] K. Tsushima, T. Tamaki, and R. Yamaura, in *Proceedings of the International Conference in Magnetism: ICM-73*, Nauka, Moscow (1974) **5**, p. 270.
[14] Y. Uesaka, I. Tsujikawa, K. Aoyagi, K. Tsushima, and S. Sugano, J. Phys. Soc. Jpn. **31**, 1380 (1971).
[15] B. L. Joesten and F. C. Brown, Phys. Rev. **148**, 919 (1966).
[16] S. Lai and M. V. Klein, Phys. Rev. Lett. **44**, 1087 (1980).
[17] M. V. Klein, M. D. Sturge, and E. Cohen, Phys. Rev. B **25**, 4331 (1982).
[18] N. Kojima, I. Tsujikawa, K. Aoyagi, and K. Tsushima, J. Phys. Soc. Jpn. **54**, 4804 (1985).
[19] N. Kojima, I. Tsujikawa, and K. Tsushima, J. Phys. Soc. Jpn. **54**, 4794 (1985).
[20] N. Kojima, K. Aoyagi, K. Tsushima, I. Tsujikawa, and S. Sugano, J. Phys. Soc. Jpn. **49**, 1463 (1980).
[21] R. L. Greene, D. D. Sell, W. M. Yen, A. L. Schawlow, and R. M. White, Phys. Rev. Lett. **15**, 656 (1965).
[22] N. Kojima, H. Okada, M. Kawarazaki, I. Mogi, M. Takeda, G. Kido, Y. Nakagawa, and K. Tsushima, J. Phys. Soc. Jpn. **64**, 3082 (1995).
[23] N. Kojima, M. Kawarazaki, H. Okada, I. Mogi, M. Takeda, G. Kido, Y. Nakagawa, and K. Tsushima, J. Phys. Soc. Jpn. **64**, 3090 (1995).
[24] N. Kojima, K. Tsushima, and I. Tsujikawa, J. Phys. Soc. Jpn. **49**, 1449 (1980).
[25] S. Shtrikman, B. M. Wanklyn, and I. Yaeger, Int. J. Magn. **1**, 327 (1971).
[26] N. Kojima, K. Tsushima, S. Kurita, and I. Tsujikawa, J. Phys. Soc. Jpn. **49**, 1456 (1980).
[27] S. Decurtins, P. Gütlich, C. P. Köhler, H. Spiering, and A. Hauser, Chem. Phys. Lett. **105**, 1 (1984).
[28] O. Sato, T. Iyoda, A. Fujishima, and K. Hashimoto, Science **272**, 704 (1996).
[29] S. Koshihara, A. Oiwa, M. Hirasawa, S. Katsumoto, Y. Iye, C. Urano, H. Takagi, and H. Munekata, Phys. Rev. Lett. **78**, 4617 (1997).
[30] A. Hauser, Chem. Phys. Lett. **124**, 545 (1986).
[31] S. Kurita, K. Toyokawa, K. Tsushima, and S. Sugano, Solid State Commun. **38**, 235 (1981).
[32] T. Tamaki and K. Tsushima, J. Magn. Magn. Mater. **31–34**, 571 (1983).
[33] V. F. Kovalenko, E. S. Kolezhuk, and P. S. Kuts, Sov. Phys. JETP **54**, 742 (1981).
[34] V. F. Kovalenko, P. S. Kuts, and V. P. Sokhatskii, Sov. Phys. Solid State **24**, 80 (1982).
[35] E. I. Golovenchitz and V. A. Sanina, Fiz. Tverd. Tela, **24**, 375 (1982) [Sov. Phys. Solid State **24**, 213 (1982)].
[36] M. Eibschütz, L. Holmes, J. P. Maita, and L. G. Van Uitert, Solid State Commun. **8**, 1815 (1970).
[37] M. Kaneko, S. Kurita, and K. Tsushima, J. Phys. Solid State Phys. **10**, 1979 (1977).
[38] K. Toyokawa, S. Kurita, and K. Tsushima, Phys. Rev. B **19**, 274 (1979).
[39] H. Makino and Y. Hidaka, IEEE Trans. Magn. **MAG-8**, 444 (1972).
[40] M. Abe, K. Kaneta, M. Gomi, Y. Mori, and S. Nomura, Jpn. J. Appl. Phys. **16**, 1799 (1977).
[41] V. V. Eremenko, S. L. Gnatchenko, I. S. Kachur, V. G. Piryatinskaya, A. M. Ratner, and V. V. Shapiro, Phys. Rev. B **61**, 10670 (2000).
[42] V. V. Eremenko, S. L. Gnatchenko, I. S. Kachur, V. G. Piryatinskaya, M. B. Kosmyna, B. P. Nazarenko, and V. M. Puzikov, Appl. Phys. Lett. **79**, 734 (2001).
[43] V. V. Eremenko, S. L. Gnatchenko, I. S. Kachur, V. G. Piryatinskaya, A. M. Ratner, V. V. Shapiro, M. Fally, and R. A. Rupp, Fiz. Nizk. Temp. *27*, 30 (2001) [Low Temp. Phys. **27**, 22 (2001)].
[44] V. A. Bedarev, V. I. Gapon, S. L. Gnatchenko, M. Baran, R. Szymczak, J. M. Desvignes, and H. Le Gall, Fiz. Nizk. Temp., **28**, 51 (2002) [Low Temp. Phys. **28**, 37 (2002)].
[45] K. Tsushima, *Growth of a Highly Bismuth-Substituted Rare-earth Iron Garnet and its Application to an Optical Isolator*, in *Japan Annual Reviews in Electronics, Computers Tele-Communications*, Vol. 21, *Recent Magnetics for Electronics*, Y. Sakurai (Ed), Ohmsha & North-Holland Amsterdam & Tokyo (1985/1986), p. 113.
[46] A general review is given by K. Shinagawa: *Faraday and Kerr Effects in Ferromagnets, Magneto-Optics, Springer Series in Solid State Sciences*, Vol. 128, S. Sugano and N. Kojima (Eds.) (2000), p. 137.
[47] A general review is given, for example, by K. Ando, *Magneto-Optics of Diluted Magnetic Semiconductors: New Materials and Applications, Magneto-Optics, Springer Series in Solid State Sciences*, Vol. 128, S. Sugano and N. Kojima (Eds.) (2000), p. 211.
[48] W. Zaets and K. Ando, Appl. Phys. Lett. **77**, 1593 (2000).
[49] A general review is given by M. Kaneko, *Magneto-Optical Recording, Magneto-Optics, Springer Series in Solid State Sciences*, Vol. 128, S. Sugano and N. Kojima (Eds) (2000), p. 271.

This article was published in English in the original Russian journal. Reproduced here with stylistic changes by the Translation Consultant.

Elementary excitations in solid oxygen (Review)

Yu. A. Freiman*

B. Verkin Institute for Low Temperature Physics and Engineering of the National Academy of Sciences of Ukraine, 47 Lenin Ave., Kharkov 61103, Ukraine

H. J. Jodl**

Fachbereich Physik, Universität Kaiserslautern, Erwin Schrödinger Strasse, D 67663 Kaiserslautern, Germany; LENS, European Laboratory for Non Linear Spectroscopy, Largo E. Fermi 2, I-50125 Firenze, Italy

(Submitted May 13, 2002)
Fiz. Nizk. Temp. **28**, 691–708 (July 2002)

Theoretical results on lattice excitations in solid oxygen at equilibrium vapor pressure are reviewed with the emphasis on the behavior of phonons, librons, and magnons in the orientationally and magnetically ordered α phase. Results on the magnetooptics of solid oxygen and their impact on the advancement of magnetic studies of solid oxygen are briefly reviewed. Some results under discussion are new: among these are theoretical results on the magnon heat capacity, the analysis of the behavior of librons at the α–β transition, and anisotropy of the magons spectrum. © *2002 American Institute of Physics.*
[DOI: 10.1063/1.1496658]

1. INTRODUCTION

Solid oxygen, a unique combination of a molecular cryocrystal and a magnet

Solid oxygen belongs to a small group of atomic (He, Ne, Ar, Kr, Xe) or simple molecular solids (H_2,N_2,O_2,F_2,CO,CO_2,N_2O,CH_4), which are often lumped together as solidified gases or cryocrystals.

The oxygen molecule, owing to unique combination of the molecular parameters forms a substance which in all phases—solid, liquid, and gaseous—is a physical object of considerable fundamental interest.

In the ground electronic state the oxygen molecule possesses nonzero electronic spin $S=1$, which makes the O_2 molecule a magnetic system. As a result, solid oxygen combines properties of a molecular crystal and of a magnet.

The low-temperature phase of solid oxygen is the only electron-spin antiferromagnetic insulator consisting of a single element. Why the combination of a simple molecular crystal and a magnet is so interesting? The answer is the following: the binding energy in molecular cryocrystals is determined by weak van der Waals forces and, unlike conventional magnets, the magnetic interaction is a significant part of the total lattice energy. Namely, the binding energy in the case of solid oxygen is of the order 1000 K and the magnetic energy is of the order of 100 K, that is, makes up around 10% of the binding energy. In the case of conventional magnets, the magnetic energy is of the same order, but the binding energy is an order of magnitude higher; that is, the magnetic energy is at most about 1% of the lattice energy. Therefore the magnetic and lattice properties in solid oxygen are very closely related, a fact which manifests itself in numerous anomalies of virtually all its properties—thermal, magnetic, acoustic, optical, etc.

Studies of solid oxygen commenced at the very beginning of the twentieth century. The modern state of the art is a result of the combined continuous efforts of a large number of cryogenic laboratories throughout the world. At the present time solid oxygen is a playground for the most sophisticated modern solid-state experimental methods, including studies in diamond anvil cells (DAC) and high magnetic fields in combination with Raman, infrared (FIR, FTIR), synchrotron x-ray, and Brillouin and other optical technics.

Under equilibrium vapor pressure oxygen exists in three crystallographic modifications.[1]

Neutron diffraction[2–5] and x-ray studies[1,6,7] have shown that the low-temperature α phase of oxygen is orientationally and magnetically ordered and has a monoclinic base-centered structure of symmetry $C2/m$. It was established that α-O_2 has the simplest orientational structure, in which the molecular axes are collinear and perpendicular to the close-packed (001) layers (Fig. 1).

The structure of the intermediate β phase of solid oxygen was established by Hörl in an electron-diffraction study[8] and confirmed in neutron-diffraction[2–5] and x-ray studies.[1,7] It was shown that β-O_2 has a rhombohedral lattice of symmetry $R\bar{3}m$ with the same extremely simple orientational structure as α-O_2 (Fig. 2a). This lattice can be seen as a distorted fcc structure obtained by packing not spherical but

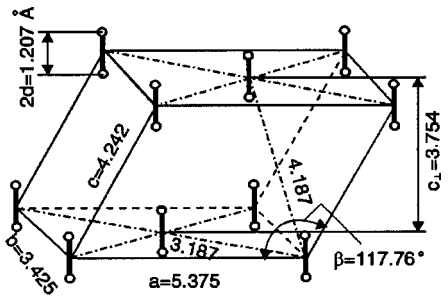

FIG. 1. Structure of α-O_2.

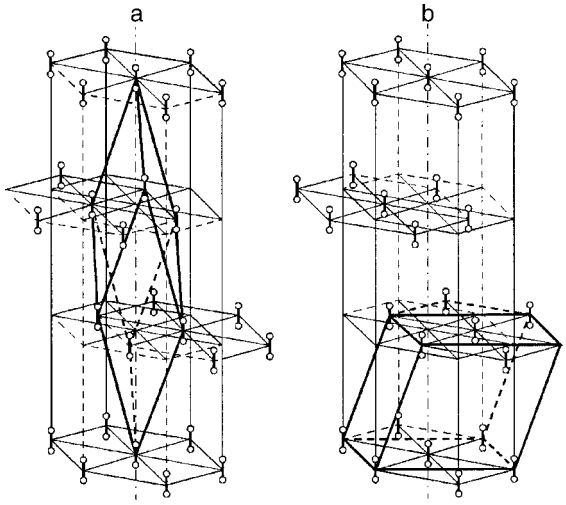

FIG. 2. Structure of β-O_2 in rhombohedral and hexagonal axes (a). The structure of β-O_2 can be represented as a monoclinic cell isostructural to α-O_2 (b).

dumbbell-shaped molecules oriented along one of the spatial diagonals of the cube. The primitive rhombohedral cell is found to be stretched in the direction $\langle 111 \rangle$ singled out by the molecular axes. The angle of the rhombohedron is found to be about 45° instead of 60° for the fcc lattice.

The structures of the two low-temperature phases are similar, and formally, a monoclinic cell can be singled out in β-O_2 as well (Fig. 2b).

As was shown in a single-crystal x-ray study by Jordan *et al.*,[9] γ-O_2 has an eight-molecule cubic cell with an orientationally disordered structure of space group $Pm3n$ (Fig. 3). Molecules in the cell are located in two nonequivalent states. Two of the eight molecules (''spheres'') have a spherically symmetric distribution of electron density, while the remaining six molecules (''discs'') have an electron density distribution in the form of an oblate spheroid. The disc-shaped molecules form chains extending in the three $\langle 100 \rangle$ directions.

At the present time the existence of six solid-state phases is established unambiguously.[10] In addition to the α, β, and γ phases, which exist under equilibrium vapor pressure three high- pressure stable phases exist in the investigated domain of pressures and temperatures. They are the δ (''orange''), stable at room temperature between 9.6 and 10 GPa, ϵ (''red'') (10–96 GPa), and ζ (metallic) (above 96 GPa)

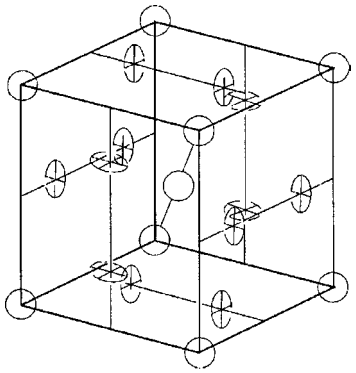

FIG. 3. Structure of γ-O_2.

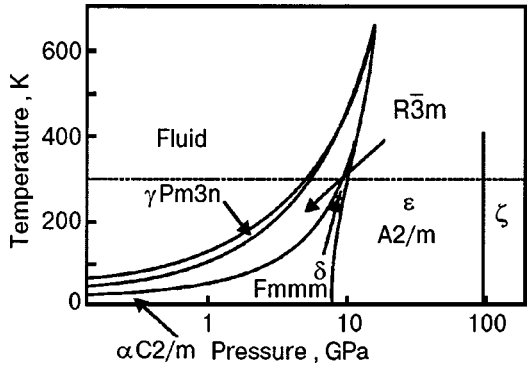

FIG. 4. Phase diagram of solid oxygen.

phases. The resulting $P-T$ phase diagram, which reflects the phase boundaries of these six phases, is given in Fig. 4.

2. CHARACTERISTIC FEATURES OF ELEMENTARY EXCITATION SPECTRA IN SOLID OXYGEN

Compared with a conventional magnet, the problem of the elementary excitation spectrum in solid oxygen presents a considerable challenge both to the experimenters and theoreticians. In the case of α-O_2 we are dealing with three systems of coupled quasiparticles—phonons, librons, and magnons. Though β-O_2 has the simplest orientational structure among the molecular cryocrystals, the presence of the strong short-range magnetic order makes the β phase quite a cumbersome problem. A very specific case is the orientationally and magnetically disordered γ phase.

The first calculations of the lattice dynamics of solid oxygen were carried out in the 1970s.[1,7,11,12] Though no account has been taken in these calculations of the magnetic nature of solid oxygen, they represent a necessary and rather informative step in the development of the theory. They provided a test, in the first approximation, of various potentials, enabled identification in Raman and IR spectra, and gave an estimate of the effect of anharmonicity.

Important estimates concerning translational and librational vibrations follow from simple mean-field considerations.[13,14] Translationally the molecules in α-O_2 vibrate as three-dimensional, nearly harmonic oscillators. Two of the fundamental frequencies that correspond with the vibrations in the ab plane are nearly equal, while the third fundamental frequency for the vibrations in the $c_\perp$ direction is about 50% higher. The potential is markedly stiffer in the $c_\perp$ direction. This is confirmed by the smaller root-mean-square (rms) amplitude of vibrations in this direction (Table I). As can be seen from Table I, the rms amplitudes are quite different in the three independent crystal directions, which gives an indication of the crystal anisotropy. The ratio of the ground state rms translational displacement to the intermolecular distance R_{nn} is $\langle u_a^2+u_b^2+u_{c_\perp}^2 \rangle^{1/2}/R_{nn}=0.056$, which is nearly twice as large as for solid N_2 [Ref. 16].

The librational states of the molecules are rather localized in α- and β-O_2 and look like weakly anharmonic two-dimensional oscillator states, slightly anisotropic in the case of α-O_2 and isotropic in β-O_2 (Table I). The lower frequency in α-O_2 corresponds with liberation about the a axis,

TABLE I. Translational and librational amplitudes in α- and β-O_2.

α-O_2				β-O_2			
Parameter	Value	Parameter	Value	Parameter	Value	Parameter	Value
$\langle u_a^2 \rangle^{1/2}$	0.1092 Å[a]		9.1° [b]	$\langle u_{a;b}^2 \rangle^{1/2}$	0.1200 Å[c]		10.4° [d]
$\langle u_b^2 \rangle^{1/2}$	0.1115 Å[a]	$\langle \vartheta^2 \rangle^{1/2}$	10.84° [a]			$\langle \vartheta^2 \rangle^{1/2}$	11.164° [c]
$\langle u_{c_\perp}^2 \rangle^{1/2}$	0.0889 Å[a]		12.8° [e]	$\langle u_{c_\perp}^2 \rangle^{1/2}$	0.0940 Å[c]		11.6° [f]

[a]Theory[14] for $T=0$ K.
[b]Experiment[15] for $T=0$ K.
[c] Theory[14] for $T=30$ K.
[d]Experiment[15] for $T=28$ K.
[e]Theory[11] for $T=10$ K.
[f]Experiment[13] for $T=30$ K.

the higher one with libration about the b axis. The rms angular displacements are about 11°, as compared with 16° for α-N_2 at $T=0$ K.[16]

As can be seen from a comparison of the ground state rms amplitudes, the translational vibrations in solid oxygen are more anharmonic than those in solid nitrogen, but for librational vibrations the reverse is true. This difference reflects the distinction in the structures of the intermolecular potentials for the two substances and ultimately the difference in the nature of the stability of α-O_2 and α-N_2.

The zero-point energy E_{zp} at $P=0$ for α-O_2 according to Ref. 17 is 204.7 K. Judging from the rms amplitudes obtained in this paper, which are slightly overestimated compared with data from Table I, E_{zp} is overestimated as well and should be considered as an upper bound. The zero-point energy is approximately 20% of the binding energy, of which approximately 40% is due to the librational motion. The high value of the reduced zero-point energy indicates that O_2 displays properties typical for quantum crystals. One such property is a small value of the ratio $T_{\rm melt}/\Theta_D$ ($T_{\rm melt}$ is the melting temperature, Θ_D is the Debye temperature), which for solid O_2 is approximately 0.5 (the inequality $T_{\rm melt}/\Theta_D<1$ is a recognized signature of a quantum crystal). It is interesting to note that although the reduced value of the zero-point energy for solid N_2 is nearly the same as that for solid O_2 (see Table 10.1 in Ref. 16), the ratio $T_{\rm melt}/\Theta_D$ for solid N_2 is approximately 0.75, markedly higher than for solid O_2, due to less anharmonic translational vibrations.

The problem of the magnetism of solid oxygen turned out to be a considerable challenge. Ever since the mid-sixties, when neutron diffraction experiments[2–5] showed unambiguously that α-O_2 is an antiferromagnet, the magnitude of the exchange interaction between oxygen molecules has been a controversial subject of numerous studies. A rather surprising thing is that the first estimates of the exchange field were obtained not from data on the magnetic susceptibility—a property directly connected with the exchange field, but "in a series of elegant experiments" (citing Ref. 18) on the double intramolecular electronic excitation transitions by Eremenko, Litvinenko and co-workers.[19–21]

The lowest electron configuration of the oxygen molecule gives rise to three states: $^3\Sigma_g^-$, $^1\Delta_g$, $^1\Sigma_g^+$.

The transitions

$$(^3\Sigma_g^-)\rightarrow(^1\Delta_g) \quad 7882\ \text{cm}^{-1},$$

$$(^3\Sigma_g^-)\rightarrow(^1\Sigma_g^+) \quad 13120\ \text{cm}^{-1}$$

are electric dipole forbidden and are very weak. In the condensed phases and in compressed gaseous oxygen, the intensity of these transitions increases significantly. In addition, three new absorptions are found and assigned to simultaneous excitation of a pair of oxygen molecules as follows:

$$(^3\Sigma_g^-)(^3\Sigma_g^-)\rightarrow(^1\Delta_g)(^1\Delta_g) \quad 16800\ \text{cm}^{-1},$$

$$(^3\Sigma_g^-)(^3\Sigma_g^-)\rightarrow(^1\Delta_g)(^1\Sigma_g^+) \quad 21000\ \text{cm}^{-1},$$

$$(^3\Sigma_g^-)(^3\Sigma_g^-)\rightarrow(^1\Sigma_g^+)(^1\Sigma_g^+) \quad 27700\ \text{cm}^{-1}.$$

Excellent comprehensive spectroscopic studies of these double molecular transitions are presented in papers by Landau *et al.*[22] and Eremenko *et al.*[19] The effects of temperature and impurity (N_2) have been studied by Eremenko, Litvinenko, and Garber.[20,21] An overview of these double transitions are presented in Fig. 5.

To give an interpretation of the spectroscopic data obtained and their connection with the magnitude of the exchange field, we quote the abstract to the paper by Litvinenko, Eremenko, and Garber, "Antiferromagnetic ordering effect on the light absorption spectrum by crystalline oxygen:"[21] "The optical double transition spectrum of crystalline oxygen is studied in the frequency range of 15000 to 31000 cm^{-1} at different temperatures (5 to 27 K) and nitrogen concentrations (0 to 40%). A sharp integral intensity decrease of the absorption bands, their shift, and broadening

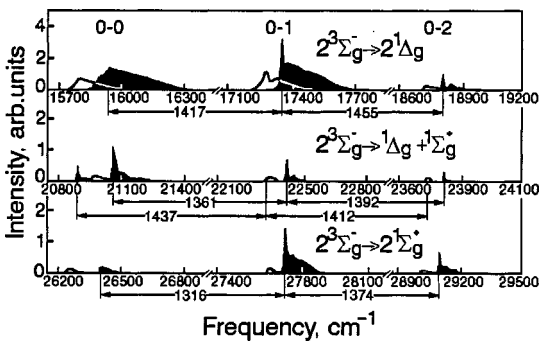

FIG. 5. General view of the light absorption spectrum by solid α-oxygen at $T=5$ K in the 15000 to 30000 cm^{-1} region: $2^3\Sigma_g^-\rightarrow 2^1\Delta_g$ (v=0,1,2,3), $2^3\Sigma_g^-\rightarrow {}^1\Delta_g+{}^1\Sigma_g^+$ (v=0,1,2,3), and $2^3\Sigma_g^-\rightarrow 2^1\Sigma_g^+$ (v=0,1,2,3).[21] The lines at the frequency scale are calculated values for free molecules.

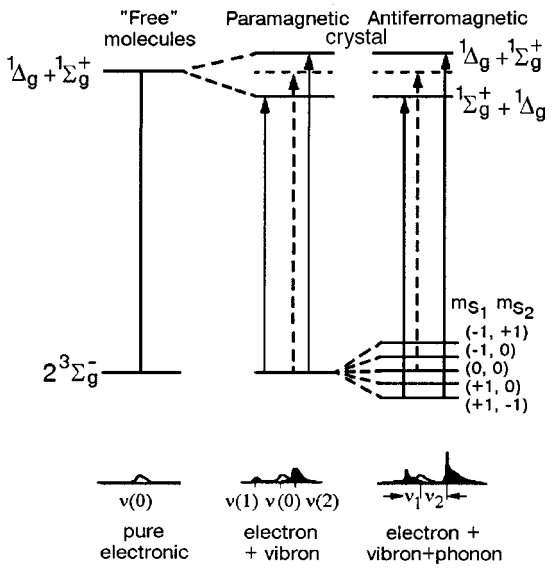

FIG. 6. Energy level diagram of oxygen in the region of a possible vibronic transition in the free molecule as well as in the crystal with magnetic interactions.[21]

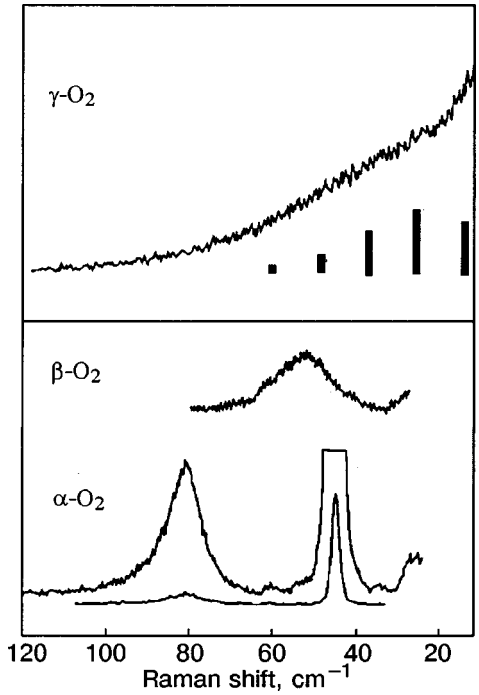

FIG. 7. Raman spectra of α-, β- and γ-oxygen in the low-frequency region. Different spectra are monitored with different resolutions. The vertical lines are the contributions from freely rotating oxygen molecules at $T=48$ K (Ref. 15).

are found in the temperature range investigated. With the insertion of nitrogen into oxygen new absorption bands with spectral positions close to the pure oxygen band frequencies appeared in the oxygen spectrum. The results show that the double transitions in oxygen are considerably induced by exchange interaction. It is also shown that the 0–0 band intensity of the $2^3\Sigma_g^- \rightarrow 2^1\Delta_g$ and $2^3\Sigma_g^- \rightarrow 2^1\Sigma_g^+$ transitions is determined by the interaction not with acoustic phonons, as it was considered before, but with magnons corresponding to the Brillouin zone boundary and having energy equal to the exchange one $g\mu_B H_E$. The 0–0 band of the $2^3\Sigma_g^- \rightarrow 2^1\Delta_g$ and $2^3\Sigma_g^- \rightarrow {}^1\Sigma_g^+ + {}^1\Sigma_g^+$ transition is interpreted as a pure electronic band. A consistent scheme, based on considering the exchange splitting of the $^3\Sigma_g^-$ state of the oxygen molecules and the magnon excitation at light absorption is suggested to explain the double transition structures and their band behaviors at magnetic ordering.''

In the absence of interaction between a pair of excited molecules, the observed spectrum is simply the sum of the excitations of the two molecules. The perturbations arising from the molecular interactions (of the Coulomb, exchange, and molecular types) lift the degeneracy, strengthen the corresponding transition, and produce splitting and frequency shifts (Fig. 6). The shift decreases with temperature and also with increasing concentration of N_2. The exchange energy, as measured by the magnon shift, is constant up to 10 K and then falls off smoothly with increasing temperature to about 85% of its low-temperature value before falling rapidly to zero at the α–β transition.

The series of papers cited as Refs. 19–21 had a pronounced impact on studies of teh magnetic and optical properties of solid oxygen. A large number of experimental and theoretical works published in the seventies and subsequent years (see, for instance, Refs. 18, 23–30) were directly inspired by results of the magnetooptical studies by Eremenko *et al.* Effects found in these studies and their interpretation are still a subject of great interest for investigators (see Refs. 31–33).

3. LIBRONS

The first Raman studies of condensed oxygen were made by Cahill and Leroi.[15] In the lattice frequency range they found (Fig. 7) one strong line in the β phase (at $\approx$51 cm^{-1} at 28 K), and two lines in the α phase (at $\approx$43 cm^{-1} and $\approx$78 cm^{-1} at 22 K).

In accordance with the correlation diagram in Fig. 8, they assigned the line at 51 cm^{-1} in β-O_2 to the twofold-degenerate E_g libration and the low frequency band in α-O_2 to the B_g libration (libration around the **a** axis and the higher frequency one to the A_g libration (libration around the **b** axis).

Mathai and Allin[25] in the Raman study of α-$^{16}O_2$ and α-$^{18}O_2$ isotopes confirmed Cahill and Leroi's assignment but found that the isotope shift of the two modes were only about two-thirds of that to be expected on the basis of the inverse ratio of the square roots of the reduced masses. The discrepancy was attributed to differences in the anharmonicity of the two isotopes.

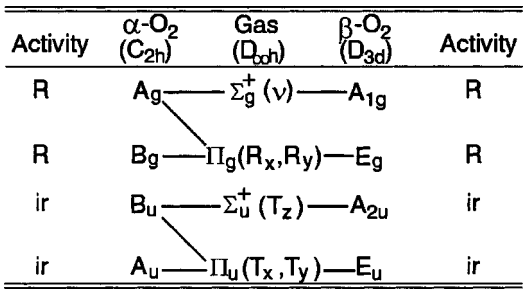

FIG. 8. Correlation diagrams for α- and β-oxygen.[15]

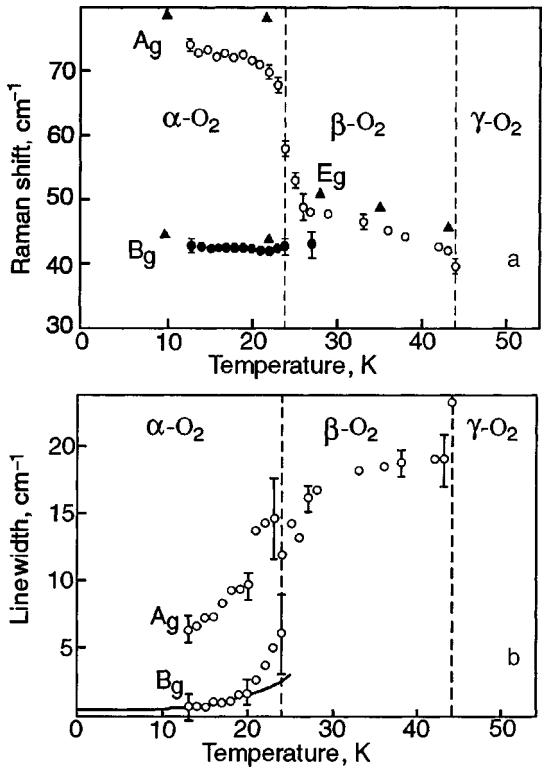

FIG. 9. Temperature dependence of the librational frequencies (a) and bandwidth (b) of solid oxygen (▲ from Refs. 15 and 35).

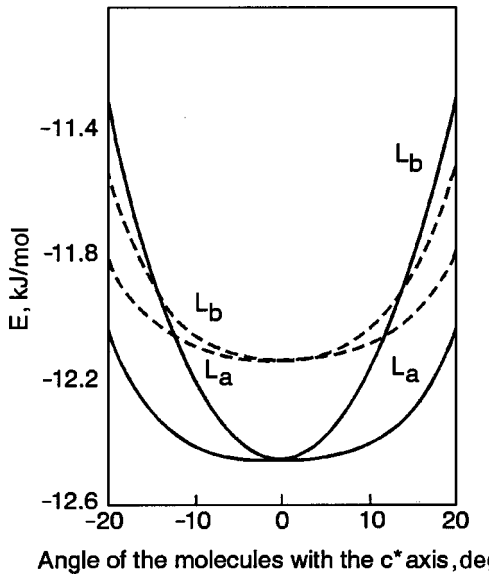

FIG. 10. A plot of the lattice potential of α-O_2 along the normal coordinates for the B_g and A_g librons, with (solid curves) and without (dashed curves) the contribution of the Heisenberg term.[14]

There was a long discussion in literature[1,7,12,17,34] concerning the assignment of the 43 and 78 cm^{-1} lines in the Raman spectra of α-O_2. On the basis of lattice dynamics calculations those authors have cast doubts on the assignment of these lines as librons by Cahill and Leroi.[15] As follows from these lattice dynamics calculations based on different models of the anisotropic forces, at the β–α transition the libron spectrum is only insignificantly changed. The lowering of the symmetry at this transition leads to lifting of the twofold degeneracy of the frequency of the $\mathbf{k}=0$ libron mode with a splitting of a few cm^{-1}. At the same time, according to Raman data,[15] the doubly degenerate E_g mode of β-O_2 with frequency $\approx$51 cm^{-1} is split into B_g and A_g modes with frequencies 43 and 78 cm^{-1}, respectively. According to these authors, the experimentally observed Raman line at 78 cm^{-1} could be a two-particle, either magnon–libron[1,7] or two-libron,[12,17,34] line while the B_g and A_g splitting is not resolved. Etters *et al.*[34] have proposed that the higher frequency belongs to a libron mode which lies at the edge of the Brillouin zone for the structural lattice, but which has $\mathbf{q}=0$ in the magnetic Brillouin zone. This mode could become visible in Raman spectroscopy when there is a strong coupling between the librons and spins. The weakest point of all these interpretations, however, is that at various temperatures and pressures no indication of the doublet character of the lowest peak α-O_2 has been observed.

Subsequent experimental and theoretical studies gave an insight into what really happens with the libron spectrum at the α–β transition. Measurements by Bier and Jodl[35] and by Prikhot'ko *et al.*[36] have given strong evidence that the assignment by Cahill and Leroi[15] is correct (Fig. 9a).

The experimental data indicate that the upper A_g mode exhibits typical soft-mode behavior and at the α–β transition transforms into the E_g mode of the β phase. The intensity and linewidth of the A_g mode increase rapidly in the vicinity of the transition and go over continuously to the respective characteristics of the E_g mode (Fig. 9b). The B_g mode frequency is nearly constant with temperature, but its intensity decreases rapidly when nearing the phase transition point, and the line vanishes discontinuously on passage through the phase transition.

From the theoretical side, Krupskii *et al.*[1] suggested that the large splitting of the libron spectrum at the β–α transition could be due to an additional term in the libron Hamiltonian, which is proportional to the magnetic order parameter. Since for $T>T_{\alpha\text{-}\beta}$ the magnetic order parameter goes to zero, this term is nonvanishing only in the α phase. Jansen and van der Avoird[14,37] found that because of the very strong dependence of the exchange coupling parameter on the molecular orientations, the Heisenberg term from the spin Hamiltonian should be included in the libron spectrum calculations.

A plot of the lattice potential along the normal coordinates for the B_g and A_g librons, with and without the contribution of the Heisenberg term, clearly demonstrates its role in this problem (Fig. 10), Ref. 14. This term lowers the lattice energy of α-O_2 in the equilibrium geometry. At the same time, it increases the stiffness of the potential drastically in the A_g direction but much less in the B_g direction.

An integrated formalism that includes magnon–phonon and magnon–libron coupling in the dynamics of the orientationally ordered α and β phases of solid oxygen was developed by Jansen van der Avoird[14] on the basis of the time-dependent Hartree method (random phase approximation). We will consider the problem of magnon–libron coupling following the simpler approach of Refs. 38 and 39.

The intermolecular exchange constant can be written as a sum of a part which is independent of the orientations of the O_2 molecules and an orientationally dependent term. The

latter part contributes to the anisotropic intermolecular potential, which determines the spectrum of librons in the orientationally ordered α and β phases. Both the exchange part and the spin-independent part of the intermolecular potential may be written as a sum of products of the invariants $(\mathbf{\Omega}_1\mathbf{n})$, $(\mathbf{\Omega}_2\mathbf{n})$, and $(\mathbf{\Omega}_1\mathbf{\Omega}_2)$:

$$U(\mathbf{\Omega}_1,\mathbf{\Omega}_2,\mathbf{R})=\sum_{i,k,l} A_{ikl}(R)(\mathbf{\Omega}_1\mathbf{n})^i(\mathbf{\Omega}_2\mathbf{n})^k(\mathbf{\Omega}_1\mathbf{\Omega}_2)^l, \tag{1}$$

$$J(\mathbf{\Omega}_1,\mathbf{\Omega}_2,\mathbf{R})=\sum_{i,k,l} B_{ikl}(R)(\mathbf{\Omega}_1\mathbf{n})^i(\mathbf{\Omega}_2\mathbf{n})^k(\mathbf{\Omega}_1\mathbf{\Omega}_2)^l, \tag{2}$$

where i, k, l are integers, the pairwise sums of which are even numbers; A_{ikl}, B_{ikl} are expansion coefficients, which are functions of molecular parameters and the intermolecular distance R. Here $\mathbf{\Omega}_1$, and $\mathbf{\Omega}_2$ are unit vectors along the molecular axis, $\mathbf{R}$ is the vector joining molecular centers, and $\mathbf{n}=\mathbf{R}/R$. The anisotropic parts can obtained from the expansions of Eqs. (1), (2) after excluding the terms with $i+k+l=0$, which correspond to the isotropic parts of the exchange constant and spin-independent intermolecular potential. In fact, the representation of the Kohin potential[16] is an example of the expansion Eq. (1) up to terms with $i+k+l\leqslant 3$, which includes all terms necessary for the derivation of the harmonic approximation.

Taking into account the explicit form of the intermolecular exchange interaction and averaging Eq. (2) over the ground spin state, we obtain the total anisotropic intermolecular interaction $V_{\text{anis}}(\mathbf{\Omega}_1,\mathbf{\Omega}_2,\mathbf{R})$, which can be written as a sum of the spin-independent and spin-dependent contributions:

$$V_{\text{anis}}(\mathbf{\Omega}_1,\mathbf{\Omega}_2,\mathbf{R})=U_{\text{anis}}(\mathbf{\Omega}_1,\mathbf{\Omega}_2,\mathbf{R}) + J_{\text{anis}}(\mathbf{\Omega}_1,\mathbf{\Omega}_2,\mathbf{R})\langle\mathbf{S}_1\mathbf{S}_2\rangle, \tag{3}$$

where $\langle\mathbf{S}_1\mathbf{S}_2\rangle$ is the spin correlation function. Finally we have

$$V_{\text{anis}}(\mathbf{\Omega}_1,\mathbf{\Omega}_2,\mathbf{R})=\sum_{\substack{i,k,l\\ i+k+l\neq 0}} (A_{ikl}+B_{ikl}\langle\mathbf{S}_1\mathbf{S}_2\rangle) \times(\mathbf{\Omega}_1\mathbf{n})^i(\mathbf{\Omega}_2\mathbf{n})^k(\mathbf{\Omega}_1\mathbf{\Omega}_2)^l. \tag{4}$$

As can be seen from Eq. (4), the anisotropic intermolecular potential, which determines the spectrum of librons in the orientationally ordered α and β phases, contains an additional term, which depends on the character and value of the magnetic order. In the molecular field approximation we have $\Gamma_{\mathbf{mn}}=\langle\mathbf{S_mS_n}\rangle=0$ in the β phase and $\Gamma_{\mathbf{mm}}=-s^2$, where s is the average spin, for the nearest molecules from the different sublattices in the α phase. For the ordered three-sublattice magnetic structure we would have $\Gamma_{\mathbf{mn}}=-s^2/2$, which can serve as an estimate of the spin correlation function for the case of the short-range magnetic order.

The expansion coefficients A_{ikl}, B_{ikl} are, generally speaking, of the same order of magnitude, which means that the additional term cannot be treated as a small perturbation but must be taken into account in the zero approximation.

The system of interacting rotors is described by the Hamiltonian

$$\mathcal{H}=\mathcal{H}_{\text{kin}}+V_{\text{anis}}, \tag{5}$$

where the kinetic energy operator is

$$\mathcal{H}_{\text{kin}}=-B_{\text{rot}} \times\sum_{\mathbf{f}}\left(\frac{1}{\sin\vartheta_{\mathbf{f}}}\frac{\partial}{\partial\vartheta_{\mathbf{f}}}\sin\vartheta_{\mathbf{f}}\frac{\partial}{\partial\vartheta_{\mathbf{f}}}+\frac{1}{\sin^2\vartheta_{\mathbf{f}}}\frac{\partial^2}{\partial\varphi_{\mathbf{f}}^2}\right). \tag{6}$$

Here $B_{\text{rot}}=\hbar^2/2I$ (I is the molecular moment of inertia) is the characteristic rotational constant; $\vartheta_{\mathbf{f}}$ and $\varphi_{\mathbf{f}}$ are the angles determining the molecular orientation at site **f**.

Since $B_{\text{rot}}\ll V_{\text{anis}}$, the rotor wave functions have localized near $\vartheta=0$; that is, the anharmonic terms are small and librons are well-defined quasi-particles. Retaining only the harmonic terms in the Hamiltonian (5) and neglecting the interplane interaction, we obtain the following expressions for the frequencies of librons in α- and β-O_2 at the center of the Brillouin zone:

$$\beta\text{-O}_2:\ (\hbar\Omega_{E_g})^2=6B_{\text{rot}}\{(2A_{200}^{\beta}+A_{111}^{\beta})+(2B_{200}^{\beta}+B_{111}^{\beta})\Gamma^{\beta}\}; \tag{7}$$

$$\alpha\text{-O}_2:\ (\hbar\Omega_{A_g})^2=6B_{\text{rot}}\{(2A_{200}^{1\alpha}+A_{111}^{1\alpha})+(2B_{200}^{1\alpha}+B_{111}^{1\alpha})\Gamma_1^{\alpha}\}; \tag{8}$$

$$(\hbar\Omega_{B_g})^2=B_{\text{rot}}\{4(A_{200}^{1\alpha}+2A_{200}^{2\alpha})+2(A_{111}^{1\alpha}+2A_{111}^{2\alpha}) +2(2B_{200}^{1\alpha}+B_{111}^{1\alpha})\Gamma_1^{\alpha}+4(2B_{200}^{2\alpha}+B_{111}^{2\alpha})\Gamma_2^{\alpha}\}, \tag{9}$$

where A_{ikl}^{β}, B_{ikl}^{β} are the values of the respective parameters of the intermolecular potential for the intermolecular distances in the β phase; $A_{ikl}^{1\alpha}$, $B_{ikl}^{1\alpha}$ and $A_{ikl}^{2\alpha}$, $B_{ikl}^{2\alpha}$ are the values of the respective parameters of the intermolecular potential for the intermolecular distances in the α phase for the nearest neighbors from the opposite and the same magnetic sublattices, respectively; Γ^{β} is the spin correlation function for two nearest spins in the β phase; $\Gamma^{1\alpha}$, and $\Gamma^{2\alpha}$ are the spin correlation functions in the α phase for two nearest neighbors from the opposite and the same sublattices, respectively.

Neglecting the small monoclinic distortion at the α–β transition, that is, the small difference between $A_{ikl}^{1\alpha}$, $A_{ikl}^{2\alpha}$, and A_{ikl}^{β} (and the same for the B_{ikl} parameters), we can simplify Eqs. (7)–(9):

$$(\hbar\Omega_{E_g})^2=6B_{\text{rot}}\{(2A_{200}+A_{111})+(2B_{200}+B_{111})\Gamma^{\beta}\}; \tag{10}$$

$$(\hbar\Omega_{A_g})^2=6B_{\text{rot}}\{(2A_{200}+A_{111})+(2B_{200}+B_{111})\Gamma_1^{\alpha}\}; \tag{11}$$

$$(\hbar\Omega_{B_g})^2=6B_{\text{rot}}\left\{(2A_{200}+A_{111})+\frac{1}{3}(2B_{200}+B_{111}) \times(\Gamma_1^{\alpha}+2\Gamma_2^{\alpha})\right\}. \tag{12}$$

Equations (7)–(9) and (10)–(12) provide an explanation of the main anomalous features of the temperature dependence of librons in the α and β phases (Fig. 9a)—large and strongly asymmetric splitting, a strong temperature dependence of the A_g mode, and a weak temperature dependence of the B_g mode.

According to data from Raman scattering spectra,[15,35] at the α–β transition the twofold degeneracy of the libron spec-

trum is lifted and the doubly degenerate E_g mode of β-O_2 with frequency $\sim 51\ \mathrm{cm}^{-1}$ is split into the B_g and A_g modes with frequencies ~ 43 and $\sim 78\ \mathrm{cm}^{-1}$. The reconstruction of the structure accompanying the phase transition and the related changes in the anisotropic part of the intermolecular potential cannot be the cause of such large splitting. If we disregard terms proportional to Γ in Eqs. (7)–(9), the resulting splitting of the E_g mode is

$$\Delta = \frac{B_{\mathrm{rot}}}{\hbar \Omega_{E_g}} [2(A_{200}^{2\alpha} - A_{200}^{1\alpha}) + (A_{111}^{2\alpha} - A_{111}^{1\alpha})]. \tag{13}$$

Estimates $\Delta < 5\ \mathrm{cm}^{-1}$. were obtained[1,7,12]

As follows from Eqs. (10)–(12), the large splitting is completely due to the spin–libron interaction:

$$\Delta = \frac{2B_{\mathrm{rot}}}{\hbar \Omega_{E_g}} (2B_{200} + B_{111})(\Gamma_1^{\alpha} - \Gamma_2^{\alpha}). \tag{14}$$

Other anomalous features of the libron spectrum are also due to the spin–libron interaction. The displacements $\Delta A_g = (\Omega_{A_g} - \Omega_{E_g})$, $\Delta B_g = (\Omega_{E_g} - \Omega_{B_g})$ of the A_g and B_g modes, respectively of the E_g mode of β-O_2 can be found from the following equations:

$$(\hbar \Omega_{A_g})^2 - (\hbar \Omega_{E_g})^2 = 6B_{\mathrm{rot}}(2B_{200} + B_{111})(\Gamma_1^{\alpha} - \Gamma^{\beta}); \tag{15}$$

$$(\hbar \Omega_{E_g})^2 - (\hbar \Omega_{B_g})^2 = 6B_{\mathrm{rot}}(2B_{200} + B_{111}) \times \left[\Gamma^{\beta} - \frac{1}{3}(\Gamma_1^{\alpha} + 2\Gamma_2^{\alpha}) \right]. \tag{16}$$

In a general theory the spin correlation functions should be found in a self-consistent way together with the libron spectrum, but as a zero approximation they could be found independently from the spin Hamiltonian. The following estimates can be obtained:

$$|\Gamma^{\beta}| \ll |\Gamma_1^{\alpha}|, |\Gamma_2^{\alpha}|; \tag{17}$$

$$|\Gamma_1^{\alpha} + 2\Gamma_2^{\alpha}| \ll |\Gamma_1^{\alpha}|, |\Gamma_2^{\alpha}|. \tag{18}$$

As follows from Eqs. (15), (16) and inequalities Eqs. (17), (18), $\Delta B_g \ll \Delta A_g$, that is, the splitting is strongly asymmetric around Ω_{E_g}.

This asymmetry can be understood qualitatively as follows.[40] When the molecules librate around the **b** axis (A_g symmetry) the interaction with four nearest-neighbor molecules from the opposite magnetic sublattice, is mostly involved, but when they librate around the **a** axis (B_g symmetry) the interaction with two next-nearest-neighbor molecules from the same magnetic sublattice is involved. The latter is much weaker than for the A_g librational mode. As a result, $\Delta B_g \ll \Delta A_g$.

The variation of the libron frequencies with temperature is caused by three factors: first, there are anharmonic temperature shifts of the frequencies with temperature, second, the parameters A_{ikl}, B_{ikl} vary with temperature due to the thermal expansion of the lattice, and third, there is temperature dependence of the spin correlation functions $\langle \mathbf{S}_i \mathbf{S}_j \rangle$. In the case of the α phase, the last factor is the most important. In the case of the β phase, the temperature shift of the E_g mode is mostly determined by the thermal expansion of the lattice. The resulting temperature dependence can be written in the form

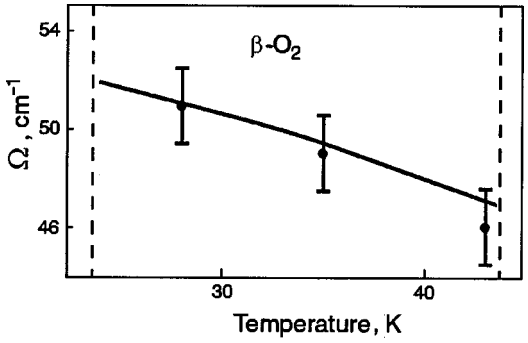

FIG. 11. Temperature dependence of the frequency of the E_g libron mode of β-O_2. The solid line is the theoretical result from Ref. 1, and the points are experimental data (Ref. 15).

$$\left(\frac{\partial \mathbf{\Omega}}{\partial T} \right)_P = \left(\frac{\partial \mathbf{\Omega}}{\partial T} \right)_V + \left(\frac{\partial \mathbf{\Omega}}{\partial V} \right)_T \left(\frac{\partial V}{\partial T} \right)_P. \tag{19}$$

Anharmonic corrections to the librational frequencies of the β phase were calculated in the mean-field approximation in Ref. 13. The anharmonicity is manifested in explicit temperature dependence of the librational frequencies. It was shown that, contrary to solid N_2, the sign of the anharmonic correction in β-O_2 is positive. Since $(\partial \Omega / \partial T) = (\partial \Omega / \partial \eta) \times (\partial \eta / \partial T)$ while $(\partial \eta / \partial T) < 0$ (where η is the orientational order parameter), the sign of the anharmonic correction is determined by the sign of the derivative $(\partial \Omega / \partial \eta)$, which could be either positive or negative, depending on the signs and values of molecular and crystal field constants in the self-consistent potential. As a result, in the case of β-O_2 the derivative $(\partial \Omega / \partial \eta) < 0$ and $(\partial \Omega / \partial T) > 0$. Numerical estimates give $(T/\Omega)(\partial \Omega / \partial T) \approx 10^{-3}$, and the effect is dominated by the second term in Eq. (19), the thermal expansion of the crystal. A comparison of the calculated[1] and experimental temperature dependences of the E_g frequency is given in Fig. 11.

The effect of an external magnetic field on the libron spectrum of α- and β-O_2 was calculated by Jansen and van der Avoird.[14] They predicted that the libron frequencies will be shifted by the external magnetic field, which changes the spin correlation function and, according to Eq. (4), affects the anisotropic part of the intermolecular potential. Due to the high rigidity of the magnetic structure of α-O_2, the resulting shift of the A_g and B_g librons is small even in strong fields and amounts to 2.5 cm^{-1} for fields up to 30 T (Fig. 12a). The magnetic-field-induced shift of the E_g mode for β-O_2 is given in Fig. 12b.

When the magnetic field is parallel to the *ab* plane of the β phase one might expect several symmetry-breaking effects.[14] The threefold symmetry is distorted in this case with the result that the E_g mode will be slightly split.

Due to the zone-folding effect, extra phonon or libron peaks may become visible in the IR or Raman spectra, though their intensities are predicted to be small.

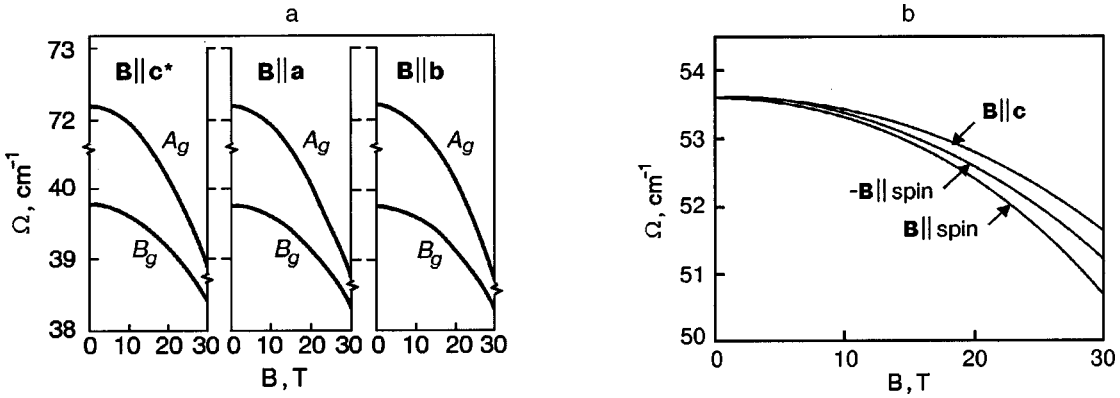

FIG. 12. The magnetic-field-induced shift of the A_g and B_g librons in α-O_2 (a) and the E_g libron mode in β-O_2 (b).[14]

4. TRANSLATIONAL PHONONS

The magnon–phonon coupling leads to zone folding:[38] the magnetic unit cell contains two molecules, and as a result, in the folded zone the phonon zone is subdivided into acoustical and optical phonons and the number of libron and magnon branches is doubled.

The most extensive zero-temperature lattice dynamics harmonic calculations based upon both the one-molecular crystallographic unit cell and the two-molecular magnetic cell have been made by Etters *et al.*[34] At the first step the Gibbs free energy was minimized with the parameters of the monoclinic lattice cell of α-O_2 and the intramolecular bond length as independent variable parameters. The equilibrium lattice parameters obtained were used in harmonic lattice-dynamics calculations. The calculations were based on the site–site Etters–Kobashi–Belak (EKB) potential.[34] Since the strong anisotropy of the Heisenberg term is not taken into account in the EKB potential, the calculated dispersion curves suffer from the same shortcomings as all older lattice dynamics calculations and reproduce the libron modes incorrectly. Nonetheless, many qualitative results of these calculations retain their validity.

The magnetic unit cell contains two molecules in the unit cell, twice as large as the structural unit cell. There are six phonon modes, four libron modes, and four magnon modes for every wave vector **q** in the smaller Brillouin zone, that is, compared with the crystallographic cell, the magnetic unit cell supports one additional vibron, two additional libron modes, three additional optical phonon modes, and two additional magnon modes. The problem is that none of these modes has been observed in experiment. Recently the range 10–85 cm^{-1} was investigated very carefully by Medvedev[31] using the modern FTIR technique and perfect crystals, and no additional IR-active modes were found.

Integrated lattice dynamics calculations in the random phase approximation have been made by Jansen and van der Avoird.[14] It was found that the mixing between the lattice modes, phonons and librons, and magnons is in general small. The only substantial amount of mixing occurs in those regions of the Brillouin zone where the dispersion curves for the lattice modes and those for the magnons would cross. Even the weak coupling then leads to an avoided crossing and to interchange of the characters of the modes involved.

The translational lattice frequencies for orientationally disordered γ-O_2 have been calculated by Kobashi, Klein, and Chandrasekharan[12] using different empirical Lennard-Jones (6–12) intermolecular potentials to account for the interactions between nearest discs, between the nearest disc and sphere and between the second-nearest discs. The model completely neglects the effect of molecular rotation. The model was able to account for the low shear constant of γ-O_2 but considerably overestimated the elastic anisotropy. This discrepancy was attributed to the neglect of translation–rotation coupling.

The role played by the molecular reorientational motions in the crystal dynamics of γ-O_2 was examined by Klein, Levesque, and Weis[41] in a molecular dynamics study of a system of molecules interacting via an atom–atom potential. The simulated crystal revealed two types of molecules with two quite different types of dynamical behavior. Very slow transverse acoustic phonon modes were found, with $v_l/v_t \approx 3.5$, in fair agreement with experiment.[42,43] The liquid has been shown to be very similar in structure and dynamical behavior to the γ phase.

5. MAGNONS

The first observation of the resonant FIR absorption in α-O_2 was made by Blocker, Kinch, and West.[23] They found a strong line at about 27 cm^{-1} with a linewidth of about 1.4 cm^{-1} and attributed it to the antiferromagnetic resonance (AFMR) mode of the system. This peak shifts to lower frequencies and decreases markedly in intensity with increasing temperature and is unobserved above the α–β transition (Fig. 13a). The experimental proof of the magnon nature of the line was obtained by Wachtel and Wheeler,[18,24] who demonstrated that no detectable isotope effect was observed. The temperature dependence of the high-energy magnon was studied by several groups[23,30,44] with similar results.

Looking for the low-frequency AFMR line, Wachtel and Wheeler[24] found an absorption line at 6.4 cm^{-1} at 1.5 K (Fig. 13b). To support the assignment of the observed FIR absorption lines as AFMR modes, FIR spectra were measured as a function of applied magnetic field.[18,24,44,45]

The dispersion relations for magnons in the presence of magnetic field were calculated in Refs. 24, 45–47. A comparison of experimental and calculated results is given in Fig. 14.[45] The experimental absorption band corresponding to the low-energy magnon is split: one absorption maximum

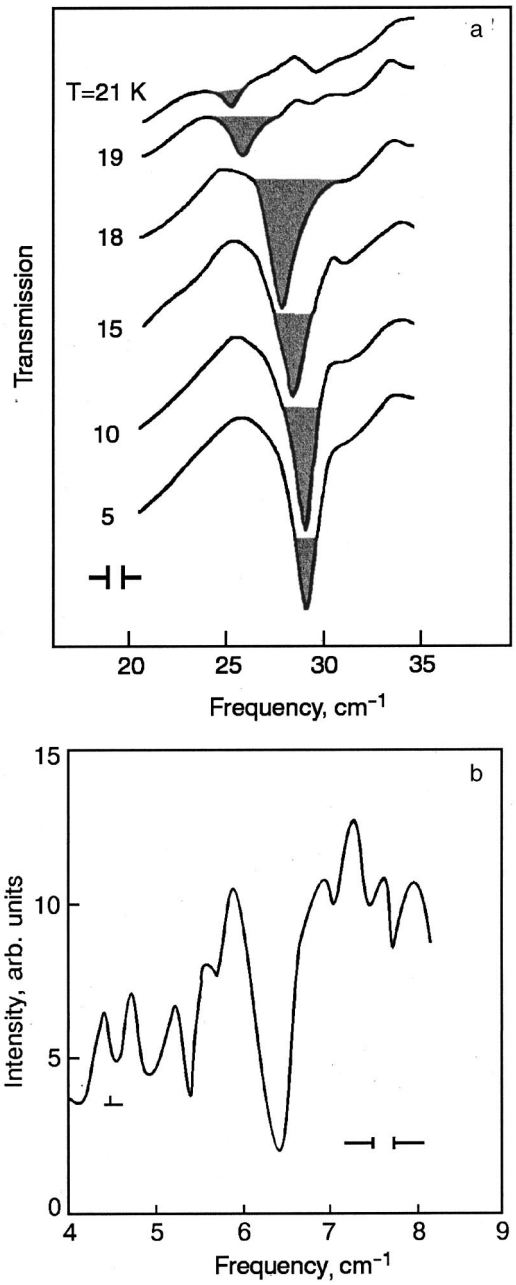

FIG. 13. Spectroscopic proof of magnon excitations in solid oxygen. The temperature dependence of far IR absorption due to magnon excitation at 27 cm^{-1} in solid oxygen[23] (a). The magnon at 6 cm^{-1} is clearly recognizable in the far-IR absorption spectra of solid oxygen[24] (b).

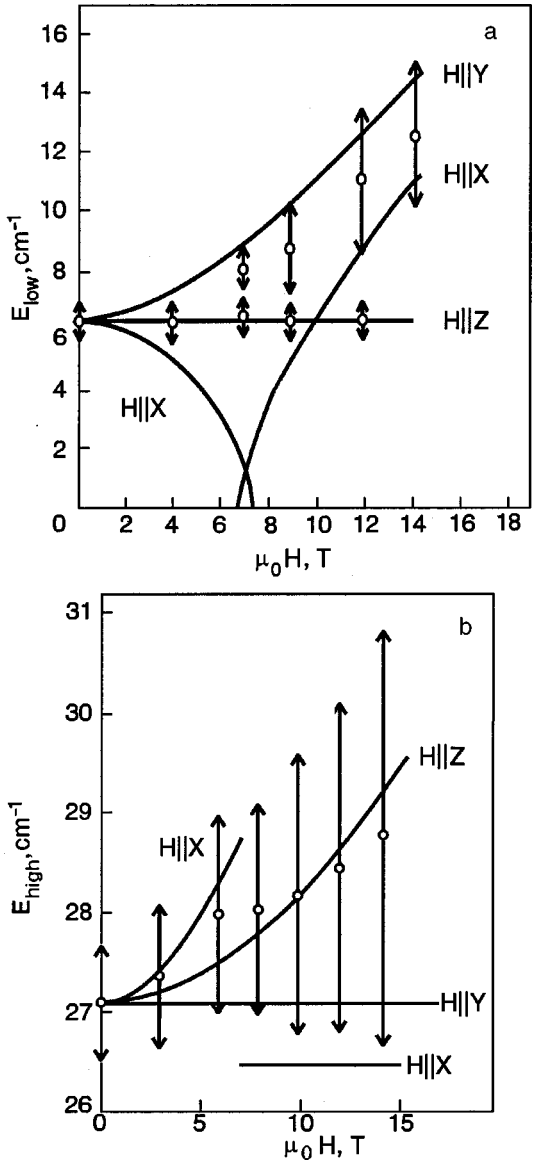

FIG. 14. Magnetic-field dependence of the frequency of the low-energy (a) and high-energy (b) magnons, measured on polycrystalline samples of α-O_2. Experimental absorption maxima are represented by open dots, and the vertical arrows indicate the FWHM (full width at half maximum). The $H\|X$ curve starting at $H=0$ corresponds to the non-spin-flopped phase; the other $H\|X$ curve corresponds to the spin-flopped phase.[45]

does not shift when the field increases, and the frequency of another increases with the field (Fig. 14a). In the case of the high-energy magnon the splitting was not found (Fig. 14b).

The experimental results of Refs. 18–21, 23–25 provided an experimental basis for the development of a theory of the magnetic properties of solid oxygen, first and formost of all of the spin excitation spectrum.

The magnetic properties of solid oxygen are generally described by the Hamiltonian[17,18,24,29,45–50]

$$\mathcal{H}=\sum_{\mathbf{f}}\,[A(S_{\mathbf{f}}^{z})^2+B(S_{\mathbf{f}}^{y})^2]+\frac{1}{2}\sum_{\mathbf{f},\mathbf{f}'}\,J_{\mathbf{ff}'}\mathbf{S_f}\mathbf{S_{f'}}\,, \tag{20}$$

where $\mathbf{S_f}$ is the spin operator at site $\mathbf{f}$ ($S=1$), $A>0$ and $B>0$ are constants of single-molecule anisotropy, and $J_{\mathbf{ff}'}$ is the exchange interaction constant of molecules at sites $\mathbf{f}$ and $\mathbf{f}'$. The z axis in Eq. (20) coincides with the molecular axis, while the x axis is directed along the monoclinic **b** axis.

The first calculation of the spin excitation spectrum was done by Wachtel and Wheeler.[18,24] According to the usual excitation wave method, the diagonalization of the Hamiltonian (20) was performed in two steps. First, the Hamiltonian (20) was written as a sum of a single-particle mean-field Hamiltonian $\mathcal{H}_0$

$$\mathcal{H}_0=\sum_{i}\,(AS_{zi}^2+BS_{yi}^2+J(0)\langle S_x\rangle S_{xi}) \tag{21}$$

and the interaction Hamiltonian $\mathcal{H}_{\rm int}=\mathcal{H}-\mathcal{H}_0$, where $\langle S_x\rangle$ is the expectation value of the operator S_x in the single-molecule ground state, which must be found from self-consistency conditions. Here the direction of the moments (b

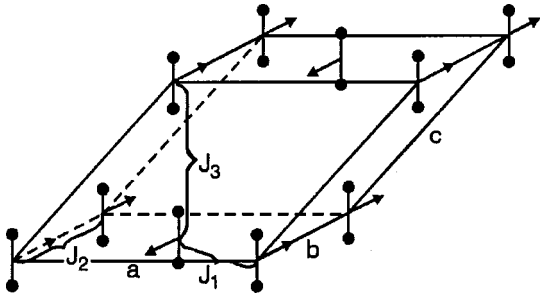

FIG. 15. Monoclinic structure of α-O_2. The magnetic structure is indicated by the arrows. The exchange interaction between the in-plane and out-of-plane nearest neighbors is described by the respective exchange interaction constants J_1, J_2, J_3.

axis) is taken as the axis of spin quantization. The exchange field $J(0)=J(\mathbf{k}=0)$; $J(\mathbf{k})=\Sigma_{\boldsymbol{\delta}} J_{\mathbf{f},\mathbf{f}+\boldsymbol{\delta}} e^{i\mathbf{k}\cdot\boldsymbol{\delta}}$ is the magnetic structure factor, and δ are lattice vectors.

With the nearest, next-nearest and next-next-nearest neighbors taken into account we have the following expression for the exchange field:

$$J(0)=n_1J_1-n_2J_2+n_3J_3, \tag{22}$$

where n_1, and n_2, n_3 are the numbers of the respective neighbors ($n_1=4$, $n_2=2$, $n_3=4$) and J_1, J_2, J_3 are the respective exchange constants (see Fig. 15).

As a result, the magnetic structural factor for the α-oxygen structure can be written in the form

$$J(\mathbf{k})=J(0)\,\gamma_{\mathbf{k}};$$

$$\gamma_{\mathbf{k}}=\frac{1}{1-\kappa/2+\alpha}\times\left[\cos\frac{k_x}{2}\cos\frac{k_y}{2}-\frac{1}{2}\,\kappa\cos k_y+\alpha\cos\frac{k_y}{2}\cos\left(\frac{k_x}{2}-k_z\right)\right], \tag{23}$$

where two dimensionless parameters $\alpha=J_2/J_1$ and $\kappa=J_3/J_1$ have been introduced. Thus, if the interaction with more distant neighbors is neglected the magnetic Hamiltonian (20) is described by a set of 5 parameters: J_1, α, κ, A, B.

The eigenvalue problem for $\mathcal{H}_0$ can be solved in a straightforward manner, yielding the following eigenvalues:

$$\epsilon_{\frac{0}{2}}=\frac{A+B}{2}\mp\sqrt{\left(\frac{A-B}{2}\right)^2+J^2(0)<S_x>^2}; \tag{24}$$

$$\epsilon_1=A+B$$

(ϵ_0 is the ground-state energy, and ϵ_1, ϵ_2 are the first and second excited states, respectively). The resulting eigenfunctions then used as the basis for transformation of the Hamiltonian $\mathcal{H}=\mathcal{H}_0+\mathcal{H}_{\text{int}}$ into a second-quantized representation in terms of the fermion creation and annihilation operators $c_{fi}^{\dagger}$, c_{fi}. Different approaches and approximations of the excitation wave method[1,7,18,24,29,45–49] and of the Green function method[46,48] have been used to treat the problem.

At low temperatures the occupation number of the ground state $n_{f0}=c_{f0}^{\dagger}c_{f0}$ is close to unity. In this limit terms not quadratic in the ground state may be neglected (so-called Bogolyubov approximation). Introducing the product operators $a_{fi}^{\dagger}=c_{fi}^{\dagger}c_{f0}$ and $a_{fi}=c_{f0}^{\dagger}c_{fi}$, which approximately obey the Bose commutation relations, and transforming the Hamiltonian to these operators, we obtain the Hamiltonian quadratic in Bose excitation operators. The next simplification consists in neglecting excitations from the ground state to the second excited state. The resulting dispersion relations (energy vs quasimomentum relations) can be written in the form:

$$E_n^2(\mathbf{k})=[\Delta_{10}+(-1)^nJ(\mathbf{k})\sin 2\vartheta]^2-J^2(\mathbf{k});n=1;2, \tag{25}$$

where $\Delta_{10}=\epsilon_1-\epsilon_0$ is the energy necessary to excite the molecule from the ground state to its first excited state; ϵ_0, ϵ_1 are given by Eq. (24); ϑ is a mixing parameter which determines the ratio of $|+1\rangle$ and $\langle -1|$ in the ground state. It depends on the relative magnitudes of the anisotropy parameters A and B:

$$\tan 2\vartheta=(A-B)/[2J(0)\langle S_x\rangle]. \tag{26}$$

It is important to note that because of complexity of the commutation relations for spin operators, there is no single ''true'' dispersion relation which would be independent of the way of transformation of the spin Hamiltonian into the bosonic Hamiltonian and of the subsequent approximations used for its diagonalization. All these approaches are so-called uncontrollable approximations, in contrast to a few controllable ones (among these are the high-temperature expansions[51] and the low-temperature Dyson approach.[52]) That is why it is important to use different approximations for the derivation of the dispersion relation, and then, comparing the magnetic characteristics calculated with different dispersion relations, to decide which approach is preferable.

The simplest approximation not based explicitly on the assumption of small fluctuations of the spin density is the random phase approximation (RPA), which coincides with the Tyablikov approximation[53] in the case of the ordered phase. This approximation was used by Slusarev *et al.*[49,50] to develop a theory of the magnetic properties of the α and β phases.

After applying the decoupling procedure usual for the RPA approximation, a set of linearized equation of motion in $\mathbf{k}$ space was obtained, where the spin components S_x, S_y, S_z are coupled to the components of the quadrupole magnetic moment $Q_{ij}=(1/2)(S_iS_j+S_jS_i)-(2/3)\delta_{ij}$, with the result that the order of the system is doubled.

As a result, the following expression was obtained for two lower branches of the spin wave spectrum:[49,50]

$$E_n^2(\mathbf{k})=\frac{J^2(0)}{2-\gamma_{\mathbf{k}}^2}\left\{\eta[1+(-1)^n\gamma_{\mathbf{k}}]-(-1)^n\frac{2B\xi_1}{\eta J(0)}\,\gamma_{\mathbf{k}}\right\}\times\left\{\eta[1-(-1)^n\gamma_{\mathbf{k}}]+(-1)^n\frac{2A\xi_2}{\eta J(0)}\,\gamma_{\mathbf{k}}\right\};$$

$$n=1;2. \tag{27}$$

Here η is the spin order parameter of the system,

$$\eta=\frac{1}{N}\sum_{\mathbf{k}}\langle S_{\mathbf{k}}^x\rangle, \tag{28}$$

and ξ_1 and ξ_2 are order parameters of quadrupole magnetic ordering,

$$\xi_1=\frac{1}{N}\sum_{\mathbf{k}}\left(\langle S^x_{\mathbf{k}}S^x_{-\mathbf{k}}\rangle-\langle S^z_{\mathbf{k}}S^z_{-\mathbf{k}}\rangle\right);$$

$$\xi_2=\frac{1}{N}\sum_{\mathbf{k}}\left(\langle S^x_{\mathbf{k}}S^x_{-\mathbf{k}}\rangle-\langle S^y_{\mathbf{k}}S^y_{-\mathbf{k}}\rangle\right). \tag{29}$$

The self-consistency parameters are determined by integrals over the Brillouin zone, which makes it possible to neglect anisotropies contributing only to the center and to the band edges. In this approximation $\xi_1=\xi_2=\xi$. As follows from Eq. (27), the AFMR frequencies $E_1(0)$, $E_2(0)$ are defined by the exchange field $J(0)$, the respective anisotropy constants, and the quadrupole magnetic order parameter ξ:

$$E_1(0)=\sqrt{4B\xi J(0)};E_2(0)=\sqrt{4A\xi J(0)}. \tag{30}$$

At $T=0$ K the order parameters η and ξ satisfy two self-consistency conditions:

$$\xi=2-\frac{3}{2}\eta R;\quad \eta=2\xi R, \tag{31}$$

where

$$R=\frac{1}{N}\sum_{\mathbf{k}}\left[1-\gamma^2(\mathbf{k})\right]^{-1/2}. \tag{32}$$

According to Ref. 54, in the two-dimensional case $R=1.393$, and in the three-dimensional case $R=1.156$. The self-consistency parameters η and ξ, determined by the set of equations Eq. (31), are for 2D and 3D:

$$2D:\quad \eta=0.817;\quad \xi=0.293; \tag{33}$$

$$3D:\quad \eta=0.923;\quad \xi=0.399. \tag{34}$$

In numerical calculations the values of these parameters were used for the two-dimensional case ($\alpha=J_2/J_1\ll 1$).

Bearing in mind that we will compare different forms of the dispersion relation obtained in different approximations for the Hamiltonian (20), we will recast Eqs. (25) and (27) in a form more convenient for such comparison.

The dispersion relation (25) has the same total number of parameters as the original magnetic Hamiltonian (20), but the anisotropy parameters A and B enter into Eq. (23) through quantities Δ_{10} and $\sin 2\vartheta$. The appearance of these quantities reflects the method used to obtain the dispersion relation in this specific form. They can be expressed in terms of the exchange field $J(0)$, and the frequencies of two AFMR modes, $E_1(0)$ and $E_2(0)$. As a result of straightforward transformations, Eq. (25) takes the form

$$E_n(\mathbf{k})=\{[a_+ +(-1)^n a_-\gamma_{\mathbf{k}}]^2-J^2(\mathbf{k})\}^{1/2}, \tag{35}$$

where the parameters $a_\pm$ are given by

$$a_\pm=\frac{1}{2}\{\sqrt{E_2(0)^2+J^2(0)}\pm\sqrt{E_1(0)^2+J^2(0)}\}. \tag{36}$$

After similar transformations Eq. (27) can be written in the following form:

$$E_n(\mathbf{k})=\frac{1}{\sqrt{2-\gamma^2_{\mathbf{k}}}}\{[a_+ +(-1)^n a_-\gamma_{\mathbf{k}}]^2-J^2(\mathbf{k}) +[1-\gamma^2_{\mathbf{k}}](J^2(0)\eta^2-a_+^2)\}^{1/2}. \tag{37}$$

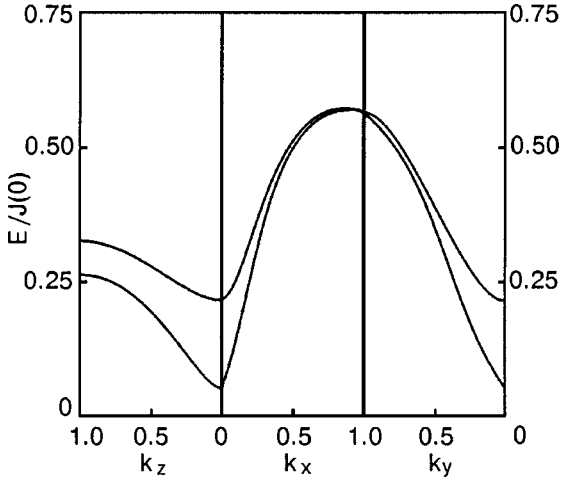

FIG. 16. Dispersion curves for magnon modes in α-O_2.

A comparison of the proposed dispersion equations can be readily done in the form of Eqs. (35) and (37). It is seen that they coincide at $\mathbf{k}=0$ ($\gamma_{\mathbf{k}}=1$). At small wave vectors the dispersion curves given by these equations agree very closely, but the difference becomes more and more essential with increasing wave vectors. If we use these equations to fit the experimental data to the calculated values we find that the magnetic properties such as the magnetic heat capacity, which sample the whole Brillouin zone, can be described far better with the dispersion relation (27)[49,50] than with other dispersion relations proposed in literature.

Dispersion curves for the dispersion relation (27) or (37) are given in Fig. 16. As can be seen, the magnon spectrum is strongly anisotropic. For directions in the basal plane *ab* the spectrum is characterized by more significant dispersion than for magnons with wave vectors normal to the basal plane.

For magnons with $\mathbf{k}$ in the basal plane the maximal frequency is

$$E_{\max}\approx J(0)\,\eta/\sqrt{2}. \tag{38}$$

The first estimate of the magnitude of the exchange field was obtained by Wachtel and Wheeler.[18,24] They used the Hamiltonian (20) and calculated the magnon spectrum of α-O_2 within a model with an isotropic exchange interaction, neglecting the intrasublattice coupling constant J_2 and assuming that the nearest-neighbor number $z=n_1+n_3=8$, $J_1=J_3\equiv J$ ($\alpha=1,\kappa=0$). To determine the three unknown parameters *J*, *A*, and *B* they set the two calculated zone-center magnon frequencies to the experimental AFMR frequencies, obtaining two of three necessary equations. The third equation was derived by assuming that the magnon frequency at the zone edge is equal to 37.5 cm^{-1}, the characteristic frequency obtained by the Eremenko group[19–21] from the sideband spectra in the double excitation bands $2^3\Sigma_g^-\rightarrow 2^1\Delta_g$ and $2^3\Sigma_g^-\rightarrow 2^1\Sigma_g^+$ (see Sec. 2). As a result, they obtained $J(0)=32$ cm^{-1}.

But as was shown in Refs. 1 and 7, Wachtel and Wheeler's model with isotropic exchange interaction is in contradiction with the low-temperature specific heat data. Namely, the analysis of the low-temperature specific heat of α-O_2 performed in Refs. 1 and 7 revealed that for $T<10$ K, when the contribution of molecular librations is negligible, the sum

of the lattice and magnon components to the specific heat, with the latter calculated with the magnon spectrum from Refs. 18 and 24, exceeds the experimental data significantly. Moreover, as was pointed out by Slusarev *et al.*,[49,50] the magnetic susceptibility of α-oxygen, corresponding to the magnetic parameters found by Wachtel and Wheeler, exceeds the experimental susceptibility by a factor of 6.

The authors of Refs. 1 and 7 came up the opinion that the main drawback of Wachtel and Wheeler's approach was the assumption that the exchange interaction is isotropic and put forward the model that α-O_2 is a quasi-two-dimensional antiferromagnet, i.e., $\alpha \ll 1$. This conjecture launched a long discussion in literature[45,55–57] but subsequently obtained direct support in *ab initio* calculations of the exchange interaction of oxygen molecules.[58,59]

A theory of the magnetic properties (the magnetic heat capacity, the magnetic susceptibility, and the frequencies of antiferromagnetic resonance) of the two low-temperature phases as a quasi-2D Heisenberg system was developed by Slusarev *et al.*[49,50] In order to obtain information on the parameters of the magnetic system of solid oxygen, the experimental magnetic heat capacity must be compared with theoretical estimates. The theoretical magnetic heat capacity is determined by the spin-wave spectrum $E(\mathbf{k})$ and can be written as a sum over two branches of the spectrum $E_1(\mathbf{k})$ and $E_2(\mathbf{k})$:

$$C_{\mathrm{mag}}/R = \sum_{n=1,2} \frac{1}{(2\pi)^3} \int_{-\pi}^{\pi} d^3k \, \frac{(E_n/T)^2 \exp(E_n/T)}{[\exp(E_n/T)-1]^2}. \tag{39}$$

The experimental points were obtained as a difference between the heat capacity C_V^{exp} and the phonon contribution. The former value was obtained from the data on C_P (Ref. 60) and the $C_P - C_V$ correction, which was calculated using the data on the isothermal compressibility[42,61] and thermal expansion.[1,7] The phonon contribution was calculated[62] in the Debye approximation with $\Theta_D = 104$ K, taking into account the $\Theta_D(T)$ dependence obtained from the temperature dependence of the sound velocities.[42,61,63] The libron contribution is negligible in the given temperature range.

Thus the magnon heat capacity Eq. (39) contains three variable parameters, and it is most convenient to use in this capacity the exchange field $J(0)$ and the two dimensionless parameters α and κ. The sensitivity of the magnetic heat capacity to changes in these parameters can be readily seen from the low-temperature asymptotic for C_{mag}:

$$C_{\mathrm{mag}}/R = \frac{4}{(2\pi)^{3/2}} \frac{(1+\alpha-k/2)^{3/2}}{\sqrt{\alpha}\sqrt{1+\alpha-2k}} \times \left(\frac{E_1(0)}{J(0)\eta}\right)^3 \left(\frac{E_1(0)}{T}\right)^{1/2} e^{-E_1(0)/T}. \tag{40}$$

As can be seen, the dimensionless interplane exchange coupling constant α enters into Eq. (40) as a singular factor, and thus the low-temperature magnon heat capacity is very sensitive to this parameter. The best choice obtained by comparison of the calculated and experimental magnetic heat capacity (see Fig. 17) is $J(0) = 125.9\ \mathrm{cm}^{-1}$; $\alpha = 0.025$. The fact that the inequality $\alpha \ll 1$ holds means that α-O_2 is a quasi-two-dimensional antiferromagnet.

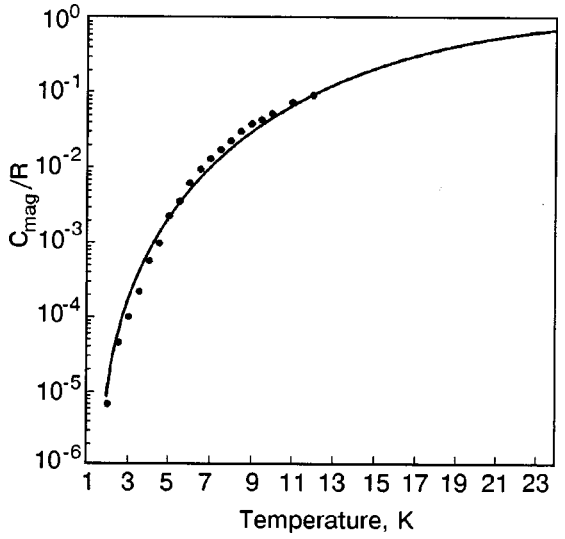

FIG. 17. Magnetic heat capacity. Experimental points—see text; the solid curve is the best fit to Eq. (39).

The dimensionless intrasublattice exchange parameter κ also enters into Eq. (40) as a singular factor. For the quasi-two-dimensional antiferromagnet ($\alpha \ll 1$) it imposes on the magnitude of κ the condition

$$\kappa < 1/2, \tag{41}$$

which is a direct consequence of the condition of stability of the collinear antiferromagnet structure.[64] If the condition (41) is violated, the calculated magnon frequencies become imaginary for a region of wave vectors along the direction $\mathbf{k} = (0,k,0)$. For the 3D antiferromagnet ($\alpha = 1$) the magnitude of κ, instead of the condition Eq. (41), should meet the condition

$$\kappa < 1. \tag{42}$$

For the value of the exchange field obtained by the fit to the experimental data for the magnon heat capacity ($J(0) = 125.9\ \mathrm{cm}^{-1}$), the maximum magnon frequency (see Fig. 16) $E_{\max} = 72.7\ \mathrm{cm}^{-1}$. The magnon frequencies at the Brillouin zone boundaries for magnons with wave vectors $\mathbf{k}$ in the *ab* plane are close to $E_{\max}$ (around 70 cm^{-1} for both branches). For the magnons with $\mathbf{k}$ normal to the basal plane, due to the anisotropy of the exchange interaction there is a gap between the two spectral branches at the boundary of the Brillouin zone. The edge frequencies for the two branches are

$$E_{\frac{1}{2}}^{1}(0,0,\pi) = \left[E_{\frac{1}{2}}^{2}(0) + \frac{4\alpha}{1-\kappa/2} J^2(0)\eta^2\right]^{1/2}. \tag{43}$$

For the adopted parameters we have the following estimates: $E_1(0,0,\pi) \approx 33.2\ \mathrm{cm}^{-1}$, $E_2(0,0,\pi) \approx 42.4\ \mathrm{cm}^{-1}$, and the gap $\Delta_1 = E_2(0,0,\pi) - E_1(0,0,\pi)$ amounts to 9.2 cm^{-1}.

These theoretical estimates for the edge frequencies are very close to those obtained by Eremenko *et al.*[20,21] (38 and 75 cm^{-1}). It is important to stress that no spectroscopic data were used in their derivation and these estimates are based on the fit to the data on the magnon heat capacity and magnetic susceptibility.

It has been speculated[1] that the observed doubling of the exciton–magnon absorption lines[65] is related to the discussed nature of the magnon spectrum of α-O_2.

Allowance for the intrasublattice exchange interaction ($\kappa \neq 0$) makes magnons with wave vectors along the *a* and *b* axes inequivalent. The degeneracy at the zone edge for the high-symmetry directions is lifted, and another gap exists between the two spectral branches at the boundary of the Brillouin zone at $\mathbf{k}=(\pi,0,0)$ and $(0, \pi, 0)$. The gap is proportional to the dimensionless intrasublattice coupling constant κ:

$$\Delta_2 = \frac{\kappa}{8\eta\sqrt{2}} \frac{E_2^2(0) - E_1^2(0)}{J(0)}. \tag{44}$$

The gap is rather small but, in principle, measurable ($\Delta \approx 0.25\ \mathrm{cm}^{-1}$).

Recently, systematic Fourier transform infrared spectroscopy studies of electronic excitations in solid oxygen were carried out by Jodl group.[32] Though their data confirmed considerable anisotropy of the magnon spectrum, estimates for the magnon frequencies at the Brillouin zone boundaries obtained in this study turned out to be significantly different from those obtained by Eremenko *et al.*[20,21] This discrepancy needs clarification.

The dispersion relation (27) contains one important feature of the dispersion curves which is lacking in other forms of the dispersion relation. Since the maximal energy of magnons described by Eq. (27) is proportional to the magnetic order parameter [Eq. (38)], which is a decreasing function of temperature, the dispersion curves of magnons are strongly temperature dependent. Among the possible experimental implications we note here the anomalous temperature dependence of the sound velocities.[61,63]

A qualitative model which provides a possible explanation of how the anomalous behavior of the sound velocities stems from the strong temperature dependence of the magnon dispersion curves is illustrated in Fig. 18. One can see that when the zone-edge magnon frequency $\omega_{\max}^{(1)}$ decreases with temperature, the slope of the acoustic coupled phonon–magnon mode nearly goes to zero at the α–β transition.

The libron, magnon, and phonon branches of the spectrum of elementary excitations exhibit essentially different anisotropy. The former two display significant anisotropy[1,7] while for the latter the anisotropy is far less pronounced.[11] Librons and magnons with wave vectors in the *ab* plane are characterized by significant dispersion, while for librons and magnons propagating along the normal to the *ab* plane the bandwidths are comparatively small. The nonequivalence of the different spectral branches is due to the fact that the anisotropic and exchange interactions are more short-ranged than the isotropic interaction determining the phonon spectrum.

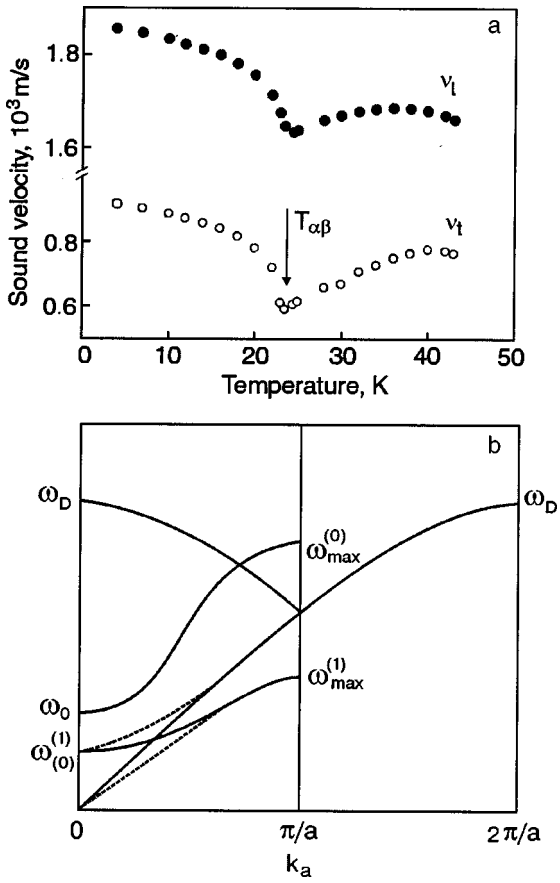

FIG. 18. Temperature dependence of the sound velocities in α-and β-O_2 (Refs. 42, 61) (a). Schematic dispersion curves of phonons and magnons in α-O_2, illustrating the way the phonon–magnon coupling results in strong temperature dependence of the phonon velocity. The solid curves are uncoupled acoustic translational (based upon crystallographic unit cell) and magnon modes (based upon the magnetic unit cell); the coupled modes in the folded zone are given by dashed curves. ω_0, $\omega_{\max}^{(0)}$ and $\omega_0^{(1)}$, $\omega_{\max}^{(1)}$ are, respectively, the zone-center and zone-edge magnon frequencies at $T=0$ K and at a nonzero temperature (b).

6. SUMMARY

We have reviewed results on the lattice dynamics calculations concerning the elementary excitation spectra of α-, β-, and γ-oxygen. An important characteristic feature of solid oxygen as a magnetic system is an anomalously large coupling between lattice and magnetic subsystems. It was shown, in particular, that it is essential to include the Heisenberg term in the lattice dynamics calculations to explain the long-state problem of the anomalously large libron splitting in α-O_2. The integrated scheme developed for lattice dynamics and spin-wave calculations provides a good approach for the theoretical treatment of the system. The calculated spectrum of magnons permits one to describe the magnetic properties of α-O_2 in a fair agreement with experiment.

Among theoretical problems that remain to be solved are as follows:

Detailed calculations of the dispersion curves and density of states for phonons, librons and magnons;

Calculations of thermal and magnetic properties with the obtained density of states;

Calculations of anharmonic phonon and libron effects;

Calculations of kinetic and relaxational properties;

Lattice dynamics calculations of the high-pressure phases.

The authors dedicate this work to Prof. V. V. Eremenko on the occasion of his 70th birthday.

*E-mail: freiman@ilt.kharkov.ua
**E-mail: jodl@physik.uni-kl.de; jodl@lens.unifi.it

[1] I. N. Krupskii, A. I. Prokhvatilov, Yu. A. Freiman, and A. I. Erenburg, Fiz. Nizk. Temp. **5**, 271 (1979) [Sov. J. Low Temp. Phys. **5**, 130 (1979)].
[2] R. A. Alikhanov, Zh. Éksp. Teor. Fiz. **45**, 812 (1963) [Sov. Phys. JETP **18**, 556 (1964)].
[3] R. A. Alikhanov, E. B. Vul, and Yu. G. Fedorov, Acta Crystallogr. **A 21**, 92 (1966).
[4] R. A. Alikhanov, JETP Lett. **5**, 349 (1967).
[5] M. F. Collins, Proc. Phys. Soc. **89**, 415 (1966).
[6] C. S. Barrett, L. Meyer, and J. Wasserman, J. Chem. Phys. **47**, 592 (1967).
[7] I. A. Burakhovich, I. N. Krupskii, A. I. Prokhvatilov, Yu. A. Freiman, and A. I. Erenburg, JETP Lett. **25**, 33 (1977).
[8] E. M. Hörl, Acta Crystallogr. **15**, 845 (1962).
[9] T. H. Jordan, W. E. Streib, H. W. Smith, and W. N. Lipscomb, Acta Crystallogr. **17**, 777 (1964).
[10] Yu. A. Freiman and H. J. Jodl [to be published in Phys. Rep. (2002)].
[11] J. E. Jelinek, A. M. Karo, and L. J. Slutsky, J. Phys. Chem. Solids **33**, 1279, 1291 (1972).
[12] K. Kobashi, M. L. Klein, and V. Chandrasekharan, J. Chem. Phys. **71**, 843 (1979).
[13] A. P. Brodyanskii, V. A. Slusarev, and Yu. A. Freiman, Fiz. Nizk. Temp. **6**, 533 (1980) [Sov. J. Low Temp. Phys. **6**, 256 (1980)].
[14] A. P. J. Jansen and A. van der Avoird, J. Chem. Phys. **86**, 3583, 3597 (1987).
[15] J. E. Cahill and G. E. Leroi, J. Chem. Phys. **51**, 97 (1969).
[16] *Physics of Cryocrystals*, V. G. Manzhelii and Yu. A. Freiman (Eds.), NY, AIP Press (1997).
[17] A. Helmy, K. Kobashi, and R. D. Etters, J. Chem. Phys. **80**, 2782 (1984); Errata: **82**, 473 (1985).
[18] E. J. Wachtel and R. G. Wheeler, J. Appl. Phys. **42**, 1581 (1971).
[19] V. V. Eremenko, Yu. G. Litvinenko, and E. M. Ogneva, Zh. Éksp. Teor. Fiz. **48**, 1611 (1965) [Sov. Phys. JETP **21**, 1083 (1965)].
[20] V. V. Eremenko and Yu. G. Litvinenko, Zh. Éksp. Theor. Phys. **53**, 539 (1967) [Sov. Phys. JETP **26**, 350 (1968)].
[21] Yu. G. Litvinenko, V. V. Eremenko, and T. I. Garber, Phys. Status Solidi **30**, 49 (1968).
[22] A. Landau, E. J. Allin, and H. L. Welsh, Spectrochim. Acta **18**, 1 (1962).
[23] T. G. Blocker, M. A. Kinch, and F. G. West, Phys. Rev. Lett. **22**, 853 (1969).
[24] E. J. Wachtel and R. G. Wheeler, Phys. Rev. Lett. **24**, 233 (1970).
[25] P. M. Mathai and E. J. Allin, Can. J. Phys. **49**, 1973 (1971).
[26] E. G. Petrov, V. M. Loktev, and Yu. B. Gaididei, Phys. Status Solidi B **41**, 117 (1970).
[27] R. Bhandari and L. M. Falicov, J. Phys. C: Solid State Phys. **6**, 479 (1973).
[28] T. Fujiwara, J. Phys. Soc. Jpn. **36**, 36 (1974).
[29] Yu. B. Gaididei, V. M. Loktev, A. P. Prikhot'ko, and L. I. Shanskii, Fiz. Nizk. Temp. **1**, 1365 (1975) [Sov. J. Low Temp. Phys. **1**, 653 (1975)].
[30] I. M. Pritula and L. V. Khashchina, Fiz. Nizk. Temp. **18**, 1035 (1992) [Sov. J. Low Temp. Phys. **18**, 727 (1992)].
[31] S. Medvedev, *Elementary Excitations in Solid Oxygen*, Thesis, University of Kaiserslautern (2002).
[32] S. A. Medvedev, A. P. Brodyanski, and H. J. Jodl, Phys. Rev. B **63**, 184302 (2001).
[33] M. Minenko, M. Vetter, A. Brodyanski, and H. J. Jodl, Fiz. Nizk. Temp. **26**, 947 (2000) [Low Temp. Phys. **26**, 699 (2000)].
[34] R. D. Etters, K. Kobashi, and J. Belak, Phys. Rev. B **32**, 4097 (1985).
[35] D. Bier and H. J. Jodl, J. Chem. Phys. **81**, 1192 (1984).
[36] A. F. Prikhot'ko, Yu. G. Pikus, L. I. Shanskii, and D. G. Danilov, Sov. Phys. JETP **42**, 253 (1985).
[37] A. P. J. Jansen and A. van der Avoird, Phys. Rev. B **31**, 7500 (1985).
[38] Yu. B. Gaididei, V. M. Loktev, and V. S. Ostrovskii, Fiz. Nizk. Temp. **11**, 740 (1985) [Sov. J. Low Temp. Phys. **11**, 406 (1985)].
[39] Yu. B. Gaididei, V. M. Loktev, V. S. Ostrovskii, and A. P. Prikhot'ko, Fiz. Nizk. Temp. **12**, 61 (1986) [Sov. J. Low Temp. Phys. **12**, 36 (1986)].
[40] B. Kuchta, Chem. Phys. **95**, 391 (1985).
[41] M. L. Klein, D. Levesque, and J.-J. Weis, Phys. Rev. B **21**, 5785 (1980).
[42] P. A. Bezugly, L. M. Tarasenko, and Yu. S. Ivanov, Fiz. Tverd. Tela (Leningrad) **10**, 2119 (1969) [Sov. Phys. Solid State **10**, 1660 (1969)].
[43] H. Kiefte and M. J. Clouter, J. Chem. Phys. **62**, 4780 (1975).
[44] R. J. Meier, J. H. Colpa, and H. Sigg, J. Phys. C: Solid State Phys. **17**, 4501 (1984).
[45] R. J. Meier, *On the Magnetic and Optical Properties of Condensed Oxygen*, Thesis, Amsterdam University (1984).
[46] *Kriokristally*, B. I. Verkin and A. F. Prikhot'ko (Eds.), Naukova Dumka, Kiev (1983).
[47] Yu. B. Gaididei and V. M. Loktev, Fiz. Tverd. Tela (Leningrad) **16**, 3438 (1975) [Sov. Phys. Solid State **16**, 2226 (1975)].
[48] Yu. B. Gaididei and V. M. Loktev, Ukr. Fiz. Zh. (Russ. Ed.) **23**, 1147 (1978).
[49] V. A. Slusarev, Yu. A. Freiman, and R. P. Yankelevich, JETP Lett. **30**, 270 (1979).
[50] V. A. Slusarev, Yu. A. Freiman, and R. P. Yankelevich, Fiz. Nizk. Temp. **6**, 219 (1980) [Sov. J. Low Temp. Phys. **6**, 105 (1980)].
[51] D. C. Mattis, *The Theory of Magnetism*, NY, Harper and Row publishers (1965).
[52] F. Dyson, Phys. Rev. **102**, 1217, 1230 (1956).
[53] S. V. Tyablikov, *Methods in the Quantum Theory of Magnetism*, Plenum, London (1967).
[54] P. W. Anderson, Phys. Rev. **83**, 1260 (1951); **86**, 694 (1952).
[55] G. S. DeFotis, Phys. Rev. B **23**, 4714 (1981).
[56] P. W. Stephens, R. J. Birgeneau, C. F. Majkrzak, and G. Shirane, Phys. Rev. B **28**, 452 (1983).
[57] C. Uyeda, K. Sugiyama, and M. Date, J. Phys. Soc. Jpn. **54**, 1107 (1985).
[58] M. C. van Hemert, P. E. S. Wormer, and A. van der Avoird, Phys. Rev. Lett. **51**, 1167 (1983).
[59] P. E. S. Wormer and A. van der Avoird, J. Chem. Phys. **81**, 1929 (1984).
[60] C. H. Fagerstroem and A. C. Hollis Hallett, J. Low Temp. Phys. **1**, 3 (1969).
[61] P. A. Bezugly and L. M. Tarasenko, Fiz. Nizk. Temp. **1**, 1144 (1975) [Sov. J. Low Temp. Phys. **1**, 548 (1975)].
[62] A. I. Erenburg, *Structure, Thermal Expansion and Thermal Properties of Cryocrystals Formed by Linear Molecules*, Thesis, Institute for Low Temperature Physics and Engineering, Kharkov (1984).
[63] B. I. Verkin, V. G. Manzhelii, and V. N. Grigor'ev *et al.*, *Handbook of Properties of Condensed Phases of Hydrogen and Oxygen*, Hemisphere Publishing Corporation NY (1991).
[64] V. A. Slusarev, Yu. A. Freiman, and R. P. Yankelevich, Fiz. Nizk. Temp. **7**, 536 (1981) [Sov. J. Low Temp. Phys. **7**, 265 (1981)].
[65] Y. B. Gaididei, V. M. Loktev, A. F. Prikhot'ko, and L. I. Shanskii, Opt. Spektrosk. **41**, 855 (1975).

This article was published in English in the original Russian journal. Reproduced here with stylistic changes by the Translation Consultant.

MAGNETOOPTICS OF MAGNETS

Spin–phonon interaction and mode softening in NiF_2

D. J. Lockwood*

Institute for Microstructural Sciences, National Research Council, Ottawa, ON KIA OR6
(Submitted October 29, 2001)
Fiz. Nizk. Temp. **28**, 709–715 (July 2002)

The temperature dependence of the four Raman-active phonons in NiF_2 is investigated at temperatures above and below the antiferromagnetic ordering temperature of $T_N = 73$ K. All four modes exhibit distinct anomalies in their intensities and frequencies near T_N due to spin–phonon coupling. The phonon linewidths also exhibit weak anomalies. From the temperature dependences of the phonon frequencies, estimates are made of the spin–phonon coupling coefficients. The B_{1g} phonon exhibits anomalous mode softening with decreasing temperature from 300 K to T_N. © *2002 American Institute of Physics.* [DOI: 10.1063/1.1496657]

1. INTRODUCTION

Although there have, by now, been numerous light scattering measurements of magnetic excitations in solids,[1] much less is known from such studies of their interactions with phonons. This is because direct interactions of magnons, or higher-lying excitons, with phonons are less likely in the range of wave vectors near the Brillouin zone center accessed in Raman spectroscopy. Nevertheless, such strong interactions have been observed, for example, in $FeCl_2 \cdot 2H_2O$, $CsCoCl_3$, and $RbCoCl_3$, where there is an accidental near-degeneracy of the magnon and phonon frequencies.[2] More generally, spin–phonon interactions manifest themselves through modifications to the normal temperature dependences of the optic phonons. The exchange coupling between magnetic ions influences the phonon frequency, integrated intensity, and linewidth. Such spin-dependent effects have been reported in the phonon Raman spectra of $KCoF_3$, VI_2, $CsCoBr_3$, EuSe, EuTe, EuO, EuS, $CdCr_2S_4$, and $CdCr_2Se_4$ (Refs. 2 and 3). Of the transition metal fluorides with the rutile structure, which are the main concern of this work, detailed results and comparisons with theory have been reported for the antiferromagnets FeF_2 and MnF_2 (Refs. 4–8), and the diluted antiferromagnet $Fe_{1-x}Zn_xF_2$ (Ref. 9). For these compounds, the Raman-active phonon frequencies and intensities, but not the linewidths, were affected to varying extents by the antiferromagnetic ordering, and from the data spin–phonon coupling coefficients were deduced.[7,8] It is of interest to determine the magnitudes of such effects, because they can also influence the magnon Raman scattering.[10]

Here we report results from a temperature dependent study of the Raman active phonons in antiferromagnetic NiF_2 ($T_N = 73.2$ K), which has the same rutile crystal structure of FeF_2 and MnF_2 but differs in the spin alignment. Instead of lying along the crystal *c* axis, the spins in NiF_2 lie in the *ab* plane and are tilted slightly away from the principal axes. This spin canting modifies the magnetic properties of NiF_2 and gives rise to a lower ''ferromagnetic'' spin wave branch as well as the usual antiferromagnetic branch found in isomorphous FeF_2 and MnF_2 (Ref. 11). These unusual magnetic properties are presumed responsible for the more pronounced spin–phonon coupling reported here for NiF_2 (spin $S=1$) compared with that observed previously in FeF_2 ($S=2$) and MnF_2 ($S=5/2$). Nevertheless, the anomalous effects of the exchange coupling on the phonon Raman line parameters can be quite subtle and were not observed in the earlier temperature-dependent study by Hutchings *et al.*[11]

2. EXPERIMENT

The single crystal of green-colored NiF_2 used in this study was grown from the melt at Oxford University. The optical-quality crystal was x-ray oriented, cut into a cuboid of dimensions $4.0 \times 4.2 \times 1.1$ mm, and then polished with 1 μm diamond powder. For the low temperature measurements, the sample was mounted in the helium exchange-gas space of a Thor S500 continuous flow cryostat. The sample temperature was controlled to within 0.1 K and was monitored with a gold–iron/Chromel thermocouple mounted on the sample surface.

The Raman spectrum was excited with 300 mW of 514.5 nm argon laser light that had been filtered with an Anaspec S300 prism monochromator. The NiF_2 crystal is essentially transparent to 514.5 nm light and there is little laser heating at this wavelength, as was also reported in an earlier study.[12] The light scattered at 90° was dispersed with a Spex 14018 double monochromator at a resolution of 2.5 cm^{-1}, detected with a cooled RCA 31034A photomultiplier, and recorded under computer control.[13] The polarization of the scattered light was analyzed with Polaroid film, but the light was then polarization-scrambled before entering the monochromator. The conventional *X*, *Y*, *Z* orthogonal laboratory axis system that is used to describe the scattered light polarization was chosen such that *X*, *Y*, and *Z* were parallel to the crystal [110], $[1\bar{1}0]$, and [001] directions, respectively.

3. PHONON RAMAN SPECTRUM

A factor group analysis of the rutile crystal structure (space group $P4/mnm$) predicts four Raman-active modes of A_{1g}, B_{1g}, B_{2g}, and E_g symmetry, respectively.[14] The phonon Raman spectrum of NiF_2 has been reported previously by Hutchings *et al.*[11] and Hwang *et al.*[12] and we have obtained similar results from our measurements in both $X(\cdot\cdot)Y$ and $Z(\cdot\cdot)Y$ polarizations. The mode frequencies at 295 (10) K are $A_{1g}=407.9$ (414.5) cm^{-1}, $B_{1g}=71.6$ (68.7) cm^{-1}, $B_{2g}=535.3$ (541.0) cm^{-1}, and $E_g=305.6$ (308.0) cm^{-1}. Note the anomalous decrease in B_{1g} mode frequency with decreasing temperature, which will be discussed later. The temperature dependences of the mode frequencies are shown in Fig. 1. All modes show an anomalous change away from the smoothly varying behavior expected for nonmagnetic rutile compounds such as MgF_2 (see Ref. 4, for example), with the A_{1g}, B_{1g}, and B_{2g} modes showing a distinct increase in frequency below T_N. In contrast, the E_g mode exhibits a decrease in frequency below T_N due to the magnetic exchange. The effect is weakest for the B_{2g} mode and strongest for the A_{1g} and B_{1g} modes.

The corresponding phonon linewidth (full width at half maximum) data are given in Fig. 2. Generally, the phonon linewidth increases steadily with increasing temperature above ~50 K, as is observed in other rutile compounds.[4–8] However, for the A_{1g}, B_{2g}, and E_g modes a sharp rise in the linewidth of about 20% of the 10 K value is evident at a temperature near T_N. The B_{1g} line is very sharp at all temperatures, and no anomaly was detected in the linewidth at temperatures near T_N within the experimental uncertainty.

Results obtained for the temperature dependence of the integrated intensity for each mode are presented in Fig. 3. The data were all obtained in $Z(\cdot\cdot)Y$ polarization, so that even though the intensity units are arbitrary, the respective mode strengths are related. All modes exhibit pronounced intensity increases with decreasing temperature below ~100 K, being strongest for the B_{2g} mode (nearly a factor of 2 increase) and weakest for the B_{1g} mode.

4. ANALYSIS AND COMPARISON WITH FeF_2 and MnF_2

In the rutile-structure antiferromagnets, the exchange-dependent term in the Hamiltonian may be given by[7,8]

$$H_{\rm ex}=\sum_{i,j} J_{ij}(\mathbf{r}_1,\mathbf{r}_2,\mathbf{r}_3,\mathbf{r}_4)\mathbf{S}_i\cdot\mathbf{S}_j, \tag{1}$$

where i and j denote magnetic sites on sublattices of opposite spin orientation and J_{ij} is the dominant intersublattice exchange interaction. This exchange also depends on the position coordinates $\mathbf{r}_n$ of the four nonmagnetic F^- ions in the unit cell, because of the indirect superexchange mechanism[15] operating in these antiferromagnets. In rutile compounds, the four Raman-active modes at the Brillouin zone center involve displacements of these F^- ions, whereas the magnetic ions remain stationary.[16] Thus these lattice vibrations all modulate J_{ij}. By using a Taylor series expansion and expressing the coordinates $\mathbf{r}_n$ in terms of phonon variables, the spin–phonon coupling Hamiltonian can be derived.[7,8]

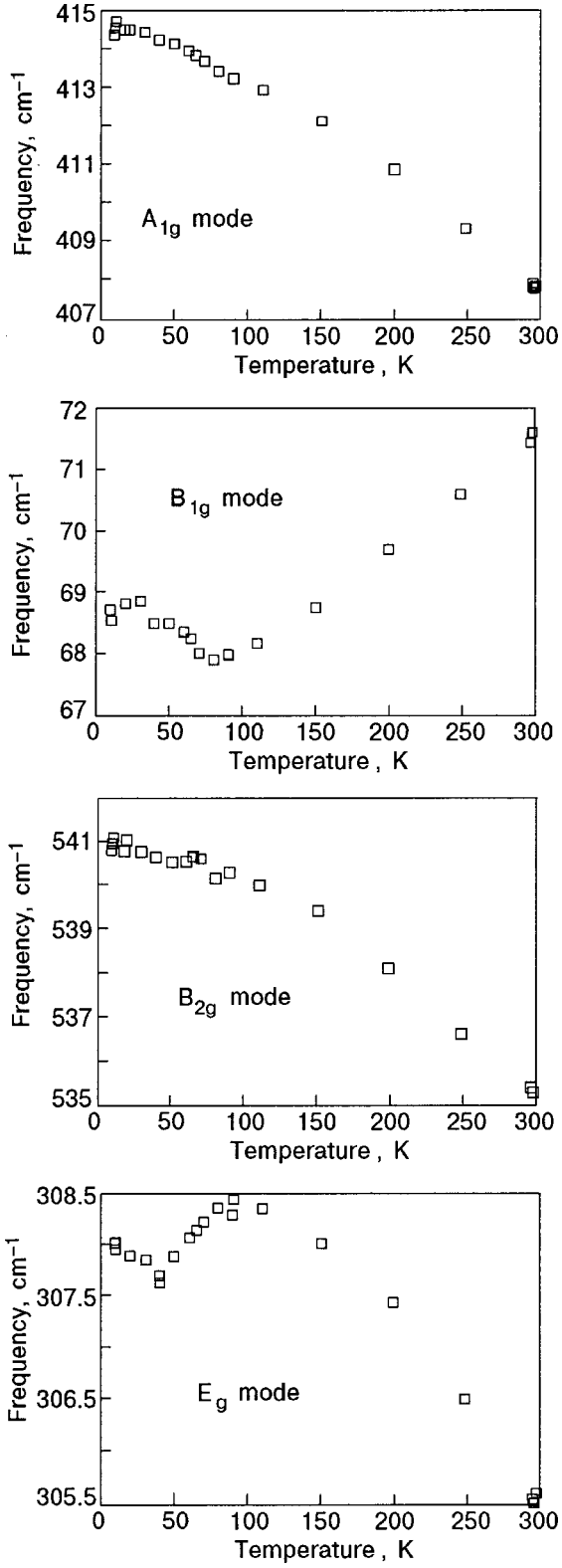

FIG. 1. Temperature dependence of the frequencies of the A_{1g}, B_{1g}, B_{2g}, and E_g Raman-active phonons in NiF_2.

Phonon frequencies

The result thus obtained for the renormalization of the phonon frequency $\omega_{\rm ph}$ is[7,8]

$$\omega_{\rm ph}=\omega_{\rm ph}^0+\lambda\langle\mathbf{S}_i\cdot\mathbf{S}_j\rangle. \tag{2}$$

Here $\omega_{\rm ph}^0$ is the phonon frequency in the absence of spin–phonon coupling, and $\langle\mathbf{S}_i\cdot\mathbf{S}_j\rangle$ denotes a statistical mechani-

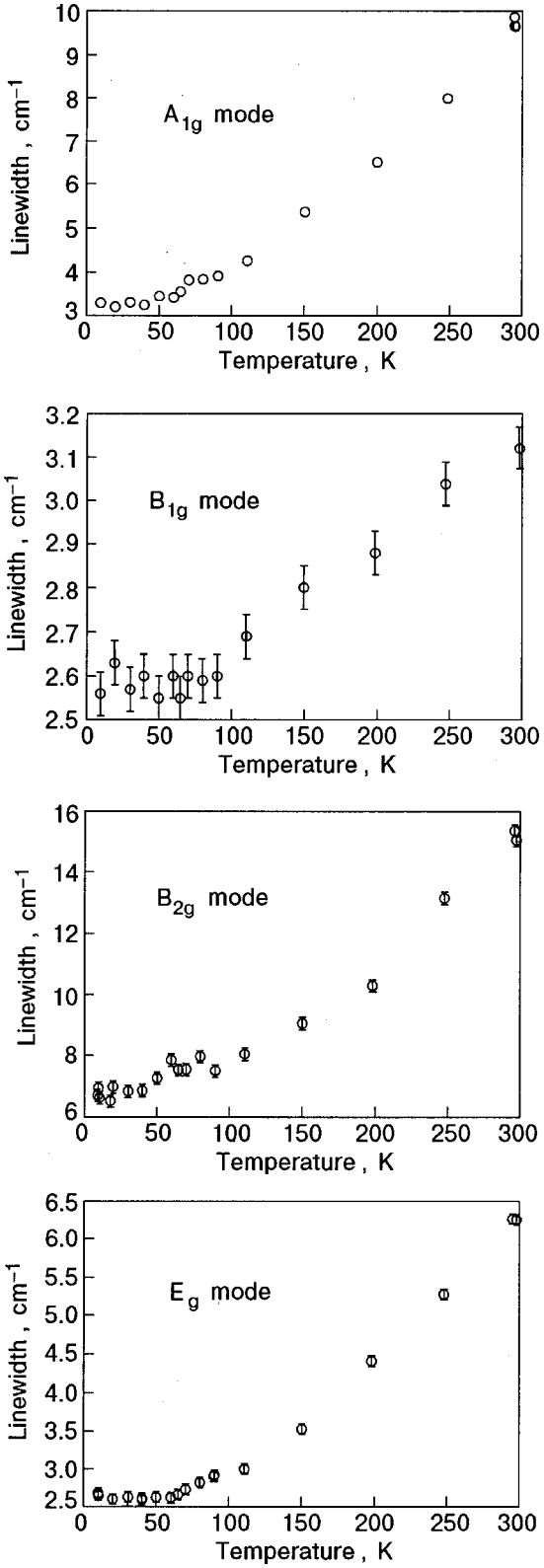

FIG. 2. Temperature dependence of the linewidths of the A_{1g}, B_{1g}, B_{2g}, and E_g Raman-active phonons in NiF_2.

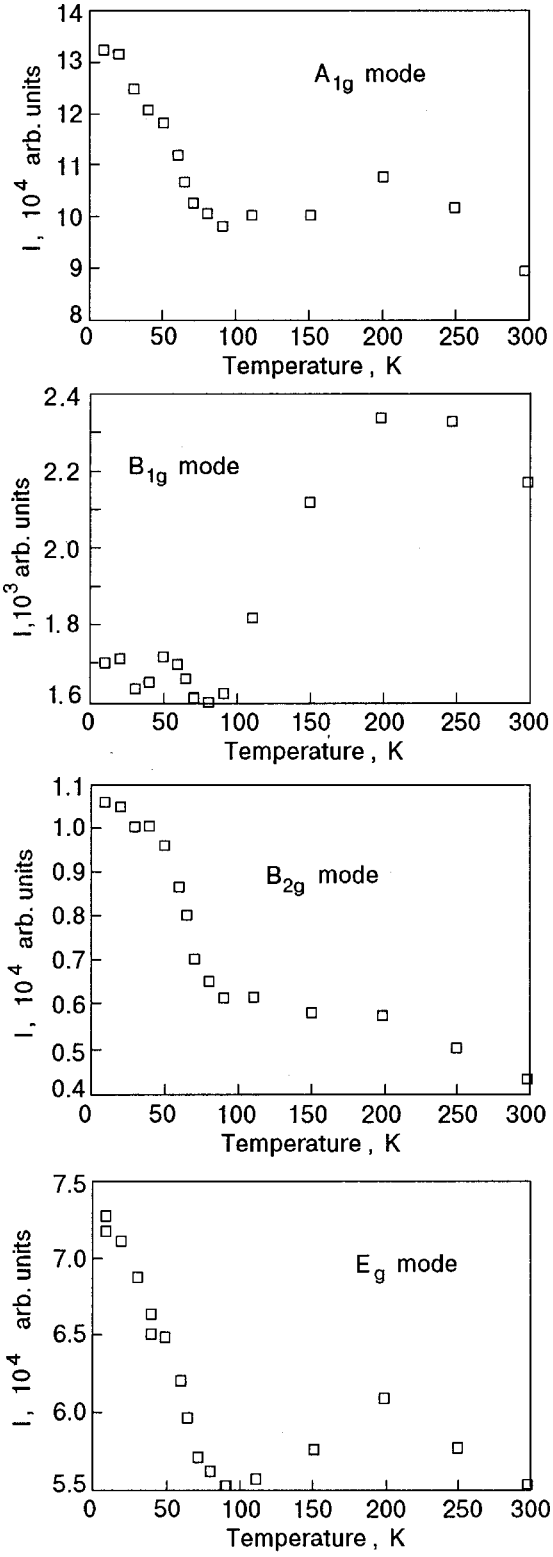

FIG. 3. Temperature dependence of the integrated intensities I of the A_{1g}, B_{1g}, B_{2g}, and E_g Raman-active phonons in NiF_2. The integration times for the A_{1g}, B_{1g}, B_{2g}, and E_g mode measurements were 1, 8, 4, and 1 s, respectively.

cal average for adjacent spins on opposite sublattices. The coupling coefficient λ is different for each phonon and may have either sign. The frequency shift of the phonon due to spin dependent effects is thus

$$\Delta\omega_{\mathrm{ph}}(T) = -\lambda\langle \mathbf{S}_i \cdot \mathbf{S}_j \rangle, \tag{3}$$

which may be rewritten as

$$\Delta\omega_{\mathrm{ph}}(T) = -\lambda S^2 \phi(T). \tag{4}$$

Here $\phi(T)$ is the short-range order parameter defined by

$$\phi(T) = |\langle \mathbf{S}_i \cdot \mathbf{S}_j \rangle| / S^2. \tag{5}$$

TABLE I. Spin–phonon coupling coefficients λ (cm^{-1}) in rutile-structure antiferromagnets.

Phonon	FeF_2	MnF_2[a]	NiF_2
A_{1g}	1.3[a]/1.49[b]	−0.4	−1.6
B_{1g}	−0.4[a]	−0.3	−2.9
B_{2g}	−0.3[a]	−0.3	−0.8
E_g	0.5[a]/ 0.54[b]	0.2	0.9

Notes: [a]From Ref. 8; [b]From Ref. 9.

For a detailed comparison of theory and experiment it is thus necessary to evaluate $\phi(T)$ at temperatures above and below T_N. Although this has not yet been done for the $S=1$ case of NiF_2, $\phi(T)$ has been calculated for the case of $S=2$ (FeF_2) and $S=5/2$ (MnF_2) for temperatures up to $2T_N$. The $\phi(T)$ curves for $S=2$ and 5/2 are very similar over the temperature range $0 \leqslant T \leqslant 2T_N$.[8] Although slight differences can be expected for the $S=1$ case, the use of the $S=2$ results for $\phi(T)$ should provide reasonable first estimates of the spin–phonon coupling coefficients in NiF_2. By using the $S=2$ values for $\phi(0)$ and $\phi(2T_N)$ and estimating $\Delta\omega_{\rm ph}(0)$ and $\Delta\omega_{\rm ph}(2T_N)$ from the frequency versus temperature results given in Fig. 1 in the same way as was done before[7,8] for FeF_2 and MnF_2, approximate values for λ were obtained.

The results obtained for λ in NiF_2 are compared with the FeF_2 and MnF_2 cases in Table I. Overall the spin–phonon coupling coefficient for each phonon is larger in NiF_2 than in FeF_2 and MnF_2, and the enhancement for the B_{1g} mode is particularly pronounced (by an order of magnitude). This may be a consequence of the low frequency of this mode in conjunction with the two spin-wave branches in NiF_2. The sign of the coupling coefficients for NiF_2 and MnF_2 is the same for each phonon, and also for FeF_2 with the exception of the A_{1g} mode.

Phonon linewidths

The linewidth anomalies noted above have not been seen in MnF_2 and FeF_2.[7,8] Phonon linewidths in crystalline solids arise from three- (and four-) phonon anharmonic interactions, with zone center modes decaying into pairs of phonons with equal and opposite wave vectors. Usually, the higher the phonon frequency the wider the Raman line, as observed here for NiF_2 (see Fig. 2), owing to the higher number of available decay paths. The low frequency B_{1g} mode can only decay into acoustic modes and hence its extreme sharpness even at room temperature. In antiferromagnets below T_N, there is an additional decay channel possible–into pairs of magnons of equal and opposite wave vector. Also, as discussed in detail by Wakamura for ferrimagnetic $FeCr_2S_4$ (Ref. 17), a rapid variation in optical phonon damping near T_N can be induced from the interaction between the spin ordering and phonons at or near the Brillouin zone boundary. However, the lack of an observable anomaly near T_N in MnF_2 and FeF_2 indicates that these additional decay mechanisms are not favored for the four optic modes. However, in NiF_2 there exists the low frequency ''ferromagnetic'' branch, which approximates an acoustic phonon type dispersion for wave vectors away from the Brillouin zone center. It is thus possible that phonon decays into this branch are responsible for the observed changes in linewidth of the A_{1g}, B_{2g}, and E_g modes in NiF_2 near T_N. On the other hand, the B_{1g} mode is too low in energy to avail itself of this extra decay path and thus exhibits no observable anomaly.

Phonon intensities

An expression for the phonon Raman intensities can be obtained in a similar way to that of the phonon frequencies, by expanding the Raman polarizability tensor in terms of spin operators and the F^- ion displacements. The Stokes integrated intensity can be written as[7]

$$I=(n_{\rm ph}+1)[|A+B\langle \mathbf{S}_i\cdot\mathbf{S}_j\rangle|^2+C^2\langle S^Z\rangle^2], \tag{6}$$

where $n_{\rm ph}$ is the Bose population factor for phonons, and A, B, and C are constants. Coefficient A represents the intensity behavior in the absence of spin–phonon coupling.

It is not possible at this stage to separate out the two spin-dependent contributions to the Raman intensity, as the relative weights of B and C are not known. However, by using Eq. (5) and taking the mean field approximation, where $\phi(T)=(\langle S^Z\rangle/S)^2$, Eq. (6) can be approximated by

$$I=(n_{\rm ph}+1)[|A+BS^2\phi(T)|^2+C^2S^2\phi(T)]. \tag{7}$$

At $T=0$ we have $\phi(T)=1$, and for $S=1$ Eq. (7) becomes

$$I=(n_{\rm ph}+1)[|A+B|^2+C^2]. \tag{8}$$

The integrated intensity data for the four phonons given in Fig. 3 all exhibit an increase with decreasing temperature below T_N, and reach a saturation value at $T=0$ for the B_{1g} mode and maxima for the other modes. This indicates that the net contribution of coefficients B and C in Eq. (8) must be positive. These coefficients can, in principle, have either sign. To have some indication of the magnitude of these coefficients, we consider the case of the A_{1g} phonon. From Fig. 3 we estimate at $T=0$ that $A^2\simeq 9$ and that $|A+B|^2+C^2 \simeq 13.5$ (ignoring the 10^4 multiplicative factor and the Bose factor). Thus $A\simeq 3$, and $B\simeq -3\pm\sqrt{13.5-C^2}$. Taking the extreme case of $B=0$, we then have $|C|\simeq 2$. At the other extreme of $C=0$, then $B\simeq 0.7$ or -7. For C to be a real quantity, we see that B cannot be less than about -7 or greater than about 0.7. Likewise for B to be real, $|C|$ cannot be greater than about 2. Thus although B and C cannot be uniquely determined at present, their magnitudes can be of the same order as A.

In the other rutile antiferromagnets FeF_2 and MnF_2, the A_{1g} and E_g modes exhibit the same marked increase in intensity with decreasing temperature below T_N as in NiF_2 (Refs. 5 and 7). The intensities of the B_{1g} and B_{2g} phonons in MnF_2 are not as sensitive to the magnetic ordering,[7] whereas the B_{1g} phonon in FeF_2 exhibits a pronounced decrease in intensity.[5] Clearly there is a variation in the magnitudes and signs of B and C for the various phonons in the different rutile-structure antiferromagnets.

5. B_{1g} MODE SOFTENING

The anomalous behavior of the B_{1g} mode frequency $\omega_{B_{1g}}$ with temperature (see Fig. 1) or pressure in rutile-structure compounds such as TiO_2, SnO_2, MnF_2, and FeF_2 has been noted previously.[5,6,18] It was postulated earlier that

TABLE II. Parameters ω_0 and α from Eq. (9) for the B_{1g} mode softening in rutile structure compounds and the virtual transition temperature T_V.

Compound	ω_0, cm^{-1}	α, cm^{-2}/K	T_V, K
MnF_2[a]	54.2	2.37	−1240
FeF_2[b]	67.6	2.56	−1780
NiF_2	66.0	2.56	−1700

Note: [a]From Ref. 6; [b]From Ref. 5.

the B_{1g} mode softening might be the precursor of a structural phase transition[19] with $\omega^2_{B_{1g}} \propto (T-T_C)$, where T_C is the phase transition temperature. Indeed the frequency data for the B_{1g} mode in NiF_2 are an excellent fit to such a law for $T>100$ K:

$$\omega^2_{B_{1g}}[\mathrm{cm}^{-2}] = \alpha T + \omega_0^2 \tag{9}$$

with $\alpha = 2.56$ and $\omega_0^2 = 4353$. Extrapolation of $\omega^2_{B_{1g}}$ to zero results in a virtual transition temperature T_V of -1700 K. A comparison of these NiF_2 results with those obtained earlier for FeF_2 and MnF_2 is given in Table II (Refs. 5 and 6). This Table shows that the results obtained for NiF_2 and FeF_2 are remarkably similar and not too different from those of MnF_2. The parameter T_V is a large negative number in all cases, and thus it is unlikely that such a mode softening could ever result in a structural phase transition, even if it were highly first-order in nature.

More recently, Merle *et al.*[20] have demonstrated that the pressure-dependent softening of the B_{1g} phonon in TiO_2 does not exhibit a special sensitivity to an orthorhombic distortion and that it arises from atomic displacements associated with pure rotations of anions around the central cation. Similarly, a detailed analysis of the temperature-dependent softening of the B_{1g} phonon in FeF_2 led to the conclusion that it results from the lattice thermal contraction, which disproportionally influences the forces between nearest-neighbor fluorine ions in adjacent planes perpendicular to the *c* axis.[5] Although a structural transition mechanism cannot strictly be ruled out, it is thus most likely that the B_{1g} phonon softening in NiF_2, which is so similar to that in FeF_2, is also a consequence of changes in the anion force constants with lattice contraction. Unfortunately, lattice dynamical models[16] for rutile-structure antiferromagnets are not reliable enough to test this proposition.[5] However, further support for this viewpoint comes from a recent thorough analysis of the B_{1g} phonon temperature and pressure dependence in isostructural MgF_2. This study has confirmed that the anomalous mode softening observed with decreasing temperature in this compound is indeed caused by the thermal contraction of the lattice.[21]

CONCLUSIONS

From a study of the temperature dependences of the four Raman-active modes in NiF_2, considerable spin–phonon coupling has been revealed from the phonon line parameters of frequency, linewidth, and intensity. Coupling parameters were deduced from the phonon frequencies and found to be larger than those for the isostructural antiferromagnets FeF_2 and MnF_2. Large intensity coupling parameters were also deduced. The anomalous softening of the B_{1g} mode with decreasing temperature is ascribed to lattice thermal contraction rather than evidence for some (virtual) structural phase transition.

The expert technical assistance of H. J. Labbe in the Raman measurements is gratefully acknowledged.

*E-mail: David.Lockwood@nrc.ca

[1] M. G. Cottam and D. J. Lockwood, *Light Scattering in Magnetic Solids*, Wiley, New York (1986).
[2] For a review of this work and further references see Ref. 1, pp. 220–221.
[3] For details of the spin–phonon coupling in the europium and cadmium–chromium compounds, see the extensive review by G. Guntherodt and R. Zeyher, in *Light Scattering in Solids IV*, M. Cardona and G. Guntherodt (Eds.) Springer-Verlag Heidelberg (1984).
[4] J. L. Sauvajol, R. Almairac, C. Benoit, and A. M. Bon, in *Lattice Dynamics*, M. Balkanski (Ed.) Flammarion, Paris (1978), p. 199.
[5] D. J. Lockwood, R. S. Katiyar, and V. C. Y. So, Phys. Rev. B **28**, 1983 (1983).
[6] D. J. Lockwood, in *Proceedings of the IXth International Conference on Raman Spectroscopy*, M. Tsuboi (Ed.), Chem. Soc. Jpn., Tokyo (1984), p. 810.
[7] D. J. Lockwood and M. G. Cottam, in *Magnetic Excitations and Fluctuations II*, U. Balucani, S. W. Lovesey, M. G. Rasetti, and V. Tognetti (Eds.), Springer, Berlin (1987), p. 186.
[8] D. J. Lockwood and M. G. Cottam, J. Appl. Phys. **64**, 5876 (1988).
[9] C. Binek and W. Kleeman, J. Phys.: Condens. Matter **4**, 65 (1992).
[10] M. G. Cottam, J. Phys. C **7**, 2901 (1974).
[11] M. T. Hutchings, M. F. Thorpe, R. J. Birgeneau, P. A. Fleury, and H. J. Guggenheim, Phys. Rev. B **2**, 1362 (1970).
[12] D.-M. Hwang, T. T. Chen, and H. Chang, Solid State Commun. **18**, 1101 (1976).
[13] N. L. Rowell, D. J. Lockwood, and P. Grant, J. Raman Spectrosc. **10**, 119 (1981); D. J. Lockwood and C. P. Cantin, in *Proceedings of the XIth International Conference on Raman Spectroscopy*, R. J. H. Clark and D. A. Long (Eds.) Wiley, Chichester (1988), p. 947.
[14] W. Hayes and R. Loudon, *Scattering of Light by Crystals*, Wiley, New York (1978), p. 119.
[15] M. G. Cottam and D. J. Lockwood, *Light Scattering in Magnetic Solids*, Wiley, New York (1986), p. 6.
[16] R. S. Katiyar, J. Phys. C **3**, 1087 (1970); *ibid.* **3**, 1693 (1970).
[17] K. Wakamura, Solid State Commun. **71**, 1033 (1989).
[18] References to the pressure-dependent studies of TiO_2 and SnO_2 are given in Ref. 5.
[19] G. A. Samara and P. S. Peercy, Phys. Rev. B **7**, 1131 (1973).
[20] P. Merle, J. Pascual, J. Camassel, and H. Mathieu, Phys. Rev. B **21**, 1617 (1980).
[21] A. Perakis, E. Sarantopoulou, Y. S. Raptis, and C. Raptis, Phys. Rev. B **59**, 775 (1999).

This article was published in English in the original Russian journal. Reproduced here with stylistic changes by the Translation Consultant.

Electronic Raman scattering through a stripe ordering transition in $La_{2-x}Sr_xNiO_4$

V. P. Gnezdilov* and A. V. Yeremenko

B. Verkin Institute for Low Temperature Physics and Engineering of the National Academy of Sciences of Ukraine, 47 Lenin Ave., Kharkov 61103, Ukraine

Yu. G. Pashkevich

A. Galkin Donetsk Physicotechnical Institute of the National Academy of Sciences of Ukraine, 72 R. Luxemburg Str., Donetsk 83114, Ukraine

P. Lemmens

Physikalisches Institut, RWTH Aachen, Aachen 52056, Germany

G. Güntherodt and J. M. Tranquada

Brookhaven National Laboratory, Upton, NY 11973, USA

D. J. Buttrey

University of Delaware, Newark, Delaware 19716, USA

K. Nakajima

Neutron Scattering Laboratory ISSP, University of Tokyo, Tokai, Ibaraki, Japan

(Submitted February 28, 2002)
Fiz. Nizk. Temp. **28**, 716–723 (July 2002)

We describe the results of electronic Raman scattering experiments in two differently doped single crystals of $La_{2-x}Sr_xNiO_4$ ($x=0.225$ and 1/3). In B_{1g} symmetry a crossover from weakly interacting to pseudogap-like behavior is observed at a charge-ordering temperature T_{co}. In B_{2g} symmetry a redistribution of electronic continua with decreasing temperature is accompanied by a loss of spectral weight below T_{co} in the low-frequency region due to opening of a pseudogap. The slope of the Raman response at vanishing frequencies is investigated, too. Its temperature behavior in B_{2g} symmetry, which predominantly selects charge carriers with momenta along the diagonals of the NiO_2 bonds, provides clear evidence for one-dimensional charge transport in the charge-ordered phase.
[DOI: 10.1063/1.1496659]

INTRODUCTION

Stripe ordering of charge and spin in transition-metal oxides has been of intense interest to condensed-matter physics from the theoretical and experimental points of view as an example of a nontrivial ordering phenomenon that originates from the interplay between charge hybridization and interaction. The first evidence for unusual magnetic correlations was obtained in a neutron diffraction study on a single crystal of $La_{1.8}Sr_{0.2}NiO_{3.96}$.[1] Indications of charge order in $La_{2-x}Sr_xNiO_4$ were found in electron diffraction[2] and transport measurements[3] on ceramic samples. Neutron diffraction studies[4,5] of a $La_2NiO_{4.125}$ crystal were the first to detect diffraction from both the magnetic and charge order in the same sample. In the first studies of $La_{2-x}Sr_xNiO_4$ it has been suggested that ordering of the dopant-induced holes occurs only commensurately at special values of x, such as 1/2 and 1/3 (Refs. 2 and 3). Later it was found that a single crystal with $x=0.2$, although not at a special value of x, shows commensurate order,[6] albeit with a short in-plane correlation length of ~40 Å. In contrast, the stripe order in $La_2NiO_{4+\delta}$[4,5] and $La_{1.775}Sr_{0.225}NiO_4$[7] was found to be incommensurate, with the wave vector varying significantly with temperature.

The stripe order in Sr-doped nickelates has been characterized in detail by neutron diffraction, and some summary of the results is given in Ref. 8. While many features of the ordering are now clear, some questions remain. One of them is the question of the possibility of finite conductivity in the stripe-ordered state. One can expect two possible scenarios, which could lead to conductivity. According to the first one the stripes themselves are insulating but the system can be metallic due to fluctuations and motion of stripes.[9] Alternatively, metallic conductivity may exist along the charge threads without a violation of stripe ordering as a whole. In the latter case, Coulomb interactions between neighboring stripes should lead to charge-density-wave order along stripes at sufficiently low temperatures and in the absence of stripe fluctuations.[10] In our previous optical conductivity study of a $La_{1.775}Sr_{0.225}NiO_4$ single crystal a strong Fano antiresonance was observed in the optical conductivity spectra.[11] Based on a careful analysis of the phonon spectra, we concluded that the energy of the antiresonance corresponds to Ni-O bond stretching motions along the stripes. It was concluded that the antiresonance, which results from electron-phonon coupling, provides strong evidence for finite conductivity along the stripes in the incommensurately

stripe-ordered sample, at least at optical-phonon frequencies.

Raman scattering (RS) is a powerful method for studying the excitations of charge carriers in solids. In recent years this method has been widely applied to study the scattering of electrons in metals, insulators, semiconductors, and superconductors. Via light's coupling to the electron's charge, inelastic light scattering reveals symmetry-selective properties of the electron dynamics over a wide range of energy scales and temperatures. In this work we report on electronic Raman scattering spectra of two $La_{2-x}Sr_xNiO_4$ single crystals with $x=0.225$ and $x=1/3$ and with charge ordering temperatures $T_{co}=150$ K and 240 K, respectively.[7,12] The hole density per Ni site in the sample with $x=0.225$ is less than 1 (in contrast to $x=1/3$, where the density is exactly 1). It is known that in-plane resistivity ρ_{ab} of Sr-doped lantanium nickelates is doping-dependent: it increases with hole concentration decreasing. And independently of the doping level, the resistivity increases by several orders below T_{co},[3,13,14] which indicates quenching of the charge degrees of freedom due to the ordering. At first glance the increase of the resistivity below T_{co} is incompatible with possible conductivity along the threads of the stripes, which remain in the charge-ordered state. This contradiction can be removed by stripe domain formation, which occurs below T_{co}. One can expect the appearance of two type thermodynamical stripe-domains in which stripes run perpendicular to each other. Thus, only a small part of the threads of charges can participate in the charge transfer. Three principal symmetries A_{1g}, B_{1g}, and B_{2g}, were examined. As has been described in detail in other publications,[15–19] there exists a relationship between the charge-carrier momenta and light polarization through the symmetry properties of the Raman vertex. In B_{1g} and B_{2g} symmetry the charge carriers with momenta along the principal axes and the diagonals, respectively, are preferentially weighted. A_{1g} is a weighted average over the entire Brillouin zone.

EXPERIMENT

Raman spectra were measured on fresh chemically etched surfaces in a quasi-backscattering configuration utilizing a triple monochromator (DILOR XY), a liquid nitrogen cooled CCD detector, and a 514.5-nm Ar-ion laser. The laser beam of 20 mW was focused on an area of 0.1 mm^2 on the *ab* plane of the mirrorlike polished crystal surface. The orientation of the crystals in the $I4/mmm$ setting was monitored by x-ray Laue diffraction.

All measurements were performed with the polarization of incident and scattered light as $(\hat{\mathbf{E}}_i,\hat{\mathbf{E}}_s)=(xx)$, (xy), and (ab), respectively. Here $a=[100]$ and $b=[010]$ are directions along the Ni–O–Ni bonds; the x and y directions are parallel to [110] and $[1\bar{1}0]$. Such geometries allow measuring the $A_{1g}+B_{2g}$, B_{1g}, and B_{2g} symmetry components of the Raman-scattering cross section. The Raman response functions $\chi''(\omega)$ were obtained by dividing the original spectra $I(\omega,T)$ by Bose–Einstein thermal factor, since they are related to each other through $I(\omega,T)\sim[1-\exp\times(-\hbar\omega/k_B)]^{-1}\chi''(\omega,T)$.

RESULTS AND DISCUSSION

Raman scattering spectra of $La_{2-x}Sr_xNiO_4$ ($x=1/3$, 0.225) and $La_2NiO_{4.125}$ in the *xx* and *xy* scattering geometries are presented elsewhere.[11,20–22] The average symmetry of the lattice is described by space group $I4/mmm$. The corresponding Raman-active phonons are distributed among the irreducible representations of the space group as $2A_{1g}+2E_g$. At room temperature all the observed modes are weak and broad. Conspicuous changes were observed in the phonon spectra below the charge-ordering temperature T_{co}. The occurrence of stripe order, with a characteristic wave vector $\mathbf{Q}_c$, lowers the translational symmetry and leads to the appearance of extra lines both in the *xx* and *xy* spectra. Low-temperature scans in the *xy* geometry reveal also two wide bands that were interpreted as two-magnon excitations within the antiferromagnetic domains and across the domain walls.[11,20–22] Phonon and two-magnon excitations are superposed on top of a significant electronic background that changes its shape with changing temperature.

As was noted in Ref. 23, RS experiments in strongly correlated systems (ranging from mixed-valence materials to Kondo insulators to high-temperature superconductors) show temperature-dependent electronic Raman spectra that are both remarkably similar and quite anomalous, suggesting a common mechanism governing transport. While theories that describe RS in weakly correlated metals[18] and band insulators[24] have been known for some time, a theory that connects the metallic and insulating states and describes materials near the metal-insulator transition has been developed only recently.[23] The theoretical model contains two types of electrons: itinerant band electrons and localized (*d* or *f*) electrons. The band electrons can hop between nearest neighbors (with hopping integral $t^*/(2\sqrt{d})$ on a *d*-dimensional cubic lattice), and they interact via screened Coulomb interaction with the localized electrons (which is described by an interaction strength U between electrons that are located at the same lattice site). The Hamiltonian is written as

$$H=-\frac{t^*}{2\sqrt{d}}\sum_{(i,j)} d_i^\dagger d_j+E_f\sum_i w_i-\mu\sum_i (d_i^\dagger d_i+w_i)$$
$$+U\sum_i d_i^\dagger d_i w_i,$$

where $d_i^\dagger(d_i)$ is the spinless conduction electron creation (annihilation) operator at lattice site i and $w_i=0$ or 1 is a classical variable corresponding to the localized *f*-electron number at site i. Both E_f and μ were adjusted so that the average filling of the *d* electrons is 1/2 and the average filling of the *f* electrons is 1/2 ($\mu=U/2$ and $E_f=0$). For half-filling, $U<0.65$ corresponds to a weakly correlated metal, while a pseudogap phase appears for $0.65<U<1.5$, passing through a quantum critical point at $U=1.5$ to the insulator phase $U>1.5$ (the values of U are presented in units of t^*).

Figures 1a and 2a show the A_{1g} experimental Raman spectra for the samples under study at different temperatures, that were obtained by subtracting the (*ab*) spectra from the (*xx*) ones. Figures 1b and 2b present the electronic Raman response for the A_{1g} channel evaluated at different temperatures by fitting the experimental curves and it is seen that the

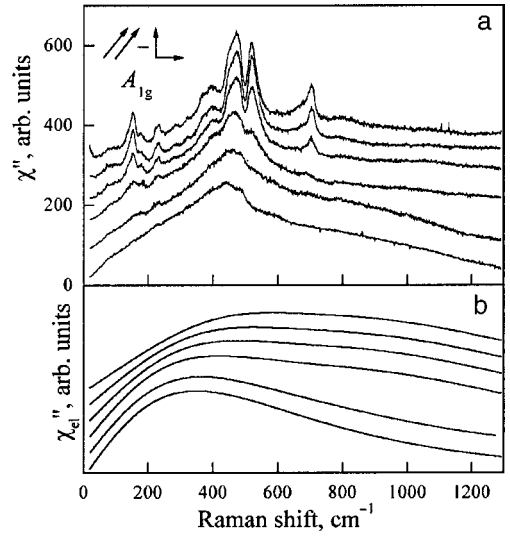

FIG. 1. Experimental A_{1g} Raman response of $La_{1.775}Sr_{0.225}NiO_4$ at different temperatures ($T=5$, 50, 100, 150, 200, and 295 K from top to bottom). The spectra are plotted on the same scale but are displaced vertically for clarity (a). Electronic A_{1g} Raman response at the same temperatures evaluated from the experimental spectra (b).

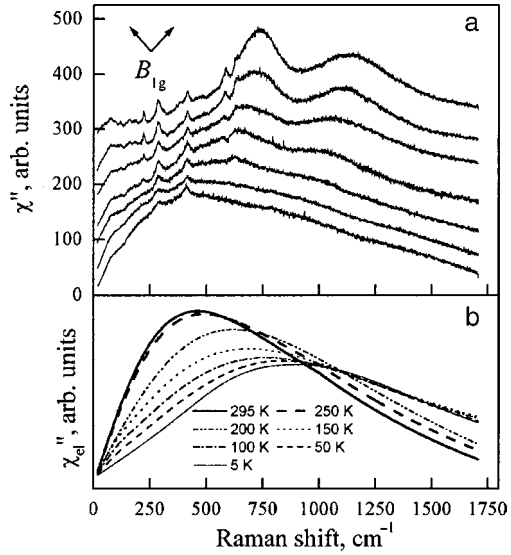

FIG. 3. Experimental B_{1g} Raman response of $La_{1.775}Sr_{0.225}NiO_4$ at different temperatures ($T=5$, 50, 100, 150, 200, 250, and 295 K from top to bottom). The spectra are plotted on the same scale but are displaced vertically for clarity (a). Electronic A_{1g} Raman response at the same temperatures evaluated from the experimental spectra (b).

general behavior of the A_{1g} response is similar for both samples. As follows from the theory,[23] the A_{1g} Raman response has a bell-like shape at all values of U and increases and sharpens as U increases. The peak of the response becomes more symmetric in shape and moves to higher energies also. Above T_{co}, our samples display behavior consistent with the theory[23] and resistivity measurements:[3,13,14] (i) the Raman response function has an asymmetric line shape characteristic for $U<1.5$; (ii) the peak position shifts to lower energy with increasing hole concentration (decreasing resistivity).

Below T_{co}, the A_{1g} Raman responses change to shapes composed of a rapidly increasing part from $\omega\sim 0$ to the leading edge energies and a weakly ω-dependent part above them. The position of the leading edge depends on the temperature and shifts to higher energy as the temperature decreases.

In Figures 3a and 4a we plot (xy) spectra versus temperature. Figures 3b and 4b present the electronic Raman response for the B_{1g} channel evaluated from the experimental spectra. In the charge-disordered state (above T_{co}) the B_{1g} electronic Raman spectra for both samples are close to the ideal ''bad metal'' spectra. Note that the magnitude of resistivity above T_{co} corresponds to a ''bad metal'' also. As the temperature crosses T_{co}, dramatic changes are observed in the spectra: the low-frequency response depletes and the

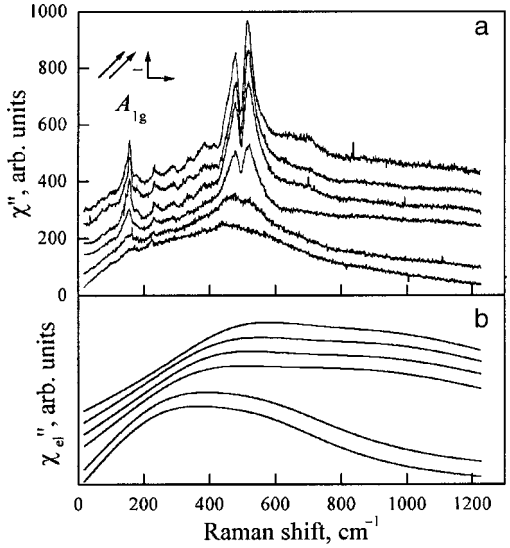

FIG. 2. Experimental A_{1g} Raman response of $La_{5/3}Sr_{1/3}NiO_4$ at different temperatures ($T=5$, 50, 100, 150, 250, and 295 K from top to bottom). The spectra are plotted on the same scale but are displaced vertically for clarity (a). Electronic A_{1g} Raman response at the same temperatures evaluated from the experimental spectra (b).

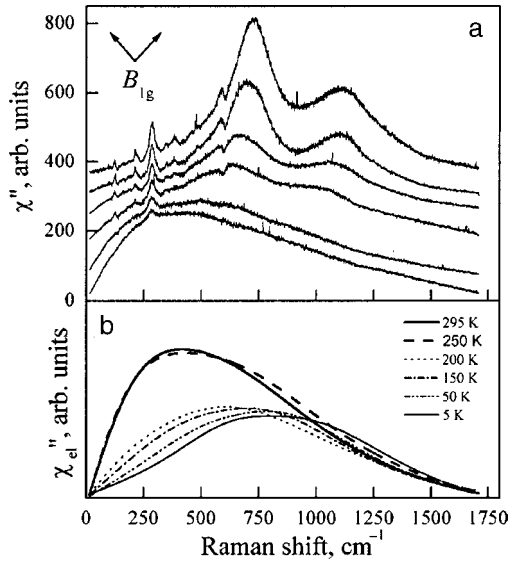

FIG. 4. Experimental B_{1g} Raman response of $La_{5/3}Sr_{1/3}NiO_4$ at different temperatures ($T=5$, 50, 150, 200, 250, and 295 K from top to bottom). The spectra are plotted on the same scale but are displaced vertically for clarity (a). Electronic A_{1g} Raman response at the same temperatures evaluated from the experimental spectra (b).

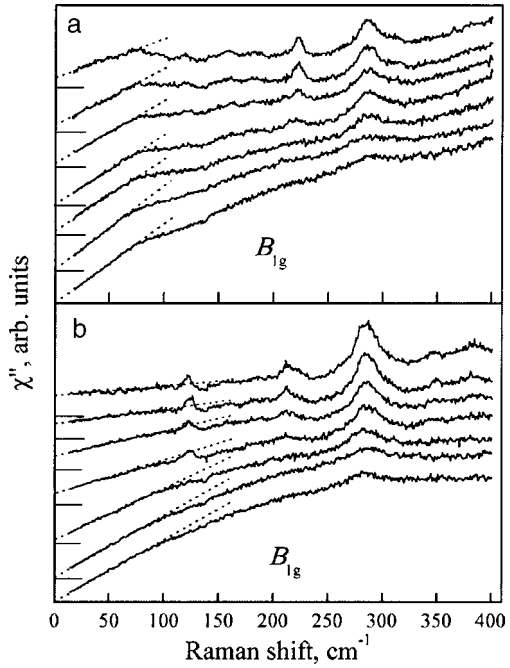

FIG. 5. Low-frequency B_{1g} Raman response of $La_{1.775}Sr_{0.225}NiO_4$ (a) and $La_{5/3}Sr_{1/3}NiO_4$ (b) single crystals obtained at temperatures 5, 50, 100, 150, 200, 250, and 295 K (from top to bottom). The dashed lines in the figures represent the slope of $\chi''(\omega)$ as $\omega \to 0$.

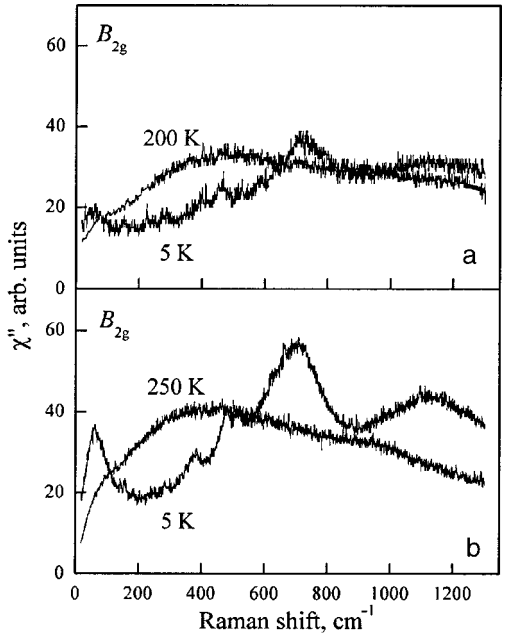

FIG. 7. Experimental B_{2g} Raman response of $La_{1.775}Sr_{0.225}NiO_4$ (a) and $La_{5/3}Sr_{1/3}NiO_4$ (b) single crystals measured at temperatures above and below charge-ordering temperature in the frequency region 0–1300 cm^{-1}.

spectral weight shifts into a charge-transfer peak. The position of the charge-transfer peak for the sample with $x = 0.225$ was estimated as $\sim$840 cm^{-1} at $T = 5$ K. The same charge gap value was obtained from the optical conductivity spectra.[11] For the sample with $x = 1/3$, a surprisingly lower position ($\sim$900 cm^{-1}) of the charge transfer peak was observed in our Raman experiments in comparison with the value of 2090 cm^{-1} for the charge gap from the optical conductivity measurements.[25]

Summarizing the comparison of our results with the theoretical calculations,[23] one may conclude that the B_{1g} response for both measured samples below T_{co} has a line shape that is closer to the pseudogap phase than to the strong insulator phase. Concerning the temperature behavior, the decreasing of the spectral weight and the shift of the peak position to a higher energy with a decreasing temperature are contrary to the theoretical predictions. It seems that the in-

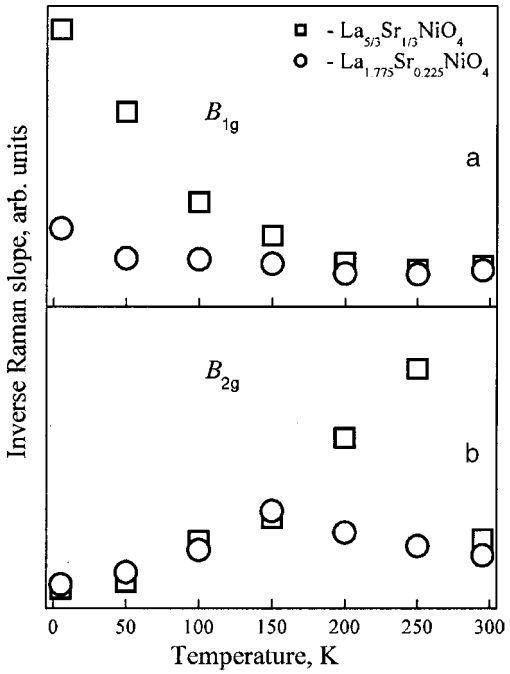

FIG. 6. Inverse slope of the B_{1g} (a) and B_{2g} (b). Raman response obtained from the experimental spectra of $La_{1.775}Sr_{0.225}NiO_4$ and $La_{5/3}Sr_{1/3}NiO_4$ single crystals.

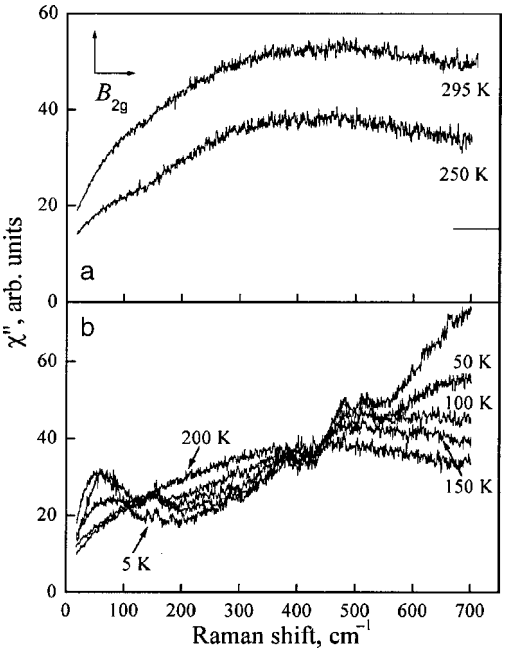

FIG. 8. B_{2g} spectra for $La_{1.775}Sr_{0.225}NiO_4$. The upper panel shows spectra at $T > T_{co}$ (a). The spectra are displaced for clarity and their zeros are indicated by a tick on the vertical axis. The lower panel shows spectra at $T < T_{co}$ (b).

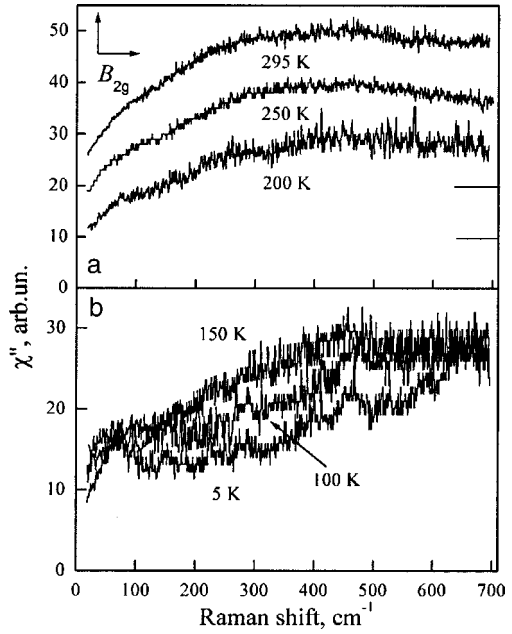

FIG. 9. B_{2g} spectra for $La_{5/3}Sr_{1/3}NiO_4$. The upper panel shows spectra at $T>T_{co}$ (a). The spectra are displaced for clarity and zero for the spectra at 295 K is indicated by a tick on the vertical axis. The low panel shows spectra at $T<T_{co}$ (b).

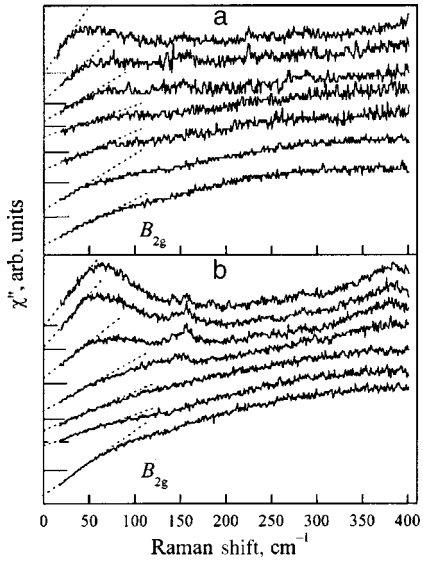

FIG. 11. Low-frequency B_{2g} Raman response of $La_{1.775}Sr_{0.225}NiO_4$ (a) and $La_{5/3}Sr_{1/3}NiO_4$ (b) single crystals obtained at temperatures 5, 50, 100, 150, 200, 250, and 295 K (from top to bottom). The dashed lines in the figures represent the slope of $\chi''(\omega)$ as $\omega\to 0$.

clusion of a strong interaction between electrons and spin fluctuations[26] or the scattering of electrons on extended impurities[27] into the theory could resolve this discrepancy.

Additional information on charge dynamics can be obtained from the slope of $\chi''(\omega)$ at vanishing frequencies. This slope can be denoted as $\Gamma_\lambda = \lim_{w\to 0} w/\chi''_\lambda(\omega)$, where $\lambda = B_{1g}$ or B_{2g}. As is clearly seen in Fig. 5, the slope of the low-energy continua for both samples changes with decreasing temperature. The inverse Raman slope characterizes the quasiparticle lifetime at regions of the Fermi surface selected by the light polarization orientations. In earlier publications[23,28] it was shown that the inverse slope $1/\Gamma_\lambda$ shows qualitatively different behavior for different doping regimes of various cuprate materials. At B_{1g} symmetry a strong doping dependence of the inverse slope was observed.[28] In Fig. 6a we plot the inverse slope of the Raman response obtained from the B_{1g} experimental spectra. The variation of the inverse slope with temperature for the $x=0.225$ sample clearly shows the pseudogap phase behavior, while for the $x=1/3$ sample the low-temperature inverse slope increases dramatically, as is characteristic for a more insulating system.

We turn now to the temperature dependence of the B_{2g} response in our samples. Our interest is connected with the attempt to observe a pseudogap in the RS spectra. The term pseudogap denotes a partial gap. An example of such a partial gap would be a situation where, within the band theory approximation, some regions of the Fermi surface become gapped while other parts retain their conducting properties.[29] A number of families of high-temperature cuprate oxides demonstrate evidence of the presence of a pseudogap in the normal state. As was convincingly proved in Ref. 30, the pseudogap is a signature of the electronic interactions above T_c and is not directly related to the superconducting pairing correlations. In the RS experiments on high-T_c cuprates the pseudogap state is characterized by a loss of spectral weight in the frequency range between zero and approximately 800 cm^{-1} and is clearly seen in B_{2g} symmetry in underdoped materials. The change of the spectra in the pseudogap state becomes very small for higher doping levels.

Figure 7 shows the B_{2g} Raman response in $La_{2-x}Sr_xNiO_4$ at two doping levels, obtained at temperatures of 295 K and 5 K. The loss of spectral weight in the low-frequency region on cooling is seen. To make things more quantitative we carried out measurements at different temperatures, and the results are shown in Figs. 8 and 9. For clarity the two temperature ranges are plotted separately. Above the charge-ordering temperature no intensity anomalies occur (Figs. 8a and 9a). For $T<T_{co}$ spectral weight is lost in the low-frequency region. In Fig. 10 we plot the difference $\Delta\chi''(\omega,T)=\chi''(\omega,T)-\chi''(\omega,T>T_{co})$ between the spectra measured at different temperatures below T_{co} and the spectrum obtained just above T_{co}. We observe the maximal amplitude of the spectral change at approximately 300 cm^{-1}

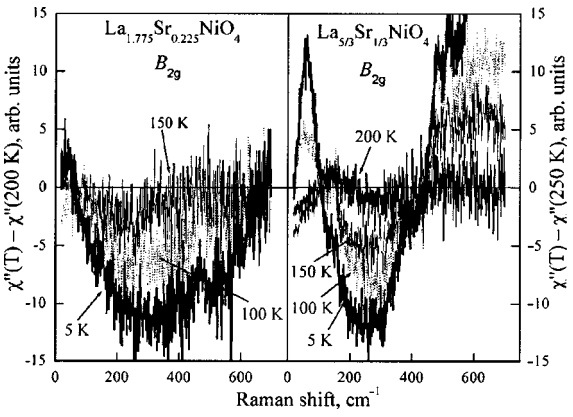

FIG. 10. The pseudogap as a function of temperature. Shown in the figure are differences between the response functions at $T<T_{co}$ and response function just above T_{co}.

($x=0.225$) and 250 cm^{-1} ($x=1/3$) (Figs. 8b and 9b). However, for a detailed analysis of the pseudogap state it would be more physical to relate the ''normal'' and ''pseudogap'' spectra at the same temperature as was done in Ref. 30, where the ''normal'' spectra at the respective temperatures were constructed. Although the pseudogap has been observed and investigated by various methods, its interpretation is still an open issue at present. In Refs. 30 and 31 it was speculated that as the energy scale of the pseudogap is comparable to that of the exchange interaction J, the driving force is magnetic.

While the B_{1g} data cannot be linked to ordinary transport, the inverse slope observed in the B_{2g} channel was found to track the temperature dependence of the dc resistivity.[28,30] Moreover, the B_{2g} response is expected to be sensitive to properties of charge stripes running along the diagonal directions between in-plane Ni–O bonds. In Fig. 11 the low-frequency B_{2g} spectra at different temperatures are shown. It is seen that the slope of the Raman response for both samples is temperature dependent. The temperature dependences of the inverse slope in the B_{2g} channel are presented in Fig. 6b, which indicates that below T_{co}, $1/\Gamma_{\lambda}$ decreases with decreasing temperature for both samples. Such metal-like behavior of the inverse Raman slope demonstrates the existence of finite conductivity within the charge stripes. A crossover from two-dimensional to one-dimensional transport behavior due to the formation of stripes was proposed by Moshalkov *et al.*[32] Direct evidence for one-dimensional transport in the stripe-ordered phase was demonstrated in Hall coefficient measurements on neodymium-doped lanthanum strontium cuprate.[33]

In summary, channel-dependent Raman scattering measurements of $La_{2-x}Sr_xNiO_4$ ($x=0.225, 1/3$) samples were carried out over a wide range of temperatures. It was found that the scattering on charge carriers for both samples is quite similar. For A_{1g}, B_{1g}, and B_{2g} symmetries a temperature-dependent redistribution of the electronic continua was observed for both compounds.

In the B_{1g} channel a crossover from the weakly interacting to pseudogap-like behavior of the electronic continua was found at the charge-ordering temperature. From the low-frequency B_{1g} spectra we have estimated the B_{1g} inverse Raman slope. Its temperature behavior is in agreement with the theoretical one for the pseudogap phase.

The pseudogap state that is characterized by a loss of spectral weight in the low-frequency region was directly observed in the B_{2g} symmetry below T_{co}. The decrease of the inverse Raman slope below T_{co} and its metal-like behavior provides evidence for one-dimensional finite conductivity within the charge stripes.

We are grateful to Prof. V. V. Eremenko for permanent interest and support of our activity and for useful discussions. This work was supported by the NATO Science Program under Grant No PST.CLG 977766.

*E-mail: gnezdilov@ilt.kharkov.ua

[1] S. M. Hayden, G. H. Lander, J. Zarestky, P. J. Brown, C. Stassis, P. Metcalf, and J. M. Honig, Phys. Rev. Lett. **68**, 1061 (1992).
[2] C. H. Chen, S.-W. Cheong, and A. S. Cooper, Phys. Rev. Lett. **71**, 2461 (1993).
[3] S.-W. Cheong, H. Y. Hwang, C. H. Chen, B. Battlogg, L. W. Rupp, Jr., and S. A. Carter, Phys. Rev. B **49**, 7088 (1994).
[4] J. M. Tranquada, D. J. Buttrey, V. Sachan, and J. E. Lorenzo, Phys. Rev. Lett. **73**, 1003 (1994).
[5] J. M. Tranquada, J. E. Lorenzo, D. J. Buttrey, and V. Sachan, Phys. Rev. B **52**, 3581 (1995).
[6] V. Sachan, D. J. Buttrey, J. M. Tranquada, J. E. Lorenzo, and G. Shirane, Phys. Rev. B **51**, 12742 (1995).
[7] J. M. Tranquada, D. J. Buttrey, and V. Sachan, Phys. Rev. B **54**, 12318 (1996).
[8] H. Yoshizawa, T. Kakeshita, R. Kajimoto, T. Tanabe, T. Katsufuji, and Y. Tokura, Phys. Rev. B **61**, R854 (2000).
[9] H. Eskes, O. Y. Osman, R. Grimberg, W. van Saarloos, and J. Zaanen, Phys. Rev. B **58**, 6963 (1998).
[10] S. A. Kivelson, E. Fradkin, and V. J. Emeri, Nature (London) **393**, 550(1998).
[11] Yu. Pashkevich, V. A. Blinkin, V. P. Gnezdilov, V. V. Tsapenko, V. V. Eremenko, P. Lemmens, M. Fisher, M. Grove, G. Guntherodt, L. Degiorgi, P. Wachter, and D. J. Buttrey, Phys. Rev. Lett. **84**, 3919 (2000).
[12] S.-H. Lee and S.-W. Cheong, Phys. Rev. Lett. **79**, 2514 (1997).
[13] R. J. Cava, B. Batlogg, T. T. Palstra, J. J. Krajewski, W. F. Peck, A. P. Ramírez, and L. W. Rupp, Phys. Rev. B **43**, 1229 (1991).
[14] J. H. Jung, D.-W. Kim, T. W. Noh, H. C. Kim, H.-C. Ri, S. J. Levett, M. R. Lees, D. McK. Paul, and G. Balakrishnan, Phys. Rev. B **64**, 165106 (2001).
[15] T. P. Devereaux, D. Einzel, B. Stadlober, R. Hackl, D. H. Leach, and J. J. Neumeier, Phys. Rev. Lett. **72**, 396 (1994).
[16] T. P. Devereaux, D. Einzel, B. Stadlober, R. Hackl, D. H. Leach, and J. J. Neumeier, Phys. Rev. Lett. **72**, 3291 (1994).
[17] J. G. Naeni, X. K. Chen, K. C. Hewitt, J. C. Irwin, T. P. Devereaux, M. Okuya, T. Kimura, and K. Kishio, Phys. Rev. B **57**, R11077 (1998).
[18] T. P. Devereaux and A. P. Kampf, Phys. Rev. B **59**, 6411 (1999).
[19] T. P. Devereaux and A. P. Kampf, Phys. Rev. B **61**, 1490 (2000).
[20] G. Blumberg, M. W. Klein, and S.-W. Cheong, Phys. Rev. Lett. **80**, 564 (1998).
[21] K. Yamamoto, T. Katsufuji, T. Tanabe, and Y. Tokura, Phys. Rev. Lett. **80**, 1493 (1998).
[22] S. Sugai, K. Kitamori, S. Hosoya, and K. Yamada, J. Phys. Soc. Jpn. **67**, 2992 (1998).
[23] J. P. Freericks and T. P. Devereauz, Phys. Rev. B **64**, 125110 (2001).
[24] A. V. A. V. Chubukov and D. M. Frenkel, Phys. Rev. B **52**, 9760 (1995).
[25] T. Katsufuji, T. Tanabe, T. Ishikawa, Y. Fukuda, T. Arima, and Y. Tokure, Phys. Rev. B **54**, R14230 (1996).
[26] F. Venturini, U. Michelucci, T. P. Devereaux, and A. P. Kcampf, Phys. Rev. B **62**, 15204 (2000).
[27] T. P. Devereaux and A. P. Kampf, Phys. Rev. B **61**, 1490 (2000).
[28] R. Hackl, G. Krug, R. Nemetschek, M. Opel, and B. Stadlober, Proc. SPIE **2696**, 194 (1996).
[29] T. Timusk and B. Statt, Rep. Prog. Phys. **62**, 61 (1999).
[30] M. Opel, R. Nemetschek, C. Hoffman, R. Philipp, P. F. Muller, R. Hackl, I. Tutto, A. Erb, B. Revaz, E. Walker, H. Berger, and L. Forro, Phys. Rev. B **61**, 9752 (2000).
[31] R. Nemetschek, M. Opel, C. Hoffmann, P. F. Muller, R. Hackl, H. Berger, L. Forro, A. Erb, and E. Walker, Phys. Rev. Lett. **78**, 4837 (1997).
[32] V. V. Moshchalkov, L. Trappeniers, and J. Vanacken, Europhys. Lett. **46**, 75 (1999).
[33] T. Noda, H. Eisaki, and Shin-ichi Uchida, Science **286**, 265 (1999).

This article was published in English in the original Russian journal. Reproduced here with stylistic changes by the Translation Consultant.

Light scattering on phonons in quasi-one-dimensional antiferromagnet $CsFeCl_3 \cdot 2H_2O$ induced by magnetic ordering

V. S. Kurnosov,* A. V. Peschanskii, V. I. Fomin, and A. V. Yeremenko

B. Verkin Institute for Low Temperature Physics and Engineering, National Academy of Sciences of the Ukraine, 47 Lenin Ave., Kharkov 61103, Ukraine

Yu. G. Pashkevich

A. Galkin Donetsk Physical and Technical Institute of the National Academy of Sciences of the Ukraine, 72 R. Luxemburg Str., Donetsk 83114, Ukraine

(Submitted February 1, 2002)
Fiz. Nizk. Temp. **28**, 724–732 (July 2002)

The appearance of new phonon lines in the Raman spectrum of the quasi-one-dimensional antiferromagnet $CsFeCl_3 \cdot 2H_2O$ as a consequence of magnetic ordering with a change of the unit cell volume was detected experimentally. An analysis of the possible mechanisms that might lead to the observed spectral features is done. A new mechanism of inducing Raman scattering on phonons from the boundary of the paramagnetic Brillouin zone is hypothesized.
 [DOI: 10.1063/1.1496660]

INTRODUCTION

The compound $CsFeCl_3 \cdot 2H_2O$ under consideration is a representative of a family of quasi-one-dimensional chained orthorhombic magnets with a general chemical formula $AMX_3 \cdot 2H_2O$, where A=Cs, Rb, M=Mn, Fe, Co and X =Cl, Br. All these crystals have D_{2h}^8 (*Pcca*) symmetry in the paramagnetic phase.[1–3] The magnetically ordered phases of crystals of this series are described by different magnetic space groups. The magnetic cell is commonly doubled along the crystallographic direction *b* compared to the paramagnetic one.[1,4,5] The $CsFeCl_3 \cdot 2H_2O$ and $RbFeCl_3 \cdot 2H_2O$ crystals are attracting interest because they are an Ising type of antiferromagnet, unlike the Heisenberg type observed in $CsMnCl_3 \cdot 2H_2O$ (Ref. 1). Moreover, the Dzyaloshinski–Moriya interaction produces a considerable canting of the spins in the antiferromagnetic phase (AF) of $CsFeCl_3 \cdot 2H_2O$ and $RbFeCl_3 \cdot 2H_2O$, resulting in an uncompensated magnetic moment within each of the paramagnetic ion chains. The total momentum of the crystals remains zero because of the alternating direction of the moments in neighboring chains. The magnetic moments of the chains are oriented in parallel with the crystallographic axis *c* of the crystals, and therefore, application of an external field along this direction can induce a first-order phase transition (PT) to a weak ferromagnetic (WF) phase.[1] A specific feature of this PT is the fact that the flip-flop of all the spins of the paramagnetic ions in each separate chain occurs through the motion of a magnetic soliton along the chain. Besides, this PT occurs with the passage of the crystal through a number of metastable intermediate phases which are characterized by different ratios between the numbers of chains with the ferromagnetic moment oriented along and opposite to the applied field.[1,6,7]

Despite the great number of experimental studies of $CsFeCl_3 \cdot 2H_2O$ motivated by its interesting magnetic properties, very few of them were carried out using optical methods. Among the experiments known to the authors, only the experiments on excitonic absorption of light in the visible range have been performed in high magnetic fields (up to those of the metamagnetic transition).[8–10] Since not all the crystals of the above family undergo structure phase transitions, while their structures are almost similar, Raman and IR spectroscopy measurements of their vibrational spectra have not aroused particular interest. Moreover, the vibrational spectra of one of the earliest representatives of the family, namely, $CsMnCl_3 \cdot 2H_2O$, have been previously studied comprehensively, including by the authors of the present paper.[11–13] The experiments reported here were motivated by the authors' interest in the specific features of the Raman scattering in the magnetically ordered phase of $CsFeCl_3 \cdot 2H_2O$ (referred to below as CFC). Foremost among these is light scattering by magnons, quite possibly by solitons. Besides, the fact that an Fe^{2+} ion has low-energy electron levels generated due to the splitting of its ground term $^5T_2$ in a low-symmetry crystal field suggests the occurrence of electronic transitions active in the Raman scattering in the low-frequency spectrum.

The experiment performed demonstrated that at the temperatures below the Néel point ($T_N = 12.75$ K [Ref. 7]) the Raman spectrum of the crystal was much richer than that of $CsMnCl_3 \cdot 2H_2O$ (CMC). But at temperatures much above the magnetic ordering points in CMC and CFC these spectra are quite similar. The low-temperature Raman spectrum of CFC displays additional lines as against the spectrum of CMC, the lines being differently sensitive to variations in temperature of the crystal and external magnetic field. Some of the lines have intensity comparable to the intensity of the strongest lines of the original phonon spectrum of CFC, which disappear on transition of the crystal to a paramagnetic (PM) (in temperature) or a WF (in field) phase. The present paper concerns mainly the nature of these lines and the physical reasons for their occurrence in the Raman spectrum.

EXPERIMENTAL PROCEDURE

The transparent pale brown single crystals of CFC were grown from an aqueous solution of CsCl and $FeCl_2 \cdot 4H_2O$ by slow evaporation at $T = 37\,^{\circ}C$ in a nitrogen atmosphere to prevent Fe^{2+} oxidation.[1,9] The single crystals keep well in oxygen-free gaseous atmospheres. The adjustment of the crystallographic directions was made according to a well-defined habit, similar to that of CMC.[4] Samples in the form of rectangular parallelepipeds with dimensions of $6 \times 5 \times 2$ mm were cut from the single crystals and polished up to optical quality of the surface. The sample faces were oriented in parallel with the principal crystallographic planes of the crystal. The Cartesian coordinate system used was related to the crystallographic directions as $x \| a$, $y \| b$, $z \| c$.

The measurements were carried out in two types of optical cryostats: (i) one type permitted the experiments to be done in a wide temperature range of 4.2 to 300 K, and (ii) the other one had a two-section Helmholtz superconducting solenoid for performing the measurements in an exchange gas of liquid helium at ~4.2 K at magnetic field strengths up to 30 kOe. The Raman scattering was excited by He–Ne and Ar^+ laser radiation (wavelength 6328 Å, power 40 mW, and wavelength 4880 Å, power 120 mW). The 90° scattered light was analyzed with a computerized Raman spectrometer based on a Jobin Yvon U-1000 double monochromator which was equipped with a cooled photomultiplier and a photon counting system. The signal-noise ratio was improved by the spectrum acquisition method with a multiple scanning of the frequency range studied.

The use of the two light sources was dictated by several reasons. In experiments with Raman scattering the illumination of a sample by a focused laser beam produces a higher overheating in the laser beam zone, relative to the sample surface, the higher the absorption at the laser wavelength. Since the crystal optical transmission at the He–Ne laser wavelength of 6328 Å is higher, that source appeared to be more attractive for the experiments. Despite the fact that the argon laser produces a much more intense overheating of the sample, it was used for the measurements in magnetic field because the solenoid drastically confines the angular aperture of the scattered light and hence, decreases significantly the intensity of the signal detected. In that case the benefit that permitted us to compensate the aperture loss consisted of two components: first, a high radiation power, and second, the Rayleigh $1/\lambda^4$ law for the Raman scattering intensity.

EXPERIMENTAL RESULTS

The Raman scattering spectrum of the CFC crystal studied at temperatures below T_N revealed two intense (182 and 501 cm^{-1}) and four weak (125, 130, 140, and 607 cm^{-1}) lines, with polarization corresponding to the diagonal components of the scattering tensor. The distinguishing feature of these lines is the fact that their intensities decrease rather fast with increasing temperature in the immediate vicinity of T_N and that they almost disappear at higher temperatures (Fig. 1). But the ''additional'' lines undergo no noticeable variations in frequency and width. It should be noted that lines ''additional'' to the original phonon spectrum can be also observed in the spectrum with off-diagonal components of the Raman tensor at temperatures below T_N. Those lines, however, are all of low intensity compared to the lines of the original phonon spectrum and do not exhibit distinctly the above-mentioned temperature dependence.[a)]

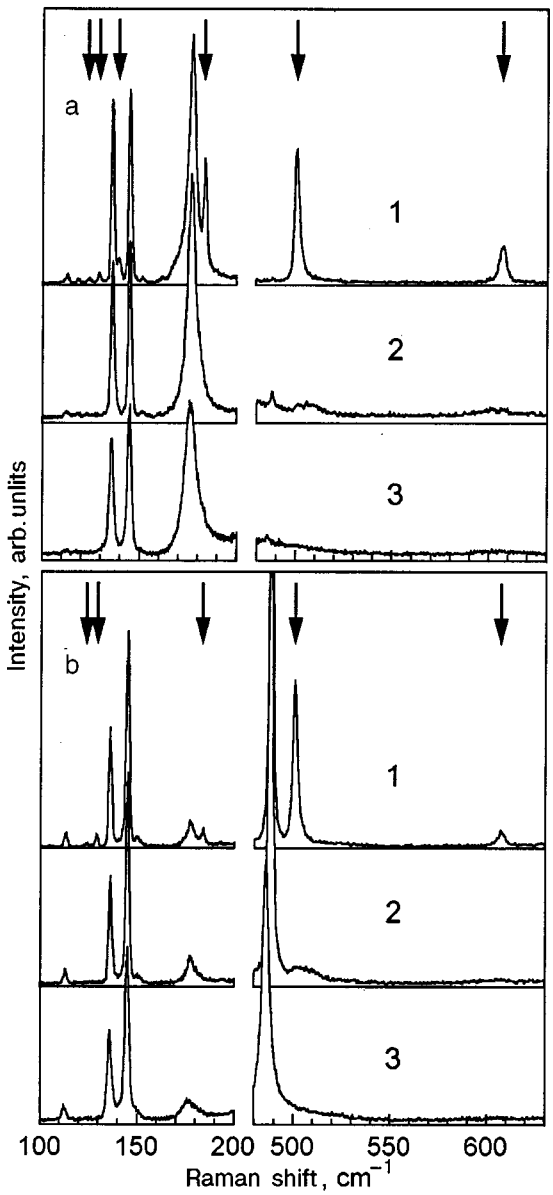

FIG. 1. Parts of the Raman spectrum of $CsFeCl_3 \cdot 2H_2O$ corresponding to scattering tensor components *yy* (a) and *zz* (b) at temperatures, K:5 (1), 25 (2), and 80 (3). The ''additional'' lines (see the text) are marked by arrows. The spectral resolution is 2 cm^{-1}.

The temperature evolution of the most intense lines, of frequencies 182 and 501 cm^{-1}, is shown in Figs. 2 and 3. The 488 and 177 cm^{-1} lines in the spectra correspond to the phonons of the original vibrational spectrum of the crystal and show no anomalous behavior in the temperature range given in the figures. The temperature dependence of the 182 cm^{-1} line area correlates well with the Néel temperature (Fig. 4). The temperature in these experiments was determined by the ratio of intensities of Stokes and anti-Stokes scattering at the lowest-frequency phonon (~30 cm^{-1}) in the crystal. This ratio satisfies the relation:

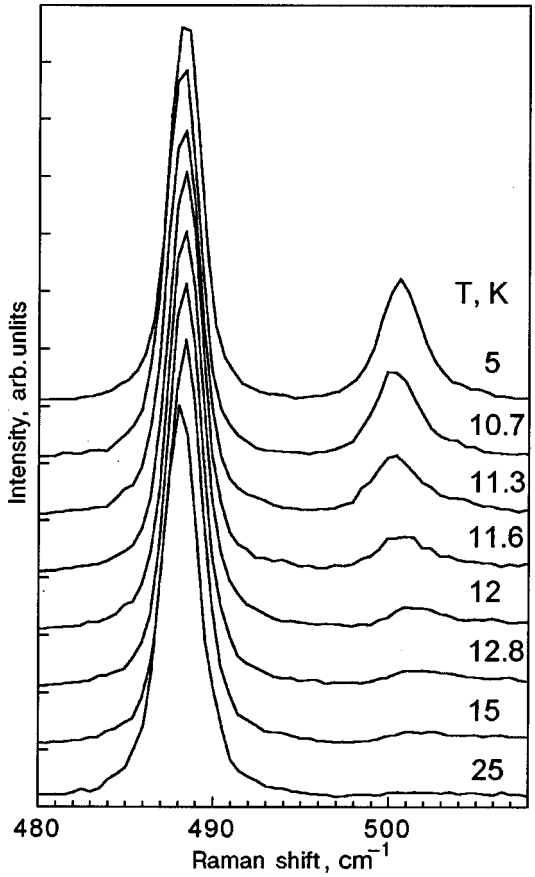

FIG. 2. The temperature evolution of part of the Raman spectrum with scattering tensor component *zz* for $CsFeCl_3 \cdot 2H_2O$.

$$I_s/I_a = \exp\frac{\hbar\omega}{kT},$$

where I_s and I_a are the Stokes and anti-Stokes components of the scattering on a phonon of energy $\hbar\omega$; T is the temperature, and k is the Boltzmann constant.

The measurements with the magnetic field directed along the crystal axis *c* show that the 182 cm^{-1} line intensity decreases rapidly as the magnetic field strength approaches a critical value, at which one can observe a PT to a new magnetic phase[1,6] (Fig. 5). The relation between intensity of the line and cyclic variations in intensity of the applied magnetic field is illustrated in Fig. 6.

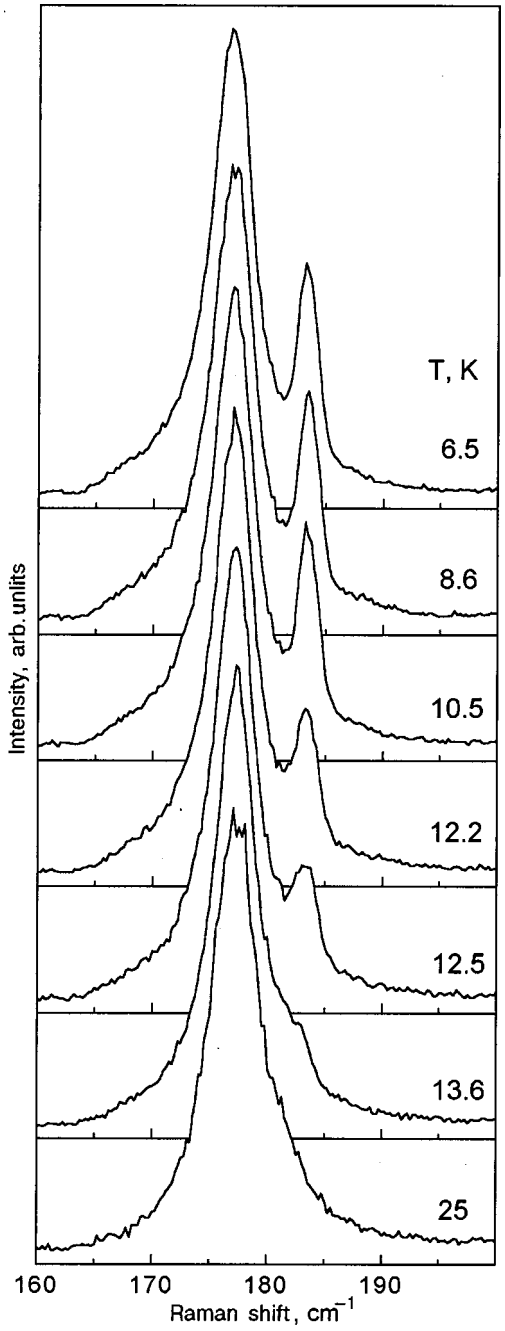

FIG. 3. The temperature evolution of part of the Raman spectrum with scattering tensor component *yy* for $CsFeCl_3 \cdot 2H_2O$.

DISCUSSION OF THE EXPERIMENTAL RESULTS

To account for the experimental results, some specific features of the crystallographic and magnetic structures of CFC should be considered.

Magnetism of CFC

In the magnetically ordered phase of CFC an octasublattice structure (Fig. 7a), the symmetry of which is described by magnetic space group $P_{2b}cca'$, is realized.[1] The available literature data[1,6,7] suggest that the magnetic structure of CFC is formed under the action of dominant antiferromagnetic superexchange interaction along the chains consisting of *cis*-octahedra of $FeCl_4O_2$ bound together by common apical ions Cl^-. The chains in the structure of the crystal are oriented along the *a* direction. The orbital and spin degeneracies of the ground state $^5T_2$ of the Fe^{2+} ion are completely lifted the by crystal-field effect of low symmetry C_2 and the spin-orbit interaction.

The three-dimensional ordering of the magnetic moments (antiferromagnetic in all directions to nearest neighbors) is brought about by the interchain superexchange, which is at least two orders of magnitude weaker than the intrachain one.[1] As a result, the magnetic cell appears to be doubled along the crystallographic direction *b* as compared to the paramagnetic one. Also noteworthy is the high value of the Dzyaloshinski–Moriya interaction, which causes the spins to be canted from the *a* direction by an angle of 15° in the *ac* plane.[1] This canting results in a ferromagnetic moment of each individual chain in the crystal which is directed

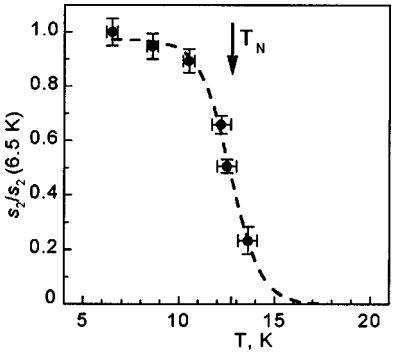

FIG. 4. The temperature dependence of relative area of the 182 cm^{-1} line in $CsFeCl_3 \cdot 2H_2O$. To make the figure more pictorial, the dashed line is plotted by eye.

collinearly with the *c* axis. The moments of all chains in the crystal compensate each other due to antiferromagnetic ordering of nearest spins of neighboring chains, so that the total magnetic moment of the crystal is zero.

On application of an external magnetic field of intensity ~9.5 kOe along the *c* axis, the crystal undergoes a PT at temperatures below T_N.[1,6,7] As a result, the ferromagnetic moments of all chains become oriented along the field direction (Fig. 7b). It should be emphasized that in the new phase the neighboring chains along the *b* direction are found to be translationally equivalent once again, and the magnetic cell volume reverts to the volume of the paramagnetic cell. The WF phase symmetry is described by space group $Pc'c'a$. During ''magnetization'' the crystal actually undergoes a number of transitions through the multitude of intermediate phases with a different specific number of chains with ''inverted'' (compared to the normal AF phase) ferromagnetic moments.[7] The moderate intensity of the magnetic field at which this PT occurs is accounted for by the small values of the interchain exchange interaction integrals along the *c* and *b* directions. As for the magnetic structure inside the chain, it remains almost unchanged in such weak fields, because it is stabilized by the high single-ion anisotropy and intrachain exchange.

In terms of the Heisenberg approximation, the magnetic parameters can be described by the following values of exchange integral $J_a/k = 6.0 \pm 0.5$ K and single-ion anisotropy constant $D/k = -40 \pm 20$ K with total spin $S = 2$ (Ref. 6). With these relations of the model parameters, the magnet at low temperatures may be approximated by the Ising model with effective spin $S_{\text{eff}} = 1/2$ and effective exchange integral $J_{\text{eff}}/k = 42 \pm 5$ K (Ref. 6).

Analysis of the Raman spectrum

The specific features of the Raman spectrum of CFC, manifesting themselves as additional (to the original phonon spectrum) lines in the magnetic phase, may be brought about by different mechanisms.

First, it should be noted that according to all the available published data, CFC, along with other representatives of this family of crystals, undergoes no structural PT. The fact is evidenced by the authors' observations. No peculiarities in the temperature behavior of the Raman spectrum which are accounted for by a structural phase transition followed by a multiplication of the unit cell volume were found. The soft mode usual at such PTs is not observed in the low-temperature phase. In the following, the authors will proceed from the fact that there are no phase transitions in CFC.

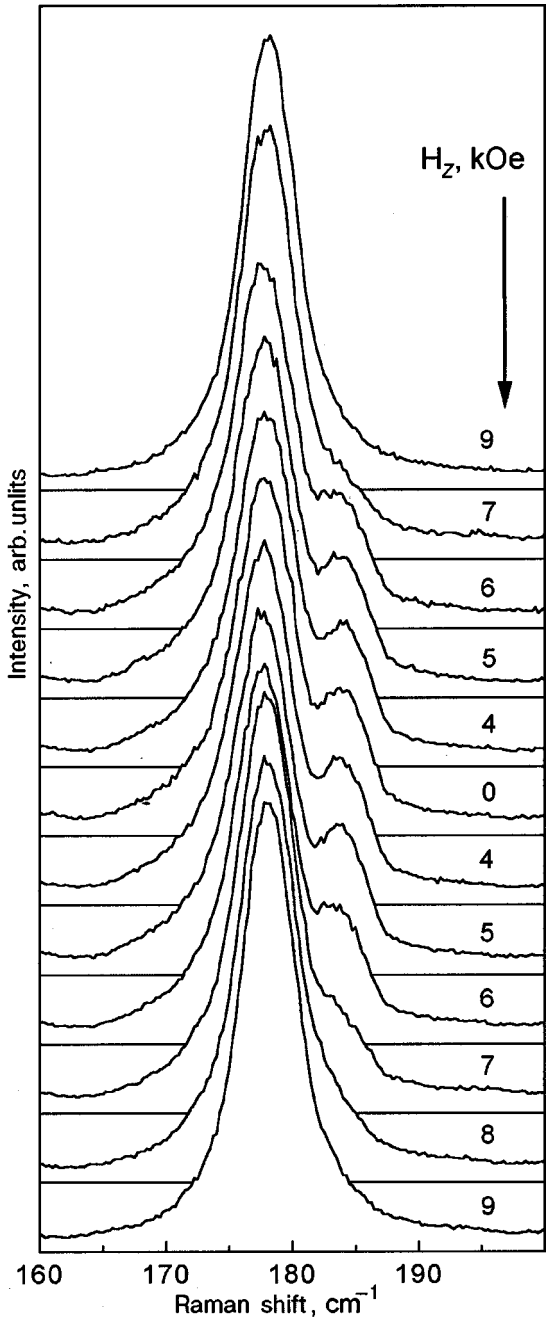

FIG. 5. The part of the Raman spectrum with scattering tensor component *yy* as a function of the external magnetic field H_Z in $CsFeCl_3 \cdot 2H_2O$. The sample temperature is ~11 K. The spectral resolution is ~3 cm^{-1}.

As mentioned in the Introduction, aside from the phonon excitations, the low-frequency Raman spectrum of CFC can contain lines caused by a scattering owing to the transition between crystal-field-split levels of the ground state term of the Fe^{2+} ion, and scattering by magnons. Turning back to the main point of the present paper, namely, to the treatment of the anomalous behavior of the additional scattering lines of frequencies 125, 130, 140, 182, and 501 cm^{-1} (Fig. 1), we should consider some possible mechanisms. To do this, we

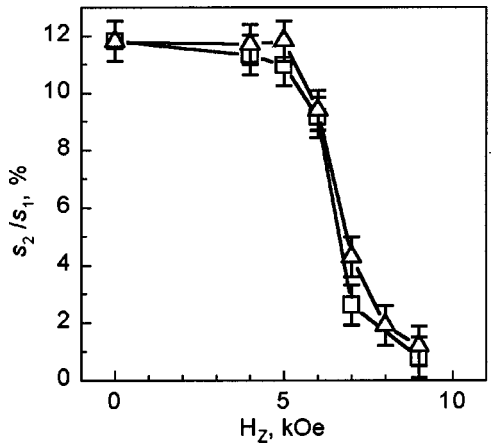

FIG. 6. The plot of the area ratio of the 182 and 177 cm^{-1} lines shown in Fig. 5 versus magnetic field. The branches with increasing and decreasing field are denoted by squares and triangles, respectively.

should first estimate the energy range within which the magnon scattering may be observed.

In terms of the Heisenberg approach for a one-dimensional chain of spins, the magnon energy dispersion within the one-dimensional Brillouin zone (BZ) can be given as follows:

$$E(\varphi)=2JS\left[\left(1+\frac{|D|}{2JS}\right)^2-\cos^2\varphi\right]^{1/2},$$

where φ is the spatial phase of a spin wave in the a direction. Using this equation, one can obtain the following estimates of magnon energies at the center and at the boundary of the one-dimensional BZ: $E(0)=42\ cm^{-1}$, $E(\pi/2)=46\ cm^{-1}$. In terms of the Ising model, the magnon energy at the BZ boundary, $E(\pi/2)=4J_{\text{eff}}S_{\text{eff}}$, is estimated as being equal to $58\ cm^{-1}$. Besides the energy of the optical magnon, the transition from the lowest component of the electron pseudo-doublet, with a total momentum projection of ±1, to the first excited singlet level, with a projection of 0, is estimated to be $80\ cm^{-1}$ (Ref. 10). All these simple estimates are rather rough, but they make it possible to place an upper limit on the energy range in which the magnon spectrum may manifest itself: to $100\ cm^{-1}$. Therefore, it is hardly probable that additional lines disappearing from the scattering spectrum at temperatures above T_N are accounted for by the magnon scattering. The two-magnon scattering, which may fall just within the frequency range studied, rarely, if ever, is of high intensity in the diagonal components of the scattering tensor. Besides, it is primary conditioned on the strong exchange along the chains which is essentially unaffected by the magnetic field applied in our experiments (see above).

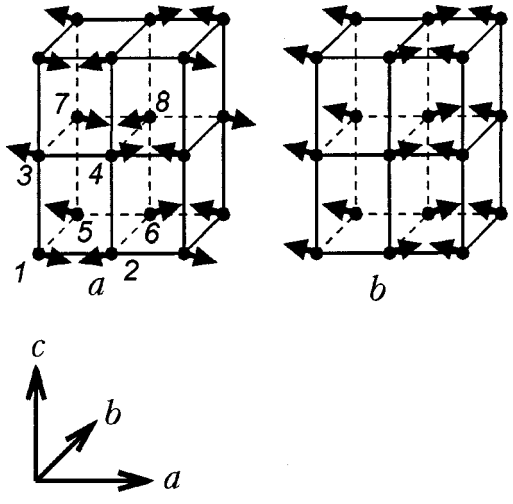

FIG. 7. The magnetic structure of $CsFeCl_3\cdot 2H_2O$ in antiferromagnetic (a) and weak ferromagnetic (b) phases.

The electron transitions also evident in the Raman spectrum of CFC exhibit a somewhat different (compared to the lines considered) evolution with increasing temperature. The electron lines in the Raman spectrum also show the decrease in area with increasing temperature, but this occurs at much higher temperatures (above 70 K in CFC) and is followed by a drastic broadening of the lines. The latter fact does not allow the suggestion that the lines are unobservable because the integral intensity vanishes. Thus the additional lines under consideration cannot be ascribed to scattering by electron transitions either.

Another feature of the magnetic structure of CFC mentioned above is the double volume of the unit cell compared to the paramagnetic one. This doubling, determined by neutron scattering,[1] is solely of a magnetic nature without any structural distortion. A double-unit-cell crystal is thought to exhibit a larger number of phonon modes in the Raman spectrum, the additional lines appearing at the magnetic BZ center from the paramagnetic BZ boundary. Despite this formal concept, there are very few experimental works on Raman scattering by phonons generated from the paramagnetic BZ boundary under magnetic ordering with a unit cell multiplication.

In the case of CFC two facts have permitted the authors to suggest that the additional lines under consideration are indeed related to scattering by phonons generated from the paramagnetic BZ boundary. These are, first, the temperature dependence, showing a fast decrease in intensity of the lines in the vicinity of T_N and their absence at higher temperatures, and, second, the field dependence of the intensity of these lines. The latter for the most intense line of frequency $177\ cm^{-1}$ demonstrates a behavior similar to the temperature dependence. When the unit cell volume returns to the paramagnetic volume, either as a result of the temperature increasing or as a result of a PT in an external magnetic field, the additional lines disappear from the Raman spectrum.

A formal increase in the number of Raman-active phonons resulting from the doubling of the unit cell volume in the magnetically ordered phase cannot explain the physical mechanisms which are responsible for the additional phonon lines in the Raman spectrum. There must be a reason causing nonequivalence of the polarizabilities associated with vibrations of the same ions from neighboring cells along the doubling direction. Otherwise, because the vibrations of identical ions in the modes from the BZ boundary are opposite in phase, the intensity of Raman scattering by them should be zero due to the complete interference damping. As a matter of fact, this is an example of the wave-vector $\mathbf{k}$ selection rule for light scattering or absorption (the $\mathbf{k}=0$ rule).

TABLE I. Irreducible spin combinations (ISC) in CFC at points $\mathbf{k}_{19}=(0,0,0)$ and $\mathbf{k}_{21}(0,\pi/b,0)$ of the paramagnetic BZ and at the center of antiferromagnetic BZ reduced along **b** (the symbols are taken from Ref. 14 and spin numbers from Fig. 7).

ISC	PM phase	AF phase
$\mathbf{F}(0)$	$\mathbf{S}_1(0)+\mathbf{S}_2(0)+\mathbf{S}_3(0)+\mathbf{S}_4(0)$	$\mathbf{S}_1+\mathbf{S}_2+\mathbf{S}_3+\mathbf{S}_4+\mathbf{S}_5+\mathbf{S}_6+\mathbf{S}_7+\mathbf{S}_8$
$\mathbf{L}_1(0)$	$\mathbf{S}_1(0)+\mathbf{S}_2(0)-\mathbf{S}_3(0)-\mathbf{S}_4(0)$	$\mathbf{S}_1+\mathbf{S}_2-\mathbf{S}_3-\mathbf{S}_4+\mathbf{S}_5+\mathbf{S}_6-\mathbf{S}_7-\mathbf{S}_8$
$\mathbf{L}_2(0)$	$\mathbf{S}_1(0)-\mathbf{S}_2(0)+\mathbf{S}_3(0)-\mathbf{S}_4(0)$	$\mathbf{S}_1-\mathbf{S}_2+\mathbf{S}_3-\mathbf{S}_4+\mathbf{S}_5-\mathbf{S}_6+\mathbf{S}_7-\mathbf{S}_8$
$\mathbf{L}_3(0)$	$\mathbf{S}_1(0)-\mathbf{S}_2(0)-\mathbf{S}_3(0)+\mathbf{S}_4(0)$	$\mathbf{S}_1-\mathbf{S}_2-\mathbf{S}_3+\mathbf{S}_4+\mathbf{S}_5-\mathbf{S}_6-\mathbf{S}_7+\mathbf{S}_8$
$\mathbf{F}(\mathbf{k}_{21})$	$\mathbf{S}_1(\mathbf{k}_{21})+\mathbf{S}_2(\mathbf{k}_{21})+\mathbf{S}_3(\mathbf{k}_{21})+\mathbf{S}_4(\mathbf{k}_{21})$	$\mathbf{S}_1+\mathbf{S}_2+\mathbf{S}_3+\mathbf{S}_4-\mathbf{S}_5-\mathbf{S}_6-\mathbf{S}_7-\mathbf{S}_8$
$\mathbf{L}_1(\mathbf{k}_{21})$	$\mathbf{S}_1(\mathbf{k}_{21})+\mathbf{S}_2(\mathbf{k}_{21})-\mathbf{S}_3(\mathbf{k}_{21})-\mathbf{S}_4(\mathbf{k}_{21})$	$\mathbf{S}_1+\mathbf{S}_2-\mathbf{S}_3-\mathbf{S}_4-\mathbf{S}_5-\mathbf{S}_6+\mathbf{S}_7+\mathbf{S}_8$
$\mathbf{L}_2(\mathbf{k}_{21})$	$\mathbf{S}_1(\mathbf{k}_{21})-\mathbf{S}_2(\mathbf{k}_{21})+\mathbf{S}_3(\mathbf{k}_{21})-\mathbf{S}_4(\mathbf{k}_{21})$	$\mathbf{S}_1-\mathbf{S}_2+\mathbf{S}_3-\mathbf{S}_4-\mathbf{S}_5+\mathbf{S}_6-\mathbf{S}_7+\mathbf{S}_8$
$\mathbf{L}_3(\mathbf{k}_{21})$	$\mathbf{S}_1(\mathbf{k}_{21})-\mathbf{S}_2(\mathbf{k}_{21})-\mathbf{S}_3(\mathbf{k}_{21})+\mathbf{S}_4(\mathbf{k}_{21})$	$\mathbf{S}_1-\mathbf{S}_2-\mathbf{S}_3+\mathbf{S}_4-\mathbf{S}_5+\mathbf{S}_6+\mathbf{S}_7-\mathbf{S}_8$

Symmetry analysis of polarizability

The phase transition to a magnetically ordered phase $P_{2b}cca'$ (see Table I) occurs at the point $\mathbf{k}_{21}$ of the paramagnetic BZ and is described by the order parameter $L_{3x}(\mathbf{k}_{21})$ or $L_{1z}(\mathbf{k}_{21})$ which transforms according to the irreducible representation $\tau_3(\mathbf{k}_{21})$. For the required polarizability α_{ij}^{ν} to be obtained, the dielectric permittivity tensor ε_{ij} should be expanded in normal coordinates of the vibrational modes U_ν at the paramagnetic BZ point $\mathbf{k}_{21}$ and in the magnetic vector η_μ corresponding to the order parameter. The latter describes the static perturbation of the medium due to the PT. The so-called "Faraday" (linear in magnetic vector) term in the expansion is of the following form at $\mathbf{k}_{19}=0$:

$$\alpha_{ij}^{\nu}=\left\langle \frac{\partial^2\varepsilon_{ij}}{\partial\eta\partial U}\,\eta_\mu(\mathbf{k}_{21})U_\nu(-\mathbf{k}_{21})\right\rangle,$$

where $\eta_\mu(\mathbf{k}_{21})\equiv L_{3x}(\mathbf{k}_{21})/\tau(\mathbf{k}_{21})$.

The nonzero polarizability tensors correspond only to the vibrational modes transforming according to the irreducible representations $\tau_6(\mathbf{k}_{21})$ and $\tau_7(\mathbf{k}_{21})$ and are of the forms:

$$\alpha^{\tau_6(\mathbf{k}_{21})}=\begin{pmatrix} . & d & . \\ -d & . & . \\ . & . & . \end{pmatrix},\quad \alpha^{\tau_7(\mathbf{k}_{21})}=\begin{pmatrix} . & . & f \\ . & . & . \\ -f & . & . \end{pmatrix}.$$

As is evident from the above analysis, under magnetic ordering the paramagnetic BZ boundary may induce only those lines which in the low-temperature phase are related to phonons of symmetries B_{1g} and B_{2g}, while the observed additional lines show symmetry A_g and occur in the diagonal components of the scattering tensor. Hence, the first order of perturbation theory cannot explain the anomalies under consideration.

Another mechanism that permits one to derive the required polarization selection rules for phonon modes generated from the paramagnetic BZ boundary under magnetic ordering can be illustrated as follows.

Since there exists a nonzero local magnetic field on ligands surrounding the paramagnetic ion, then during motion in the vibrational mode there may occur a Lorentz force perpendicular to the direction of the ion displacement. Hence, the linear trajectory of the ion motion transforms to an elliptical one. In this case the directions of traversing the ellipse are opposite because the identical ions from neighboring unit cells along the direction of doubling in the magnetic cell are connected by the antitranslation operation. Thus, for the phonon mode originating from the paramagnetic BZ boundary, where the displacements, of ions with no local magnetic field are opposite in phase, the perpendicular components of the displacements, generated by the Lorentz force, appear to be in-phase. This mechanism is illustrated schematically in Fig. 8.

As the Lorentz force is of relativistic origin it is hard to suggest that it may produce a sufficient degree of ellipticity to induce intense lines of light scattering comparable with those of the original spectrum. This hypothesis, however, does have meaning if it is remembered that the mixing of different-symmetry vibrational modes corresponding to the paramagnetic BZ boundary and center occurs just in this

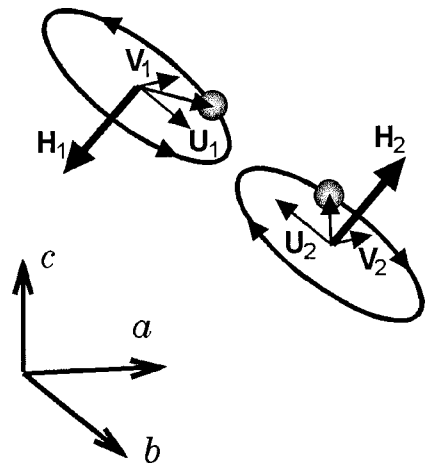

FIG. 8. The trajectory ellipticity of identical ions from neighboring-in-direction b cells in local magnetic fields $\mathbf{H}_1$ and $\mathbf{H}_2$. $\mathbf{U}_1$ and $\mathbf{U}_2$ are antiphase displacement components for the mode from the paramagnetic BZ boundary, $\mathbf{V}_1$ and $\mathbf{V}_2$ are in-phase displacement components induced by the Lorentz force.

way. If the modes are close in frequency, this channel may enhance the intensity of the additional lines at the expense of the original ones. At least, this mechanism appears to be appropriate for description of the 177 and 182 cm^{-1} modes. They have close frequencies, and the 177 cm^{-1} line of the original phonon spectrum is sufficiently wide, even at low temperatures, to overlap 182 cm^{-1} line resonantly (Fig. 3). The resonance effects are also supported by the asymmetric complex shape of the 177 cm^{-1} line at low temperatures, which becomes symmetric in the PM and WF phase in external magnetic fields (Figs. 3 and 5).

At the moment the authors propose the above mechanism as a possibility. Verification of its adequacy requires a further, more comprehensive study into the anomalies of the scattering spectrum of CFC and a development of microscopic theoretical models which would enable the above spectral features arising upon magnetic ordering to be estimated numerically.

CONCLUSIONS

The experiments with the quasi-one-dimensional chained antiferromagnet $CsFeCl_3 \cdot 2H_2O$ revealed additional, quite intense lines in the Raman spectrum at the phase transition to a magnetically ordered phase, followed by changes in the volume of the crystal magnetic cell.

It is found that in an external magnetic field the most intense additional line of 182 cm^{-1} disappears at the phase transition to a weak ferromagnetic phase.

Analysis of the symmetry of the paramagnetic, antiferromagnetic, and weak ferromagnetic structures of the crystal suggests that the new lines result from the magnetic-ordering-induced light scattering by phonons originating from the paramagnetic BZ boundary.

Analysis of the magnetic contribution to the phonon polarizability of the crystal made in the first order of perturbation theory showed no correlation with the experimental polarization selection rules for the additional lines.

A new mechanism of inducing light scattering by vibrational modes corresponding to the phonons from the paramagnetic BZ boundary is hypothesized. It is based on the mixing of different-symmetry modes from the BZ center and boundary due to the ellipticity of the ion trajectory of vibrations in their local magnetic field.

The authors are very grateful to Prof. V. V. Eremenko for his constant interest in this research and for helpful discussion.

*E-mail: Kurnosov@ilt.kharkov.ua

[a)]The nature of these excitations will be considered in a separate paper.

[1] J. A. J. Basten, Q. A. G. van Vlimmeren, and W. J. M. de Jonge, Phys. Rev. B **18**, 2179 (1978).
[2] S. J. Jensen, P. Andersen, and S. R. Rasmussen, Acta Chem. Scand. **16**, 1890 (1962).
[3] N. Thorup and H. Soling, Acta Chem. Scand. **23**, 2933 (1969).
[4] R. D. Spence, W. J. M. de Jonge, and K. W. S. Rama Rao, J. Chem. Phys. **51**, 4694 (1969).
[5] A. Herweijer, W. J. M. de Jonge, A. C. Botterman, A. L. M. Bongaarts, and J. A. Cowen, Phys. Rev. B **5**, 4618 (1972).
[6] K. Kopinga, M. Steiner, and W. J. M. de Jonge, J. Phys. C **18**, 3511 (1985).
[7] J. P. M. Smeets, E. Frikkee, W. J. M. de Jonge, and K. Kopinga, Phys. Rev. B **31**, 7323 (1985).
[8] M. Takeda, G. Kido, I. Mogi, Y. Nakawaga, H. Okada, and N. Kojima, J. Phys. Soc. Jpn. **58**, 3418 (1989).
[9] I. Mogi, M. Takeda, G. Kido, Y. Nakawaga, H. Okada, and N. Kojima, J. Magn. Magn. Mater. **104–107**, 1061 (1992).
[10] H. Okada, N. Kojima, T. Ban, and I. Tsujikawa, Phys. Rev. B **42**, 11610 (1990).
[11] D. M. Adams and D. Newton, J. Chem. Soc. A **22**, 3499 (1971).
[12] V. P. Gnezdilov, V. V. Eremenko, V. S. Kurnosov, and V. I. Fomin, Fiz. Nizk. Temp. **17**, 630 (1991) [Sov. J. Low Temp. Phys. **17**, 331 (1991)].
[13] W. Jia, E. Strauss, W. M. Yen, K. Xia, and M. Zhao, Phys. Rev. B **39**, 12853 (1989).
[14] O. V. Kovalev, *Irreducible and Induced Representations and Co-Representations of the Fedorov's Groups* (in Russian), Nauka, Moscow (1986).

This article was published in English in the original Russian journal. Reproduced here with stylistic changes by the Translation Consultant.

Nonlinear optical spectroscopy of epitaxial magnetic garnet films

V. V. Pavlov and R. V. Pisarev*

A. F. Ioffe Physical Technical Institute of the Russian Academy of Sciences, St. Petersburg, 194021 Russia

M. Fiebig and D. Fröhlich

Institut für Physik, Universität Dortmund, 44221 Dortmund, Germany
(Submitted February 1, 2002)
Fiz. Nizk. Temp. **28**, 733–738 (July 2002)

Second and third harmonic optical spectra are studied in epitaxial magnetic thin films in the spectral ranges 1.7–3.2 eV and 2.4–4.2 eV, respectively. No significant increase of the intensity of the nonlinear spectra is found above the bandgap near 3.2 eV, where the linear absorption increases by two orders of magnitude. Large magnetic contributions to the second harmonic spectra and magnetic contrast as high as 100% are observed at selected photon energies. Contrary to that, no magnetic contribution to the third harmonic spectra is found. © *2002 American Institute of Physics.* [DOI: 10.1063/1.1496661]

1. INTRODUCTION

Bulk magnetic garnets and epitaxial magnetic garnet films are two well-known groups of materials characterized by a large variety of very useful magnetic, acoustic, optical, and magneto-optical properties.[1–4] For more than four decades they have remained one of the most actively studied magnetic dielectrics, both from the fundamental point of view as multi-sublattice ferrimagnets and for the purpose of technological applications. The prototype material of bulk crystals and thin films is yttrium iron garnet $\{Y\}_3[Fe]_2(Fe)_3O_{12}$ (YIG). The unit cell contains eight formula units. The rare-earth ions R^{3+} enter 24*c* dodecahedral positions $8\{\ldots\}_3$, while the Fe^{3+} ions enter 16*a* octahedral positions $8[\ldots]_2$ and 24*d* tetrahedral positions $8(\ldots)_3$. The superexchange interaction between the magnetic Fe^{3+} ions leads to antiparallel ferrimagnetic ordering of the magnetic moments of the octahedral and tetrahedral iron sublattices. This strong interaction leads to a Curie temperature in the range of $T_C = 500-600$ K. The superexchange interaction between the rare-earth magnetic ions and the iron sublattices leads to an antiparallel orientation of the rare-earth magnetic moments with respect to the magnetization of the tetrahedral sublattice. A remarkable feature of magnetic garnets is the possibility of substituting ions in all three magnetic sublattices by many other magnetic and nonmagnetic ions from the periodic table of the elements. This degree of freedom allows one to vary practically all of the physical properties of bulk crystals and epitaxial films over a very wide range.

The magnetic iron garnets are highly transparent in the near infrared range 0.2–1.0 eV (Ref. 5). At lower energy the absorption rapidly increases due to lattice vibrations. The absorption increases progressively at photon energies higher than about 1 eV due to the intrinsic localized electronic transitions between the $(3d)^5$ levels of the Fe^{3+} ions and, subsequently, above 3.2 eV due to intense charge-transfer and interband transitions, finally approaching absorption coefficients as high as 5×10^5 cm^{-1} above 5 eV.[6] The linear magneto-optical properties of garnets, and in particular bismuth-substituted garnets, have attracted a lot of interest due to the fact that very high values of the specific Faraday rotation up to 10^5 deg/cm were observed at room temperature. To our knowledge, these values are probably the highest ever observed at room temperature due to a spontaneous magnetization.

Bulk crystals of magnetic garnets belong to the centrosymmetric cubic point group $m3m$ (space group $Ia3d$). In the thin films, however, the observation of a linear magnetoelectric effect proved that the inversion symmetry is broken.[7] This is related to the fact that the films, which are grown by a liquid-phase epitaxial method on substrates cut from bulk cubic crystals of gadolinium gallium garnet $Gd_3Ga_5O_{12}$ (GGG) or substituted GGG (SGGG), possess a lattice parameter different from that of the substrate, which leads to a distorted noncubic crystal structure. Previous studies of second harmonic generation (SHG) in magnetic garnet films were restricted to a few selected photon energies determined by the pump lasers, such as 1.17 eV (Nd:YAG lasers) or $\simeq$1.5 eV (Ti-sapphire lasers).[8] Though breaking of inversion is not important in the analysis of the magnetic properties, it plays an essential role for the electro-optical and nonlinear optical properties. In particular, it allows crystallographic and the magnetic contributions to SHG in the electric dipole approximation. Obviously, studies at selected photon energies could not clarify relations between observed SHG signals and particular features of electronic structure, absorption spectra and magneto-optical spectra. In the present paper we report first results on a spectroscopic study of SHG and third harmonic generation (THG) in magnetic garnet films below and above the fundamental band gap near 3.2 eV.

2. ELECTRONIC TRANSITIONS IN IRON GARNETS

Optical absorption and reflection spectra of concentrated and diluted iron garnets have been studied in a large number of publications and the most important data are summarized in Ref. 4. In spite of numerous publications along these lines, the assignments of spectral features remain doubtful in most cases due to the complexity of the spectra. Experimental data and crystal field calculations are summarized in Fig. 1. In its

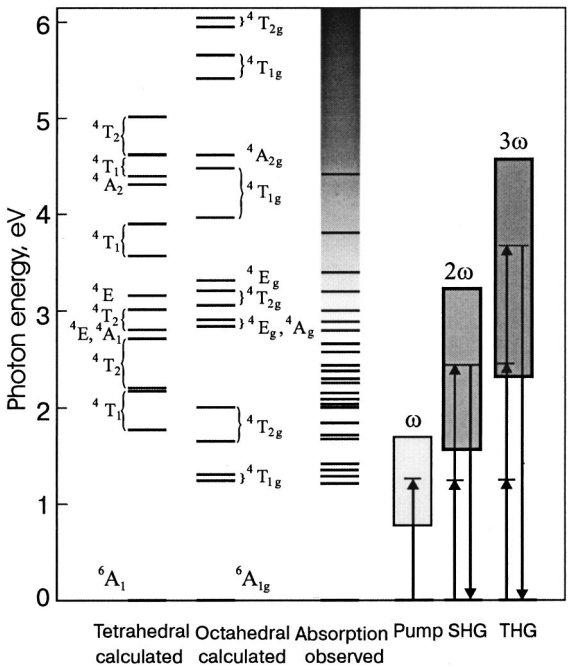

FIG. 1. The two columns on the left show the crystal field energy states of the Fe^{3+} ion in the distorted tetrahedral and octahedral positions in the garnet structure. The column in the middle shows the experimentally observed electronic transitions and the continuous absorption at higher photon energy. The right part of the figure shows the energy range of the pump beam and that of the SH and TH spectra.

middle part Fig. 1 shows experimentally observed transition energies in YIG as reported in several papers.[5,6,9–15] The electronic structure of iron garnets has been a subject of calculations based on crystal field theory and molecular orbital theory.[5,9,14,16–18] The left panels of Fig. 1 show the localized states of the Fe^{3+} ions in the tetrahedral and octahedral sublattices. These states are given according to crystal field calculations which take into account tetragonal distortions in the tetrahedral sublattice and trigonal distortions in the octahedral sublattice.[18] The calculations show that the relevant splittings and shifts of the electronic states may of the order of 0.5 eV and therefore comparable to the splitting of the states in the cubic crystal fields of T_d and O_h symmetry.

Below the band gap the electronic transitions could be studied by transmission methods based on optical and magneto-optical techniques, whereas for transitions above the band gap of ≈3.2 eV reflection methods are in general more favorable.[9,11,12] With the use of very thin YIG films ($t=0.26\ \mu$m) absorption spectra could be obtained up to 5.0 eV.[6] It should be noticed that all optical transitions between the localized states of the Fe^{3+} ions are spin-forbidden. In addition, the transitions in the octahedral sublattice are parity-forbidden in the electric-dipole approximation and become allowed due to interaction with odd phonons.

Optical absorption of YIG in the near infrared spectral range commences at about 1.2 eV and is due to the localized electronic transition $^6A_{1g} \rightarrow {}^4T_{1g}$ between the $(3d)^5$ levels of the Fe^{3+} ions in the octahedral sublattice. This transition is magnetic-dipole-allowed and leads to two very weak absorption lines.[10] It is readily seen from Fig. 1 that at higher energy the transitions in the octahedral and the tetrahedral sublattices are overlapping, so that the unambiguous assignment of the states becomes difficult. In fact, the experimentally observed spectrum of YIG is characterized by a more complicated structure than expected from theory even if the case of very low symmetries is taken into account. Aside from their dependence on the cubic and noncubic crystal field parameters, the positions of the electronic levels are also subject to several other parameters, such as the intra-atomic interaction parameters, spin-orbit coupling, exchange interaction, etc. In strongly correlated systems like iron garnets, paired transitions may lead to additional absorption bands in the optical spectra. For example, absorption bands in the spectral range around 2.5 eV are at least in part due to paired transitions. These factors, being sometimes of comparable magnitude or not exactly known, complicate the unique assignment of optical absorption bands. Low-temperature optical and magneto-optical studies resolve the splittings of the transitions, revealing a rather complicated energy-level structure.

The exact position of the band gap remains not well defined and is usually assumed to lie near 3.2–3.4 eV, where the absorption coefficient of YIG starts to increase more rapidly, approaching values of $\alpha=5\cdot10^5\ \mathrm{cm}^{-1}$ above 5 eV (Ref. 6). This absorption value is typical for interband transitions in transition-metal oxides. The substitution of Bi^{3+} for Y^{3+} in iron garnets leads to a shift of the strong absorption edge to lower energy and to a huge increase of magneto-optical effects in the visible and ultraviolet spectral range. The suggested microscopic mechanisms of the enhanced magneto-optical Faraday and Kerr effects are assumed to originate in an increase of the spin-orbit interaction due to the formation of a molecular orbit between the $3d$ orbitals of the Fe^{3+} ions and the $2p$ orbitals of O^{2-}. This is further mixed with the $6p$ orbitals of Bi^{3+}, which has a large spin-orbit interaction coefficient. A recent analysis shows that the most important electronic transitions responsible for the Faraday rotation in bismuth-substituted garnets lie at 2.6, 3.15, and 3.9 eV (Ref. 19).

3. EXPERIMENT

In the present study we used thin films of magnetic garnets grown by a liquid-phase epitaxial method. Films were grown on transparent nonmagnetic substrates cut from bulk cubic crystals of gadolinium gallium garnet $Gd_3Ga_5O_{12}$ or substituted GGG. The films were grown on substrates with the four different orientations (001), (110), (111), and (210) and differed in their compositions, lattice parameters, and thicknesses.[8] Optical absorption spectra were measured using a Cary 2300 spectrophotometer and were found to be in agreement with published data. Absorption spectra measured at T=15 K in three films are shown in Fig. 2. Optical densities higher than $D=4.5$ are above the working range of the spectrophotometer and could not be measured.

The setup for the SHG and THG experiments is shown in Fig. 3. A Nd:YAG laser system and a β-BaB_2O_4 operated optical parametric oscillator (OPO) were used as the light source, the performance of which was monitored with a wavemeter. The pulse energy was measured for normalizing the observed SH and TH intensities. For proper normalization it was necessary to measure the absorption of the fundamental beam by placing a photodiode behind the sample,

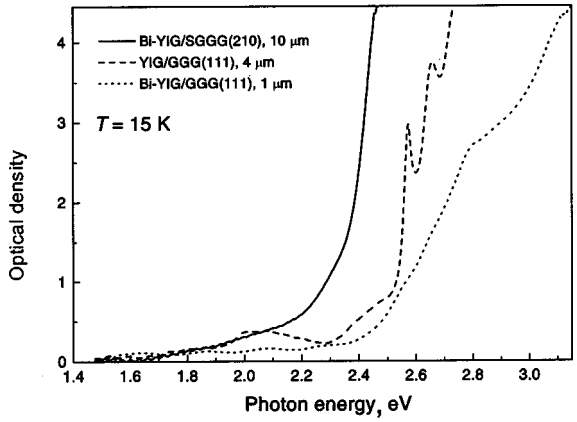

FIG. 2. Optical absorption spectra in the three garnet films studied in the paper. The films differ in their compositions and thicknesses. Optical densities higher than $D=4.5$ are out of the range of the spectrophotometer and could therefore not be measured.

since in all samples the absorption varies strongly as function of the photon energy. Wave plates, polarizers, and optical filters were used to set the polarization of the fundamental light, analyze the polarization of the SH and TH light, and separate the fundamental light from the SH and TH light behind the sample. In some cases, a monochromator was included in the setup in order to exclude the possibility of two-photon luminescence contributions to the observed signals. By a telephoto lens the signal light was projected on a cooled CCD camera or a photomultiplier. The data were corrected for the spectral response of the filters and the detection system. The magnetic contrast was determined from the normalized difference between the SH intensity for opposite orientations of the saturating transverse magnetic field.

4. NONLINEAR OPTICAL SUSCEPTIBILITIES

In magnetically ordered materials the relation between the induced polarization $\mathbf{P}$ and the electric field $\mathbf{E}(\omega)$ of the fundamental beam in the electric dipole approximation can be written as

$$\mathbf{P}=\varepsilon_0(\hat{\chi}^{(1)}\mathbf{E}(q)+\hat{\chi}^{(2)}\mathbf{E}(\omega)\mathbf{E}(\omega) + \hat{\chi}^{(3)}\mathbf{E}(\omega)\mathbf{E}(\omega)\mathbf{E}(\omega)\ldots). \quad (1)$$

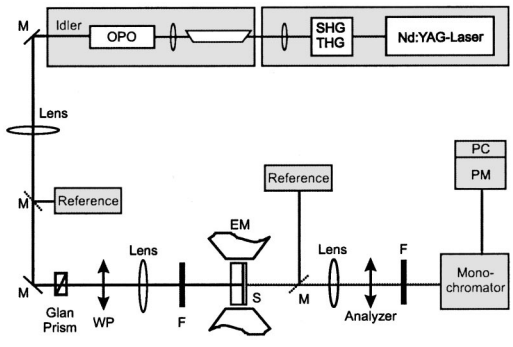

FIG. 3. Transmission setup for SH/TH spectroscopy. SHG/THG: second harmonic/third harmonic generation; OPO: optical parametric oscillator; WP: wave plate; F: filter; S: sample; EM: electromagnet; PM: photomultiplier; PC: personal computer; M: mirror.

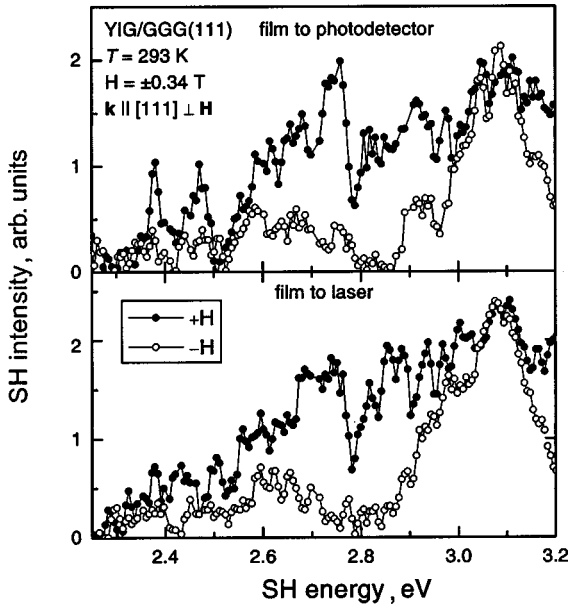

FIG. 4. SH spectra in the YIG/GGG(111) film for opposite orientations of the transverse magnetic field. The upper and lower panels depict SH spectra for two sides of the film.

In the electric-dipole approximation, odd tensors $\hat{\chi}^{(1)}$, $\hat{\chi}^{(3)}$,… are allowed in all media, whereas even tensors $\hat{\chi}^{(2)}$, $\hat{\chi}^{(4)}$,… are allowed only in noncentrosymmetric media. For crystals with a spontaneous or a magnetic-field-induced magnetization $\mathbf{M}$ the optical susceptibility tensors contain crystallographic (nonmagnetic) contributions and magnetic contributions:

$$\hat{\chi}^{(n)}=\hat{\chi}^{\mathrm{cr}}+\hat{\chi}^{m}\mathbf{M}. \quad (2)$$

The intensity of SH and TH signals can be written as

$$I(2\omega)\propto E_0^4|\hat{\chi}^{\mathrm{cr}}(-2\omega;\omega,\omega)\pm\hat{\chi}^{m}(-2\omega;\omega,\omega,0)M|^2,$$
$$I(3\omega)\propto E_0^6|\hat{\chi}^{\mathrm{cr}}(-3\omega;\omega,\omega,\omega)\pm\hat{\chi}^{m}(-3\omega;\omega,\omega,\omega,0)M|^2, \quad (3)$$

where the crystallographic and magnetic contributions are described by polar tensors $\hat{\chi}^{\mathrm{cr}}$ and axial tensors $\hat{\chi}^{m}$, respectively. The sign $\pm$ refers to the opposite projections of the magnetization $\mathbf{M}$. The symmetry properties of the tensors $\hat{\chi}^{\mathrm{cr}}$ and $\hat{\chi}^{m}$ are strictly defined by the crystallographic point group. Nonzero components of $\hat{\chi}^{\mathrm{cr}}$ and $\hat{\chi}^{m}$ are given in Ref. 8 for SHG and in Table for THG for the case of $3m$ symmetry. If nonlinear optical waves of crystallographic and magnetic origin are both present, their interference will lead to different SH and TH intensities for opposite orientations of the magnetization and thus to a magnetic contrast between oppositely magnetized regions.

5. EXPERIMENTAL RESULTS AND DISCUSSION

Figure 4 shows the SH spectra in a YIG/GGG (111) film for two opposite orientations of the magnetization $\mathbf{M}$ in transverse geometry. The upper and lower panels show the results for the two cases with the SH signal being emitted directly from the free film surface (film-to-photodetector

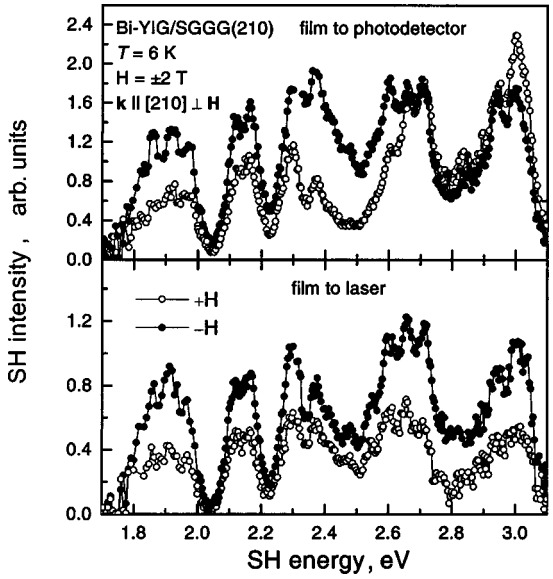

FIG. 5. SH spectra in the Bi–YIG/SGGG(210) film.

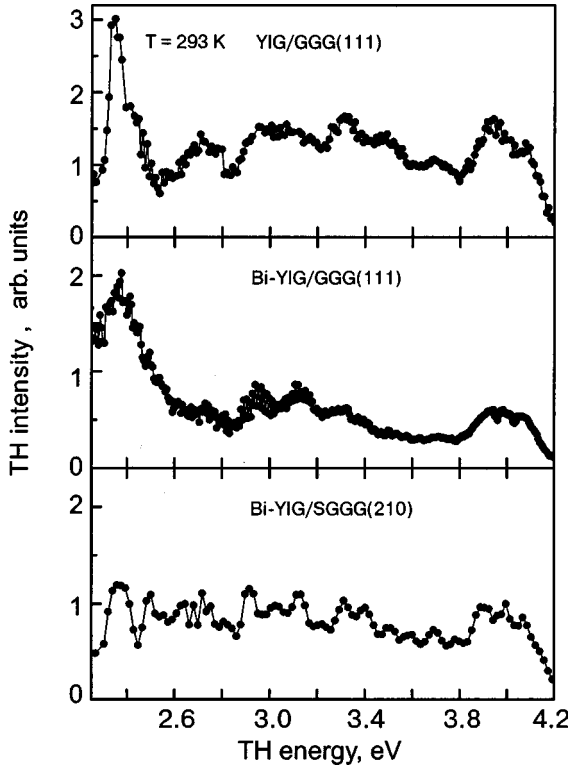

FIG. 6. TH spectra in YIG/GGG(111), Bi–YIG/GGG(111), and Bi-YIG/SGGG(210) films.

case) and from the surface of the film attached to the substrate (film-to-laser case). The two geometries lead to different SH spectra. In particular, a split transition near 2.4 eV is well resolved for the free film surface and smeared out for the more strained surface attached to the substrate. Note that magnetic contrast varies from 0 to 100%. According to the energy level diagram in Fig. 1, some features in the SH spectrum can be assigned to the crystal-field transitions in the two iron sublattices. Two other sharp absorption features near 2.57 eV (presumably due to the ${}^6A_1 \rightarrow {}^4E$, ${}^4A_1$ transition in the tetrahedral sublattice) and 2.66 eV (presumably due to the ${}^6A_1 \rightarrow {}^4E$, ${}^4A_1$ transition in the octahedral sublattice) are also observed in the SH spectrum. Two more spectral features in the absorption spectrum are observed at 2.9 and 3.2 eV, with oscillator strengths an order of magnitude higher than those for the tetrahedral transitions. However, the relevant features in the SH spectrum are of the same order of magnitude as for the transitions with the lower optical absorption.

Figure 5 shows the SH spectra of a bismuth-substituted Bi–YIG/SGGG(210) film. As a rule bismuth-substituted films show the strongest SH signals.[8] The present sample was studied in a spectral range beginning at 1.7 eV and at low temperature $T=6$ K. It shows a well-resolved structure with five strong bands of varying magnetic contrast. We note that the spectra for two sides of the film are different, as it was the case for the YIG/GGG(111) film. As in the previous case, the increase of the linear optical absorption does not lead to a noticeable increase of the SH intensity.

Figure 6 shows the third harmonic spectra in the three magnetic films. Note that even in the electric-dipole approximation a breaking of space inversion symmetry is not required for the observation of a TH signal. Although the optical absorption and the magnitudes of the linear magneto-optical signals are very different in the three films, their third harmonic spectra are similar. The tetrahedral transition ${}^6A_1 \rightarrow {}^4T_2$ centered near 2.4 eV is well resolved in the TH spectrum, and in particular in the YIG/GGG(111) film. Note that the strong increase of the linear absorption above 3 eV is not accompanied by a similar increase of the TH spectra. Contrary to the SH spectra, no difference in the TH spectra is observed within the experimental accuracy upon a reorientation of the magnetization or upon a variation of the magnetic

TABLE I. Nonzero components of the nonlinear optical tensors $\chi^{\mathrm{cr}}_{ijkl}$ and χ^{m}_{ijklm} relevant for the point group $3m(m \perp x)$ in the geometry $\mathbf{k} \| \mathbf{z}$ (films of (111) type).

$\chi^{\mathrm{cr}}_{ijkl}$	χ^{m}_{ijklm}
$\frac{1}{3}yyyy = \frac{1}{3}xxxx = xxyy = yxxy$	$yyyyx,\ yxyyy,\ yxxyx$ $xxxxx = -\frac{1}{2}yyyyx - yxyyy - \frac{1}{2}yxxyx$ $xxxyy = \frac{1}{2}yyyyx - \frac{1}{2}yxxyx$ $xxyyx = -\frac{1}{2}yyyyx + yxyyy - \frac{1}{2}yxxyx$ $xyyyy = \frac{1}{2}yyyyx + yxxyx$ $yxxxy = yyyyx - yxyyy + yxxyx$ $yxyyz = -xxxyz = -\frac{1}{3}xyyyz = \frac{1}{3}yxxxz$

field. This is surprising, because according to a phenomenological analysis a magnetic contribution to the THG is allowed both in the longitudinal and transverse geometries.

In conclusion, the SH spectra of various anisotropic magnetic garnet films were measured in a range of photon energies stretching from 1.7–3.2 eV and thus, below the fundamental band gap at ≈3.2 eV. The spectra revealed contributions of nonmagnetic and magnetic type to the total SH intensity. We also report the TH spectra in the range of 2.4–4.2 eV and thus, below and above the band gap. No studies along these lines for the magnetic transition-metal oxides have been reported so far with the only recent exception of third harmonic spectroscopy of La_2CuO_4 (Ref. 20). While the intensity of linear absorption grows progressively as a function of photon energy, the intensity of the SH and TH spectra does not show a similar behavior. We may assume that this is due to the fact that only localized d–d transitions contribute to the nonlinear spectra, with the relevant contribution vanishing for charge-transfer and interband transitions. A very interesting and puzzling result is the observation of a very large magnetic contribution to the SH spectra with a magnetic contrast of up to 100%. By contrast, no magnetic contribution is found in the TH spectra. All these observations demonstrate a strong necessity for further experimental and theoretical studies of nonlinear optical properties of magnetic garnet materials.

This work was supported by the Deutsche Forschungsgemeinschaft, the Russian Foundation for Basic Research, and the Alexander-von-Humboldt-Stiftung. We thank H.-J. Weber for the help in optical absorption measurements.

*E-mail: pisarev@pop.ioffe.rssi.ru

[1] *Physics of Magnetic Garnets*, A. Paoletti (Ed.), North Holland, Amsterdam (1978).
[2] G. Winkler, *Magnetic garnets*, Vieweg, Braunschweig (1981).
[3] *Magnetic garnet films*, A. Paoletti (Ed.), special issue of Thin Solid Films **114** (1984).
[4] Landolt-Börnstein, *Numerical Data and Functional Relationships in Science and Technology*, New Series, Group III, 27/e, Springer-Verlag, Berlin (1991).
[5] D. L. Wood and J. P. Remeika, J. Appl. Phys. **38**, 1038 (1967).
[6] G. B. Scott and J. L. Page, Phys. Status Solidi B **79**, 203 (1977).
[7] B. B. Krichevtsov, V. V. Pavlov, and R. V. Pisarev, JETP Lett. **49**, 535 (1989); Fiz. Tverd. Tela (Leningrad) **31**, 77 (1989) [Sov. Phys. Solid State **31**, 1142 (1989)].
[8] V. N. Gridnev, V. V. Pavlov, R. V. Pisarev, A. Kirillyuk, and Th. Rasing, Phys. Rev. B **63**, 184407 (2001) and references therein.
[9] F. J. Kahn, P. S. Pershan, and J. P. Remeika, Phys. Rev. **186**, 891 (1969).
[10] J. P. van der Ziel, J. F. Dillon, Jr., and J. P. Remeika, AIP Conf. Proc. **5**, 254 (1971).
[11] A. I. Galuza, V. V. Eremenko, and A. P. Kirichenko, Fiz. Tverd. Tela (Leningrad) **15**, 762 (1973) [Sov. Phys. Solid State **15**, 407 (1973)].
[12] K. W. Blazey, J. Appl. Phys. **45**, 2273 (1974).
[13] S. H. Wemple, S. L. Blank, J. A. Seman, and W. A. Biolsi, Phys. Rev. B **9**, 2134 (1974).
[14] G. B. Scott, D. E. Lacklison, and J. L. Page, Phys. Rev. B **10**, 971 (1974).
[15] B. B. Krichevtsov, O. Ochilov, and R. V. Pisarev, Fiz. Tverd. Tela (Leningrad) **25**, 2404 (1983) [Sov. Phys. Solid State **25**, 1380 (1983)].
[16] T. K. Vien, J. L. Dormann, and H. Le Gall, Phys. Status Solidi **71**, 731 (1975).
[17] A. S. Moskvin, A. V. Zenkov, E. I. Yuryeva, and V. A. Gubanov, Physica B **168**, 187 (1991).
[18] V. V. Alekseev, V. V. Druzhinin, and R. V. Pisarev, Fiz. Tverd. Tela (Leningrad) **33**, 2669 (1991) [Sov. Phys. Solid State **33**, 1507 (1991)].
[19] G. F. Dionne and G. A. Allen, J. Appl. Phys. **73**, 6127 (1993).
[20] A. Schülzgen, Y. Kawabe, E. Hanamura, A. Yamanaka, P.-A. Blanche, J. Lee, H. Sato, M. Naito, N. T. Dan, S. Uchida, Y. Tanabe, and N. Peyghambarian, Phys. Rev. Lett. **86**, 3164 (2001).

This article was published in English in the original Russian journal. Reproduced here with stylistic changes by the Translation Consultant.

Optical study of 4*f* excitations in rare earth cuprates

V. Nekvasil*

Institute of Physics, Czech Academy of Sciences, Cukrovarnická 10, 162 53 Prague 6, Czech Republic
(Submitted February 2, 2002)
Fiz. Nizk. Temp. **28**, 739–744 (July 2002)

Several recent examples are used to demonstrate that Raman and infrared spectroscopy can be successfully used as a novel experimental tool to study microscopic processes involving $4f$ electrons in rare earth (RE) cuprates. Raman-active crystal field (CF) excitations in Nd_2CuO_4 were measured under hydrostatic pressure up to ~7 GPa. The observed pressure-induced shifts of the CF levels were interpreted using density-functional-theory-based *ab initio* calculations and the superposition model. An infrared transmission study of the ^4I_J, $J=9/2$, 11/2, 13/2 multiplets of Nd^{3+} in Nd_2CuO_4 reveals a splitting of the Kramers doublets of the order of a few cm^{-1} due to the Nd-Cu exchange interaction. This study shows that these splittings can be described by an effective anisotropic exchange Hamiltonian for the Nd^{3+} ion expressed in terms of spherical tensor operators up to the sixth order. The isotropic term in the exchange Hamiltonian vanishes for symmetry reasons in this case. An analysis of the infrared transmission spectra in $RE_{1+x}Ba_{2-x}Cu_3O_{6+\delta}$ (RE=Nd,Sm) up to ~ 10 000 cm^{-1} indicates that, besides the regular sites, the RE ions also occupy Ba sites, even in the samples with the cation stoichiometry 1–2–3. [DOI: 10.1063/1.1496662]

1. INTRODUCTION

The presence of magnetic rare earth (RE) ions has no detrimental effect on superconductivity of the high-T_c cuprates. Therefore, the $4f$ states in RE cuprates have been widely used as a noninteracting probe for examination of superconductivity-related phenomena, including the doping-induced charge transfer from the charge reservoir to the ''superconducting'' CuO_2 planes, the phase-separation-related charge inhomogeneities and local structure deformations, and the pseudogap openings (for recent surveys see Refs. 1 and 2). The RE subsystem also exhibits interesting magnetic properties, including strongly anisotropic magnetic moments, Ising-like antiferromagnetism, magnetostriction, or carrier-concentration-dependent spin and lattice dimensionality of the magnetic order.[3–7]

An important prerequisite for the study of physical properties of the RE cuprates is an understanding of the microscopic interactions involving $4f$ electrons: the crystal field (CF) interaction, the magnetic exchange interaction, and the coupling of $4f$ excitations and phonons. The principal experimental tool for examining these interactions, by measurements of the $4f$ excitation spectra, has been inelastic neutron scattering.[1,2] Despite the widespread belief that optical methods are not appropriate in opaque materials, sharp and well-resolved $4f$ excitations in RE cuprates have been revealed by infrared (IR)[8] and Raman[9] spectroscopies. Surveyed in this article are recent results illustrating how these two techniques have been used to study microscopic processes involving $4f$ electrons in RE cuprates.

This article is organized as follows. The effect of hydrostatic pressure on the Raman active $4f$ state excitations in Nd_2CuO_4 is studied in the next Section. The splitting of the Kramers doublets in this compound, revealed using the IR spectroscopy, are described in terms of the anisotropic Nd-Cu exchange Hamiltonian in Sec. 3. The $4f$ excitations spectra in $REBa_2Cu_3O_{6+\delta}$ (RE=Nd,Sm) are discussed in Sec. 4.

2. 4*f* SPECTRA IN Nd_2CuO_4 UNDER PRESSURE

An interaction with the crystal field produced by the neighboring core charges and valence electronic density is the strongest perturbation of the free ion $4f$-shell state of trivalent RE ions in cuprates. The CF interaction Hamiltonian is usually considered in the form:[10]

$$H_{CF}=\sum_{k,q} B_{kq}(C_q^{[k]}+C_{-q}^{[k]}), \tag{1}$$

where the functions $C_q^{[k]}$ transform as tensor operators under simultaneous rotation of the coordinates of all the f electrons, B_{kq} are the so-called CF parameters.

The above-mentioned optical methods have made possible the determination of a sufficient number of CF energy levels in Nd_2CuO_4 to ensure reliability of the phenomenological parameters B_{kq} calculated by solving numerically the *inverse secular problem*.[9,11]

Recently, CF excitations of the Nd^{3+} ions in Nd_2CuO_4 were measured under hydrostatic pressure using Raman spectroscopy.[12] Two relatively intense CF peaks near 750 cm^{-1} and 1995 cm^{-1} were detected in applied pressure up to ~7 GPa. The energy of the 750 cm^{-1} CF excitation within the ground state J multiplet increases nearly linearly as a function of pressure at an average rate of 12.9(5) cm^{-1}/GPa (Fig. 1). It shows much larger pressure dependence than the transitions at 1992/1997 cm^{-1} from the ground state to the exchange-split Kramers doublet within the first excited J multiplet (Fig. 2). The energies of this doublet increase at rates of 1.7(2) cm^{-1} and 2.0(2) cm^{-1}/GPa.

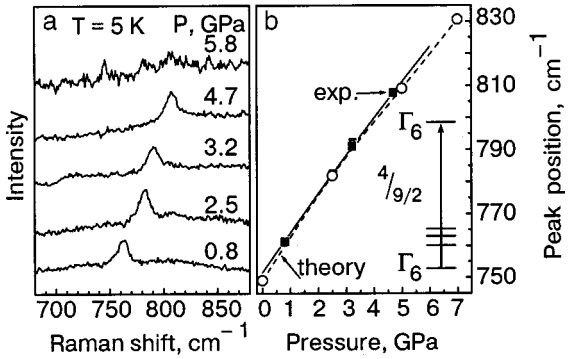

FIG. 1. (a) Raman spectra of Nd_2CuO_4 in the spectral range of the 750 cm^{-1} CF excitation for pressures of 0.8–5.8 GPa ($T=5$ K). (b) Experimental (■, solid line) and calculated (○, dashed line) pressure dependences of the peak position of the CF excitation. The lines in (b) are guides to the eye.[12]

Two theoretical methods were used to interpret the pressure dependence of the CF interaction. The $k=4$ and 6 CF parameters were predicted using the superposition model[13] that has proved to be efficient in the CF modeling in cuprates.[4] The model makes it possible to describe the parameters B_{kq} in Eq. (2) in terms of intrinsic (pair) CF parameters $b_k(R)$:

$$B_{kq}=\sum_i S_{kq}(i)b_k(R_i), \tag{2}$$

where $S_{kq}(i)$ is the geometrical factor determined by the angular coordinates of the ligands at the same distance R_i from the RE ion.

The superposition model does not apply to the $k=2$ parameters, where the long-range electrostatic contribution dominates. Therefore, the CF parameter B_{20} was calculated using the *ab initio* method, in which the electronic structure and related distribution of the ground state charge density are obtained from calculations based on the density functional theory (DFT). Within the DFT, the CF parameter B_{20}, originating from the effective potential V inside the crystal, can be written as:[14]

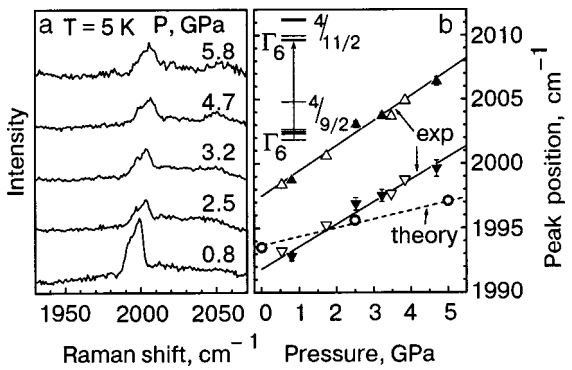

FIG. 2. (a) Raman spectra of Nd_2CuO_4 in the spectral range of the 1995-cm^{-1} CF excitation for pressures of 0.8–5.8 GPa ($T=5$ K). (b) Experimental and calculated pressure dependences of the peak positions of the CF excitations. The filled and unfilled triangles represent peak positions measured at 5 and 44 K, respectively. The lines represent linear regressions of the data.[12]

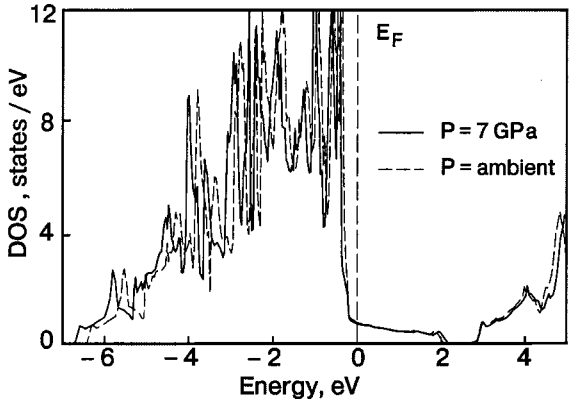

FIG. 3. Total density of electron states (DOS) of Nd_2CuO_4 calculated at ambient pressure and at 7 GPa (Ref. 12).

$$B_{20}=a_2^0\int_0^\infty |R_{4f}(r)|^2V_2^0(r)r^2dr, \tag{3}$$

where nonspherical components $V_2^0(r)$ reflect not only the nuclear potentials and Hartree part of the inter-electronic interaction but also the exchange correlation term, which accounts for many-particle effects. The radial wave function R_{4f} describes the radial shape of the localized $4f$ charge density of the RE^{3+} ion in the compound studied.

The calculation of the pressure dependence of the CF parameters included two steps. First, Eqs. (2) and (3) were used to calculate the theoretical ratio $B_{kq}(P)/B_{kq}(0)$ with allowance for the data on the pressure evolution of the Nd_2CuO_4 crystal structure measured by synchrotron x-ray powder diffraction[15] and the available superposition model parameters.[4] The effect of pressure on the underlying electronic density of states (DOS) is shown in Fig. 3. It is worth noting that the DOS curve is broadened by ~0.5 eV at an applied pressure of 7 GPa. This broadening is connected with a slight redistribution of the charge density, which results in an increase of the absolute value of the calculated parameter B_{20}. In the second step each phenomenological parameter B_{kq}[11] was multiplied by the theoretical ratio $B_{kq}(P)/B_{kq}(0)$. As an illustration, the CF parameters obtained in this way for the applied pressure 7 GPa are compared with the ambient pressure parameters in Table I. The absolute values of the individual CF parameters are increased by ~6–18% at 7 GPa compared to those at zero pressure.

The theoretical approach described above gives transition frequencies increasing nearly linearly at rates of ~11.7 and ~0.7 cm^{-1}/GPa for excitations near 750 and 1992(1997)

TABLE I. CF parameters B_{kq} in Nd_2CuO_4 (in cm^{-1}) obtained from a fit to IR absorption data at ambient pressure [11] and calculated at 7 GPa using the superposition model and the DFT based *ab initio* method (see text).

Parameter	$P=0$ (Ref. 11)	$P=7$ GPa (Ref. 12)
B_{20}	−335	−373
B_{40}	−2219	−2574
B_{44}	1634	1935
B_{60}	224	246
B_{64}	1494	1584

TABLE II. Splitting of the Nd^{3+} Kramers doublets in Nd_2CuO_4 as measured by infrared transmission[16] and calculated using Eq. (4)[19] (all energies in cm^{-1}).

J multiplet	CF level (Ref. 10)	Observed splitting	Calculated splitting
9/2	Ground state	5.5	5.7
11/2	1995	3.5	3.7
	2006	3.5	3.5
	2013	4.0	3.7
	2077	2.0	2.1
	2414	3.0	2.9
13/2	3950	2.5	2.7
15/2	5868	2.0	1.3

cm^{-1}, respectively. Regarding the lower-energy transition, very good agreement is achieved with the experimental result of 12.9 cm^{-1} (Fig. 1). The calculated value of the pressure dependence of the higher energy transitions is smaller than the experimental values of $\sim$1.7 and 2.0 cm^{-1} for the peaks at 1992 and 1997 cm^{-1} (Fig. 2), respectively. It bears noting that these transitions include the ground-state level and the lowest energy level in the $J=11/2$ multiplet. The CF calculation shows that the pressure dependences of these levels are very similar, -4.5 and -3.8 cm^{-1}/GPa, respectively. This explains why the resulting pressure-induced shift of the transition energy is small. The remaining discrepancy between the experimental and calculated values is ascribed to a small pressure-induced shift of the free ion levels, not taken into account in the above calculations.

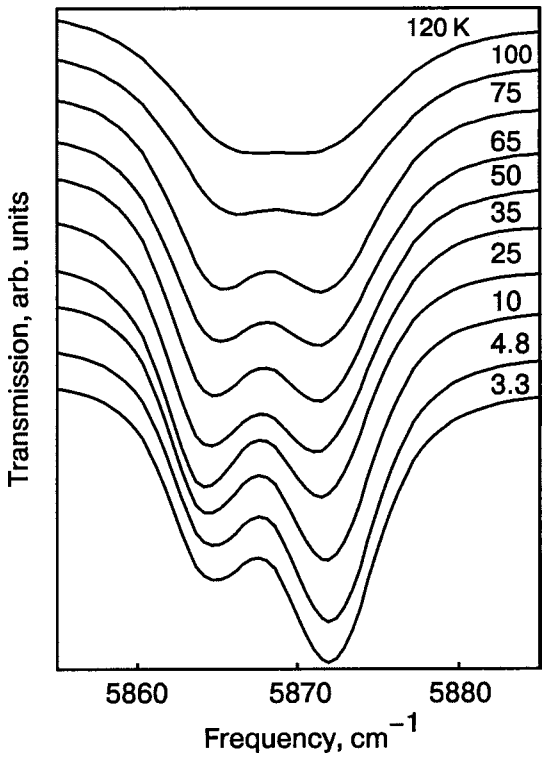

FIG. 4. Nd_2CuO_4 IR transmission as a function of temperature (Ref. 16).

TABLE III. The best-fit values of the exchange parameters α_{kq} (in cm^{-1}) in Eq. (4) (Ref. 19).

	Exchange parameter α_{kq}
α_{00}	$-7(4)$
α_{20}	$-491(130)$
α_{40}	$-177(33)$
α_{44}	$-257(12)$
α_{60}	15(16)
α_{64}	47(13)

A detailed analysis of the pressure-induced increase in the separation of the doublet near 1995 cm^{-1} (Fig. 2) indicated that in addition to the CF parameters the parameters α_{kq} of the Hamiltonian of the anisotropic Nd–Cu exchange interaction, Eq. (4), are pressure dependent.[12]

3. ANISOTROPY OF THE Nd-Cu EXCHANGE INTERACTION IN RE CUPRATES

The IR transmission study of the $4f$ spectra in the antiferromagnet Nd_2CuO_4 yielded a splitting of the CF Kramers doublets of the order of a few cm^{-1} due to the exchange interaction between Nd and Cu (see the third column of Table II).[16] An example of the experimental spectra of the transition from the ground state to an exchange-split Kramers doublet at $\sim$5870 cm^{-1} is shown in Fig. 4. The exchange anisotropy due to the orbital moments of the f electrons is pronounced in this case: the isotropic Heisenberg-type exchange alone appears to be completely incapable of explaining the observed doublet splittings.[11] To account for these splittings one has to consider the complete Hamiltonian

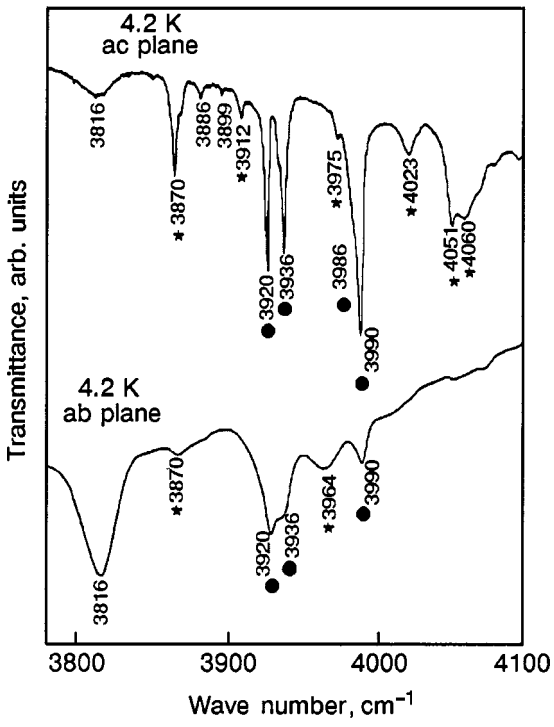

FIG. 5. IR spectra of CF transitions in $NdBa_2Cu_3O_6$ from the ground state multiplet $^4I_{9/2}$ to the second excited multiplet $^4I_{13/2}$ (*ab* and *ac* platelets at 4.2 K). The filled circles and asterisks indicate strong and weak absorption bands, respectively. See Ref. 24 for additional details.

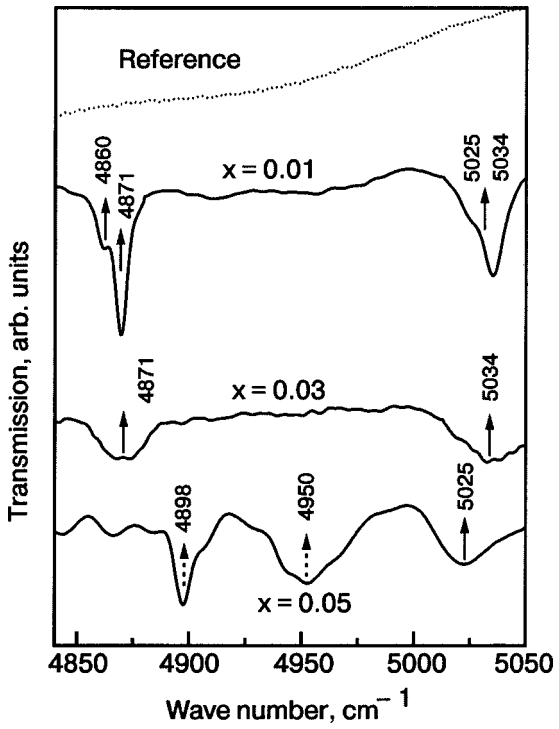

FIG. 6. IR spectra of CF transitions ($^6H_{5/2} \rightarrow {}^6H_{13/2}$) in $Sm_{1+x}Ba_{2-x}Cu_3O_{6+\delta}$ in the 4800–5050 cm^{-1} range. The dashed arrows indicate CF transitions associated with Sm/Ba sites. See Ref. 25 for additional details.

within the molecular field approximation describing the exchange interaction of the $4f$ electrons of an Nd ion with the magnetically polarized Cu sublattice.[17,18]

The perturbation single-ion Hamiltonian under consideration then includes, besides the standard CF term H_{CF} from Eq. (1), an exchange term $H_{\rm exch}$:

$$H_{\rm exch} = -2\sum_{k,q} \alpha_{kq} \sum_i T_q^{[k]}(i)\mathbf{s}(i)\cdot\mathbf{n}, \tag{4}$$

where α_{kq} are the exchange parameters, $T^{[k]}(i)$ are the irreducible unit tensor operators which act on the orbital part of the Nd wave function, $\mathbf{s}(i)$ is the spin of a Nd electron, and $\mathbf{n}$ is the spin of a Nd electron, and $\mathbf{n}$ is the unit vector directed along the magnetization of the Cu sublattice. There are six independent parameters α_{kq} in $H_{\rm exch}$ for Nd ions occupying the tetragonal symmetry sites in Nd_2CuO_4.

A least-squares procedure has been utilized to fit the splitting of the eight observed Kramers doublet splittings using the above-mentioned perturbation Hamiltonian.[19] The results of the final fit are summarized in Table II; the corresponding best-fit values of α_{kq} are given in Table III. It is worthwhile to note that the contributions of the second- andfourth-order terms to the splittings are two orders of magnitude larger than that of the isotropic term ($k=q=0$) in the exchange operator. This finding is compatible with the symmetry considerations indicating that the isotropic term in the exchange Hamiltonian vanishes when only the nearest Cu neighbors of Nd are considered.[20] It also shows the importance of the higher-order terms in Eq. (4), neglected in magnetic studies in which the anisotropic RE-Cu coupling in Nd_2CuO_4 (Refs. 20 and 21) and $PrBa_2Cu_3O_{6+\delta}$ (Refs. 22 and 23) is represented by a pseudo-dipolar term.

TABLE IV. CF parameters (in cm^{-1}) in $Sm_{1+x}Ba_{2-x}Cu_3O_6$ (Ref. 6) and $Nd_{1+x}Ba_{2-x}Cu_3O_6$ (Ref. 5) obtained by an analysis of the IR spectra (see text).

B_{kq}	D_{4h} site		C_{4v} site
kq	Sm	Nd	Sm
2 0	282(5)	380(28)	−227
4 0	−2481(12)	−2956(34)	24
4 4	1307(10)	1664(25)	−331
6 0	321(12)	526(15)	−427
6 4	1931(6)	2021(10)	624

4. CRYSTAL FIELD STUDY IN $RE_{1+x}Ba_{2-x}Cu_3O_{6+\delta}$ (RE=Nd,Sm)

In this Section we report a systematic study of CF transitions in $NdBa_2Cu_3O_{6+\delta}$ ($\delta\sim 0$) and $Sm_{1+x}Ba_{2-x}Cu_3O_{6+\delta}$ $\times (x\leqslant 0.01,\ x=0.03,\ 0.05,$ and $0.11;\ \delta\sim 0$) by IR absorption.[24,25] The transitions involving Kramers doublets within the lowest-energy ^4I term and ^6H term in the Nd and Sm compounds, respectively, were determined. Examples of these transitions are shown in Figs. 5 and 6. The large number of peaks in the experimental spectra indicates that there exists more than one type of RE site. We observe that the f-f transitions are electric-dipole forbidden for the RE ions at regular D_{4h}-symmetry sites in ideal $REBa_2Cu_3O_6$.

A phenomenological CF analysis of the IR data (Sec. 2), including the neutron scattering data for the $J=9/2$ multiplet in $NdBa_2Cu_3O_6$ (Ref. 26), allowed identification and fitting of the CF spectra of Nd and Sm ions at regular sites. Detailed CF calculations using the superposition model and the *ab initio* method based on the density-functional theory described in Sec. 2 indicate[27] that additional bands in the IR spectra correspond to the RE^{3+} ions in the C_{4v}-symmetry Ba sites. The sets of the CF parameters for regular as well as Ba sites obtained using the above-mentioned methods are summarized in Table IV.

Concluding this part, we note that the CF transitions at RE/Ba sites have been observed in all $RE_{1+x}Ba_{2-x}Cu_3O_{6+\delta}$ samples studied, including those with $x=0$. This finding supports recent data indicating that the presence of a relatively small quantity of the magnetic Pr^{3+} ions at the Ba sites is the main reason for anomalous behavior of $PrBa_2Cu_3O_7$, including the suppression of superconductivity as well as the appearance of the antiferromagnetic ordering in the Pr sublattice at a temperature at least one order of magnitude higher than for other RE elements.[28]

The assistance of the Grant Agency of the Czech Republic in the form of its grant No. 202/00/1602 is gratefully acknowledged.

*E-mail: nekvasil@fzu.cz

[1] U. Staub and L. Soderholm, in *Handbook on the Physics and Chemistry of Rare Earth*, Vol. 30, K. A. Gschneidner, Jr., L. Eyering, and M. B. Maple (Eds.), North Holland, Amsterdam (2001), p. 491.
[2] J. Mesot and A. Furrer, J. Supercond. **10**, 623 (1997).
[3] T. W. Clinton and J. W. Lynn, Phys. Rev. B **51**, 15429 (1995).
[4] V. Nekvasil, J. Magn. Magn. Mater. **140–144**, 1265 (1995); V. Nekvasil, M. Divis, G. Hilscher, and E. Holland-Moritz, J. Alloys Compd. **225**, 578 (1995).

[5] V. Nekvasil, S. Jandl, T. Strach, T. Ruf, and M. Cardona, J. Magn. Magn. Mater. **177–181**, 535 (1998).
[6] I. K. Aminov, B. Z. Malkin, and M. A. Teplov, in *Handbook on the Physics and Chemistry of Rare Earth*, Vol. 22, K. A. Schneider, Jr. and L. Eyering (Eds.), North-Holland, Amsterdam (1996), p. 295.
[7] V. V. Eremenko, T. V. Sukhareva, and V. N. Samovarov, Fiz. Tverd. Tela (St. Petersburg) **42**, 797 (2000) [Phys. Solid State **42**, 816 (2000)].
[8] M. L. Jones, D. W. Shortt, B. W. Sterling, A. L. Schawlow, and R. M. Macfarlane, Phys. Rev. B **46**, 611 (1992).
[9] S. Jandl, M. Iliev, C. Thomsen, M. Cardona, B. M. Wanklyn, and C. Changkang, Solid State Commun. **87**, 609 (1993); S. Jandl, P. Dufour, T. Strach, T. Ruf, M. Cardona, V. Nekvasil, C. Chen, and B. M. Wanklyn, Phys. Rev. B **52**, 15558 (1995).
[10] B. G. Wybourne, *Spectroscopic Properties of Rare Earths*, Wiley, New York (1965).
[11] S. Jandl, P. Dufour, P. Richard, V. Nekvasil, D. I. Zhigunov, S. A. Barilo, and S. V. Shiryaev, J. Lumin. **78**, 197 (1998).
[12] I. Loa, K. Syassen, M. Divis, V. Nekvasil, S. Jandl, A. A. Nugroho, and A. A. Menovsky, Phys. Rev. B **64**, 214106 (2001).
[13] D. J. Newman and Betty Ng, Rep. Prog. Phys. **52**, 699 (1989).
[14] M. Divis, V. Nekvasil, and J. Kuriplach, Physica C **301**, 23 (1998); M. Divis and V. Nekvasil, J. Alloys Compd. **323–324**, 567 (2001).
[15] H. Wilhelm, C. Cross, E. Reny, G. Demazeau, and M. Hanfland, J. Mater. Chem. **8**, 2729 (1998).
[16] S. Jandl, P. Richard, V. Nekvasil, D. I. Zhigunov, S. N. Barilo, and S. V. Shiryaev, Physica C **314**, 189 (1999).
[17] P. M. Levy, Phys. Rev. **135**, 155 (1964).
[18] W. P. Wolf, J. Phys. (Paris), Colloq. **32**, C1-26 (1971).
[19] A. A. Nugroho, V. Nekvasil, I. Veltrusky, S. Jandl, P. Richard, A. A. Menovsky, F. R. de Boer, and J. J. M. Franse, J. Magn. Magn. Mater. **226–230**, 973 (2001).
[20] R. Sachidanandam, T. Yilidirim, A. B. Harris, A. Aharony, and O. Entin-Wohlman, Phys. Rev. B **56**, 260 (1997).
[21] Ph. Bourges, L. Boudarene, and D. Petitgrand, Physica B **180–181**, 128 (1992).
[22] S. V. Maleev, JETP Lett. **67**, 947 (1998).
[23] S. J. S. Lister, A. T. Boothroyd, N. H. Andersen, B. H. Larsen, A. A. Zhokhov, A. N. Christensen, and A. R. Wildes, Phys. Rev. Lett. **86**, 5994 (2001).
[24] A. A. Martin, T. Ruf, M. Cardona, S. Jandl, D. Barba, V. Nekvasil, M. Divis, and T. Wolf, Phys. Rev. B **59**, 6528 (1999).
[25] D. Barba, S. Jandl, V. Nekvasil, M. Marysko, M. Divis, T. Wolf, A. A. Martin, C. T. Lin, and M. Cardona, Phys. Rev. B **63**, 54528 (2001).
[26] P. Allenspach, J. Mesot, U. Staub, M. Guillaume, A. Furrer, S.-I. Yoo, M. J. Kramer, R. W. McCallum, H. Maletta, H. Blank, H. Mutka, R. Osborn, M. Arai, Z. Bowden, and A. D. Taylor, Z. Phys. B: Condens. Matter **95**, 301 (1995).
[27] M. Divis and V. Nekvasil, J. Alloys Compd. **323–324**, 567 (2001).
[28] H. A. Blackstead, J. D. Dow, I. Felner, and W. B. Yelon, Phys. Rev. B **63**, 094517 (2001).

This article was published in English in the original Russian journal. Reproduced here with stylistic changes by the Translation Consultant.

Electronic structure and magneto-optical Kerr effect in the compound $UCuP_2$

O. Horpynyuk and V. V. Nemoshkalenko

Institute of Metal Physics, 36 Vernadsky Str., 252142 Kiev, Ukraine

V. N. Antonov* and B. N. Harmon

Ames Laboratory, Iowa State University, Ames, Iowa 50011, USA

A. N. Yaresko

Max Planck Institute CPFS, 40, Nöthnitzer Str., D-01187 Dresden, Germany

(Submitted November 12, 2001)
Fiz. Nizk. Temp. **28**, 745–751 (July 2002)

The optical and magneto-optical (MO) spectra of the fernary compound $UCuP_2$ are investigated from first principles, using the fully relativistic Dirac linear-muffin-tin-orbital band structure method and density-functional theory in the local spin-density approximation. Within a band-like description of the $5f$ electrons, good agreement with the measured MO spectra is obtained. The origin of the Kerr rotation in the compound is examined. © *2002 American Institute of Physics.* [DOI: 10.1063/1.1496663]

1. INTRODUCTION

Actinide compounds occupy an intermediate position between itinerant $3d$ and localized $4f$ systems,[1,2] and one of the fundamental questions concerning the actinide materials is whether their f states are localized or itinerant. This question is most frequently answered by comparison between experimental spectroscopies and the different theoretical descriptions. Optical and magneto-optical (MO) spectroscopy, like photoelectron spectroscopy and bremsstrahlung isochromat spectroscopy, supply direct information about the energy states (both occupied and unoccupied) around the Fermi energy[3] and can provide a means of discrimination between the two theoretical limits.

Intensive experimental and theoretical study over more than two decades[4–8] has revealed that $5f$ magnetism is quite complex because Coulomb, spin-orbit, crystalline field, and exchange energies in $5f$ systems are of the same order of magnitude. Today it is well established that many unusual physical properties of the light actinide metals are a reflection of the particular nature of the $5f$ electrons. Friedel[9] proposed many years ago that the bonding in these materials must involve the $5f$ electrons. The argument for $5f$ bonding can be understood as a consequence of the extended nature of the $5f$ wave function relative to the rare-earth $4f$ wave functions. This causes them to form in bandlike states.[10]

The itinerant nature of the $5f$ electrons in the light actinide metals is well known.[4] Their electronic structure and optical properties is well described by local spin-density approximation (LSDA) band structure calculations.[11,12] On the other hand, the decreasing f-band width (W) and the increasing intra-atomic Coulomb energy (U) results in a Mott localization between plutonium and americium,[5,13,14] and the correlation effects are not properly described in the LSDA.[7,15]

Actinide compounds are excellent subjects for MO research. The participation of the $5f$ states in bonding is reflected in strongly hybridized bands near the Fermi level, with a high density of states and significant $d \rightarrow f$ oscillator strengths for optical transitions. The $5f$ delocalization favors higher magnetic ordering temperatures. In fact, many uranium compounds have ordering temperatures which are one order of magnitude higher than those in similar lanthanide compounds.[3,16] Regarding the magnitude of the MO effects compared to rare-earth materials, an enhancement due to the larger spin-orbit energy can be expected and is in part experimentally verified.[3,16] For actinide compounds the figure of merit $\sqrt{R(\theta_K^2+\varepsilon_K^2)}$, where R is the optical reflectivity and θ_K and ε_K are the Kerr angle and Kerr ellipticity, respectively, is one order of magnitude larger than for the best transition or rare-earth compounds.[3] Besides the issue of radioactivity (minimal for depleted uranium) a hindrance for successful application of actinide compounds in storage devices is that the typical Curie temperatures are below room temperature. This is not a fundamental problem, and can probably be overcome by suitable alloying.

For actinide materials much of the MO experimental effort up to now[3,16] has been focused on binary UX NaCl-type uranium chalcogenides (X=S,Se,Te) and pnictides (X=P,As,Sb), uranium compounds U_3X_4 (X=P,As) with the Th_3P_4 crystal structure, and some ternary compounds such as UAsTe, the tetragonal compounds $UCuP_2$ and $UCuAs_2$, and the hexagonal compounds UCu_2P_2, UMn_2Si_2, and UMn_2Ge_2.

There are quite a few first-principle calculations of the MO spectra of uranium compounds.[17–22] The MO spectra of such compounds as UAsSe[19] and U_3P_4 (Refs. 20 and 22) are well described in the LSDA, and we can conclude that they have at least partially itinerant electron behavior. On the other hand the MO spectra in US, USe, and UTe can be well described only in the LSDA+U approximation[21] supporting the localized description for their $5f$ electrons.

In the present work we report a detailed theoretical investigation of the electronic structure and the optical and MO Kerr properties of the ternary compound $UCuP_2$. The paper

is organized as follows. The computational details are explained in Sec. 2. Section 3 presents the theoretical electronic structure and MO spectra of $UCuP_2$. The results are then compared to the experimental data. Finally, the results are summarized in Sec. 4.

2. THEORETICAL FRAMEWORK

Using straightforward symmetry considerations it can be shown that all MO phenomena are caused by the symmetry reduction—compared to the paramagnetic state—caused by magnetic ordering.[23] Concerning the optical properties this symmetry reduction only has consequences when spin-orbital (SO) coupling is considered in addition. To calculate the MO properties one therefore has to take into account the magnetism and SO coupling while at the same time dealing with the electronic structure of the material considered. In performing the corresponding band structure calculations it is normally sufficient to treat the SO coupling in a perturbative way. A more rigorous scheme, however, is obtained by starting from the Dirac equation set up in the framework of relativistic spin density functional theory:[24]

$$[c\,\boldsymbol{\alpha}p+\beta mc^2+IV+V_{sp}\beta\sigma_z]\psi_{n\mathbf{k}}=\varepsilon_{n\mathbf{k}}\psi_{n\mathbf{k}}, \tag{1}$$

with $V_{sp}(\mathbf{r})$ the spin-polarized part of the exchange-correlation potential corresponding to the z quantization axis. All other parts of the potential are contained in $V(\mathbf{r})$. The 4×4 matrices $\boldsymbol{\alpha}$, $\boldsymbol{\beta}$, and $\mathbf{I}$ are defined by

$$\boldsymbol{\alpha}=\begin{pmatrix}0 & \boldsymbol{\sigma}\\ \boldsymbol{\sigma} & 0\end{pmatrix},\quad \beta=\begin{pmatrix}\mathbf{1} & 0\\ 0 & -\mathbf{1}\end{pmatrix},\quad \mathbf{I}=\begin{pmatrix}\mathbf{1} & 0\\ 0 & \mathbf{1}\end{pmatrix}, \tag{2}$$

where $\boldsymbol{\sigma}$ represents the standard Dirac matrices, and $\mathbf{1}$ is the 2×2 unit matrix.

There are quite a few band structure methods available now that are based on the above Dirac equation.[25] In the first scheme the basis functions are derived from the proper solution to the Dirac equation for the various single-site potentials.[26,27] In the second one, the basis functions are obtained initially by solving the Dirac equation without the spin-dependent term[28–30] and then this term is taken into account only in the variational step.[26,31,32] In spite of this approximation used, the second scheme nevertheless gives results in very good agreement with the first one,[25] while being very simple to implement.

Phenomenologically, optical and magneto-optical properties of solids are treated by means of a dielectric tensor. The dielectric tensor is composed of the diagonal component ε_{xx} and ε_{zz} and the off-diagonal component ε_{xy} in the form

$$\varepsilon=\begin{pmatrix}\varepsilon_{xx} & \varepsilon_{xy} & 0\\ -\varepsilon_{xy} & \varepsilon_{xy} & 0\\ 0 & 0 & \varepsilon_{zz}\end{pmatrix}. \tag{3}$$

In the polar geometry, where the z axis is chosen to be perpendicular to the solid surface and parallel to the magnetization direction, the expression for the Kerr angle can be obtained easily for small angles and is given by:[3]

$$\theta_K(\omega)+i\varepsilon_K(\omega)=\frac{-\sigma_{xy}(\omega)}{\sigma_{xx}(\omega)\sqrt{1+\dfrac{4\pi i}{\omega}\sigma_{xx}(\omega)}}, \tag{4}$$

where θ_K is the Kerr rotation and ε_K is the so-called Kerr ellipticity. $\sigma_{\alpha\beta}(\alpha,\beta\equiv x,y,z)$ is the optical conductivity tensor, which is related to the dielectric tensor $\varepsilon_{\alpha\beta}$ through

$$\varepsilon_{\alpha\beta}(\omega)=\delta_{\alpha\beta}+\frac{4\pi i}{\omega}\sigma_{\alpha\beta}(\omega). \tag{5}$$

The optical conductivity tensor, or equivalently, the dielectric tensor is the important spectral quantity needed for the evaluation of the Kerr effect.[33] The optical conductivity can be computed from the energy band structure by means of the Kubo–Greenwood[34] linear-response expression:[35]

$$\sigma_{\alpha\beta}(\omega)=-\frac{ie^2}{m^2\hbar V_{uc}}\times\sum_{\mathbf{k}}\sum_{nn'}\frac{f(\varepsilon_{n\mathbf{k}})-f(\varepsilon_{n'\mathbf{k}})}{\omega_{nn'}(\mathbf{k})}\frac{\Pi^{\alpha}_{n'n}(\mathbf{k})\Pi^{\beta}_{nn'}(\mathbf{k})}{\omega-\omega_{nn'}(\mathbf{k})+i\gamma}, \tag{6}$$

where $f(\varepsilon_{nk})$ is the Fermi function, $\hbar\omega_{nn'}(\mathbf{k})\equiv\varepsilon_{n\mathbf{k}}-\varepsilon_{n'\mathbf{k}}$ is the energy difference of the Kohn–Sham energies $\varepsilon_{n\mathbf{k}}$, and γ is the lifetime parameter, which is included to describe the finite lifetime of excited Bloch electron states. The $\Pi^{\alpha}_{nn'}$ are the dipole optical transition matrix elements, which in a fully relativistic description are given by:[36]

$$P_{nn'}(\mathbf{k})=m\alpha\langle\psi_{n\mathbf{k}}|c\,\boldsymbol{\alpha}|\psi_{n'\mathbf{k}}\rangle, \tag{7}$$

where $\psi_{n\mathbf{k}}$ is the four-component Bloch electron wave function.

Equation (6) for the conductivity contains a double sum over all energy bands, which naturally separates into the so-called interband contribution, i.e., $n\neq n'$, and the intraband contribution, $n=n'$. The intraband contribution to the diagonal components of $\boldsymbol{\sigma}$ may be rewritten for zero temperature as

$$\sigma_{\alpha\alpha}(\omega)\equiv\frac{(\omega_{p,\alpha})^2}{4\pi}\frac{i}{\omega+i\gamma_D}, \tag{8}$$

where $\omega_{p,\alpha}$ are the components of the plasma frequency, which are given by

$$(\omega_{p,\alpha})^2\equiv\frac{4\pi e^2}{m^2V_{uc}}\sum_{n\mathbf{k}}\delta(\varepsilon_{n\mathbf{k}}-E_F)|\Pi^{\alpha}_{nn}|^2, \tag{9}$$

and E_F is the Fermi energy. For cubic symmetry, we furthermore have $\omega_p^2\equiv\omega_{p,x}^2=\omega_{p,y}^2=\omega_{p,z}^2$. Equation (8) is identical to the classical Drude result for the ac conductivity, with $\gamma_D=1/\tau_D$, where τ_D is the phenomenological Drude electron relaxation time. The intraband relaxation time parameter γ_D may be different from the interband relaxation time parameter γ. The latter can be frequency dependent,[37] and, because excited states always have a finite lifetime, will be nonzero, whereas γ_D will approach zero for very pure materials. Here we adopt the perfect crystal approximation, i.e., $\gamma_D\to0$. For the interband relaxation parameter, on the other hand, we shall use, unless stated otherwise, $\gamma=0.4$ eV. This

value has been found to be on average a good estimate of this phenomenological parameter. The contribution of intraband transitions to the off-diagonal conductivity usually is not considered. Also, we did not study the influence of local field effects on the MO properties.

We mention, lastly, that the Kramers–Kronig transformation has been used to calculate the dispersive parts of the optical conductivity from the absorptive parts.

3. CRYSTAL STRUCTURE AND COMPUTATIONAL DETAILS

Self-consistent energy band-structure calculations of $UCuP_2$ were performed by means of the fully relativistic, spin-polarized linear-muffin-tin-orbital (SPR LMTO) method using the atomic sphere approximation with combined corrections included.[26,29–32] The LSDA part of the energy band structure calculations were based on the spin-density-functional theory with von Barth–Hedin parameterization[38] of the exchange-correlation potential. Core charge densities were recalculated at every iteration of the self-consistency loop. The **k**-space integrations were performed with the improved tetrahedron method[39] and the charge was obtained self-consistently with 349 irreducible k points. The basis consisted of U s, p, d, f, and g; Cu s, p, d, and f; P s, p, and d LMTOs. The energy expansion parameters $E_{\nu Rl}$ were chosen at the centers of gravity of the occupied parts of the partial state densities; this gives high accuracy for the charge density.

$UCuP_2$ belongs to the layered tetragonal $ZrAl_3$ type crystal structure (Fig. 1) with the space group $I4/mmm$ (No. 139) with U at the $4e$ position, Cu at the $4d$ position, and P at the $4c$ and $4e$ positions. The phosphorous atoms have two nonequivalent positions: the plane with P_1 atoms is situated between uranium planes, while the plane containing the P_2 atoms lies between uranium and copper planes (see Fig. 1). The lattice constants are $a=3.803$ Å, $c=18.523$ Å (Ref. 40). The corresponding Brillouin zone is shown in Fig. 2. The unit cell of $UCuP_2$ contains 8 atoms.

4. RESULTS AND DISCUSSION

The uranium pnictide ternary compounds with copper or nickel crystallize in a high-symmetry structure: $UCuP_2$, $UCuAs_2$, and $UNiAs_2$ are tetragonal[41] and UCu_2P_2 and UCu_2As_2 are hexagonal.[42] The U-Cu ternaries order ferromagnetically, in contrast to the U-Ni ternaries, which are all antiferromagnets.[3] The magnetic ordering temperatures are among the highest known so far for uranium compounds, reaching 216 K for UCu_2P_2 (Ref. 43). The magnetic and transport properties of $UCuP_2$ were investigated by Kaszorowski *et al.*[44] on single-crystal specimens. They found that the compound is ferromagnetic below 75 K, with a spontaneous magnetic moment of 0.98 μ_B, and in the magnetically ordered region it exhibits large magnetocrystalline anisotropy constants. The electrical resistivity of $UCuP_2$ at low temperature behaves as T^2, while in the temperature range above T_C the observed negative slope of $\rho(T)$ may point to Kondo lattice behavior.[44]

The energy dependence of the Kerr rotation and ellipticity of $UCuP_2$ have been measured by Funagalli *et al.*[45] The measurements were done on a natural grown surface perpendicular to the c axis. Although $UCuP_2$ has a lower uranium concentration in comparison with UX and U_3X_4 (X=P,As) compounds, its Kerr rotation reaches 1.6° (Ref. 45).

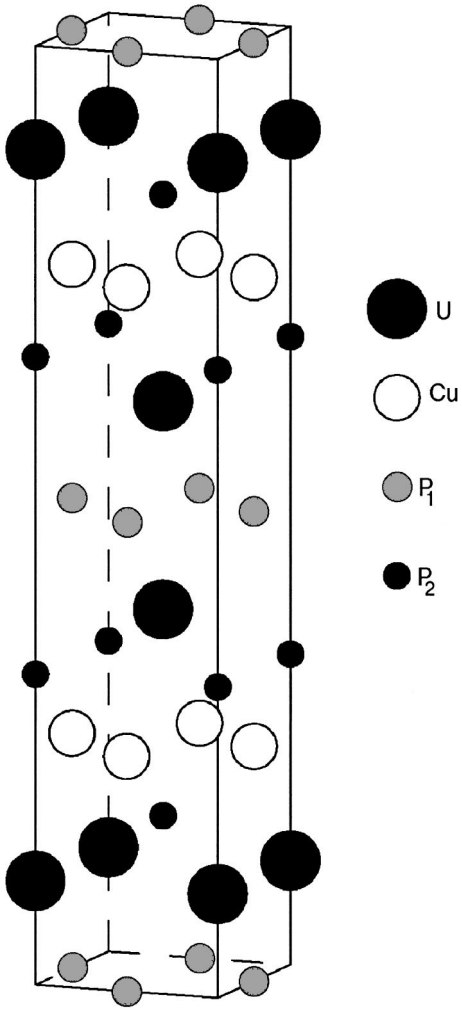

FIG. 1. Crystal structure of tetragonal $UCuP_2$.

The fully relativistic spin-polarized energy band structure of ferromagnetic $UCuP_2$, shown in Fig. 3, is rather complicated. It may, however, be understood from the total and partial density of states (DOS) presented in Fig. 4. The bands in the lowest region between -13.4 and -7.2 eV have mostly a P s character with some amount of U and Cu spd character mixed in. The energy bands between -7.2 and -0.4 eV are P $3p$ states strongly hybridized with the Cu $3d$ and U $6d$ states. There is a quasi-gap between P s and p states. The Cu $3d$ states are fully occupied and situated around 5.0 eV below the Fermi level. The U $5f$ energy bands are located above and below E_F at about -0.4 to 3.0 eV. The highest region above the Fermi energy can be characterized

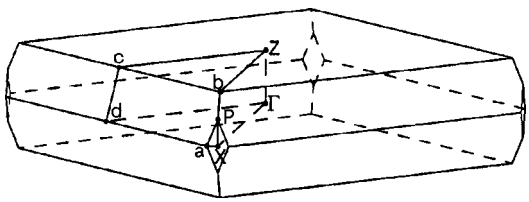

FIG. 2. Brillouin zone of tetragonal $UCuP_2$.

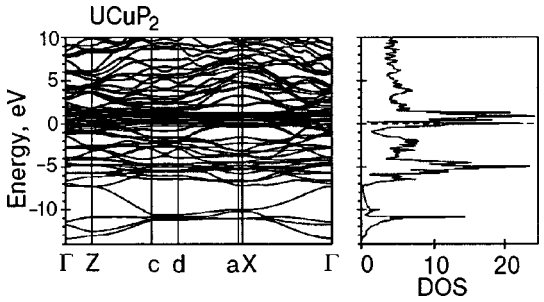

FIG. 3. Self-consistent fully relativistic, spin-polarized energy band structure and total DOS [in states/(unit cell eV)] of $UCuP_2$.

as anti-bonding U $6d$ states. It is interesting to note that the $3p$ partial density of states for P_1 and P_2 sites differ from each other significantly. This reflects the different positions for the two phosphorus atoms. As we mentioned above, the plane with P_1 atoms is situated between uranium planes, whereas the plane with P_2 atoms lies between uranium and copper planes (see Fig. 1). The P_1 atoms have as neighbors four P_1 atoms at a distance of 2.688 Å and four uranium atoms at 2.793 Å. On the other hand, the P_2 atoms have four Cu neighbor atoms at a distance of 2.423 Å and four uranium atoms at 2.898 Å. As a result, the $3p$ partial density of states for the P_1 site has one peak structure for occupied states, reflecting strong hybridization between the P_1 $3p$ and U $6d$ states, whereas the $3p$ partial density of states for the P_2 site has two peaks due to the hybridization of P_2 $3p$ states with both Cu $3d$ and U $6d$ states.

After consideration of the above band structure properties we turn to the MO spectra. In Fig. 5 we show the calculated and experimental[45] MO Kerr spectra of $UCuP_2$. There exists rather good agreement between the experimental Kerr spectra and the *ab initio* LSDA calculated one. Overall, the experimental features are reasonably well reproduced, except the theoretically calculated spectra have sharper features in comparison with the experimentally observed spectra. There is also a small red energy shift by about 0.1 eV in the position of the main Kerr rotation and ellipticity peaks in comparison with the experiment. We can conclude, therefore, that the spectral behavior of the MO Kerr spectra in $UCuP_2$ is well described by LSDA band-structure theory.

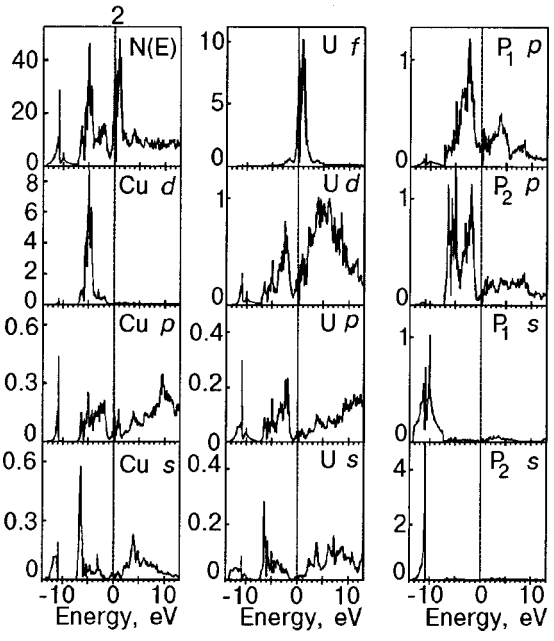

FIG. 4. Fully relativistic, spin-polarized total [in states/(unit cell eV)] and partial densities of state [in states/(atom eV)] calculated for $UCuP_2$.

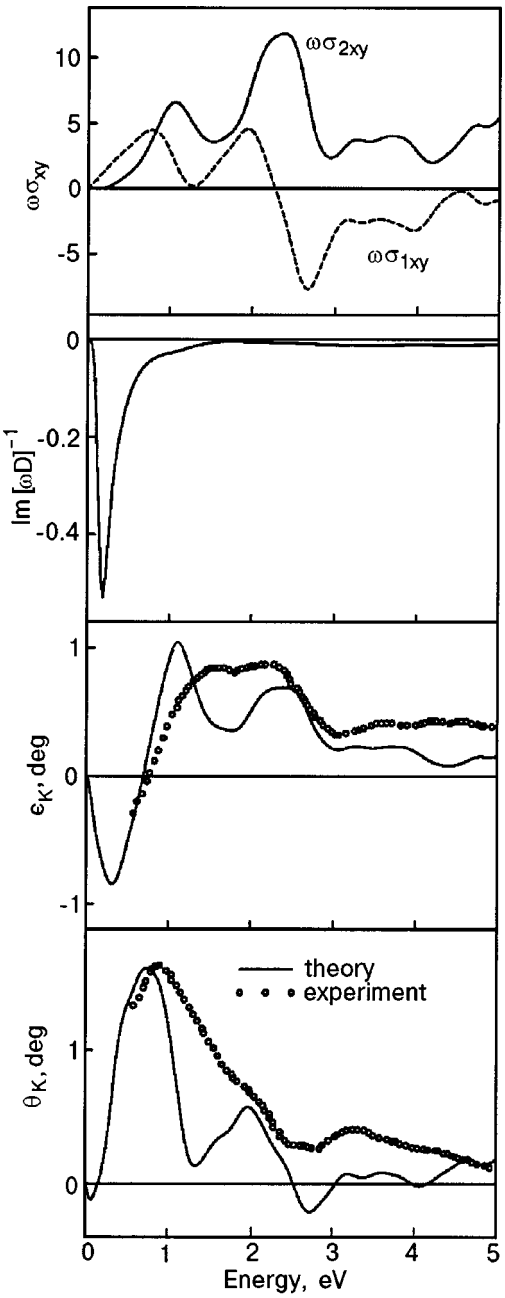

FIG. 5. Calculated and experimental[45] Kerr rotation (θ_K) and Kerr ellipticity (ε_K) spectra of $UCuP_2$ as well as the theoretically calculated off-diagonal optical conductivity σ_{xy} and function $\mathrm{Im}[\omega D]^{-1}$ (see the explanation in the text).

To investigate the origin of the Kerr spectra, we consider the separate contributions of both the numerator of Eq. (4), i.e., $\sigma_{xy}(\omega)$ and the denominator, $D(\omega) \equiv \sigma_{xx}\sqrt{1+(4\pi i/\omega)\sigma_{xx}}$. In Fig. 5 we show how the separate contributions of numerator and denominator bring about the Kerr angle and Kerr ellipticity of $UCuP_2$. The imaginary part of the inverse denominator (times the photon frequency), $\mathrm{Im}[\omega D]^{-1}$, displays a strong resonance structure at

TABLE I. The experimental and LSDA calculated spin, orbital and total magnetic moments (in μ_B) of $UCuP_2$. The experimental data are from Ref. 44.

Atom	M_s	M_l	M_{total}	Experiment
U	−0.886	1.148	0.262	0.89
Cu	−0.009	−0.002	−0.011	
P_1	0.012	0.001	0.013	
P_2	−0.006	−0.001	−0.007	

about 0.2 eV. However, the imaginary and real parts of $\omega\sigma_{xy}$, i.e., $\omega\sigma_{2xy}$ and $\omega\sigma_{1xy}$, display a very small value at this energy. Therefore the first minimum in the Kerr rotation and Kerr ellipticity at around 0.2 eV results from a deep resonance structure of the denominator. Outside the infrared peak, for energies above 0.5 eV, the Kerr rotation and ellipticity spectra are fully determined by the shape of σ_{xy}, which in turn are known to be due to the interplay of SO coupling and spin polarization. The two peaks at about 0.7 and 2.0 eV in the Kerr rotation spectrum originate mostly from U $6d \rightarrow 5f$ interband transitions (see Figs. 3 and 4). The interband transitions from the Cu $3d$ to the U $5f$ band start above 4 eV. In the 1 to 5 eV energy region the theoretical and experimental curves deviate from one another in some details.

The theoretically calculated figure of merit $\sqrt{R(\theta_K^2+\varepsilon_K^2)}$ in $UCuP_2$ has a maximum value of 1.2° at 0.7 eV, which is higher than that in PtMnSb (0.83° at 1.57 eV)[46] but smaller than that in U_3As_4 (6.0° at 0.35 eV).[22]

In spite of the reasonably close correspondence between the experimental and theoretical Kerr spectra, we find that not all properties of $UCuP_2$ are equally well represented. For example, the calculated total magnetic moment of uranium in $UCuP_2$ is only $0.262\mu_B$ (Table I) (with spin moment $-0.886\mu_B$ and orbital moment $1.148\mu_B$), which is considerably smaller than the experimental moment of about $0.89\mu_B$.[44]

The calculated moment is dominated by $5f$ states: the $5f$ components of the spin and orbital moment are $-0.845\mu_B$ and $1.137\mu_B$, respectively. It is a well-known fact, however, that within the LSDA the total magnetic moment of uranium compounds in general comes out too small.[47–51] Corrections which simulate Hund's second rule interactions in solids, describing orbital correlations absent in the homogeneous electron gas, such as the orbital polarization (OP), are needed to bring the magnetic moment into better agreement with experiment.[48–51] Interestingly, the fact that the OP is too small within the LSDA does not preclude a reasonable explanation of the MO Kerr spectrum. The same conclusion was also reached previously for UAsSe (Ref. 19) and U_3X_4 (X=P, As, Sb, and Bi) (Ref. 22) compounds.

5. SUMMARY

On the basis of the good agreement between experimental and theoretical MO characteristics we conclude that the U $5f$ electrons in the ternary $UCuP_2$ compound are essentially itinerant. However, the difference in the main peak position of the Kerr rotation and ellipticity spectra requires further investigation of the electron self-energies.

*E-mail: anton@caskad.imp.kiev.ua; Permanent address: Institute of Metal Physics, 36 Vernadsky Str., 252142 Kiev, Ukraine

[1] J. D. Becker, J. M. Wills, L. Cox, and B. R. Cooper, Phys. Rev. B **54**, 17265R (1996).
[2] L. M. Sandratskii and J. Kübler, Phys. Rev. B **55**, 11395 (1997).
[3] W. Reim and J. Schöenes, in *Ferromagnetic Materials*, E. P. Wohlfarth, and K. H. J. Buschow (Eds.), North-Holland, Amsterdam (1990), Vol. 5, p. 133.
[4] A. J. Freeman and D. D. Koelling, *The Actinides: Electronic Structure and Related Properties*, A. J. Freeman and J. E. Darby (Eds.), Academic Press, New York (1974), Vol. 1; E. Warren, E. Picket, A. J. Freeman, and D. D. Koelling, Phys. Rev. B **22**, 2965 (1980).
[5] B. Johansson, Phys. Rev. B **11**, 2740 (1975).
[6] H. I. Skriver, O. K. Andersen, and B. Johansson, Phys. Rev. Lett. **41**, 42 (1978); *ibid.* **44**, 1230 (1980).
[7] M. S. S. Brooks, J. Magn. Magn. Mater. **29**, 257 (1982); J. Phys. F: Met. Phys. **13**, 103 (1983).
[8] *Handbook of Physics and Chemistry of the Actinides*, edited by A. J. Freeman and G. H. Lander, North-Holland, Amsterdam (1984).
[9] J. Friedel, J. Phys. Chem. Solids **1**, 175 (1956).
[10] R. C. Albers, A. M. Boring, J. M. Wills, L. E. Cox, O. E. Eriksson, and N. E. Christensen, Phys. Rev. B **54**, 14405 (1996).
[11] V. N. Antonov, A. I. Bagljuk, A. Ya. Perlov, V. V. Nemoshkalenko, Vl. N. Antonov, O. K. Andersen, and O. Jepsen, Fiz. Nizk, Temp. **19**, 689, (1993) [Sov. J. Low Temp. Phys. **19**, 792 (1993)].
[12] T. Gasche, M. S. S. Brooks, and B. Johansson, Phys. Rev. B **54**, 2446 (1996).
[13] J. Kollar, L. Vitos, and H. L. Skriver, Phys. Rev. B **55**, 15353 (1997).
[14] P. Söderlind, J. M. Wills, B. Johansson, and O. Eriksson, Phys. Rev. B **55**, 1997 (1997).
[15] J. van Ek, P. A. Sterne, and A. Gonis, Phys. Rev. B **48**, 16280 (1993).
[16] W. Reim, J. Magn. Magn. Mater. **58**, 1 (1986).
[17] T. Kraft, P. M. Oppeneer, V. N. Antonov, and H. Eschrig, Phys. Rev. B **52**, 3561 (1995).
[18] B. R. Cooper, S. P. Lim, I. Avgin, Q. G. Sheng, and D. L. Price, J. Phys. Chem. Solids **56**, 1509 (1995).
[19] P. M. Oppeneer, M. S. S. Brooks, V. N. Antonov, T. Kraft, and H. Eschrig, Phys. Rev. B **53**, 10437R (1996).
[20] J. Köhler, L. M. Sandratskii, and J. Käber, Phys. Rev. B **55**, 10153R (1997).
[21] P. M. Oppeneer, V. N. Antonov, A. Ya. Perlov, A. N. Yaresko, T. Kraft, and H. Eschrig, Physica B **230–232**, 544 (1997).
[22] V. N. Antonov, B. N. Harmon, A. N. Yaresko, and A. Ya. Perlov, Phys. Rev. B **59**, 14571 (1999).
[23] W. H. Kleiner, Phys. Rev. **142**, 318 (1966).
[24] A. H. MacDonald and S. H. Vosko, J. Phys. C: Solid State Phys. **12**, 2977 (1979).
[25] H. Ebert, H. Freyer, A. Vernes, and G.-Y. Guo, Phys. Rev. B **53**, 7721 (1996).
[26] H. Ebert, Phys. Rev. B **38**, 9390 (1988).
[27] I. V. Solovyev, A. B. Shik, V. P. Antropov, A. I. Liechtenstein, V. A. Gubanov, and O. K. Andersen, Fiz. Tverd. Tela (Leningrad) **31**, 13, (1989) [Sov. Phys. Solid State **31**, 1285 (1989)].
[28] D. D. Koelling and B. N. Harmon, J. Phys. C: Solid State Phys. **10**, 3107 (1977).
[29] O. K. Andersen, Phys. Rev. B **12**, 3060 (1975).
[30] V. V. Nemoshkalenko, A. E. Krasovskii, V. N. Antonov, Vl. N. Antonov, U. Fleck, H. Wonn, and P. Ziesche, Phys. Status Solidi B **120**, 283 (1983).
[31] V. N. Antonov, A. Ya. Perlov, A. P. Shpak, and A. N. Yaresko, J. Magn. Magn. Mater. **146**, 205 (1995).
[32] V. V. Nemoshkalenko and V. N. Antonov, *Computational Methods in Solid State Physics*, Gordon and Breach, London (1998).
[33] J. Schoenes, in *Materials Science and Technology*, Vol. 3A: *Electronic and Magnetic Properties of Metals and Ceramics*, Verlag Chemie, Weinheim (1992), p. 147.
[34] R. Kubo, J. Phys. Soc. Jpn. **12**, 570 (1957).
[35] C. S. Wang and J. Callaway, Phys. Rev. B **9**, 4897 (1974).
[36] V. N. Antonov, A. I. Bagljuk, A. Ya. Perlov, V. V. Nemoshkalenko, Vl. N. Antonov, O. K. Andersen, and O. Jepsen, Fiz. Nizk. Temp. **19**, 689 (1993) [Low Temp. Phys. **19**, 494 (1993)]
[37] A. Santoni and F. J. Himpsel, Phys. Rev. B **43**, 1305 (1991).
[38] U. von Barth and L. A. Hedin, J. Phys. C: Solid State Phys. **5**, 1692 (1972).

[39] P. E. Blöchl, O. Jepsen, and O. K. Andersen, Phys. Rev. B **49**, 16223 (1994).
[40] P. Villars and L. D. Calvert, *Pearson's Handbook of Crystallographic Data for Intermetallic Phases*, ASM International, Materials Park (1991).
[41] Z. Zolnierek, D. Kaczorowski, and R. Troc, J. Less-Common Met. **128**, 265 (1987).
[42] Z. Zolnierek, H. Nöel, and D. Kaczorowski, J. Less-Common Met. **132**, 265 (1987).
[43] Z. Zolnierek, D. Kaczorowski, R. Troc, and H. Nöel, J. Less-Common Met. **121**, 193 (1986).
[44] D. Kaczowski, R. Troc, and H. Nöel, J. Phys.: Condens. Matter **3**, 4959 (1991).
[45] P. Fumagalli, J. Schöenes, and D. Kaczorowski, Solid State Commun. **65**, 173 (1988).
[46] H. Ikekame, K. Sato, K. Takanashi, and H. Fujimori, J. Appl. Phys. **32**, 284 (1993).
[47] M. S. S. Brooks and B. Johansson, in *Handbook of Magetic Mateials*, K. H. J. Buschow (Ed.), North-Holland, Amsterdam (1993), Vol. 7, p. 139.
[48] M. S. S. Brooks, Physica B **130**, 6 (1985).
[49] O. Eriksson, M. S. S. Brooks, and B. Johansson, Phys. Rev. B **41**, 7311 (1990).
[50] L. Severin, M. S. S. Brooks, and B. Johansson, Phys. Rev. Lett. **B71**, 3214 (1993).
[51] A. Mavromaras, L. Sandratskii, and J. Kübler, Solid State Commun. **106**, 115 (1998).

This article was published in English in the original Russian journal. Reproduced here with stylistic changes by the Translation Consultant.

EXITATIONS IN STRONGLY CORRELATED SYSTEMS

Electronic excitations and correlations in quantum bars

I. Kuzmenko, S. Gredeskul,* K. Kikoin, and Y. Avishai

Department of Physics, Ben-Gurion University of the Negev, P.O. Box 84105 Beer-Sheva, Israel
(Submitted February 1, 2002)
Fiz. Nizk. Temp. **28**, 752–762 (July 2002)

The spectrum of boson fields and two-point correlators are analyzed in a quantum bar system (a superlattice formed by two crossed interacting arrays of quantum wires), with a short-range interwire interaction. The standard bosonization procedure is shown to be valid, within the two-wave approximation. The system behaves as a sliding Luttinger liquid in the vicinity of the Γ point, but its spectral and correlation characteristics have either 1D or 2D nature depending on the direction of the wave vector in the rest of the Brillouin zone. Due to the interwire interaction, unperturbed states propagating along the two arrays of wires are always mixed, and the transverse components of the correlation functions do not vanish. This mixing is especially strong around the diagonals of the Brillouin zone, where the transverse correlators have the same order of magnitude as the longitudinal ones. [DOI: 10.1063/1.1496664]

1. INTRODUCTION

Diverse $D-1$ dimensional objects embedded in D-dimensional structures were recently investigated experimentally and analyzed theoretically. Rubbers and various percolation networks are examples of such disordered $D-1$ objects, whereas self-organized stripes in oxicuprates, manganites, nanotube ropes, and quantum Hall systems are examples of ordered (periodic) structures of this kind. In some cases, the effective dimensions of such structures may be intermediate, e.g., between $D=1$ and $D=2$. They are especially promising candidates for studying novel electronic correlation properties, which, in particular, are relevant for the search of Luttinger liquid (LL) fingerprints in two dimensions. This challenging idea is motivated by noticing some unusual properties of electrons in Cu-O planes in high-T_c materials.[1] However, the Fermi liquid state seems to be rather robust in two dimensions. In this respect, a 2D system of weakly coupled 1D quantum wires[2–4] looks promising. Indeed, a theoretical analysis of stable LL phases was recently presented for a system consisting of coupled parallel quantum wires[5–7] and for 3D stacks of sheets of such wires in parallel and crossed orientations.[8] In most of these cases, the interaction between the parallel quantum wires is assumed to be perfect along the wire,[8] whereas the interaction between the modes generated in different wires depends only on the interwire distance. Along these lines, generalization of the LL theory for quasi-2D (and even 3D) systems is reported in Ref. 8, where the interaction between two crossed arrays of parallel quantum wires forming some kind of a network depends on the distance between points belonging to different arrays. As a result, the grid of crossed arrays retains its LL properties for propagation along both subsets of parallel wires, whereas the cross-correlations remain nonsingular. This LL structure can be interpreted as a quantum analog of a classical sliding phases of coupled XY chains.[9] A special case of 2D grid where the crossed wires are coupled by tunneling interaction is considered in Refs. 4 and 10.

In the present paper, a different course is elaborated. We ask the question of whether it is possible to encode *both 1D and 2D electron liquid regimes in the same system within the same energy scale*. In order to unravel the pertinent physics we consider a grid with *a short-range capacitive interwire interaction*. This approximation might look shaky if applied for crossed stripe arrays in the cuprates. On the other hand, it seems natural for 2D grids of nanotubes[11,12] or artificially fabricated bars of quantum wires with grid periods $a_{1,2}$ which exceed the lattice spacing of a single wire or the diameter of a nanotube. It will be shown below that this interaction can be made effectively weak. Therefore, such a quantum bar (QB) retain the 1D LL character for the motion along the wires, similarly to the case considered in Ref. 8. At the same time, however, boson mode propagation along the diagonals of the grid is also feasible. This process is essentially a two-dimensional one, as are the shape of the Brillouin zone and equipotential surfaces in the reciprocal QB lattice.

Before developing the formalism, a few words about the main assumptions are in order. Our attention here is mainly focused on charge modes, so it is assumed that there is a gap for spin excitations. Next, we are mainly interested in electronic properties of QBs which are not related to simple charge instabilities like commensurate CDWs, so that the (for simplicity equal) periods $a_1=a_2=a$ are supposed to be incommensurate with the lattice spacing. The Brillouin zone (BZ) of the QB superlattice is two-dimensional, and the nature of excitations propagating in this BZ is determined by Bragg interference of modes with the superlattice wave vector. This interference (umklapp processes) is, of course destructive for LL excitations with both wave vector components close to multiple integers of $Q\equiv 2\pi/a$. However, in case of weak scattering, only two-wave interference pro-

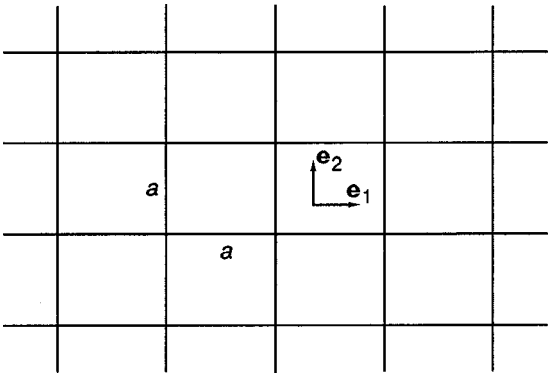

FIG. 1. Square quantum bars formed by two interacting arrays of parallel quantum wires. $\mathbf{e}_1$, $\mathbf{e}_2$ are the unit vectors of the superlattice.

cesses near the boundaries of the BZ are significant. One can then hope that the harmonic boson modes survive in the major part of the BZ, and that the Hamiltonian of the QB might still be diagonalized without losing the main characteristic features of the LL physics.

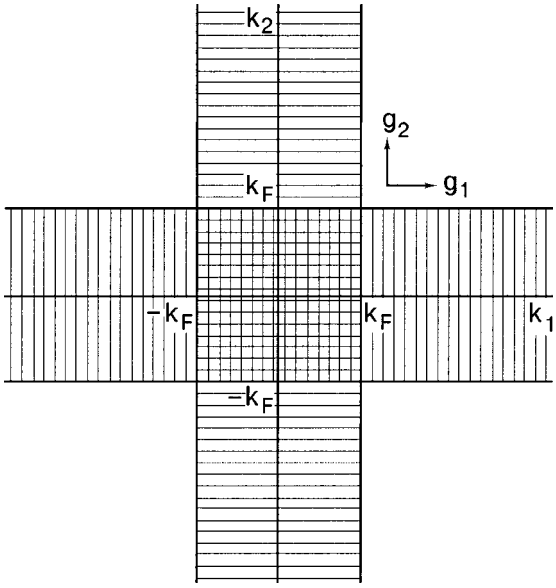

FIG. 2. Fermi surface of square metallic quantum bars in the absence of charge transfer between wires. $\mathbf{g}_1$, $\mathbf{g}_2$ are the unit vectors of the reciprocal superlattice.

2. QUANTUM BARS: BASIC NOTIONS

Quantum bars may be defined as a 2D periodic grid, i.e., two crossed periodic arrays of 1D quantum wires with a period $\mathbf{a}=(\mathrm{a}_1,\mathrm{a}_2)$. In fact these arrays are placed on two parallel planes separated by an interplane distance,[12] but in this section we consider QB as a genuine 2D system. The arrays are oriented along the unit vectors $\mathbf{e}_{1,2}$ with an angle φ between them. Here we consider a square grid ($\varphi=\pi/2$) formed by identical wires of length L with basis vectors $\mathbf{a}_j = a\mathbf{e}_j$, $j=1,2$ (Fig. 1). The interaction between the excitations in different wires is assumed to be concentrated near the crossing points with coordinates $n_1\mathbf{a}_1+n_2\mathbf{a}_2 \equiv(n_1a,n_2a)$. The integers n_j enumerate the wires within the jth array. Such interaction imposes a superperiodicity on the energy spectrum of initially one-dimensional quantum wires, and the eigenstates of this superlattice are characterized by a 2D quasimomentum $\mathbf{q}=q_1\mathbf{g}_1+q_2\mathbf{g}_2\equiv(q_1,q_2)$. Here $\mathbf{g}_{1,2}$ are the unit vectors of the reciprocal superlattice satisfying the standard orthogonality relations $(\mathbf{e}_i\cdot\mathbf{g}_j)=\delta_{ij}$. The corresponding basis vectors of the reciprocal superlattice have the form (m_1Q,m_2Q), where $Q=2\pi/a$ and $m_{1,2}$ are integers.

In conventional 2D systems, forbidden states in reciprocal space arise due to Bragg diffraction in a periodic potential, whereas the whole plane is allowed for wave propagation in real space, at least until the periodic potential is weak enough. In sharply anisotropic QBs most of the real space is forbidden for electron and plasmon propagation, whereas the Bragg conditions for the wave vectors are still the same as in conventional 2D plane modulated by a periodic potential. The excitation motion in QBs is one-dimensional in the major part of the 2D plane, and the anisotropy in real space imposes restrictions on the possible values of the 2D coordinates $\mathbf{x}=(x_1,x_2)$. At least one of them, e.g., x_2 should be an integer multiple of the interwire distance a, so that the coordinate $\mathbf{x}=(x_1,n_2a)$ characterizes the point with the 1D coordinate x_1 lying at the n_2th wire of the first array.

The 2D Brillouin zone of a QB is constructed as an extension of the 1D Brillouin zones of two crossed arrays and subsequent folding of this BZ in accordance with the square superstructure. However, one cannot resort to the standard basis of 2D plane waves when constructing the eigenstate with a given wave vector $\mathbf{k}$ in the BZ because of the kinematic restrictions mentioned above. Even in *noninteracting* arrays of quantum wires the 2D basis is formed as a superposition of two sets of 1D waves. The first of them is a set of 1D excitations propagating along *each* wire of the first array characterized by a unit vector $k_1\mathbf{e}_1$ with a phase shift ak_2 between adjacent wires. The second set is the similar manifold of excitations propagating along the wires of the second array with a wave vector $k_2\mathbf{e}_2$ and phase shift ak_2. The states of equal energy obtained by means of this procedure form straight lines in the 2D BZ. For example, the QB Fermi surface developed from the points $\pm k_F$ for an individual quantum wire consists of two sets of lines $|k_{1,2}| = k_F$. Accordingly, the Fermi sea is not a circle with radius k_F like in the case of free 2D gas, but a cross in the k plane bounded by these four lines[4] (see Fig. 2). Of course, these equipotential lines describe the 1D excitations in the BZ of a QB.

Due to weakness of the interwire interaction, the excitations in the 2D BZ depicted in Fig. 3 acquire genuine two-dimensionality characterized by the quasimomentum $\mathbf{q} =(\mathrm{q}_1,\mathrm{q}_2)$. However, in case of weak interaction the 2D waves constructed from the 1D plane waves in accordance with the above procedure form an appropriate basis for the description of elementary excitations in QB in close analogy with the nearly free electron approximation in conventional crystalline lattices. It is easily foreknown that the interwire interaction does not completely destroy the above quasimomentum classification of eigenstates, and the 2D reconstruction of the spectrum may be described in terms of wave mixing similarly to the standard Bragg diffraction in a weak periodic potential. Moreover, the classification of eigenstates of noninteracting crossed arrays of 1D wires (''empty superlattice'') may be effectively used for the classification of energy bands in a real QB superlattice. Our next step is to construct a complete 2D basis for this empty superlattice.

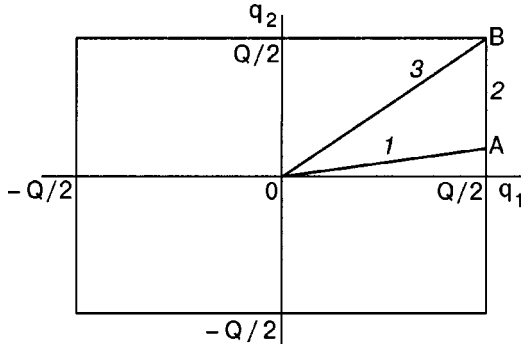

FIG. 3. Two dimensional Brillouin zone of a square QB. The three directions along which the dispersion of Bose excitations is calculated in Sec. 5 are marked by the indices *1, 2, 3*.

Due to LL nature of the excitations in a given wire, they are described as plane waves $L^{-1/2}\exp(ikx)$ with wave number k and initial dispersion law $\omega_0(k)=v|k|$. Each excitation in a corresponding ''empty superchain'' is described by its quasi-wavenumber q and the band number p ($p=1, 2,...$). Its wave function has the Bloch-type structure

$$\psi_{p,q}(x)=\frac{1}{\sqrt{L}}e^{iqx}u_{p,q}(x) \tag{1}$$

with the Bloch amplitude

$$u_{p,q}(x)=\sum_{n=-\infty}^{\infty}\frac{\sin\xi_n}{\xi_n}\times\cos[(2p-1)\xi_n]\exp\left(-4i\xi_n\frac{q}{Q}\right),$$

$$\xi_n=\frac{\pi}{2}\left(\frac{x}{a}-n\right).$$

The corresponding dispersion law $\omega_p(q)$ has the form

$$(vQ)^{-1}\omega_p(q)=\frac{2p-1}{4}+\sum_{n=1}^{\infty}\frac{2(-1)^p}{\pi^2(2n+1)^2}\cos\frac{2\pi(2n+1)}{Q}.$$

Within the first BZ of a superchain, $|q|\leqslant Q/2$, expressions for the Bloch amplitude and dispersion law are substantially simplified:

$$u_{p,q}(x)=\exp\left\{iQx(-1)^{p-1}\left[\frac{p}{2}\right]\operatorname{sgn}q\right\}, \tag{2}$$

$$\omega_p(q)=vQ\left(\left[\frac{p}{2}\right]+(-1)^{p-1}\frac{|q|}{Q}\right). \tag{3}$$

The 2D basis of periodic Bloch functions for an empty superlattice is constructed in terms of the 1D Bloch functions (1), (2):

$$\Psi_{p,q',\mathbf{q}}(\mathbf{r})=\psi_{p,q_1}(x_1)\psi_{p',q_2}(x_2). \tag{4}$$

Here p, $p'=1, 2,...$, are the band numbers and the 2D quasimomentum $\mathbf{q}=(q_1,q_2)$ belongs to the first BZ, $|q_j|\leqslant Q/2$. The corresponding eigenfrequencies are

$$\omega_{pp'}(\mathbf{q})=\omega_p(q_1)+\omega_{p'}(q_2). \tag{5}$$

We will use this basis in the next Section when constructing the excitation spectrum of QBs within the reduced band scheme.

3. HAMILTONIAN

The full Hamiltonian of the QBs is

$$H=H_1+H_2+H_{\text{int}}, \tag{6}$$

where H_j describes the 1D boson field in the jth array

$$H_1=\frac{\hbar v}{2}\sum_{n_2}\int_{-L/2}^{L/2}dx_1\left\{g\pi_1^2(x_1,n_2a)+\frac{1}{g}(\partial_{x_1}\theta_1(x_1,n_2a))^2\right\},$$

$$H_2=\frac{\hbar v}{2}\sum_{n_1}\int_{-L/2}^{L/2}dx_2\left\{g\pi_2^2(n_1a,x_2)+\frac{1}{g}(\partial_{x_2}\theta_2(n_1a,x_2))^2\right\},$$

and (θ_j,π_j) are the conventional canonically conjugate boson fields (see, e.g., Ref. 13). The Fermi velocities $v_{1,2}=v$ and the LL parameters $g_{1,2}=g$ are taken to be the same for both arrays. Generalization to the case of different parameters v_j, g_j, a_j is straightforward.

The interwire interaction results from a short-range contact capacitive coupling in the crosses of the bar,

$$H_{\text{int}}=\sum_{n_1,n_2}\int_{-L/2}^{L/2}dx_1dx_2V(x_1-n_1a,n_2a-x_2)\times\rho_1(x_1,n_2a)\rho_2(n_1a,x_2).$$

Here $\rho_i(\mathbf{r})$ are density operators, and $V(\mathbf{r}_1-\mathbf{r}_2)$ is a short-range interwire interaction. Physically, it represents the Coulomb interaction between charge fluctuations $e\varsigma(x/r_0)$, $\varsigma(0)=1$ around the points $\mathbf{r}_1=(x_1,n_2a)$ and $\mathbf{r}_2=(n_1a,x_2)$. The size of these fluctuations is determined by the screening radius r_0 within the wire. One may neglect the interwire tunneling and restrict oneself to the capacitive interaction only, provided the vertical distance between the wires d is substantially larger than the screening radius r_0. Therefore the interaction has the form

$$V(\mathbf{r})=\frac{V_0}{2}\Phi\left(\frac{x_1}{r_0},\frac{x_2}{r_0}\right),$$

where the function $\Phi(\xi_1,\xi_2)$ is

$$\Phi(\xi_1,\xi_2)=\frac{\varsigma(\xi_1)\varsigma(\xi_2)}{\sqrt{1+\left(\frac{r_0}{d}\right)^2(\xi_1^2+\xi_2^2)}}. \tag{7}$$

It is seen from these equations that $\Phi(\xi_1,\xi_2)$ is an even function of its arguments; it vanishes for $|\xi_{1,2}|\geqslant 1$ and is normalized by condition $\Phi(0,0)=1$. The effective coupling strength is

$$V_0=\frac{2e^2}{d}.$$

In terms of boson field operators θ_i, the interaction is written as

$$H_{\rm int}=V_0\sum_{n_1,n_2}\int_{-L/2}^{L/2}dx_1dx_2\Phi\left(\frac{x_1-n_1a}{r_0},\frac{n_2a-x_2}{r_0}\right)\times\partial_{x_1}\theta_1(x_1,\,n_2a)\partial_{x_2}\theta_2(n_2a,\,x_2).$$

In the quasimomentum representation (4), (1), (2) the full Hamiltonian (6) acquires the form

$$H=\frac{\hbar vg}{2a}\sum_{j=1}^{2}\sum_{p}\sum_{\mathbf{q}}\pi^{+}_{jp\mathbf{q}}\pi_{jp\mathbf{q}}+\frac{\hbar}{2vga}\sum_{jj'=1}^{2}\sum_{pp'}\sum_{\mathbf{q}}W_{jpj'p'\mathbf{q}}\theta^{+}_{jp\mathbf{q}}\theta_{j'p'\mathbf{q}} \tag{8}$$

with matrix elements for interwire coupling given by

$$W_{jpj'p'\mathbf{q}}=\omega_{jp\mathbf{q}}\omega_{j'p'\mathbf{q}}[\,\delta_{jj'}\delta_{pp'}+\phi_{jpj'p'\mathbf{q}}(1-\delta_{jj'})].$$

Here

$$\omega_{jp\mathbf{q}}\equiv\omega_p(q_j)=v\left(\left[\frac{p}{2}\right]Q+(-1)^{p+1}\left|q_j\right|\right) \tag{9}$$

are eigenfrequencies (3) of the ''unperturbed'' 1D mode pertaining to an array j, band p, and quasimomentum $q_j\mathbf{g}_j$. The coefficients

$$\phi_{jpj'p'\mathbf{q}}=\phi(-1)^{p+p'}\,\mathrm{sgn}(q_1q_2)\Phi_{jpj'p'\mathbf{q}}\phi=\frac{gV_0r_0^2}{\hbar va} \tag{10}$$

are proportional to the dimensionless Fourier component of the interaction strengths,

$$\Phi_{1p2p'\mathbf{q}}=\int d\xi_1d\xi_2\Phi(\xi_1,\xi_2)\mathrm{e}^{-ir_0(q_1\xi_1+q_2\xi_2)}\times u^{*}_{p,q_1}(r_0\xi_1)u^{*}_{p',q_2}(r_0\xi_2)=\Phi_{2p'1p\mathbf{q}}. \tag{11}$$

The Hamiltonian (8) describes a system of coupled harmonic oscillators, which can be exactly diagonalized with the help of a certain canonical linear transformation (note that it is already diagonal with respect to the quasimomentum $\mathbf{q}$). The diagonalization procedure is, nevertheless, rather cumbersome due to the mixing of states belonging to different bands and arrays. However, it will be shown below that the dimensionless interaction parameter ϕ (10) is effectively weak, and a perturbation approach is applicable.

4. MAIN APPROXIMATIONS

As was mentioned in the Introduction, we consider rarefied QBs with a short-range capacitive interaction. In the case of QBs formed by nanotubes, this is a Coulomb interaction screened at a distance of the order of the nanotube radius[14] R_0, and therefore $r_0\sim R_0$. The minimal radius of a single-wall carbon nanotube is about $R_0=0.35$–0.4 nm (see Ref. 15). The intertube vertical distance d in artificially produced nanotube networks is estimated as $d\approx 2$ nm.[12] Therefore the dimensionless interaction ϕ (10) can be estimated as

$$\phi\sim\sqrt{\varepsilon}\frac{R_0}{a}, \tag{12}$$

where

$$\sqrt{\varepsilon}=\frac{2R_0}{d}\frac{ge^2}{\hbar v}. \tag{13}$$

The first factor is about 0.35. The second one, which is nothing but the ''fine structure'' constant for the nanotube QBs, can be estimated as 0.9 (we used the values $d=1/3$ and $v=8\times10^7$ cm/s [Ref. 11]). Therefore ε is approximately equal to 0.1. The modulus of the matrix element (11) with the exponential form of $\zeta(\xi)=\exp(-|\xi|)$ does not exceed unity, so that the interaction (11) is really weak.

The smallness of dimensionless interaction ϕ enables one to apply perturbation theory. In this limit, the systematics of unperturbed levels and states is grossly conserved, at least in the low-energy region corresponding to the first few bands. This means that they should be described by the same quantum numbers (array number, band number, and quasimomentum). Indeed, as follows from the unperturbed dispersion law (9), the interband mixing is significant only along the high-symmetry directions in the first BZ (BZ boundaries and lines $g_i=0$). In the rest of the BZ this mixing can be taken into account perturbatively. The interarray mixing within the same energy band is strong for waves with quasimomenta close to the diagonal of the BZ. Away from the diagonal, it can also be calculated perturbatively.

For quasimomenta far from the BZ diagonals and high-symmetry directions, and in second order of perturbation theory, the above-mentioned canonical transformation results in the following renormalized field operators for the first array:

$$\tilde{\theta}_{1p\mathbf{q}}=\left(1-\frac{1}{2}\beta_{p\mathbf{q}}\right)\theta_{1p\mathbf{q}}+\sum_{p'}\phi_{pp'\mathbf{q}}\theta_{2p'\mathbf{q}}, \tag{14}$$

where

$$\phi_{pp'\mathbf{q}}=\frac{\phi_{1p2p'\mathbf{q}}\omega_{1p\mathbf{q}}\omega_{2p'\mathbf{q}}}{\omega^2_{1p\mathbf{q}}-\omega^2_{2p'\mathbf{q}}}$$

and

$$\beta_{p\mathbf{q}}=\sum_{p'}\phi^2_{pp'\mathbf{q}}. \tag{15}$$

Below, the specific values of these coefficients

$$\phi_{p\mathbf{q}}\equiv\phi_{1p\mathbf{q}}, \tag{16}$$

$$\phi_{\mathbf{q}}\equiv\phi_{1\mathbf{q}}\equiv\phi_{11\mathbf{q}}, \tag{17}$$

$$\beta'_{p\mathbf{q}}=\sum_{p'\neq p}\phi^2_{pp'\mathbf{q}} \tag{18}$$

will also be used. The renormalized eigenfrequencies for the first array are

$$\tilde{\omega}^2_{1p\mathbf{q}}=\omega^2_{1p\mathbf{q}}\left(1+\sum_{p'}\gamma_{pp'\mathbf{q}}\right), \tag{19}$$

where

$$\gamma_{pp'\mathbf{q}}=\frac{\phi^2_{1p2p'\mathbf{q}}\omega^2_{2p'\mathbf{q}}}{\omega^2_{1p\mathbf{q}}-\omega^2_{2p'\mathbf{q}}}.$$

Corresponding formulas for the second array are obtained by replacing $1p \to 2p$, and $1p' \to 2p'$.

Consider now the frequency correction in Eq. (19) more attentively. In the case under consideration, all terms in Eq. (19) are nonsingular. Then, away from the BZ boundary ($|\mathbf{q}| \ll Q/2$) the following estimate is valid:

$$\frac{\omega_{jp\mathbf{q}}^2}{\omega_{jp\mathbf{q}}^2 - \omega_{j'1\mathbf{q}}^2} \approx 1 + O\left(\frac{q_{j'}^2}{(pQ)^2}\right),$$

$$(j,j') = (1,2),(2,1); \quad p > 1.$$

Therefore, the correction term can be estimated approximately as $\omega_{11\mathbf{q}}^2 S_{\mathbf{q}}$, with

$$S_{\mathbf{q}} = \sum_p \phi_{112p\mathbf{q}}^2 = \varepsilon \frac{R_0^2}{a^2} \sum_p \Phi_{112p\mathbf{q}}^2. \tag{20}$$

Due to the short-range character of the interaction, the matrix elements $\Phi_{112p\mathbf{q}}$ vary slowly with band number, being of the order of unity for $p < p_{\max} \sim a/R_0$, and decrease rapidly for $p > p_{\max}$. Therefore, the right-hand side in Eq. (20) can roughly be estimated as

$$S_{\mathbf{q}} - \varepsilon \frac{R_0}{a} = 0.1 \frac{R_0}{a} \ll 1. \tag{21}$$

One should also remember that the energy spectrum of nanotube remains one-dimensional only for frequencies smaller than some ω_m. Therefore, an external cutoff arises at $p = ak_m$, where $k_m \sim \omega_m / v$. As a result, one gets the estimate

$$S_{\mathbf{q}} - \varepsilon \frac{R_0}{a} k_m R_0. \tag{22}$$

Hence, one could hope to gain here an additional power of the small interaction radius, but for nanotubes, k_m is of the order of $1/R_0$ (see Refs. 11 and 16) and the two estimates coincide.

For quasimomenta close to the BZ center, the coefficient $S_{\mathbf{q}}$ can be calculated exactly. Due to smoothness of the matrix elements $\phi_{112p\mathbf{q}}$ with respect to the band number p, the sum over p in Eq. (20) can be replaced by an integral over the extended BZ with wave vector $\mathbf{k}$ whose components are

$$k_j = a_j + \mathrm{sgn}(q_j)(-1)^{p_j+1}[p_j/2]Q. \tag{23}$$

For $|\mathbf{q}| \leqslant Q/2$ one gets $|S_{\mathbf{q}}| \leqslant |S_0|$, where

$$S_0 = \frac{\varepsilon R_0^2}{2\pi a} \int_{-\infty}^{\infty} dk \Phi^2(k)$$

and

$$\Phi(k) = \int d\xi_1 d\xi_2 \Phi(\xi_1, \xi_2) \mathrm{e}^{-ir_0 k \xi_2}.$$

Finally, one obtains

$$S_0 = \varepsilon \Phi_0^2 \frac{R_0}{a}, \tag{24}$$

where the constant

$$\Phi_0^2 = \int d\xi d\xi_1 d\xi_2 \Phi(\xi_1, \xi) \Phi(\xi_2, \xi)$$

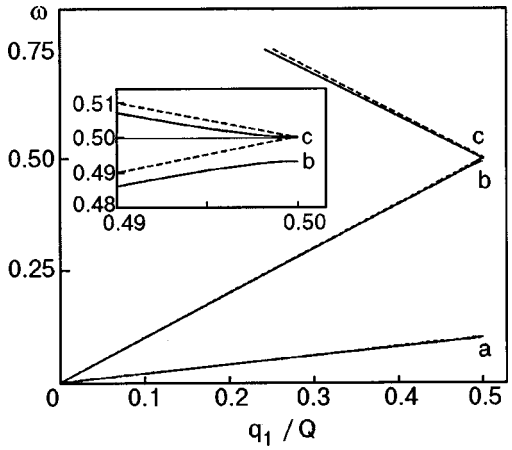

FIG. 4. The energy spectrum of QB (solid lines) and noninteracting arrays (dashed lines) for quasi-momenta at line *1* of Fig. 3 ($q_2 = 0.2q_1$). Points *a*, *b*, *c* on the figure correspond to the point *A* at the BZ boundary. Inset: Zoomed vicinity of the point $q_1/Q = 0.5$; $\omega = 0.5$.

for the exponential form of $\varsigma(\xi) \propto \exp(-|\xi|)$ is ≈ 1.5. As a result, instead of the preliminary estimate (21), we have

$$S_0 = 0.14 \frac{R_0}{a}.$$

Thus the correction term in Eq. (19) is in fact small.

5. ENERGY SPECTRUM

In the major part of the BZ, for quasimomenta $\mathbf{q}$ lying far from the diagonal, the spectrum is described by Eqs. (14), (19). Here each eigenstate (14) mostly conserves its initial systematics, i.e., belongs to a given array, and mostly depends on a given quasimomentum component. The corresponding dispersion laws (19) remain linear, being slightly modified near the BZ boundaries only. The main changes are therefore reduced to a renormalization of the plasmon velocity. In Fig. 4 the dispersion curves, corresponding to quasimomenta varying along line *1* of Fig. 3, are plotted in comparison with those for noninteracting arrays. (In all figures within this Section we use the units $\hbar = Q = v = 1$.) In what follows we use the (j,p) notation for the unperturbed boson propagating along the jth array in the pth band. Then the lowest curve in Fig. 4 is, in fact, the slightly renormalized dispersion of a (2,1) boson, the middle curve describes a (1,1) boson, and the upper curve is the dispersion of a (1,2) boson. The fourth frequency, corresponding to a (2,2) boson, is far above and is not displayed in the figure. It is seen that the dispersion remains linear along the whole line *1* except in the nearest vicinity of the BZ boundary (see inset in Fig. 4).

The interband hybridization gap for the bosons propagating along the first array can be estimated as

$$\Delta\omega_{12} \sim vQ\varepsilon \frac{r_0}{a}.$$

Similar gaps exist near the boundary of the BZ for each odd and next even energy band, as well as for each even and next odd band near the lines $q_1 = 0$ or $q_2 = 0$. The energy gap between the pth and $(p+1)$-th bands is estimated as

$$\Delta\omega_{p,p+1} \sim vQ\varepsilon \frac{r_0}{a} o(p^{-1}).$$

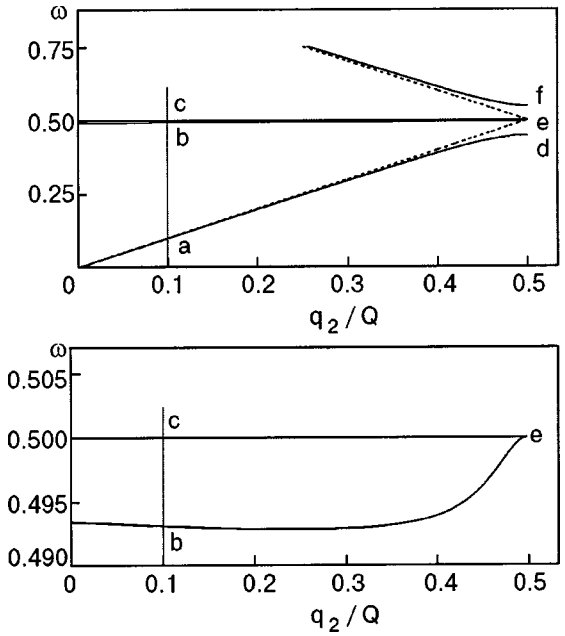

FIG. 5. Upper panel: The energy spectrum of QB (solid lines) and noninteracting arrays (dashed lines) for quasi-momenta at the BZ boundary (line *2* in Fig. 3). Points *d*, *e*, *f* in the figure correspond to the corner *B* of the BZ. Lower panel: Zoomed vicinity of the line $\omega=0.5$.

For large enough band number p interaction is effectively suppressed, $\phi_{1p2p'}\to 0$, and the gaps vanish.

Dispersion curves corresponding to quasi-momenta lying at the BZ boundary $q_1=Q/2$, $0\leqslant q_2\leqslant Q/2$ (line *2* in Fig. 3), are displayed in Fig. 5. Again, the dispersion laws are nearly linear, and deviations from linearity are observed only near the corner of the BZ. The lowest curve describes the dispersion of the (2,1) wave. Its counterpart in the second band (2,2) is described by the highest curve in the figure. In the zero the approximation, two modes $(j,1)$ propagating along the first array are degenerate with unperturbed frequency $\omega=0.5$. The interaction lifts the degeneracy. The lowest of two middle curves corresponds to the $(1,u)$ boson, and the upper of them describes the $(1,g)$ boson. Here the indices *g*, *u* denote a boson parity with respect to the transposition of the band numbers. Note that the $(1,g)$ boson exactly conserves its unperturbed frequency $\omega=0.5$. The latter fact is related to the square symmetry of the QBs. The points *a*, *b*, *c* in Figs. 4 and 5 are the same.

Now consider the dispersion of modes with quasimomenta on line *3* in Fig. 3. We start with $\mathbf{q}$ not too close to the BZ corner $q_1=q_2=Q/2$. In this case, the initial frequencies of modes belonging to the same band coincide, $\omega_{1p\mathbf{q}}=\omega_{2p\mathbf{q}}\equiv\omega_{p\mathbf{q}}$. Therefore the modes are strongly mixed:

$$\tilde{\theta}_{gp\mathbf{q}}=\frac{1}{\sqrt{2}}\left(1-\frac{1}{2}\beta_{p\mathbf{q}}\right)(\theta_{2p\mathbf{q}}+\theta_{1p\mathbf{q}})$$

$$-\frac{1}{\sqrt{2}}\sum_{p'\neq p}(\phi_{p'p\mathbf{q}}\theta_{1p'\mathbf{q}}-\phi_{pp'\mathbf{q}}\theta_{2p'\mathbf{q}}), \tag{25}$$

$$\tilde{\theta}_{up\mathbf{q}}=\frac{1}{\sqrt{2}}\left(1-\frac{1}{2}\beta_{p\mathbf{q}}\right)(\theta_{2p\mathbf{q}}-\theta_{1p\mathbf{q}})$$

$$-\frac{1}{\sqrt{2}}\sum_{p'\neq p}(\phi_{p'p\mathbf{q}}\theta_{1p'\mathbf{q}}+\phi_{pp'\mathbf{q}}\theta_{2p'\mathbf{q}}). \tag{26}$$

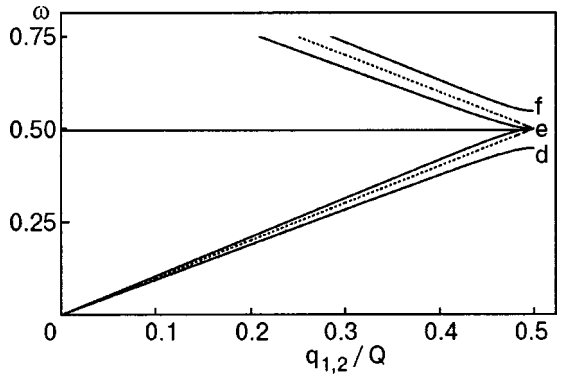

FIG. 6. The energy spectrum of QB (solid lines) and noninteracting arrays (dashed lines) for quasi-momenta on the diagonal of the BZ (line *3* in Fig. 3). Points *d*, *e*, *f* in the figure correspond to corner *B* of the BZ.

The corresponding eigenfrequencies are shifted from their bare values

$$\tilde{\omega}^2_{gp\mathbf{q}}=\omega^2_{p\mathbf{q}}\left[1+\phi_{1p2p\mathbf{q}}+\sum_{p'\neq p}\gamma_{pp'\mathbf{q}}\right], \tag{27}$$

$$\tilde{\omega}^2_{up\mathbf{q}}=\omega^2_{p\mathbf{q}}\left[1-\phi_{1p2p\mathbf{q}}+\sum_{p'\neq p}\gamma_{pp'\mathbf{q}}\right]. \tag{28}$$

In zeroth order of perturbation theory, the modes (25), (26) have a definite *j*-parity with respect to transposition of array numbers $j=1, 2$. Due to the repulsive character of the interaction, the odd modes (u,p), $p=1, 2$, (26) correspond to lower frequencies (28) and the even modes (g,p) (25) correspond to the higher ones (27). The dispersion curves at the BZ diagonal are displayed in Fig. 6. The points *d*, *e*, and *f* in Fig. 6 are the same as in the Fig. 5.

At the BZ corner $q_1=q_2=Q/2$ all four initial modes in the zeroth approximation are degenerate and have also a definite *p*-parity with respect to transposition of band numbers $p=1, 2$. The interwire interaction partially lifts the degeneracy. In zeroth-order approximation, the lowest frequency corresponds to a (g,u) boson, symmetric with respect to transposition of the array numbers, but antisymmetric with respect to the transposition of band numbers. The upper curve describes a (u,u) boson with odd *j*-parity and *p*-parity. Degeneracy of two middle modes with even band parity, (g,g) and (u,g) bosons, is provided by the symmetry of interaction in a square superlattice (7). Note once more that their frequency equals to its unperturbed value $\omega=0.5$.

All these results show that the quantum states of the 2D quantum bar conserve the quasi-1D character of the Luttinger-like liquid in the major part of momentum space, and that the 2D effects can be successfully calculated within the framework of perturbation theory. However, bosons with quasimomenta close to the diagonal of the first BZ are strongly mixed bare 1D bosons. These excitations are essentially two-dimensional, and therefore the lines of equal energy in this part of BZ are modified by the 2D interaction (see Fig. 7). It is clearly seen that deviations from linearity occur only in a small part of the BZ. The crossover from LL to FL behavior around isolated points of the BZ due to a single-particle hybridization (tunneling) for Fermi excita-

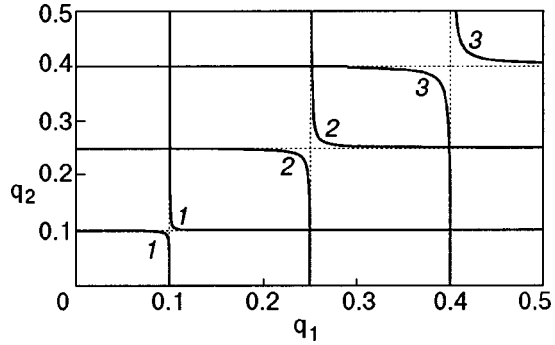

FIG. 7. The lines of equal frequency for QB (solid lines) and noninteracting arrays (dashed lines). Lines *1*, *2*, *3* correspond to the frequencies $\omega_1=0.1$, $\omega_2=0.25$, $\omega_3=0.4$.

tions was noticed in Refs. 4 and 10, where a mesh of horizontal and vertical stripes in superconducting cuprates was studied.

6. CORRELATIONS AND OBSERVABLES

The structure of the energy spectrum analyzed above predetermines optical and transport properties of the QBs. Let us consider an ac conductivity whose spectral properties are given by a current-current correlator

$$\sigma_{jj'}(\mathbf{q},\omega)=\sigma'_{jj'}(\mathbf{q},\omega)+i\sigma''_{jj'}(\mathbf{q},\omega)$$
$$=\frac{1}{\omega}\int_0^\infty dt e^{i\omega t}\langle[J_{j1\mathbf{q}}(t),J^\dagger_{j'1\mathbf{q}}(0)]\rangle.$$

Here $J_{jp\mathbf{q}}=\sqrt{2}vg\pi_{jp\mathbf{q}}$ is a current operator of the jth array. For simplicity we restrict ourselves to the first band. For noninteracting wires, the current-current correlator is reduced to the conventional LL expression,[17]

$$\langle[J_{j1\mathbf{q}}(t),J^\dagger_{j'1\mathbf{q}}(0)]\rangle_0=-2ivg\omega_{j1\mathbf{q}}\sin(\omega_{j1\mathbf{q}}t)\delta_{jj'}$$

with metallic Drude peak

$$\sigma'_{jj'}(\mathbf{q},\omega>0)=\pi vg\,\delta(\omega-\omega_{j1\mathbf{q}})\delta_{jj'}. \tag{29}$$

The corresponding imaginary part contains a single pole at the resonance frequency $\omega_{j1\mathbf{q}}$,

$$\sigma'_{jj'}(\mathbf{q},\omega>0)=\frac{2vg\omega^2_{jp\mathbf{q}}}{\omega(\omega^2-\omega^2_{jp\mathbf{q}})}\delta_{jj'}.$$

For interacting wires, where $\phi_{jpj'p'\mathbf{q}}\neq 0$, the correlators may easily be calculated after diagonalization of the Hamiltonian (8) by the transformations (14) for $\mathbf{q}$ off the diagonal of the first BZ, or by the transformations (25) and (26) for $\mathbf{q}$ lying on the diagonal of the BZ.

Consider first the quasi-momenta $\mathbf{q}$ lying far from the diagonal of the first BZ. In this case, the transformations for the field momenta can be obtained in a similar manner to the transformations (14) for the field coordinates. As a result, one has:

$$\langle[J_{11\mathbf{q}}(t),J^\dagger_{11\mathbf{q}}(0)]\rangle=-2ivg(1-\beta_{1\mathbf{q}})\tilde\omega_{11\mathbf{q}}\sin(\tilde\omega_{11\mathbf{q}}t)$$
$$-2ivg\sum_p\phi^2_{p\mathbf{q}}\tilde\omega_{2p\mathbf{q}}\sin(\tilde\omega_{2p\mathbf{q}}t),$$

$$\langle[J_{11\mathbf{q}}(t),J^\dagger_{21\mathbf{q}}(0)]\rangle=-2ivg\phi_{\mathbf{q}}$$
$$\times[\tilde\omega_{11\mathbf{q}}\sin(\tilde\omega_{11\mathbf{q}}t)-\tilde\omega_{21\mathbf{q}}\sin(\tilde\omega_{21\mathbf{q}}t)],$$

where $\beta_{p\mathbf{q}}$, $\phi_{p\mathbf{q}}$ and $\phi_{\mathbf{q}}$ are defined in Eqs. (15), (17), (18). Then, for the optical absorption σ' one obtains

$$\sigma'_{11}(\mathbf{q},\omega)=\pi vg(1-\beta_{1\mathbf{q}})\delta(\omega-\tilde\omega_{11\mathbf{q}})$$
$$+\pi vg\sum_p\phi^2_{p\mathbf{q}}\delta(\omega-\tilde\omega_{2p\mathbf{q}}), \tag{30}$$

$$\sigma'_{12}(\mathbf{q},\omega)=\pi vg\,\phi_{\mathbf{q}}[\delta(\omega-\tilde\omega_{11\mathbf{q}})-\delta(\omega-\tilde\omega_{21\mathbf{q}})]. \tag{31}$$

The longitudinal optical absorption (30) (i.e. the conductivity within a given set of wires) has its main peak at frequency $\tilde\omega_{11\mathbf{q}}\approx v|q_1|$, corresponding to the first band of the pertinent array, and an additional weak peak at the frequency $\tilde\omega_{21\mathbf{q}}\approx v|q_2|$, corresponding to the first band of a complementary array. It contains also a set of weak peaks at frequencies $\tilde\omega_{2p\mathbf{q}}\approx[p/2]\ vQ$ ($p=2,3,...$) corresponding to the contribution from the higher bands of the complementary array. At the same time, a second observable becomes relevant, namely, the transverse optical conductivity (31). It is proportional to the interaction strength and has two peaks at frequencies $\tilde\omega_{11\mathbf{q}}$ and $\tilde\omega_{21\mathbf{q}}$ in the first bands of both sets of wires. For $|\mathbf{q}|\to 0$ Eq. (30) reduces to that for an array of noninteracting wires (29), and the transverse optical conductivity (31) vanishes.

In the case when the quasi-momenta $\mathbf{q}$ belong to the diagonal of the first BZ, the transformations for the field momenta are similar in form to Eqs. (25) and (26). The current-current correlation functions have the form

$$\langle[J_{11\mathbf{q}}(t),J^\dagger_{11\mathbf{q}}(0)]\rangle=-ivg(1-\beta'_{1\mathbf{q}})$$
$$\times[\tilde\omega_{g1\mathbf{q}}\sin(\tilde\omega_{g1\mathbf{q}}t)+\tilde\omega_{u1\mathbf{q}}\sin(\tilde\omega_{u1\mathbf{q}}t)]$$
$$-ivg\sum_{p\neq 1}\phi^2_{p\mathbf{q}}\tilde\omega_{p\mathbf{q}}\sin(\tilde\omega_{p\mathbf{q}}t),$$

$$\langle[J_{1\mathbf{q}}(t),J^\dagger_{2\mathbf{q}}(0)]\rangle=-ivg[\tilde\omega_{g1\mathbf{q}}\sin(\tilde\omega_{g1\mathbf{q}}t)$$
$$-\tilde\omega_{u1\mathbf{q}}\sin(\tilde\omega_{u1\mathbf{q}}t)]$$

with $\omega_{p\mathbf{q}}$ and $\beta'_{p\mathbf{q}}$ defined by Eqs. (3), (18), and the optical conductivity is estimated as

$$\sigma'_{11}(\mathbf{q},\omega>0)=\frac{\pi vg}{2}(1-\beta'_{1\mathbf{q}})\Big[\delta(\omega-\tilde\omega_{q1\mathbf{q}})+\delta(\omega-\tilde\omega_{u1\mathbf{q}})$$
$$+\pi vg\sum_{p\neq 1}\phi^2_{p\mathbf{q}}\delta(\omega-\omega_{p\mathbf{q}}), \tag{32}$$

$$\sigma'_{12}(\mathbf{q},\omega>0)=\frac{\pi vg}{2}[\delta(\omega-\tilde\omega_{q1\mathbf{q}})-\delta(\omega-\tilde\omega_{u1\mathbf{q}})]. \tag{33}$$

The longitudinal optical conductivity (32) has a split double peak at frequencies $\tilde\omega_{11\mathbf{q}}$ and $\tilde\omega_{21\mathbf{q}}$, instead of a single peak. Again, a series of weak peaks occurs at frequencies $\omega_{p\mathbf{q}}$ corresponding to contributions from higher bands $p=2$, 3, 4,... . The transverse optical conductivity (33), similarly to the nondiagonal case (31), has a split double peak at frequencies $\tilde\omega_{11\mathbf{q}}$ and $\tilde\omega_{21\mathbf{q}}$.

The imaginary part of the ac conductivity $\sigma''_{jj'}(\mathbf{q},\omega)$ is calculated within the same approach. Its longitudinal component for $\mathbf{q}$ far from the BZ diagonal equals

$$\sigma''_{11}(\mathbf{q},\omega)=2vg\,\frac{\omega_{11\mathbf{q}}^2}{\omega}\left[\frac{1-\beta_{1\mathbf{q}}}{\omega^2-\tilde{\omega}_{11\mathbf{q}}^2}+\sum_p\frac{\phi_{p\mathbf{q}}^2}{\omega^2-\tilde{\omega}_{2p\mathbf{q}}^2}\right].$$

Beside the standard pole at zero frequency and the main pole at the resonance frequency $\omega_{11\mathbf{q}}$, the real part has an additional series of high-band satellites. The corresponding expression for $\sigma''_{22}(\mathbf{q},\omega)$ can be obtained after the replacement $1\leftrightarrow 2$. For quasi-momenta at the diagonal, the longitudinal optical absorption is

$$\sigma''_{11}(\mathbf{q},\omega)=(1-\beta_{1\mathbf{q}})\,\frac{vg}{\omega}\left[\frac{\tilde{\omega}_{g1\mathbf{q}}^2}{\omega^2-\tilde{\omega}_{g1\mathbf{q}}^2}+\frac{\tilde{\omega}_{u1\mathbf{q}}^2}{\omega^2-\tilde{\omega}_{u1\mathbf{q}}^2}\right]$$
$$+2vg\,\frac{\omega_{1\mathbf{q}}^2}{\omega}\sum_{p=1}^{\infty}\frac{\phi_{p\mathbf{q}}^2}{\omega^2-\omega_{p\mathbf{q}}^2}.$$

It contains two main poles similar to two peaks in the optical conductivity, and the series of poles contributed by the higher bands. The transverse component of the imaginary part of the ac conductivity has the same form for any $\mathbf{q}$:

$$\sigma''_{12}(\mathbf{q},\omega)=2vg\,\phi_{\mathbf{q}}\omega\left[\frac{1}{\omega^2-\tilde{\omega}_{u1\mathbf{q}}^2}-\frac{1}{\omega^2-\tilde{\omega}_{g1\mathbf{q}}^2}\right].$$

It always contains two poles and vanishes for noninteracting wires.

One of the main effects specific for a QB is the appearance of a nonzero transverse momentum-momentum correlation function. In space-time coordinates $(\mathbf{x},t)$ its representation reads

$$G_{12}(\mathbf{x},t)=\langle[\pi_1(x_1,0;t),\pi_2(0,x_2;0)]\rangle. \tag{34}$$

This function describes the momentum response at the point $(0,x_2)$ of the second array at the moment t caused by initial $(t=0)$ perturbation at the point $(x_1,0)$ of the first array. Standard calculations similar to those described above lead to the following expression:

$$G_{12}(\mathbf{x},t)=-i\,\frac{V_0r_0^2}{4\pi^2\hbar v}\int_{-\infty}^{+\infty}dk_1dk_2\Phi_{k_1k_2}$$
$$\times\sin(k_1x_1)\sin(k_2x_2)$$
$$\times\frac{k_2\sin(k_2vt)-k_1\sin(k_1vt)}{k_2^2-k_1^2}. \tag{35}$$

Here $\Phi_{k_1k_2}$ is defined by Eq. (11) with $p=p_1$, $p'=p_2$, and $k_{1,2}$ from Eq. (23).

This correlator is shown in Fig. 8. Here the nonzero response corresponds to the line determined by the obvious kinematic condition $|x_1|+|x_2|=vt$. The finiteness of the interaction radius slightly spreads this peak and changes its profile.

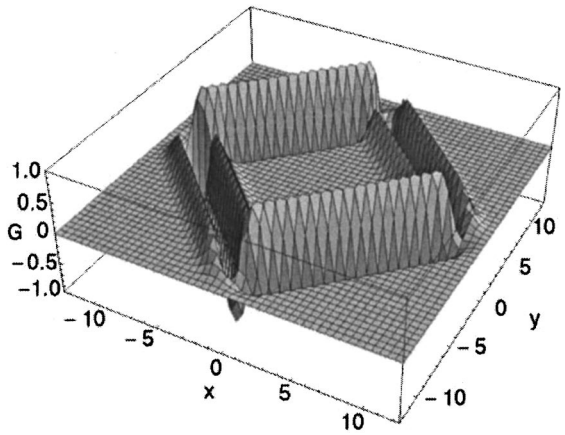

FIG. 8. The transverse correlation function $G_{12}(x_1,x_2;t)$ for $r_0=1$ and $vt=10$.

7. CONCLUSION

In conclusion, we have demonstrated that the energy spectrum of QBs shows the characteristic properties of LL at $|q|$, $\omega\to 0$, but at finite $\mathbf{q}$, the density and momentum waves may have either 1D or 2D character depending on the direction of the wave vector. Due to an interwire interaction, unperturbed states propagating along the two arrays are always mixed, and the transverse components of the correlation functions do not vanish. For quasimomentum lying on the diagonal of the BZ, such mixing is strong, and the transverse correlators have the same order of magnitude as the longitudinal ones.

S.G. and K.K. are indebted to L. Gorelik, M. Jonson, I. Krive, and R. Shekhter for helpful discussions. They also thank Chalmers Technical University, where this work was started, for hospitality and support. This research is supported in part by grants from the Israel Science foundations, the DIP German–Israel cooperation program, and the USA–Israel BSF program. S.G. is happy to see this paper published in the special issue devoted to the Jubilee of his old friend and colleague, Academician Victor Eremenko.

*E-mail: sergeyg@bgumail.bgu.ac.il

[1] P. W. Anderson, Science **235**, 1196 (1987).
[2] J. E. Avron, A. Raveh, and B. Zur, Rev. Mod. Phys. **60**, 873 (1988).
[3] Y. Avishai and J. M. Luck, Phys. Rev. B **45**, 1074 (1992).
[4] F. Guinea and G. Zimanyi, Phys. Rev. B **47**, 501 (1993).
[5] V. Emery, E. Fradkin, S. A. Kivelson, and T. C. Lubensky, Phys. Rev. Lett. **85**, 2160 (2000).
[6] A. Vishwanath and D. Carpentier, Phys. Rev. Lett. **86**, 676 (2001).
[7] J. Silva-Valencia, E. Miranda, and R. R. dos Santos, cond-mat/0107114.
[8] R. Mukhopadhyay, C. L. Kane, and T. C. Lubensky, Phys. Rev. B **63**, 081103(R) (2001); cond-mat/0102163.
[9] C. S. Hern, T. C. Lubensky, and J. Toner, Phys. Rev. Lett. **83**, 2745 (1999).
[10] A. H. Castro Neto and F. Guinea, Phys. Rev. Lett. **80**, 4040 (1998).
[11] R. Egger, A. Bachtold, M. S. Fuhrer, M. Bockrath, D. H. Cobden, and P. L. McEuen, cond-mat/0008008.
[12] T. Rueckes, K. Kim, E. Joselevich, G. Y. Tseng, C.-L. Cheung, and C. M. Lieber, Science **289**, 94 (2000).
[13] J. von Delft and H. Schoeller, Ann. Physik **7**, 225 (1998).
[14] K. Sasaki, cond-mat/0112178.
[15] S. G. Louie, in *Carbon Nanotubes*, M. S. Dresselhaus, G. Dresselhaus, and Ph. Avouris (Eds.), Topics Appl. Phys. **80**, 113 (2001), Springer, Berlin (2001).
[16] H. Ajiki and T. Ando, J. Phys. Soc. Jpn. **65**, 505 (1996).
[17] J. Voit, Rep. Prog. Phys. **58**, 977 (1994).

This article was published in English in the original Russian journal. Reproduced here with stylistic changes by the Translation Consultant.

Influence of dissipation on a low-voltage dc current in a long SNS junction

S. I. Kulinich

Department of Applied Physics, Chalmers University of Technology and Göteborg University, SE-412 96 Göteborg, Sweden; B. Verkin Institute for Low Temperature Physics and Engineering of the National Academy of Sciences of Ukraine, 47 Lenin Ave., Kharkov 61103, Ukraine

R. I. Shekhter[a)]

Dept. of Applied Physics, Chalmers University of Technology and Göteborg University, SE-412 96 Göteborg, Sweden

(Submitted April 19, 2002)
Fiz. Nizk. Temp. **28**, 763–767 (July 2002)

The dc current through a voltage-biased long transparent SNS junction in a dissipative regime is considered. The problem under certain conditions is mapped onto exactly solvable model of energy pumping into a quasiballistic 1D quantum ring driven by time-dependent magnetic flux. A rich peak-like structure of the subgap current at low voltages is predicted. The maxima in the current correspond to resonant energy absorption for fractional values of the normalized bias voltage. © *2002 American Institute of Physics.* [DOI: 10.1063/1.1496665]

INTRODUCTION

The nonequilibrium properties of mesoscopic conducting systems differ significantly from those in bulk materials. The reason is the dominant role of quantum coherent dynamics which develops on a time scale, shorter than the relaxation times in the system. As a result, quantum interference phenomena crucially affect the nonlinear kinetics of mesoscopic conductors (see, e.g., Ref. 1).

Nonsuperconducting mesoscopic structures have been shown to be extremely sensitive to external electromagnetic field, producing giant mesoscopic fluctuations of the conductance.[2] Mesoscopic rings placed in a time-dependent magnetic flux are characterized by strong resonant selection in the microwave power absorbed (fractional pumping of mesoscopic rings[3]). The origin of all of the above effects is quantum interference between different paths of dynamical evolution of electrons driven by external fields.

Superconducting nanostructures in which quantum coherence is a ''macroscopic'' feature of large numbers of electrons should reveal nonequilibrium coherent dynamics in an even more pronounced way. Energy dissipation in mesoscopic superconducting weak links is an example of phase coherence nonequilibrium phenomenon in superconducting mesoscopics.

In the present paper we will consider the effect of fractional dissipation of electric power in voltage-biased long ballistic SNS structures. Andreev levels representing the energy spectrum in a long SNS transparent junction are shown in Fig. 1. If a small voltage $eV \ll \hbar v_F/L$ is applied (v_F is the Fermi velocity, L is the junction length), the quantum evolution of Andreev states can be represented as a motion along the lines of Fig. 1 which is interrupted by scattering events in the vicinity of the crossing points. This scattering splits the trajectory and results in the appearance of a number of alternative quantum paths for the displacement of the system in energy space. The interference of such paths ends at the moment of time when relaxation stops the dynamical pumping of the system.

Two different scenarios of dynamical evolution of quasiparticles in a normal region are possible depending on the intensity of energy relaxation. In the weak dissipation limit the dynamical drift along the energy lines eventually brings the system out of the energy gap. The dissipation of energy takes place in the leads (bulk superconductors) far from the junction. This scenario corresponds to the now traditional picture of current formation by multiple Andreev reflections (MAR).[4–6] In contrast, in the strong dissipation limit (which is effectively always the case at $V \to 0$) the coherent dynamical evolution is interrupted by relaxation, preventing quasiparticles from leaving the gap region. This is the case where power emission is localized within a weak link and the formation of current is totally due to quantized Andreev states. This is the case we will consider below.

The interference pattern for energy absorption will be

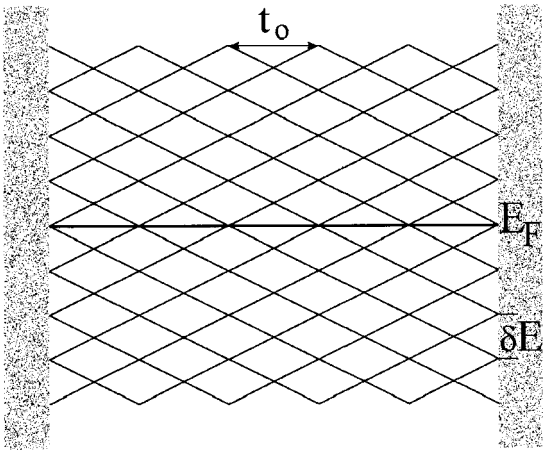

FIG. 1. The set of Andreev levels, $E_n^{\pm}$, as a function of time t in a long ballistic SNS junction. δE is a level spacing, t_0 is a ''quasiperiod'' in the problem.

sensitive to commensurability between the typical time of interscattering dynamics $t_0 \sim \hbar/eV$ and the periods $t_A \sim \hbar/\delta E$ (δE is the level spacing) characterizing the dynamics of quantized Andreev states. Since the absorbed power W directly determines the average current I in the system, the above interference should produce nonmonotonic $I-V$ characteristics with the peaks corresponding to maxima of the resonant absorption, $t_0/t_A = p/q$ (p,q are integers). The calculation of "fractional structure" of $I-V$ characteristics is the subject of the present work.

THE AVERAGE ABSORPTION ENERGY

We begin with the description of a set of bound states in a single-mode SNS junction. The energies of Andreev levels, E_n^{σ}, as a function of the phase difference $\varphi = \varphi_R - \varphi_L$ between the two superconductors are found from the transcendental equation[7]

$$\frac{E_n^{(\sigma)}}{\delta E} - \sigma\frac{\varphi}{2\pi} = n + \frac{1}{\pi}\arccos\frac{E_n^{(\sigma)}}{\Delta}, \tag{1}$$

where $\delta E = \pi\hbar v_F/L$ is the level spacing, $n = 0, \pm 1, \pm 2, \ldots$, and $\sigma = \pm 1$. In a long ($L \gg \xi_0, \xi_0$ is the coherence length) junction the spectrum Eq. (1) for $E \ll \Delta$ (Δ is the modulus of the order parameter) is reduced to a set of equidistant levels that depend linearly on φ:

$$\frac{E_n^{(\pm)}}{\delta E} = n + \frac{\pi \pm \varphi}{2\pi}. \tag{2}$$

The terms cross at points $\varphi_p = \pi p$ (p is the integer). This degeneracy is lifted in the presence of normal scattering in the junction. We will model the normal scattering by a weak point-like impurity ($U_0 \ll \delta E$, U_0 is the impurity potential) placed at one of the interfaces (asymmetric junction). In this case the gaps Δ_n that are opened at the degeneracy points are small and n-independent, $\Delta_n \simeq U_0$.

For a voltage-biased junction the phase difference φ according to the Josephson relation ($\dot{\varphi} = 2eV/\hbar$) depends linearly on time, and the problem becomes nonstationary and nonequilibrium. It can be reformulated as a transport problem in energy space, where in the general situation both the bound ($E < \Delta$) and the scattering ($E > \Delta$) states contribute to the dc current. We will consider a long ballistic SNS junction in a dissipative regime, that is, in the case when dissipation influences the dynamics of quasiparticles in the normal region. In the presence of dissipation the maximum energy gained by quasiparticles in the normal region can be much smaller than Δ. In this case only the bound states in a small strip around E_F are involved in dynamical processes, and their spectrum can be approximated as a linear one, Eq. (2). Thus, our problem is reduced to a transport problem on a set of equidistant Andreev levels (see Fig. 1).

It is evident that for a not fully transparent junction the dc current will be zero if one neglects the interlevel tunneling. So, to get finite current we have to consider electron transitions between the levels. If the ballistic time $t_0/2$ of electron motion between the transition points, $t_0 = \pi\hbar/eV$, is much larger than the characteristic scattering time $t_s \sim \hbar/U_0$, the interlevel transitions will take place mostly in the vicinity of degeneracy points, where the interlevel spacing is the smallest ($\sim U_0$). Therefore, at low voltages $eV \ll U_0 \ll \delta E$ the dynamics of quasiparticles in energy space on a set of Andreev levels can be represented as a free motion between the "transition points" $\varphi_p = \pi p$ and a scattering at these points described by a unitary 2×2-matrix $\hat{S}$. It is convenient to parametrize the scattering matrix by the amplitude τ of interlevel transition:

$$\hat{S} = \begin{pmatrix} \sqrt{1-\tau^2} & i\tau \\ i\tau & \sqrt{1-\tau^2} \end{pmatrix}.$$

At low voltages the electron transition amplitude is described by the Landau–Zener quasiclassical formula (see, e.g., Ref. 8)

$$\tau = \exp\left(-\frac{\pi^2}{2}\frac{U_0^2}{\delta E eV}\right).$$

The dc current I in a dissipative junction can be expressed in terms of the average energy accumulation rate W by the standard formula $I = W/V$. To calculate this quantity we consider the energy absorption rate averaged over the time interval $[-t_0/2, t_0/2]$,

$$W(t) = \frac{1}{t_0}\int_{t_-}^{t_+} dt' \,\mathrm{Tr}\{\rho(t')\dot{\mathcal{H}}(t')\},$$

where $t_\pm = t \pm t_0/2$, $\dot{\mathcal{H}} \equiv \partial_t \mathcal{H}(t)$. The single-electron density matrix is calculated from the equation

$$\frac{\partial\rho}{\partial t} = \frac{i}{\hbar}[\rho, \mathcal{H}] - \nu(\rho - f_0), \tag{3}$$

where ν is the relaxation rate and $f_0 \equiv f_0[\mathcal{H}]$ is the equilibrium Fermi–Dirac distribution corresponding to the Hamiltonian

$$\mathcal{H} = i\hbar v_F \sigma_3 \tau_3 \frac{\partial}{\partial x} + \Delta(x)\{\sigma_1 \cos\varphi/2 - \mathrm{sgn}\, x\, \sigma_2 \sin\varphi/2\}. \tag{4}$$

In expression (4) σ_i, τ_i are the Pauli matrices in electron-hole and "left-right" spaces, respectively, and $\Delta(x) = \Delta\Theta(|x| - L/2)$ (here $\Theta(x)$ is the Heaviside step function).

The solution of Eq. (3) can be expressed in terms of the evolution operator $u(t,t')$:

$$\rho = \nu\int_{-\infty}^{t} dt' e^{\nu(t'-t)} u(t,t') f_0\{\mathcal{H}(t')\} u^+(t,t').$$

Then for the energy absorption rate one gets

$$W(t) = \frac{1}{t_0}\int_{t_-}^{t_+} dt' \mathrm{e}^{-\nu t'} H(t') \int_{-\infty}^{t'} dt'' \mathrm{e}^{\nu t''} F(t''), \tag{5}$$

where

$$H(t) = u^+(t,0)\dot{\mathcal{H}}(t)u(t,0),$$

$$F(t) = u^+(t,0)\dot{f}_0\{\mathcal{H}(t)\}u(t,0).$$

With the help of the periodic symmetry property of the Hamiltonian (4),

$$H(t + t_0) = \sigma_3 H(t)\sigma_3,$$

it is easy to show that the average power absorption does not depend on time, $W(t) = W = \mathrm{const}$, and without any loss of

generality we can put $t=0$ in Eq. (5). It is convenient to divide the whole time interval of integration $(-\infty,t')$ in Eq. (5) into discrete intervals $[-t_0/2-mt_0;t_0/2-mt_0]$, $m=0,1,\ldots$. Finally the formula for the average energy absorption rate takes the form

$$W=\frac{1}{t_0}\mathrm{Tr}\sum_{m=0}^{\infty} e^{-2\tilde{\nu}m}HP^mFP^{-m}+Q, \tag{6}$$

where $\tilde{\nu}=1/2\nu t_0$, $P=\sigma_3 u(t_0,0)$

and $H=\int_{-t_0/2}^{t_0/2}dt\mathrm{e}^{-\nu t}H(t), F=\int_{-t_0/2}^{t_0/2}dt\mathrm{e}^{-\nu t}F(t),$

$$Q=\frac{1}{t_0}\mathrm{Tr}\int_{-t_0/2}^{t_0/2}dt'\mathrm{e}^{-\nu t'}H(t')\int_{-t_0/2}^{t'}dt''\mathrm{e}^{\nu t''}F(t'').$$

In what follows we will consider the most interesting case of moderately weak dissipation $\delta E/\Delta \ll \tilde{\nu} \ll 1$.

As one can see from Eq. (6), the only operator associated with a long-time dynamics of our system is the unitary operator P. This means that the $I-V$ characteristics of a long dissipative SNS junction at low bias voltage and for a weak dissipation are determined by a spectral properties of $P:P|\beta\rangle=e^{i\beta}|\beta\rangle$. In the basis of Andreev levels $|n,\pm\rangle$ this operator coincides with the one studied in considerable detail in Ref. 3 for the problem of energy pumping into a quasiballistic quantum ring. It was shown in Ref. 3 that the spectrum of P crucially depends on the number properties of the quantity $\alpha=\{\delta E/4eV\}$ (here $\{x\}$ stands for the fractional part of x).

For an irrational α the spectrum of P is discrete and all eigenfunctions are localized. In the limit $\nu\to 0$ the average energy absorption rate can be estimated as

$$W_i=\nu\delta E R_{\mathrm{loc}}^2, \tag{7}$$

where R_{loc} is the dimensionless localization radius.[3] An analytical expression for R_{loc} was derived in our previous paper:

$$R_{\mathrm{loc}}^2=\sum_{l=0}^{\infty}\frac{\tau^{2l}}{\sin\pi\alpha l}. \tag{8}$$

From Eqs. (7), (8) one can see that for "irrational case" the absorption power tends to zero in the limit $\nu\to 0$.

For rational values $\alpha=p/q$ ($p<q$ are integers) the eigenfunctions of P are the Bloch functions.[3] In this case the absorbed power in the limit $\nu\to 0$ takes the form

$$W_r=\frac{\delta E}{\nu}\left(\frac{eV}{\pi\hbar}\right)^2(1-\sqrt{1-\tau^{2q}})+O(\nu), \tag{9}$$

[in the last expression we assume that $p\neq 0$; if $p=0$ we must put $q=1$ in Eq. (9)].

To compare the contributions (7) and (9) to the $I-V$ curves, one first of all needs to find the relevant energy scale to satisfy $W_r \gg W_i$. It is easy to show that the above inequality will hold (for not-too-big values of q) when the bias voltage falls in the interval $\hbar\nu \ll eV \ll U_0$ and for $eV \sim \pi U_0^2/\delta E$ when the amplitude τ of interlevel transitions is not exponentially small. At these voltages the $I-V$ characteristics of a long transparent SNS junction should demonstrate specific (peak-like) structure (see Fig. 2) arising from the effect of fractional pumping of energy into the quasiballistic electron system with equidistant quantized energy levels.

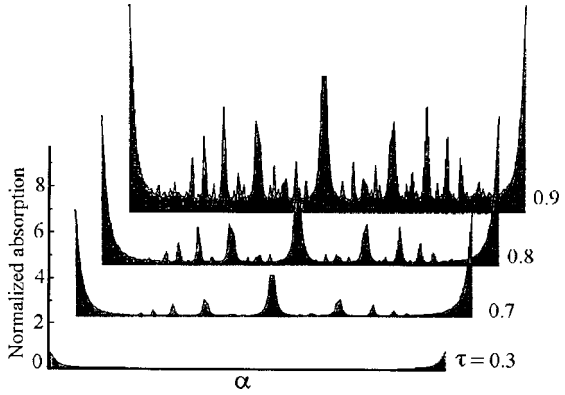

FIG. 2. The normalized absorption energy, W/W_0, as a function of parameter α, $0<\alpha<1$, for different Landau-Zener tunneling amplitudes; $W_0=\delta E/t_0$. The value $\tilde{\nu}=0.05$ for the dimensionless relaxation rate was used.

CONCLUSION

In recent experiments[9,10] the effects of quantum coherence were observed in a dissipative long SNS junction irradiated by an electromagnetic field. These experiments clearly demonstrated that dissipation in a long transparent SNS junction is unable to wash out quantum interference effects produced by the coherent dynamics of quasiparticles in the normal region. The orthodox theory[4–6] of subgap structures in $I-V$ characteristics of SNS junction is based on the Landauer–Buttiker approach, where it is assumed that dissipation occurs only in the leads (bulk superconductors) and does not influence the dynamics of electrons inside the normal region. Recently[11] a theory of MAR was applied for the description of subgap structures in long ($L\gg\xi_0$) quasiballistic junctions (see also Refs. 12 and 13). It is clear that for a real long SNS junction at sufficiently low bias voltages the dissipation will take place in the normal region, and the junction should be treated as a dissipative one.

We have proposed an approach in which both the coherent dynamics of quasiparticles in a long junction and the relaxation effects inside the normal region determine the current through a weak link.

We showed that the problem under certain conditions can be mapped onto an exactly solvable model of energy dissipation in a quasiballistic quantum ring driven by a linearly time-dependent magnetic flux. The existence of this mapping can be understood physically from the fact that the sets of energy levels of the two problems under consideration are identical.

We derived analytical expressions for the dc current through the junction at low bias voltages in the limit of moderately weak dissipation $eV(\delta E/\Delta)\ll\hbar\nu\ll\delta E$ and predicted nontrivial (peak-like) subgap structure of $I-V$ characteristic at low voltages $\hbar\nu\ll eV\ll\delta E$. The peaks in the current correspond to maxima of absorbed power and they are a manifestation of the effect of fractional pumping of energy into a quasiballistic electron system with an equidistant set of energye levels.

The authors thank L. Y. Gorelik, M. Jonson, and I. V. Krive for valuable discussions. Financial support from the Swedish NFR (S.K., R.S.) and the U.S. Department of Energy Office of Science through contract No. W-31-109-ENG-38 (R.S.) is gratefully acknowledged.

[a)]E-mail: shekhter@fy.chalmers.se

[1] L. Y. Gorelik, M. Jonson, R. I. Shekhter, and O. Tageman, in *Proceedings of the NATO Advanced Study Institute on Frontiers in Nanoscale Science of Micron/Submicron Devices*, *Kiev, August 1995*, NATO ASI Series E: Applied Sciences **328**, 225 (1996).
[2] L. Y. Gorelik, A. Grincwajg, V. Z. Kleiner, R. I. Shekhter, and M. Jonson, Phys. Rev. Lett. **73**, 2260 (1994); L. Y. Gorelik, F. Maao, R. I. Shekhter, and M. Jonson, *ibid*. **78**, 3169 (1997).
[3] L. Gorelik, S. Kulinich, Yu. Galperin, R. I. Shekhter, and M. Jonson, Phys. Rev. Lett. **78**, 2196 (1997); Fiz. Nizk. Temp. **24**, 1181 (1998) [Low Temp. Phys. **24**, 887 (1998)].
[4] G. E. Blonder, M. Tinkham, and T. M. Klapwijk, Phys. Rev. B **25**, 4515 (1982).
[5] E. N. Bratus', V. S. Shumeiko, and G. Wendin, Phys. Rev. Lett. **74**, 2110 (1995).
[6] D. Averin and A. Bardas, Phys. Rev. Lett. **74**, 1831 (1995).
[7] I. O. Kulik, Sov. Phys. JETP **57**, 1745 (1969).
[8] L. D. Landau, Phys. Z. Sov. **2**, 46 (1932); C. Zener, Proc. R. Soc. London, Ser. A **137**, 696 (1932).
[9] P. Dubos, H. Courtois, O. Buisson, and B. Pannetier, Phys. Rev. Lett. **87**, 206801 (2001).
[10] P. Dubos, H. Courtois, B. Pannetier, F. K. Wilhelm, A. D. Zaikin, and G. Schon, Phys. Rev. B **63**, 064502 (2001).
[11] A. Ingerman, G. Johansson, V. S. Shumeiko, and G. Wendin, Phys. Rev. B **64**, 1445 (2001).
[12] U. Gunsenheimer and A. D. Zaikin, Phys. Rev. B **50**, 6317 (1994).
[13] M. Hurd, S. Datta, and P. F. Bagwell, Phys. Rev. B **54**, 6557 (1996).

This article was published in English in the original Russian journal. Reproduced here with stylistic changes by the Translation Consultant.

Specific heat study of magnetic excitations in a one-dimensional $S=1$ Heisenberg magnet with strong planar anisotropy

A. Feher,* M. Orendáč, A. Orendáčová, and E. Čižmár

Department of Experimental Physics, Faculty of Science, P. J. Šafárik University, Park Angelinum 9, 04154 Košice, Slovakia

(Submitted February 14, 2002)
Fiz. Nizk. Temp. **28**, 768–773 (July 2002)

The results of experimental studies of the specific heat of the magnetic chain compounds $Ni(C_2H_8N_2)_2Ni(CN)_4$, $Ni(C_{11}H_{10}N_2O)_2Ni(CN)_4$, and $Ni(C_{10}H_8N_2)_2Ni(CN)_4\cdot H_2O$ are reported. All compounds are identified as $S=1$ planar Heisenberg magnetic chains with large planar anisotropy and different values of the in-plane anisotropy constant. The low-temperature specific heat data are interpreted assuming the existence of noninteracting excitons and antiexcitons as elementary excitations from the singlet-ground state. The extended strong-coupling model is used for analysis of the data at higher temperatures. The applicability of the models used with respect to the value of the in-plane anisotropy is discussed. © *2002 American Institute of Physics.* [DOI: 10.1063/1.1496666]

1. INTRODUCTION

The physics of one-dimensional (1d) Heisenberg magnetic systems has been of interest during the last three decades, but particularly significant progress in both experiment and theory has been made during last several years. The failure of the description of the thermodynamic properties of 1d magnetic systems in the framework of the spin-wave model demonstrated the importance of spin fluctuations and nonlinear effects in these systems.[1] For example, solitary excitations were used for the explanation of spin fluctuations in the systems possessing a Haldane gap,[2] whereas out-of-easy-plane fluctuations from the singlet ground state, i.e., (anti)excitons, have been predicted theoretically in systems with strong planar anisotropy.[3,4]

In this paper we report low-temperature specific heat results of the three magnetic chain compounds $Ni(C_2H_8N_2)_2Ni(CN)_4$, $Ni(C_{11}H_{10}N_2O)_2Ni(CN)_4$, and $Ni(C_{10}H_8N_2)_2Ni(CN)_4\cdot H_2O$ (hereafter abbreviated as NENC, NDPK, and NBYC, respectively). Our specific heat data measurements together with complementary data of susceptibility, magnetization, and ESR measurements, which were published elsewhere,[5–7] have confirmed that NENC, NDPK, and NBYC can be considered as a quantum $S=1$ magnetic chain with planar anisotropy and nonzero in-plane anisotropy. Specific-heat data were analyzed within the framework of the extended strong-coupling theory with in-plane anisotropy incorporated.[8] We focus our attention on the validity of this model with changing value of the in-plane anisotropy constant. Moreover, the specific heat of NENC and partially NDPK below 600 mK can be interpreted assuming the presence of noninteracting (anti)excitons predicted in Refs. 3 and 4.

2. STRONG-COUPLING THEORY FOR $S=1$ PLANAR MAGNETIC CHAIN

The behavior of 1d $S=1$ Heisenberg–Ising model characterized by the Hamiltonian

$$H=\sum_{n=1}^{N}\left[-2J(S_n^xS_{n+1}^x+S_n^yS_{n+1}^y+\lambda S_n^zS_{n+1}^z)+D(S_n^z)^2\right], \tag{1}$$

where n is the site index; S_n are spin operators at the nth site; J is the intrachain exchange interaction: λ is the exchange interaction anisotropy constant, and D characterizes the single-ion anisotropy. This Hamiltonian was studied numerically in dependence on the magnitude and sign of the parameters λ and D.[9] The D versus λ phase diagram for the ground state of the Hamiltonian (1) has been constructed.[10] It is evident from Fig. 1 that the relatively simple Hamiltonian (1) possesses a variety of physically different ground state phases with quantum phase transitions between them.

The spectrum of the Hamiltonian (1) depends strongly on the value of the dimensionless parameter $\alpha=D/|J|$. Here we are interested in a so-called large-D phase, for which $D/J\gg 1$ (gray area in the phase diagram on Fig. 1). For the large-D phase the exchange Hamiltonian in (1) may be treated as a perturbation.[3,4] Consequently, for the strong-coupling approximation the Hamiltonian (1) can be transformed to the form:

$$\frac{H}{D}=H_0-\frac{V}{\alpha},\quad H_0=\sum_{n=1}^{N}(S_n^z)^2,$$

$$V=\sum_{n=1}^{N}\left[\frac{1}{2}(S_n^+S_{n+1}^-+S_n^+S_{n+1}^-)+\lambda S_n^zS_{n+1}^z\right]. \tag{2}$$

In the limit $\alpha\to\infty$ $(J=0)$, the ground state of the Hamiltonian (2), $H=H_0$, is given by the product of states with vanishing azimuthal spin $|0\rangle=|0,0,...,0\rangle$ $(S_n^z=0$ for n sites). The ground state is nonmagnetic and disordered even at zero temperature. The first excited states with one nonzero azimuthal spin $(S_n^z=\pm 1)$ for any n are denoted as $|n\rangle$ and $|\overline{n}\rangle$, these are so-called exciton (e) and antiexciton $(\overline{e})$, respectively. Both $|n\rangle$ and $|\overline{n}\rangle$ are eigenstates of the unperturbed Hamiltonian H_0 for any n.

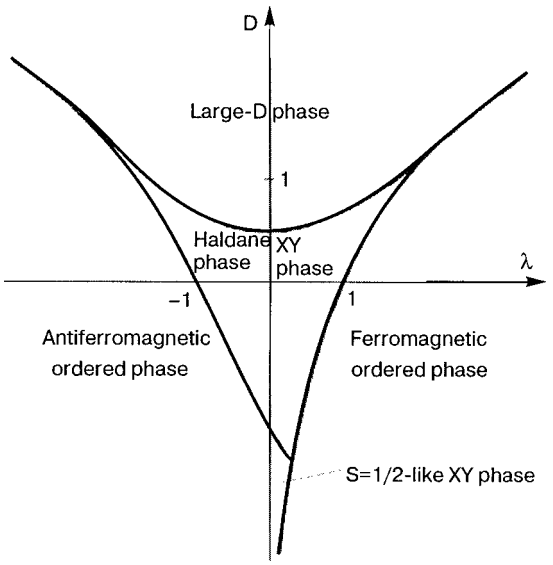

FIG. 1. (λ, D) phase diagram for the ground state of Hamiltonian (1) for $S=1$. D and λ are in the units of J.[10]

Higher excited states can be obtained by assigning the value $S_n^z=\pm 1$ to two or more sites with corresponding energies $2D$, $3D,\ldots$. Generally, excited states fall into the bands of energies iD corresponding to i sites with nonvanishing azimuthal spins of both signs. These bands are highly degenerate in the limit $\alpha\to\infty$.

A finite and sufficiently small J value may be considered as a perturbation which will transform the energy levels to bands of a finite width. The low-lying bands do not overlap for a sufficiently large D/J ratio. The elementary excitations from the singlet-ground state carrying total spin momentum ± 1 have been named excitons and antiexcitons, respectively. Perturbation theory to the third order[3] was used to derive a dispersion relation for a doubly degenerate (anti)excitonic mode, yielding:

$$\omega_k = D[1+\omega_1/\alpha+\omega_2/\alpha^2+\omega_3/\alpha_3+k], \tag{3}$$

where $\omega_1=-2\cos(k)$, $\omega_2=1+2\sin^2(k)$, $\omega_3=1/2[1+8\sin^2(k)]\cos(k)-2\lambda\sin^2(k)$; k denotes the wave vector. In addition, the energies of two-site excitations fall into a two-body continuum. Near the Brillouin zone boundary, some bound states emerge smoothly from the continuum.

This exciton dispersion was used for the calculation of the specific heat at very low temperatures, within a dilute-exciton approximation (DEA). Since (anti)excitons obey Bose statistics, their specific heat contribution will be of the form

$$C(T)=\frac{R}{\pi}\frac{d}{dT}\int_{-\pi}^{\pi}\frac{\hbar\omega(k)}{\exp(\hbar\omega(k)/k_BT)-1}\,dk. \tag{4}$$

The analysis of NENC specific heat using DEA[5] showed that the theoretical approach[3,4] requires further extension in three ways. First, to provide calculations of the specific heat that are valid beyond the low-temperature region. Second, to furnish a corresponding calculation of the magnetic susceptibility. Third, to include the effect of small in-plane anisotropy. All three problems have been addressed by Papanicolaou and Spathis in Ref. 8. They carried out a systematic strong-coupling expansion to obtain analytical approximations for the spectrum of elementary excitations, the specific heat, and the magnetic susceptibility. A comparison of these results for a uniaxial ($\varepsilon=E/D=0$, where E characterizes the in-plane anisotropy) ferromagnetic chain with an intermediate easy-plane anisotropy ($\alpha=5$) and numerical data calculated by Blöte[9] led to the following conclusions: the expanded strong-coupling approximation (ESCA) takes over decisively for temperatures larger than $T\sim 0.15D/k_B$, where the DEA, in which effects from mutual interaction of excitons are neglected, begins to deteriorate. The value of the anisotropy restricts the applicability of the ESCA. For relatively low values of the easy-plane anisotropy in the region $|\alpha|_{cr}<2.5$, the predictions of the ESCA begin to deteriorate gradually, and the disagreement between the theory and Blöte's numerical data increases. This deterioration becomes apparent by the formation of a kinklike anomaly on the low-temperature side of the specific heat. Therefore the results may be applied for $|\alpha|_{cr}>2.5$ (for $\varepsilon=0$) but with caution at the lower end of this inequality. The in-plane anisotropy ($0<\varepsilon<1$) causes a depression of the specific heat around the maximum and its enhancement at low temperatures. The latter is partly explained by the softening of one of the exciton modes at nonvanishing ε. For reasonably large values of $|\alpha|$ the theory requires a stronger condition for the value of the in-plane anisotropy ($\varepsilon\ll 1$).

3. EXPERIMENTAL DETAILS

3.1. Crystal structure

NENC crystallizes in the monoclinic space group $P2_1/n$, $a=7.104(3)$ Å, $b=10.671(3)$ Å, $c=9.940(2)$ Å, $\beta=114.68(2)°$, and $Z=2$.[11] The structure is built of neutral chains running along the c axis. The repeating unit is $[Ni(en)_2-NC-Ni(CN_2)-CN]$, where $en=C_2H_8N_2$, and two distinct nickel(II) sites are present. In the $[Ni(CN)_4]^{2-}$ anion, the nickel is in a square planar configuration, being bonded to four cyano groups through C atoms. This nickel(II) ion is diamagnetic. In the $[Ni(en)_2]^{2+}$ cation, the nickel is in a distorted octahedral configuration, where four N atoms of two en molecules are in the basal plane ($d_{Ni\text{-}N_{en}}=2.107$ Å), while two N atoms from the cyano group are in apical positions ($d_{Ni\text{-}N_{en}}=2.089$ Å). This nickel(II) ion is paramagnetic. For these paramagnetic ions, the intrachain Ni–Ni distance is 9.94 Å, whereas the shortest interchain Ni–Ni distance is 7.104 Å (along the a axis). The chain is therefore made of paramagnetic $S=1$ octahedral nickel(II) ions linked by diamagnetic square planar $NC-Ni(CN)_2-CN$ units. The chains are well insulated from each other with no chemical bonding between them. Consequently, NENC presents all the structural features required for a good quasi-1d system.

NBYC crystallizes in the orthorhombic space group *Pbcn* with cell parameters $a=14.067(1)$ Å, $b=10.1759(7)$ Å, and $c=15.755(1)$ Å. The structure consists of infinite zigzag chains containing two kinds of nickel(II) ions. The nickel(II) ion in the $[Ni(CN)_4]^{2-}$ anion is square planar coordinated and thus diamagnetic. The nickel(II) ion in the $[Ni(C_{10}H_8N_2)_2]^{2+}$ cation is paramagnetic and is located at the center of the distorted octahedron. Since

the distance between the magnetic nickel(II) ions is about 10 Å, the direct exchange interaction will be of minor importance. Although the separation between the chains is comparable to the distances between the paramagnetic ions within the chain, more complicated interchain superexchange paths are expected to allow the formation of well-isolated magnetic linear chains in this compound. A detailed structure has been published in.[12]

The detailed crystal structure of NDPK has not been determinated yet, but from infrared spectrum of the compound we can deduce the main structural features. Similarly as for NENC and NBYC, two kinds of nickel(II) ions are considered in the structure. More specifically, the nickel(II) ion surrounded by four CN groups is diamagnetic and the nickel(II) ion placed at the center of a distorted nitrogen octahedron is paramagnetic.

3.2. Specific heat

The specific heat measurements of powdered samples were performed in two experimental devices. For 50 mK $<T<$2.5 K, the dual-slope method was applied, using an Oxford Instruments dilution refrigerator. A RuO_2 thermometer (Dale RC 550 with nominal room-temperature value of 1 kΩ) was calibrated against a commercial Lake Shore thermometer (model GR 200A-30), which served as the main thermometer. A silver wire (50 μm in diameter and 7 cm long) was used as a thermal link between the cold thermal reservoir and the platform containing the sample, the RuO_2 thermometer, and a manganin heater. The resistance of the thermometer was measured by an ac (72 Hz) resistance bridge. The experimental data were corrected for the contribution of the thermometer, the manganin heater, and the varnish (GE 7031) used to anchor the powdered coin-shaped sample to the measuring platform. This additional contribution was measured in a separate run and was found to be maximum 10% of the total heat capacity.

At higher temperatures, 2 K$<T<$10 K, standard adiabatic calorimetry was used in a ^{4}He cryostat equipped with a mechanical heat switch. A 220 Ω and 1 kΩ nominal value Allen Bradley thermometer was calibrated against the Lake Shore thermometer (GR-200A-1000CD) and served as the main thermometer in this arrangement. The weights of the samples used for the heat capacity measurements were: NENC–800 mg, NBYC–345 mg and 1050 mg, and NDPK–97 mg. The overall accuracy of the dual-slope data is better than 5%, while a 3% accuracy was achieved with the quasi-adiabatic technique.

4. RESULTS AND DISCUSSION

4.1. NENC

Heat-capacity measurements were performed in the temperature region from 50 mK to 10 K. Since NENC is a magnetic insulator, only lattice and magnetic contributions to the total specific heat are assumed for the present discussion. The lattice contribution was subtracted by finding the temperature region where the data may be satisfactorily described by the equation

$$C_T(T)=\beta T^3+aT^{-2}, \tag{5}$$

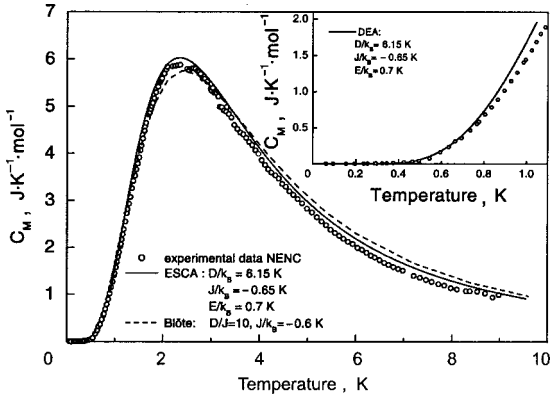

FIG. 2. The temperature dependence of the magnetic specific heat of NENC.

where βT^3 represents the low-temperature lattice contribution in the 3d Debye approximation, while the αT^{-2} contribution describes the high-temperature behavior of the magnetic heat capacity. For temperature region 5 K$<T<$9 K, a least-squares fit yielded $\alpha=(69\pm3.5)$ J·K/mol and $\beta=(3.55\pm0.15)\cdot10^{-3}$ J/(K^4·mol). The magnetic specific heat C_M is characterized by a round peak with a maximum value of $C_{\max}=(5.85\pm0.05)$ J/K·mol at $T_{\max}=(2.4\pm0.1)$ K (Fig. 2). The magnetic entropy was calculated numerically in the measured temperature region, and standard approximations were used for high and low temperatures to cover the whole temperature interval. The calculation yielded 8.68 J/K·mol, which is close to the theoretical value $R\ln(2S+1)=9.13$ J/K·mol for an $S=1$ system. This broad maximum, together with the absence of a λ-type anomaly at least down to 50 mK, indicates the presence of short-range correlations in the studied system. In the first approximation, if in-plane anisotropy is neglected ($E=0$), our system can be described by Hamiltonian (1). The specific heat of a system represented by this Hamiltonian for $\lambda=1$ was calculated numerically by Blöte.[9] The best agreement between the numerical predictions and the experimental data was obtained for $D/k_B=6$ K and $D/|J|=10-20$. The resultant $D/|J|$ ratio indicates that NENC can be considered a quantum $S=1$ system with strong planar anisotropy.

The sudden drop of C_M, observed below 1 K, suggests the existence of a gap in the energy spectrum of the spin system, and this effect is most likely associated with magnetic anisotropy. The comparison of the low-temperature specific-heat data with the theoretical prediction for DEA (taking into account a small in-plane anisotropy), using $D/k_B=6.15$ K, $J/k_B=-0.65$ K and $E/k_B=0.7$ K is shown in the inset in Fig. 2. Clearly, the trend from $T<0.8$ K is not followed at higher temperatures, since the DEA begins to fail due to exciton interactions. The temperature at which the excitonic interactions are significant in NENC ($T\sim1$ K) coincides with the value $0.15D/k_B=0.9$ K estimated for a system with $D/|J|=5$ in the theoretical work.[8] The experimental specific-heat data above 1 K can be well described by the ESCA using the same set of parameters D, J, and E (see Fig. 2). We can conclude that the magnetic specific-heat of NENC can be ascribed to the presence of low-lying elementary excitations, i.e., excitons predicted for large-D systems in the framework of the strong-coupling theory.

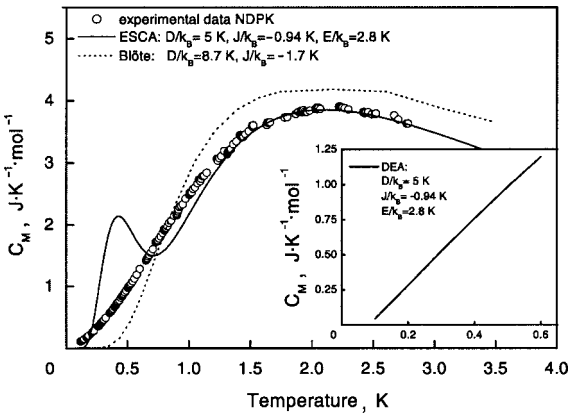

FIG. 3. The temperature dependence of the magnetic specific heat of NDPK.

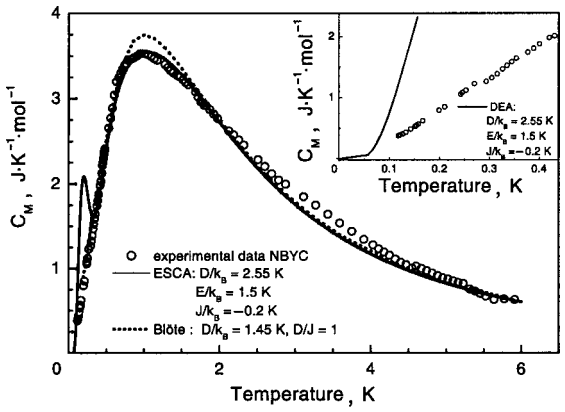

FIG. 4. The temperature dependence of the magnetic specific heat of NBYC.

4.2. NDPK

The experimental study of the specific heat of NDPK has been carried out with the aim of investigating a system located possibly close to the phase boundary between the Haldane phase and large-D phase (Fig. 1) and to check the validity of the strong-coupling model for this system. Since the group $C_{11}H_8N_2O$ is characterized by a different type of delocalization of charge density than $C_2H_8N_2$ in NENC, we have tried to change the surroundings of the paramagnetic nickel(II) ion with the expectation of obtaining a system with different anisotropy in comparison with NENC.

The specific heat of NDPK was measured in the temperature range from 100 mK to 2.5 K. A comparison of our results on the magnetic part of the specific heat with the numerical prediction of Blöte[9] gives $D/k_B=8.7$ K and $D/|J|=5$ (Fig. 3). This result suggests that although the value of $D/|J|$ for NDPK is two times smaller than that for NENC, the system is still located in the large-D phase rather than near the phase boundary. The specific heat data were analyzed using ESCA[8] with the aim of studying the influence of in-plane anisotropy E as a potential source of the discrepancy between our results and Blöte's numerical predictions. Above temperature 1.2 K we found good quantitative agreement with the experimental data for $D/k_B=5$ K, $|J|/k_B=0.94$ K and $E/k_B=2.8$ K. Note that the value of E ($\varepsilon=0.56$) indicates a large in-plane anisotropy in comparison with NENC. As was already mentioned in Sec. 2, the validity of the ESCA (for $E=0$) is limited to $|\alpha|_{\rm cr}>2.5$ and $T>0.15D/k_B$. The appearance of the kinklike anomaly of the artificial origin on the ascending side of the theoretical curve suggests a significant increase of $|\alpha|_{\rm cr}$ for large in-plane anisotropy.

Experimental data on the specific heat below $0.15D/k_B$ were analyzed in the framework of the DEA using the same set of values D, $|J|$, and E. It follows from the inset in Fig. 3 that the validity of the DEA is also restricted in the presence of large in-plane anisotropy in NDPK.

4.3. NBYC

In addition we have tried to modify the magnetic anisotropy by replacing the group $C_{11}H_8N_2O$ by $C_{10}H_8N_2$ with the aim of testing our conclusions on the validity of strong-coupling model on a system with strong in-plane anisotropy.

We have studied the heat capacity of NBYC in the temperature range from 100 mK to 6 K. The results of experimental studies of the magnetic part of the specific heat of NBYC are presented in Fig. 4. The broad maximum, together with the absence of a λ-type anomaly down to 100 mK, indicates a high degree of short-range order in this system. The magnetic specific heat was compared with numerical predictions of Blöte,[9] where only D and J were involved.

The best agreement between the numerical predictions and the experimental data was obtained when $D/k_B=1.45$ K and $D/|J|=1$. More detailed analysis of C_M was carried out using the theoretical predictions with D, J, and E taken into account in the ESCA.[8] In the temperature region $T>0.38$ K, the specific heat data can be satisfactorily described using the values $D/k_B=2.55$ K, $|J|/k_B=0.2$ K, and $E/k_B=1.5$ K. As in the case NDPK, the ESCA fails to describe the specific heat data below $T=0.15D/k_B$ as can be seen in Fig. 4. Moreover, we have tried to apply the DEA to describe the temperature behavior of the magnetic specific heat below the temperature $0.15D/k_B$. As is evident from Fig. 4 (see the inset), the DEA fails to describe the specific

TABLE I. Values of the exchange constant and magnetic anisotropy constants.

Compound	D/k_B, K	$\|J\|/k_B$, K	E/k_B, K	$\alpha=D/\|J\|$	$E/\|J\|$	$\varepsilon=E/D$	Model (temperature range)	
							DEA (mK)	ESCA (K)
NENC	6.15	0.65	0.7	9.5	1.0	0.16	50–900	0.9–6
NDPK	5	0.96	2.8	5.2	2.9	0.56	100–600	1.2–3
NBYC	2.55	0.2	1.5	12.7	7.5	0.59	–	0.38–6

heat data in the temperature range $100\ \mathrm{mK} < T < 380\ \mathrm{mK}$. This result confirms that the validity of the DEA is restricted to low in-plane anisotropy.

5. CONCLUSIONS

Our specific heat studies have confirmed that NENC, NDPK, and NBYC can be considered as a quantum $S=1$ Heisenberg chain with strong planar anisotropy and nonzero in-plane anisotropy.

Magnetic specific heat data were analyzed within the framework of the strong-coupling theory [8] for both noninteracting excitons ($T<0.15D/k_B$) and expanded strong-coupling approximation ($T>0.15D/k_B$). The values of the exchange and magnetic anisotropy constants as well as their mutual ratios for the systems studied are summarized in the Table I. We found that the region of the validity of ESCA for $|\alpha|_{\mathrm{cr}}>2.5$ is in agreement with the predictions of Papanicolaou and Spathis, i.e., for $E=0$ it is valid for temperatures larger than $0.15D/k_B$ and below this temperature a kinklike anomaly of artificial origin occurs on the ascending side of the specific heat curve for a system with strong in-plane anisotropy. The validity of the DEA is drastically suppressed with increasing value of in-plane anisotropy. We have observed very good agreement between predictions of DEA and specific-heat data only for NENC, which is characterized by a low E/D ratio. In addition, on the basis of the results obtained we propose that in-plane anisotropy should be considered in any attempt to find a compound located close to the boundary between the Haldane and large-D phases.

We are grateful to Prof. V. V. Eremenko for introducing our Košice group to the wonderful world of low-dimensional magnetism many years ago. One of us (A. F.) acknowledges the hospitality of CRTBT CNRS Grenoble during the preparation of this manuscript. Partial financial support for this work was provided by the grant No. 1/7473/20 from the Slovak Ministry of Education. The material support of U. S. Steel DZ Energetika is gratefully acknowledged.

*E-mail: feher@kosice.upjs.sk

[1] R. Steiner, J. Appl. Phys. **67**, 5593 (1990).
[2] F. D. M. Haldane, Phys. Lett. **93**, 464 (1983).
[3] N. Papanicolaou and P. Spathis, J. Phys.: Condens. Matter **1**, 5555 (1989).
[4] N. Papanicolaou and P. Spathis, J. Phys.: Condens. Matter **2**, 6575 (1990).
[5] M. Orendáč, A. Orendáčová, J. Černák, A. Feher, P. J. C. Signore, M. W. Meisel, S. Merah, and M. Verdaguer, Phys. Rev. B **52**, 3435 (1995).
[6] M. Orendáč, T. Herrmannsdoerfer, A. Feher, and F. Pobell, Czech. J. Phys. **46**, 1941 (1996).
[7] M. Orendáč, E. Čižmár, A. Orendáčová, J. Černák, A. Feher, M. W. Meisel, K. A. Abboud, S. Zvyagin, M. Sieling, T. Rieth, and B. Lüthi, Phys. Rev. B **61**, 3223 (2000).
[8] N. Papanicolaou and P. N. Spathis, Phys. Rev. B **52**, 16001 (1995).
[9] H. W. J. Blöte, Physica B **79**, 427 (1975).
[10] R. Bottet, R. Jullien, and M. Kolb, Phys. Rev. B **28**, 3974 (1983).
[11] J. Černák, J. Chomič, D. Baloghová, and M. Duhaj-Jurčo, Acta Crystallogr., Sect. C: Cryst. Struct. Commun. **44**, 192 (1983).
[12] J. Cernák and K. A. Abboud, Acta Crystallogr., Sect. C: Cryst. Struct. Commun. **56**, 783 (2000).

This article was published in English in the original Russian journal. Reproduced here with stylistic changes by the Translation Consultant.

Exchange interaction and magnetoresistance in $La_{2/3}Ca_{1/3}MnO_3$: experiment and models

A. B. Beznosov,* B. I. Belevtsev, E. L. Fertman, and V. A. Desnenko

B. Verkin Institute for Low Temperature Physics and Engineering of the National Academy of Sciences of Ukraine, 47 Lenin Ave., Kharkov 61103, Ukraine

D. G. Naugle, K. D. D. Rathnayaka, and A. Parasiris

Department of Physics, Texas A & M University, College Station, Texas 77843, USA
(Submitted March 5, 2002)
Fiz. Nizk. Temp. **28**, 774–780 (July 2002)

The magnetization $M(T)$ and electrical resistivity $\rho(T)$ of a $La_{2/3}Ca_{1/3}MnO_3$ film have been studied in the temperature range $5\,\mathrm{K} \leqslant T \leqslant 320\,\mathrm{K}$ in the magnetic field intervals $10\,\mathrm{Oe} \leqslant H \leqslant 400\,\mathrm{Oe}$ and $0 \leqslant H \leqslant 50\,\mathrm{kOe}$, respectively. It is found that the $M(T)/M(0)$ value is larger than that predicted by the conventional molecular field model below the Curie point $T = 267$ K, and that the $\ln \rho(T)$ dependence is close to linear in the temperature range $80\,\mathrm{K} < T < 200\,\mathrm{K}$ (accordingly, $\partial \ln \rho / \partial T$ is constant in this region). A model of the electrical conductivity and magnetoresistivity of the system describing qualitatively the experimental results is proposed (the $\Delta m \tau$ model). The model includes a thermally activated (with characteristic energy Δ) mechanism of conductivity, dependence of the concentration and the effective mass (m) of the itinerant charge carriers on the magnetization, as well as scattering (with characteristic time τ) of the charge carriers by static breakings of the translational symmetry, thermal fluctuations of the magnetic order, and phonons.
[DOI: 10.1063/1.1496667]

1. INTRODUCTION

Complex oxides containing manganese ions Mn^{3+} and Mn^{4+} have been attracting much attention in physics and technology in the last 10 years due to the ''colossal magnetoresistance (CMR) effect'' discovered in them: the electrical resistance of the compounds decreases substantially (in orders of magnitude) when an external magnetic field is applied to a sample in the vicinity of the Curie temperature (see reviews).[1–6] The nature of this phenomenon is being studied intensively; the main directions of the research are outlined in the above-mentioned reviews. We note here also the following original papers, references to which will be made below.[7–14]

The key point in an understanding of the CMR mechanisms is elucidating of the nature of changes of the electrical resistance on passage through the Curie point, first of all in the absence of the external magnetic field. The present work is devoted to an experimental study of the problem as well as to a theoretical modeling of the phenomenon.

The dependences of the magnetization and electrical conductivity of a $La_{2/3}Ca_{1/3}MnO_3$ film on the temperature and magnetic field are studied experimentally and analyzed. A model of the electrical conductivity and magnetoresistive behavior is proposed ($\Delta m \tau$ model). The model includes a thermally activated (with the characteristic energy Δ) mechanism of conductivity, dependence of the concentration and effective mass (m) of the itinerant charge carriers on the magnetization, as well as scattering (with the characteristic time τ) of those carriers by static breakings of translational symmetry, thermal fluctuations of the magnetic order, and phonons.

2. THE $\Delta m \tau$ MODEL OF CONDUCTIVITY

The proposed effective model of conductivity is based on the concept of thermal excitation of the charge carriers from localized states to itinerant states. We do not specify here the type of charge carriers, but for simplicity, without any loss in generality, we call them electrons. In this picture, above the Curie point the charge carriers are localized, so that their motion between the crystal sites can only be of the thermally activated kind. At the same time they appear to be nearly free in the ferromagnetically ordered state. Thus their activation energy has to be dependent on the magnetic order parameter.

2.1. Activation energy

Analysis of the results of our present measurements of the electrical resistivity and magnetization of the $La_{2/3}Ca_{1/3}MnO_3$ film (see Secs. 5 and 6) has shown that the dependence of the activation energy Δ on the ferromagnetic order parameter of the system $\sigma = M(T,H)/M_0$ in a vicinity of the Curie point T_C is close to linear (here M is the magnetization, T is the temperature, H is the magnetic field, and M_0 is the magnetization at $T = 0$). On the other hand, the conductivity must be of the nonactivated kind at $T = 0$ (the experiment gives a finite value of the corresponding electrical resistivity of the system ρ). Thus we choose the simplest dependence $\Delta(\sigma)$ satisfying the above-mentioned requirements, in the form

$$\Delta = \Delta_0(1 - \sigma), \tag{1}$$

where Δ_0 is the activation energy in the paramagnetic region and will be determined in the model by fitting to the experimental data.

Expression (1) gives for the concentration of the electrons in the ''conduction band'' the value

$$n = n_0 e^{-\Delta_0(1-\sigma)/T}, \tag{2}$$

where n_0 is the concentration of the conduction electrons in the completely ordered system ($\sigma = 1$).

Note that a dependence of the form in Eq. (2) was established for the concentration of the conduction electrons of EuO in Ref. 8.

2.2. Effective mass of charge carriers

The hopping integral of the electrons in the ''conduction band'' depends on the mutual orientation of the local spins of nearest magnetic ions [5], so that their effective mass m^* also depends on σ:

$$m^* = m_0^* \frac{2}{1+\sigma}. \tag{3}$$

Here m_0^* is the effective mass of the perfect crystal ($\sigma = 1$) and will be considered further as a fitting parameter of the model.

The expression (3) has been obtained by the averaging of the hopping integral over the crystal with a subsequent transition to the effective mass representation in a model of magnetization in which the local quantization axes for the itinerant electrons (i.e., the directions of the local magnetic moments considered as classical vectors) are deflected from the easy magnetization axis by the same polar angle at every Mn site, and the azimuth angles are randomly distributed uniformly in the interval $(0, 2\pi)$.

2.3. Transport relaxation time

The electrical resistivity of the system is calculated in the model by the Drude formula

$$\rho = \frac{m^*}{e^2 n \tau}, \tag{4}$$

where e is the electron charge, m^* and n are determined by Eqs. (1)–(3), and the transport relaxation time τ is defined by the sum

$$\tau^{-1} = \tau_{\rm st}^{-1} + \tau_{\rm ph}^{-1} + \tau_m^{-1}. \tag{5}$$

Here $\tau_{\rm st}$, $\tau_{\rm ph}$ and τ_m are the characteristic times for the scattering by the static breakings of the translational symmetry of the system (this is principally because of the random distribution of the La and Ca ions in the crystal), phonons, and fluctuations of the local magnetic moments, respectively.

Taking into account Eqs. (1), (2), (4), and (5), and using the theoretical approaches from Refs. 15–17, we write the expression for the electrical resistivity of the system in the form

$$\rho = e^{(2/3)/(\Delta/T)}(\rho_{\rm st} + \rho_{\rm ph} + \rho_m). \tag{6}$$

Here the resistivity $\rho_{\rm st}$, caused by the static breakings of the crystal-lattice translational symmetry, is given by

$$\rho_{\rm st}(\sigma) = \rho_0 \left(\frac{2}{1+\sigma}\right)^2, \tag{7}$$

where Eq. (3) and the theory of Ref. 15 have been taken into account.

The resistivity $\rho_{\rm ph}$, caused by the electron-phonon scattering, is evaluated by the Bloch–Grüneisen formula:[16]

$$\rho_{\rm ph} = 4\rho_D \left(\frac{T}{\Theta_D}\right)^5 \int_0^{\Theta_D/T} \frac{x^5 dx}{(e^x - 1)(1 - e^{-x})}, \tag{8}$$

where the Debye temperature Θ_D is taken equal to 440 K (by our estimate made using the sound velocity from Ref. 18), which is in accordance with other estimates.[6,19]

The resistivity ρ_m caused by the electron scattering on the disordered local spins is evaluated using the Kasuya expression,[17] modified for the present case by replacing the constant effective mass by a function of magnetization [Eq. (3)]:

$$\rho_m = \rho_{m\infty} \left(\frac{2}{1+\sigma}\right)^2 S(S - S\sigma^2 - \sigma + 1). \tag{9}$$

Note that as one can see from Eqs. (6), (7), and (9), all three scattering times in Eq. (5) have the same dependence on n ($\tau \propto n^{-1/3}$), $\tau_{\rm st}$ and τ_m have the same dependence on m^* ($\tau_{{\rm st}(m)}^{-1} \propto m^*$).

Exponential dependences of the electrical resistivity, compatible with Eq. (6) (i.e., with the argument of the exponential function being linearly dependent on magnetization), were observed experimentally in Refs. 7–9. Other forms of the $\rho(\sigma)$ dependence were proposed in Refs. 7 and 11–14. In our opinion, these last do not have as good agreement with the known experimental data (see Refs. 1–6) and with those obtained in this work.

3. THE MODIFIED MOLECULAR FIELD MODEL FOR MAGNETIZATION

The local spin S in Eq. (9) was put equal to 2, and the reduced magnetization $\sigma = M/M_0$ was estimated in the modified molecular field model. This model differs from the conventional form (see, for example, Ref. 20) by the additional fitting parameters a and h. They formally take into account the effect of spontaneous magnetization on the interatomic exchange parameter and the effect of the short-range order on the charge-carrier scattering above the Curie temperature. The latter is substantial in the case of a short mean free path of the carriers, because they are localized in the absence of magnetic order, as is evidenced by the change of character of the conductivity from metallic to semiconductive when going from the ferromagnetic to the paramagnetic state of the oxide.

The ferromagnetic order parameter in the model is defined by the following equation:

$$\sigma = B_S\left(\frac{h}{T} + \frac{3S}{S+1}\frac{T_C(1+a\sigma^2)}{T}\sigma\right). \tag{10}$$

Here $B_S(x)$ is the Brillouin function for spin $S = 2$, T_C is the Curie temperature, h is a fictive magnetic field modeling the effect of short-range magnetic order above T_C, and a is a magnetoelastic parameter describing the magnetostrictive shift of T_C.[21]

Note that the value $S=2$ for the local spin used in the model corresponds to the spin of the Mn^{3+} ion but not to the spin $S=3/2$ of the Mn^{4+} ion, which must actually be regarded as the local spin. This is done just because it gives a better fit (compared to $S=3/2$) of the experimental data in the low-temperature region, where molecular field theory, used in the model over the whole temperature range for simplicity, is not valid *a priori*. Thus, such a substitution can be made without any fundamental significance. In the most important region, in the vicinity of T_C, the value $S=3/2$ gives the better result in the conventional molecular field model and therefore requires a weaker correction for agreement with the experimental data.

4. NATURE OF THE ACTIVATION ENERGY Δ

As one can see from Sec. 7, this simple model (it will be referred to below as the $\Delta m\tau$ model) gives a temperature dependence of the electrical resistivity of the given oxide quite close to the experimental one. Here, however, a detailed microscopic picture of the phenomenon (i.e., mainly the nature of the activation energy Δ) is not considered. Moreover, we do not discuss here the values of all the fitting parameters (they are physically quite reasonable) and their exact origin. Obviously, behavior of the conductivity similar to that in the $\Delta m\tau$ model can be obtained in a different way, but we suppose that this model is the simplest which takes into account the most important factors that can influence the magnetoresistive effect in doped manganites.

The activation energy Δ in the model can reflect an effect of localization of the charge carriers[22] when the magnitude of the fluctuations of their exchange energies exceeds some critical value, at least for the majority of them at $T \geqslant T_C$. Apparently, a starting point for constructing a model of conductivity in manganites can be the concept of double exchange.[23–25] In reality the picture of the phenomenon appears to be more complex. The role of the charge carriers is played by magnetic polarons, which are being formed due to the interactions between the quasilocal charge carriers and magnetic moments of the surrounding lattice sites, and due to deformations of the atomic structure over distances of the order of the first coordination sphere (see the general discussion in Refs. 22, 26, and 27 and the manganite-specific one in Refs. 2, 6, and 28). Note that the origin of the local lattice deformations can be of an exchange-relativistic nature.[29] There is no necessity, however, to make more precise the character of the charge carriers in the original $\Delta m\tau$ model.

5. EXPERIMENTAL

The $La_{1-x}Ca_xMnO_3$ ($x\approx 1/3$) film (about 1500 Å thick) was grown by pulsed laser deposition on a $LaAlO_3$ substrate. A KrF excimer laser operating at 248 nm was used to ablate the target material, with a nominal composition $La_{2/3}Ca_{1/3}MnO_3$. The target was prepared by the conventional solid-state reaction method starting from high-purity powders of La_2O_3, $CaCO_3$, and $MnCO_3$. An x-ray study of the target has shown that it is homogeneous in composition and does not contain a residue of the starting chemical components. The film obtained was tested by the x-ray diffraction method and on an atomic force microscope. The resistance as a function of temperature (in the range 5–320 K) and magnetic field (up to 50 kOe) was measured by a standard four-point probe technique. The magnetoresistance $\Xi(T,H)=[\rho(T,H)-\rho(T,0)]/\rho(T,0)$ was measured in a transverse geometry (with the field perpendicular to the film plane). The magnetization was measured by a SQUID magnetometer in the field range 10 Oe$\leqslant H\leqslant$400 Oe in a longitudinal geometry (with the field parallel to the film plane).

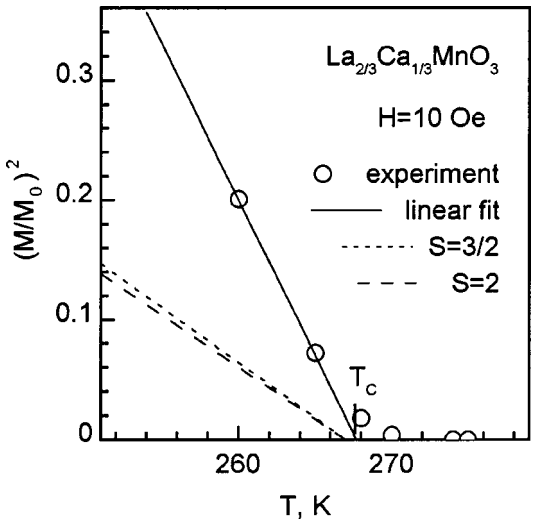

FIG. 1. Square of the reduced magnetization $(M(T)/M(0))^2$ of the $La_{2/3}Ca_{1/3}MnO_3$ film in a magnetic field $H=10$ Oe in the Curie-point region (○); the solid line determines the Curie point T_C; the dashed and dotted lines show the expected dependences in the conventional molecular field model for spins $S=2$ and $S=3/2$, respectively.

6. RESULTS OF EXPERIMENT

Figures 1–7 present the following characteristics obtained for the $La_{2/3}Ca_{1/3}MnO_3$ film studied: the square of the reduced magnetization $(M(T)/M(0))^2$ in the Curie-point region, the reduced magnetization $M(T)/M(0)$ at magnetic field $H=10$ Oe, the magnetization $M(H)$ at temperatures of 10, 20, 40, and 60 K, the electrical resistivity $\rho(T)$, the electrical resistivity in a logarithmic scale, the logarithmic temperature derivative of the resistivity $\partial \ln\rho/\partial T$, and the magnetoresistance $\Xi(T,H)$ in magnetic field $H=50$ kOe.

An extrapolation to $\sigma=0$ of the linear part of the dependence $\sigma^2(T)$ (Fig. 1) gave a value of T_C equal to 267 K. The sharp growth of the magnetization below T_C seen in Fig. 2 confirms the high homogeneity of the film. The magnetic field dependence of the magnetization is found to be nonlinear in the temperature and magnetic field ranges studied (Fig. 3). At $T=10$ K the magnetization M is equal to 86 G at $H=10$ Oe, and it obeys the equation $M[G]=85+3.75\times10^{-2}H$ [Oe] in the range 100–400 Oe. The magnetic moment per Mn atom is equal to 0.61 μ_B at $H=400$ Oe. This shows that the magnetization is far from saturation in the field range under study.

As one can see from Fig. 4, the $\rho(T)$ behavior has a semiconductive character above T_C. Below T_C the resistivity decreases sharply, falling to $\rho=90.6\,\mu\Omega\cdot$cm at $T=5$ K. As is evident from Fig. 5, the dependence $\rho(T)$ in a logarithmic scale [i.e., log $\rho(T)$] is close to linear in the range 80 K$\leqslant T\leqslant$200 K. The nearly constant value of the

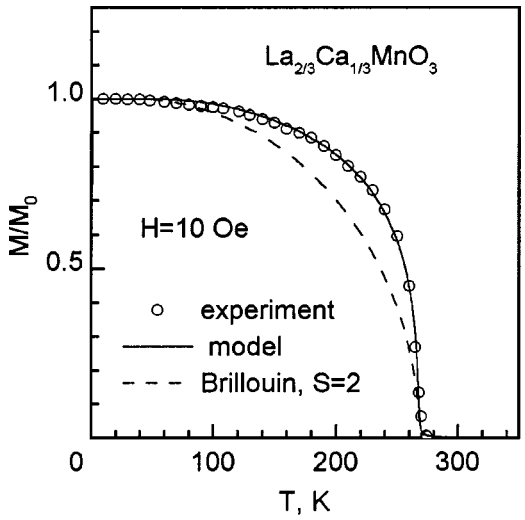

FIG. 2. Temperature dependence of the reduced magnetization $M(T)/M(0)$ of the $La_{2/3}Ca_{1/3}MnO_3$ film in a magnetic field $H=10$ Oe applied in the film surface plane: experiment (○) and calculations (solid line) in the modified molecular field model; the dashed line shows the $M(T)/M(0)$ dependence in the conventional molecular field model (the Brillouin curve) for spin $S=2$.

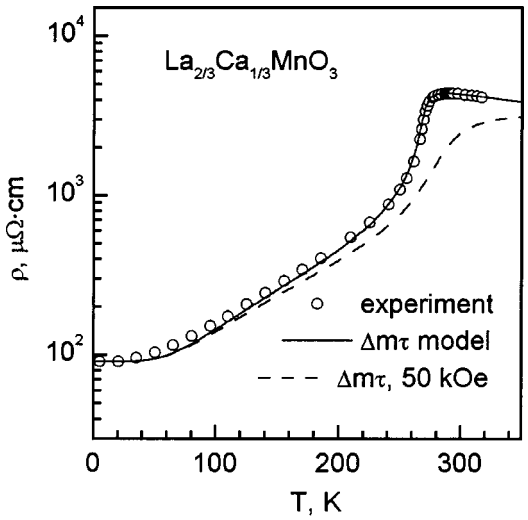

FIG. 4. Electrical resistivity of the $La_{2/3}Ca_{1/3}MnO_3$ film vs temperature (○); the solid and dashed lines represent calculations in the $\Delta m\tau$ model for magnetic fields of 0 and 50 kOe, respectively.

logarithmic derivative of $\rho(T)$ seen in Fig. 6 also confirms the exponential temperature dependence of $\rho(T)$ in this temperature range.

The temperature dependence of the Ξ at H=50 kOe presented in Fig. 7 is of the usual type for CMR manganites of fairly good crystal quality. It should be noted here that at the field 5 kOe the Ξ value was positive practically in the whole temperature range studied.

7. COMPARISON OF THE MODEL AND EXPERIMENTAL DATA

The magnetization of the film, as one can see from Figs. 1 and 2, is substantially higher than that predicted by the conventional molecular field model [$h=0$, $a=0$ in Eq. (10)]: the coefficient b in the formula $\sigma^2=b\ (1-T/T_C)$, which is valid in some neigborhood just below the Curie temperature, turned out to be about three times larger than the theoretical value (see Fig. 1). Possible reasons for this are a peculiarity of the double exchange[7] and an enhancement of the effective interatomic exchange interaction by the magnetoelastic coupling. The last has been taken into account in the modified molecular field model by the factor $(1-a\sigma^2)$ (in accordance with Ref. 21), which gives practically complete coincidence with the experimental data just below T_C (Fig. 2), in contrast to the results of Ref. 7, where the model curve increases faster than the experimental curve on lowering of the temperature.

Using Eqs. (1)–(10) and the experimental data on the magnetization and electrical resistivity, we obtained the following model parameters giving the best fit to the experimental data on resistivity presented in Fig. 4: $\Delta_0=555$ K, $\rho_0=90.6\ \mu\Omega\cdot$cm, $\rho_D=400\ \mu\Omega\cdot$cm, $\rho_{m\infty}=29.7\ \mu\Omega\cdot$cm, $h=1$ K (this corresponds to a fictitious "short-range-order

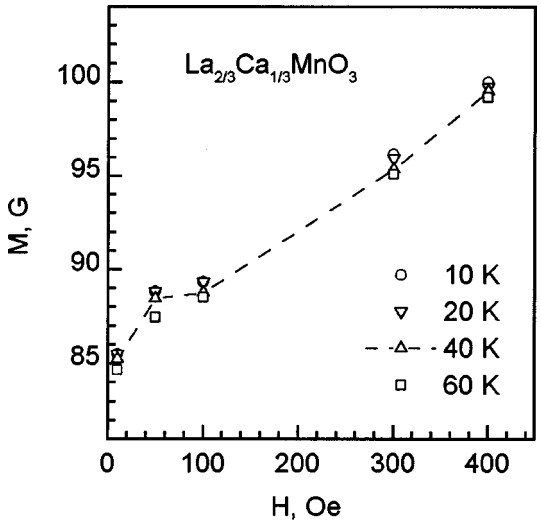

FIG. 3. Magnetization $M(H)$ vs magnetic field H applied in the surface plane of the $La_{2/3}Ca_{1/3}MnO_3$ film at temperatures of 10 K (○), 20 K (▽), 40 K (△), and 60 K (□).

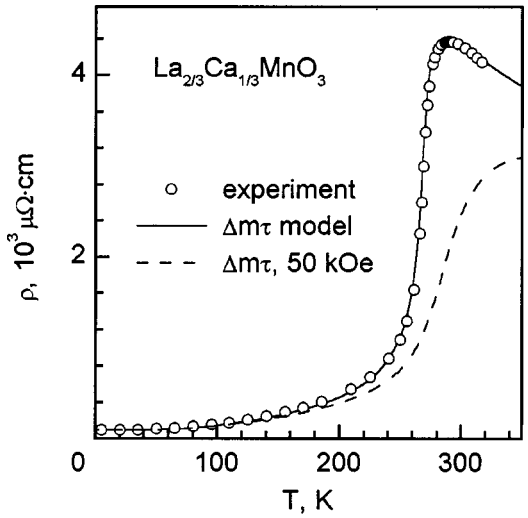

FIG. 5. Electrical resistivity of the $La_{2/3}Ca_{1/3}MnO_3$ film vs temperature in logarithmic scale (○); the solid and dashed lines represent calculations in the $\Delta m\tau$ model for magnetic fields of 0 and 50 kOe, respectively.

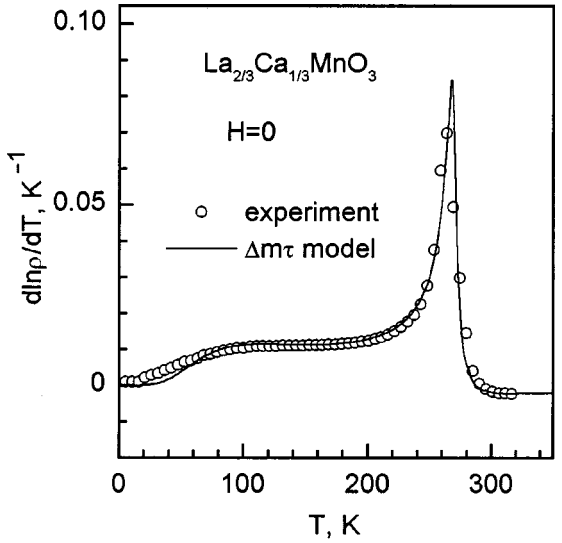

FIG. 6. The logarithmic temperature derivative of the electrical resistivity of the $La_{2/3}Ca_{1/3}MnO_3$ film vs temperature (○); solid line represents the $\Delta m\tau$ model calculations.

field'' of about 3725 Oe), $a=0.26$. The model temperature dependence $\rho_{\rm mod}(T)$ calculated with these parameters practically coincides with the experimental data for $\rho(T)$ (see Fig. 4). The model temperature dependences $\log \rho_{\rm mod}(T)$ and $\partial \ln \rho_{\rm mod}/\partial T$ also agree well with the experiment in the main temperature region (see Figs. 5 and 6).

The numerical analysis has shown that the nearly linear in T region of the $\log \rho(T)$ dependence, which can be seen clearly (Fig. 5) in the range $80\ {\rm K}<T<200\ {\rm K}$, as well as the nearly constant value of the $\partial \ln \rho/\partial T$ derivative in the same temperature interval (see Fig. 6), are caused by the compensation of the bending ''up'' of the Δ/T curve in the Eq. (6) by the bending ''down'' of the curve $\log [\rho_{\rm st}(T)+\rho_{\rm ph}(T)+\rho_m(T)]$. The first can be seen from the approximation

$$\sigma(T)=g-pT-qT^2-rT^3-\ldots,$$

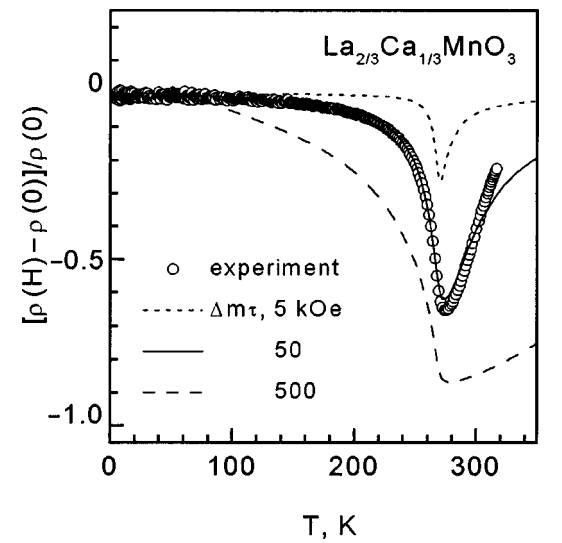

FIG. 7. Magnetoresistance $[\rho(H)-\rho(0)]/\rho(0)$ of the $La_{2/3}Ca_{1/3}MnO_3$ film vs temperature in a magnetic field of 50 kOe (○); the dotted, solid, and dashed lines represent the $\Delta m\tau$ model calculations for magnetic fields of 5, 50, and 500 kOe, respectively.

where g, p, q and r are constants, which gives immediately the bending ''up'' curve:

$$\Delta/T=\Delta_0[1-\sigma(T)]/T=\Delta_0[-(g-1)/T+p+qT+rT^2+\ldots].$$

The second is caused by the $\rho_{\rm ph}(T)$ contribution (the contribution from $\rho_m(T)$ is small in the temperature range under consideration, and the $\rho_{\rm st}$ value changes weakly there).

The character of the temperature dependence of the model magnetoresistive effect $\Xi_{\rm mod}(T,H)=[\rho_{\rm mod}(h,T,H)-\rho_{\rm mod}(h,T,0)]/\rho_{\rm mod}(h,T,0)$ also corresponds rather well to the experiment at high magnetic fields (Fig. 7), though the accuracy in this case is somewhat lower: the maximal value at $H=50$ kOe is -0.65 at $T=274$ K in the experiment, whereas the model gives -0.63 at 273 K.

A somewhat unexpected finding is the experimental observation of a positive magnetoresistive effect with a maximum near T_C at low fields ($H=5$ kOe). In the framework of the $\Delta m\tau$ model this can imply an increase of the activation energy Δ and an enhancement of the electron scattering. One of the possible reasons may be the presence of an antiferromagnetic component in the magnetic structure of the system at low fields (see Refs. 14, 27, and 30). In this case an increase of magnetization under the influence of the magnetic field should be accompanied by a reduction of the order parameter of the antiferromagnetic component and by a corresponding increase in the activation energy and electron scattering.

A detailed discussion of this effect is beyond the scope of this paper. In general, however, the character of the behavior of the model magnetoresistive effect $\Xi_{\rm mod}(H)$ in the interval $0<H<75$ kOe at $T=273$ K is quite consistent with the experiment.

8. CONCLUSION

1. The magnetization $M(T)$ and the electrical resistivity $\rho(T)$ of a 150-nm thick $La_{2/3}Ca_{1/3}MnO_3$ film have been studied in the temperature range $5\ {\rm K}\leqslant T\leqslant 320\ {\rm K}$ in the magnetic field intervals $10\ {\rm Oe}\leqslant H\leqslant 400\ {\rm Oe}$ and $0\leqslant H\leqslant 50$ kOe, respectively. It is found, that the $M(T)/M(0)$ value is larger than that predicted by the conventional molecular field model below the Curie point $T_C=267$ K, and that the $\log \rho(T)$ dependence is close to linear ($\log \rho(T)=A+BT$) in the temperature range $80\ {\rm K}<T<200\ {\rm K}$ (accordingly $\partial \ln \rho/\partial T$ is constant in this region).

2. A model of the electrical conductivity and magnetoresistivity of the system describing qualitatively the experimental results is proposed (the $\Delta m\tau$ model). The model includes a thermally activated (with characteristic energy Δ) mechanism of conductivity, dependence of the concentration and the effective mass (m) of the itinerant charge carriers on the magnetization, as well as scattering (with character time τ) of the charge carriers by static breakings of the translational symmetry, thermal fluctuations of the magnetic order, and phonons.

The authors are pleased to dedicate the paper to Academician V. V. Eremenko, whose multifaceted scientific interest and achievements in the physics of magnetic phenomena in the compounds of d and f elements are widely appreciated.

*E-mail: beznosov@ilt.kharkov.ua

[1] E. L. Nagaev, Phys. Usp. **39**, 781 (1996).
[2] J. M. D. Coey, M. Viret, and S. von Molnar, Adv. Phys. **48**, 167 (1999).
[3] N. Furukawa, in *Physics of Manganites*, T. A. Kaplan and S. D. Mahanti (Eds.), Kluwer Academic, New York (1999), p. 1.
[4] V. M. Loktev and Yu. G. Pogorelov, Fiz. Nizk. Temp. **26**, 231 (2000) [Low Temp. Phys. **26**, 171 (2000)].
[5] E. Dagotto, T. Hotta, and A. Moreo, Phys. Rep. **344**, 1 (2001).
[6] M. Salamon and M. Jaime, Rev. Mod. Phys. **73**, 583 (2001).
[7] C. W. Searle and S. T. Wang, Can. J. Phys. **48**, 2023 (1970).
[8] T. Penney, M. W. Shafer, and J. B. Torrance, Phys. Rev. B **5**, 3669 (1972).
[9] M. F. Hundley, M. Hawley, R. H. Heffner, Q. X. Jia, J. J. Neumeier, J. Tesmer, J. D. Thompson, and X. D. Wu, Appl. Phys. Lett. **67**, 860 (1995).
[10] J. Z. Sun, L. Krusin-Elbaum, S. S. Parkin, and G. Xiao, Appl. Phys. Lett. **67**, 2726 (1995).
[11] I. Esaki, P. J. Stiles, and S. von Molnar, Phys. Rev. Lett. **19**, 852 (1967).
[12] N. Furukawa, J. Phys. Soc. Jpn. **64**, 3164 (1995).
[13] M. Viret, L. Ranno, and J. M. D. Coey, Phys. Rev. B **55**, 8067 (1997-I).
[14] J. Inoue and S. Maekawa, Phys. Rev. Lett. **74**, 3407 (1995).
[15] A. J. Dekker, J. Appl. Phys. **36**, 906 (1965).
[16] F. J. Blatt, *Physics of Electronic Conduction in Solids*, McGraw-Hill Book Company (1968).
[17] T. Kasuya, Prog. Theor. Phys. **16**, 58 (1956).
[18] H. Fujishiro, T. Fukase, M. Ikebe, and T. Kikuchi, J. Phys. Soc. Jpn. **68**, 1469 (1999).
[19] M. R. Ibarra, P. A. Algarabel, C. Marquina, J. Blasco, and J. Garcia, Phys. Rev. Lett. **75**, 3541 (1995).
[20] S. V. Vonsovsky, *Magnetism*, Wiley, New York (1974).
[21] A. B. Beznosov, E. L. Fertman, V. V. Eremenko, P. P. Pal-Val, V. P. Popov, and N. N. Chebotayev, Fiz. Nizk. Temp. **27**, 430 (2001) [Low Temp. Phys. **27**, 320 (2001)].
[22] N. F. Mott and E. A. Devis, *Electron Processes in Non-Crystalline Materials*, Clarendon Press, Oxford (1979).
[23] C. Zener, Phys. Rev. **82**, 440 (1951).
[24] P. W. Anderson and H. Hasegawa, Phys. Rev. **100**, 675 (1955).
[25] P.-G. de Gennes, Phys. Rev. **118**, 141 (1960).
[26] S. Methfessel and D. C. Mattis, *Magnetic Semiconductors*, Springer-Verlag, New York (1968).
[27] E. L. Nagaev, *Physics of Magnetic Semiconductors*, Mir, Moscow (1983).
[28] J. M. De Teresa, M. R. Ibarra, P. A. Algarabel, C. Ritter, C. Marquina, J. Blasco, J. Garcia, A. del Moral, and Z. Arnold, Nature (London) **386**, 256 (1997).
[29] V. V. Eremenko, A. B. Beznosov, E. L. Fertman, P. P. Pal-Val, and V. P. Popov, Adv. Cryog. Eng. **46**, 413 (2000).
[30] J. Jiang, J. Dong, and D. Y. Xing, Phys. Rev. B **55**, 8973 (1997-II).

This article was published in English in the original Russian journal. Reproduced here with stylistic changes by the Translation Consultant.

MAGNETISM. PHASE TRANSITIONS

Anomalous magnetic and dynamic behavior in magnetoresistive compounds: origin of bulk colossal magnetoresistivity

V. Chechersky and A. Nath*

Department of Chemistry, Drexel University, Philadelphia, Pennsylvania 19104, USA
(Submitted January 2, 2002)
Fiz. Nizk. Temp. **28**, 781–789 (July 2002)

We present the results of our extensive Mössbauer effect studies carried out on a wide variety of mixed valence manganites as well as other types of magnetoresistive materials, including pyrochlore $Tl_2Mn_2O_7$ and the chalcospinels $Fe_{0.5}Cu_{0.5}Cr_2S_4$ and $FeCr_2S_4$ with absolutely different natures of the magnetism, in a search for similarities linked to their magnetoresistive behavior. The double exchange electron transfer and coupling between the electrons and Jahn–Teller lattice distortions invoked by most theories to explain the colossal magnetoresistivity and associated metal–insulator transition in manganites are not applicable to pyrochlore nor to chalcospinels. Nevertheless, we find intriguing similarities in the anomalous magnetic and dynamic behavior among these widely different systems at, above, and below the Curie temperature T_C, which shed light on the origin of bulk magnetoresistivity in general. All these compounds share the following features. The long-range ferromagnetic order breaks down even below the Curie temperature, with the formation of nano-size spin clusters. Softening of the lattice was observed near T_C. The short-range interactions in these spin clusters survive well above T_C. When an external magnetic field is applied, the spin clusters coalesce to form large clusters, with considerable lowering of the resistivity. There is a strong evidence that the existence of nano-size spin clusters with superparamagnetic-like behavior near T_C is a prerequisite for the occurrence of bulk magnetoresistivity. [DOI: 10.1063/1.1496668]

INTRODUCTION

The perovskite manganite $LaMnO_3$ is an insulating antiferromagnet. The Mn–O octahedra are highly distorted due to the Jahn–Teller effect. When La^{3+} is substituted by a bivalent ion like Ca^{2+}, a corresponding amount of Mn^{3+} is converted to Mn^{4+}. For instance, with the introduction of holes, the compound $La_{1-x}Ca_xMnO_3$ becomes a ferromagnetic metal for $0.18<x<0.5$. The hopping of an electron from Mn^{3+} to O^{2-} is accompanied by a simultaneous hop from the latter to Mn^{4+}. The probability of this double exchange (DE) electron transfer of an e_g electron depends on the orientation of the neighboring intra-atomic Hund's coupled t_{2g} spins. The hopping is facilitated if the spins are aligned parallel to each other. Thus the ferromagnetic alignment of spins and the rate of electron hopping which is responsible for its metallicity are synergistically tied to each other.[1] The probability of the hopping also depends on the $Mn^{3+}–O–Mn^{4+}$ bond angle. The latter is determined by the size of the rare earth/bivalent substituent ions. Among the four $3d$ electrons of Mn^{3+}, t_{2g}^3 electrons are weakly hybridized and constitute localized spin ($S=3/2$). In contrast, the e_g^{1-x} orbitals have lobes directed to neighboring oxygen atoms, and hybridize strongly with the O_{2p} orbitals, and the electron is itinerant below T_C in the ferromagnetic–metallic state and is believed to be localized in the ''paramagnetic'' insulating state above T_C. The resistivity increases considerably as one approaches T_C from below. On application of a magnetic field, there is a sharp decrease in resistivity due to regeneration of metallicity/ferromagnetism. This effect is known as ''colossal magnetoresistivity (CMR)''. To explain this surprising behavior, several researchers have invoked the concept that the mobile electron carries with it the Jahn–Teller (J–T) distortion of the MnO_6 octahedron. The greater the distortion, the more localized are the charge carriers; this deformation disappears in the metallic state below T_C.[2–5] In the ferromagnetic metallic state, there is a strong exchange interaction between the itinerant e_g electrons and the localized t_{2g} spins. The basic problems facing researchers are to understand the features driving the ferromagnetic metal to the ''paramagnetic'' insulator transition and the intriguing observation of large CMR upon application of modest external magnetic fields.

There are other systems, for instance, the spinel chalcogenide $FeCr_2S_4$ (Refs. 6–12), and the pyrochlore $Tl_2Mn_2O_7$ (Refs. 13–16) which exhibit CMR behavior. However, these systems do not show DE electron transfer nor Jahn–Teller distortions. In this paper, we will compare the magnetic and dynamic behavior of different families of CMR compounds and seek commonalities which could lead to a better understanding of the origin of bulk magnetoresistivity.

For our studies, we use a local probe, namely ^{57}Co. Emission Mössbauer spectroscopy constitutes a valuable tool for exploring the behavior of materials at the microscopic level. It is a couple of orders of magnitude more sensitive

than the regular absorption mode and requires only a few tens of parts per million of Mn substitution by ^{57}Co, with minimal perturbation of the system. On the other hand, one has to use 1–2% ^{57}Fe substitution for the regular absorption mode. The minuscule amount of the ^{57}Co substituent faithfully probes the subtle changes in electron density, local dynamics, lattice distortions, and magnetic behavior of the dominant host material. The probe can also sense the formation of different electronic phases. We have shown earlier[17–19] that the Auger after-effects do not cause any problem in systems having delocalized electrons, since the 50–100 eV excitation energy deposited at the epicenter/molecule (incorporating ^{57}Co) during electronic relaxation of the multiply charged site goes towards collective excitation of delocalized electrons. The plasmon decays in less than 10^{-14} s, transferring practically all its energy to an ejected electron. The strong coupling between plasmons formed from delocalized electrons and single-electron continuum states provides a neat mode of energy removal, leaving the ^{57}Fe site virtually unperturbed.[17–19] The 14.4 keV Mössbauer gamma rays which are dressed with information about the chemical environment are emitted with $\sim 10^{-7}$ s delay after the electron-capture nuclear decay and are therefore oblivious to the Auger event. The formation of a plasmon by excitation of delocalized electrons by synchrotron radiation and its decay by ejection of an electron has been verified by photoemission studies of C_{60} and C_{70} (Refs. 20 and 21). Later, we will make use of this feature of emission Mössbauer spectroscopy to buttress our claim that the CMR materials are insulating above T_C in the macroscopic sense only. On the microscopic scale, small magnetic clusters are formed with delocalized electrons. The delocalized electrons protect the site from suffering local radiation damage following Auger ionization.

CMR MANGANITES

Superparamagnetic-like behavior below and above T_C

Typical Mössbauer spectra of manganites as a function of temperature is represented by $La_{0.8}Ca_{0.2}Mn(^{57}Co)O_3$ in Fig. 1a (Ref. 22). Spectra showing similar behavior were reported earlier also.[23–27] The anomalous magnetic behavior of mixed valence CMR manganites becomes obvious by comparison with the computer simulated spectra for a regular ferromagnet given in Fig. 1b. In a regular ferromagnet, the spectral extent of the magnetically split sextet, which is proportional to the natural magnetization, diminishes continuously with temperature and finally collapses into a single line at T_C. On the other hand, for the manganite, the most important difference consists in observation of two components as one approaches T_C from below, a sextet *M* and a central peak *C*. In a regular ferromagnet we would expect to see the *C* component only above T_C.

In manganites, the coexisting central component grows at the expense of the sextet with increasing temperature. Such behavior is typical for superparamagnetic behavior of nano-size single-domain particles with a distribution in size. The grain size in all our polycrystalline samples is larger that 1 μm. Moreover, a single crystal of $La_{0.9}Ca_{0.1}Mn(^{57}Co)O_3$ also shows similar behavior,[28] and so we conclude that it is

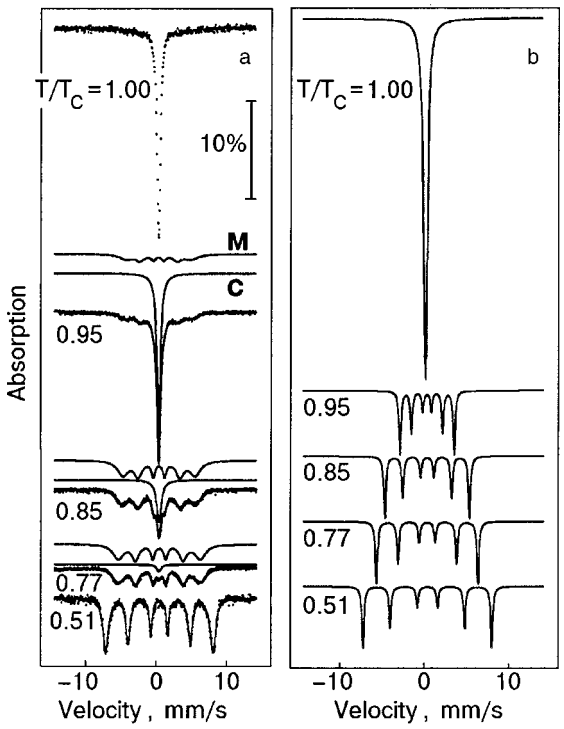

FIG. 1. Mössbauer spectra of $La_{0.8}Ca_{0.2}Mn(^{57}Co)O_3$ at different temperatures, $T_C = 198$ K (a); computer simulated Mössbauer spectra of a regular ferromagnet at various temperatures (b) [Ref. 22].

an intrinsic property of manganites that the long-range ferromagnetic order breaks down even below T_C, and nano-size magnetic clusters are formed with short-range order. If the available thermal energy at any temperature is sufficient to overcome the anisotropy barrier, then the magnetic vector of the spin clusters can flip among the easy directions at a rate faster than the Larmor frequency of the daughter ^{57}Fe (about 10^8 s^{-1}), and the internal magnetic field at the probe averages out to zero. Manganites exhibit another very interesting feature which contrasts with regular superparamagnetic behavior. The blocking temperature (the temperature at which the sextet collapses completely into a singlet/doublet when the rate of fluctuations of the magnetic vectors of all the clusters exceeds the Larmor frequency) coincides with the Curie temperature. This means that as we approach T_C from below, an increasing number of nano spin clusters are formed from the bulk, and there is always some fraction of the material exhibiting bulk-like magnetism even up to $0.99T_C$ (Fig. 2).[28,29] The sextet lines are rather broad even at $T/T_C \sim 0.3$ and become broader with increasing temperature (Fig. 1a). Only at very low temperatures ($T/T_C \sim 0.05$) does the sextet look like that of a regular ferromagnet (Fig. 1b). This broadening occurs partly due to collective excitations of clusters in directions close to the easy ones. Moreover, the exchange interactions also depend on the degree of spin alignment, which varies with the cluster size, resulting in a distribution of internal hyperfine magnetic fields experienced by the Mössbauer probe, which tend to increase with temperature.

Influence of external magnetic field

The question arises whether the collapsed singlet both below and above T_C is really due to ''superparamagnetically

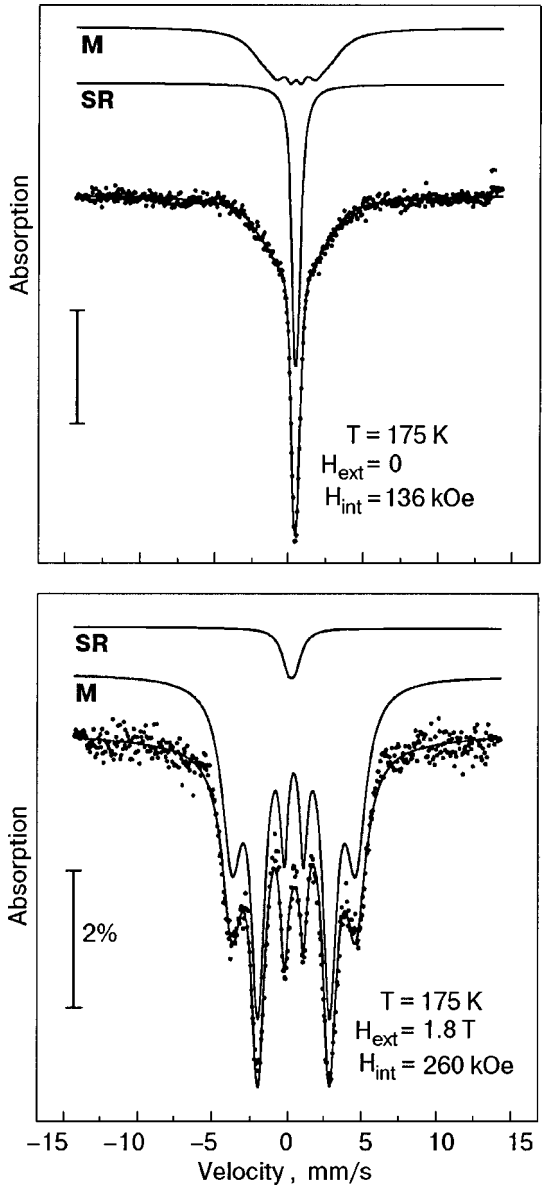

FIG. 2. Mössbauer spectra of the $La_{0.9}Ca_{0.1}Mn(^{57}Co)O_3$ single crystal with and without $H_{ext}=1.8$ T at $T=175$ K ($T/T_C=0.99$). The computer fits are shifted upward for clarity [Ref. 28].

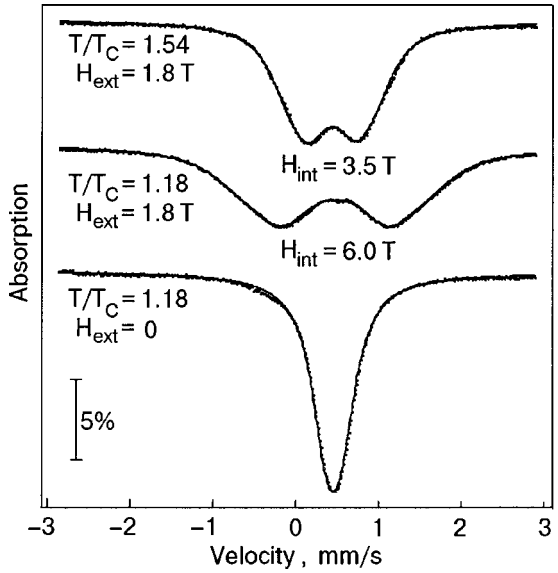

FIG. 3. Effect of $H_{ext}=1.8$ T on the Mössbauer spectra of $La_{0.8}Ca_{0.2}Mn(^{57}Co)O_3$ at $T/T_C=1.18$ and 1.54; $T_C=198$ K [Ref. 26].

relaxed'' spin clusters or due to ordinary paramagnetic species. We can get the answer by observing the Mössbauer spectrum near T_C in a modest external magnetic field H_{ext}. One can see from Fig. 2 a dramatic change in the Mössbauer spectrum with the application of $H_{ext}=1.8$ T. One observes a regular magnetically split spectrum characteristic of a bulk ferromagnet with an induced internal magnetic field $H_{int}=260$ kOe. This is very graphic evidence of the coalescence of the pre-existing nano-size clusters to form large clusters with well-ordered ferromagnetic alignment.

The next question is whether these nano spin clusters survive well above T_C. If they do not, one will not be able to rationalize the observation of magnetoresistivity above the Curie temperature. Figure 3 depicts changes in the Mössbauer spectrum at $T=1.18T_C$ and $T=1.54T_C$ in $H_{ext}=1.8$ T. The spectra can be fit by a magnetically split sextet with $H_{int}=60$ and 35 kOe, respectively, and the line intensity ratio 3:4:1:1:4:3 corresponding to magnetization of the sample perpendicular to the gamma-ray direction. These observations clearly indicate the presence of pre-existing nano spin clusters, each with an adequate total spin to react to a very modest H_{ext} at temperatures comparable to room temperature, and which consolidate into larger clusters as indicated by the relatively robust H_{int} (Fig. 3). The interaction between spin clusters aided by H_{ext} is synergetic, i.e., a better alignment of spins results in an improved DE electron transfer/metallicity, which in turn enhances the spin ordering. Therefore, a direct correlation exists between the change in the abundance of the ferromagnetic fraction and the magnetoresistivity as a function of temperature on application of H_{ext} (Ref. 26). Also a linear dependence of the resistance on the magnitude of ferromagnetic fraction in zero H_{ext} in $La_{0.8}Ca_{0.2}Mn(^{57}Co)O_3$ was observed.[25] These observations are based on simultaneous measurements of resistance and emission Mössbauer spectra. The observed correlation suggests that the current flows almost exclusively through filamentary ferromagnetic regions surrounded by superparamagnetic nano spin clusters.[25,30,31] It may be mentioned that the above-discussed evidence for the existence of nano spin clusters (magnetic polarons) above T_C can be further reinforced by the following technique. If spin clusters really exist above T_C, there is a probability that some of them could be relatively large and fluctuate slowly enough with relaxation time in a range centered at about 10^{-9} s. The Mössbauer spectra originating from such clusters may consist of a semicollapsed central part with very wide wings.[32,33] It is easy to lose these extensive wings in the background during computer analysis, while the central part can incorrectly be analyzed to be a part of the completely superparamagnetically relaxed component originating from the major fraction of smaller spin clusters. If the energy scale during the measurements is deliberately adjusted to cut the extensive wings and accommodate only the collapsed central component, it becomes possible to determine indirectly the existence of such type of clusters above T_C by observing the normalized area of the spectrum as a function of temperature. Experiment

shows that as the temperature is lowered toward T_C, the abundance (normalized area) instead of increasing, as expected according to the theory, goes down—the closer to T_C, the greater the observed loss. This suggests that by approaching T_C from above and keeping a narrow energy window, we lose gradually increasing amounts of spectral area associated with the fraction of clusters whose fluctuating rate becomes less than about 10^9 s^{-1} (Ref. 29).

De Teresa and coworkers[34] made measurements of the volume thermal expansion with and without H_{ext}, the magnetic susceptibility, and the small-angle neutron scattering (SANS). They interpreted their observations by invoking the presence of magnetic polarons dispersed in a paramagnetic matrix. Our observations given in Figs. 2 and 3 do not bear out the presence of a paramagnetic matrix: all the nano spin clusters present are equally affected and grow under the influence of H_{ext}. It may be mentioned that a specific spin does not belong always to the same spin cluster, but there is a continuous exchange of spins between the clusters. The dynamics of the exchange has to be slower than the Larmor period of ^{57m}Fe ($\sim 10^{-8}$ s), otherwise the probe nuclei would not sense the internal hyperfine field, and instead of the sextet one would observe a completely collapsed spectrum.[22,35] Related to it are the observations made by Raquet *et al.*[36] in $La_{2/3}Ca_{1/3}MnO_3$ films of giant random telegraph noise in the resistance fluctuations well below T_C. They attribute it to the dynamic mixed-phase percolative conduction process, where manganese clusters switch back and forth between two phases that differ in their conductivity and magnetization. Similar observations were made by Podzorov *et al.*[37] and Zhang *et al.*[38] In this compound, apart from two ferromagnetic phases,[39,40] we also detect nano size magnetic clusters well below T_C (Ref. 39), which can help one to understand the observations made in the above-mentioned research.

Taking into consideration the superparamagnetic-like behavior of mixed valence manganites at different temperatures[22–29,39] and the interaction energy between a modest H_{ext} and the nano spin clusters (Fig. 3), we estimate the average size of the magnetic clusters as roughly 20 Å in diameter (if approximated by a sphere), containing a couple of hundred Mn^{3+}/Mn^{4+} atoms. The distribution of cluster size and the temperature range in which clusters are formed from the bulk near T_C varies with the fraction of bivalent ion (Ca^{2+},Sr^{2+}) substitution for La^{3+}. For the 30% Ca/Sr substituted compound it was found to be narrower than for compounds with 10 and 20% Ca substitution, as discussed below. Figure 4 shows the supermagnetically relaxed fraction as a function of T/T_C. The derivative of this plot gives a qualitative feel for the distribution of cluster size (Fig. 5). However, we have to keep in mind that at any given temperature, we are not dealing with pre-existing magnetic clusters with a large distribution in size, but rather a quite narrow distribution with increasing number of clusters being formed from the bulk as the temperature is increased. As is seen from Fig. 4, there is a definite correlation between the magnetic quality of the compound (represented by the Curie temperature) and the temperature range in which transformation takes place: the higher the T_C, the narrower the range. It seems that the better the ferromagnetic material (with higher conductivity)

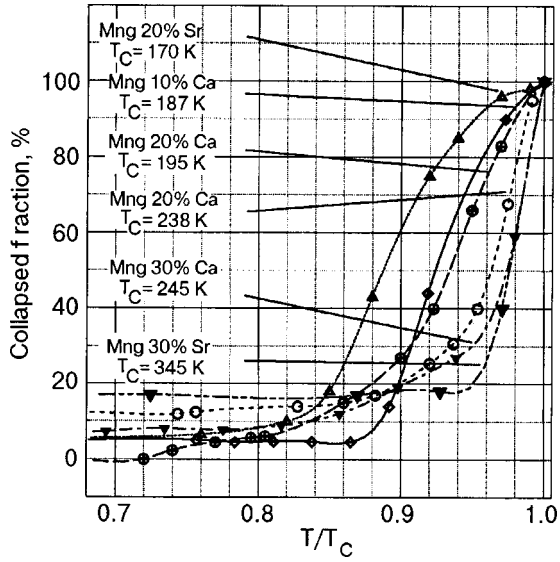

FIG. 4. Plot of superparamagnetically collapsed fraction vs T/T_C for various CMR manganites, obtained by computer analysis of the temperature evolution of their emission Mössbauer spectra. The different T_C's for samples with the same degree of substitution is a result of the different oxygen content.

the more-homogeneous clusters it will have, with a narrower distribution in size. At the same time, it is known that the CMR effect decreases with the increase of T_C. We also observe a smaller effect of H_{ext} on Mössbauer spectra of samples with higher Curie temperature. We attribute this to a smaller average cluster size in compounds with higher T_C.

Model

Now we have to address the question as to how the long-range ferromagnetic order breaks down with formation of nano size magnetic clusters below T_C and the survival of the short-range order in the spin clusters up to a temperature close to $2T_C$.[26,29,30,35] This behavior contrasts sharply with

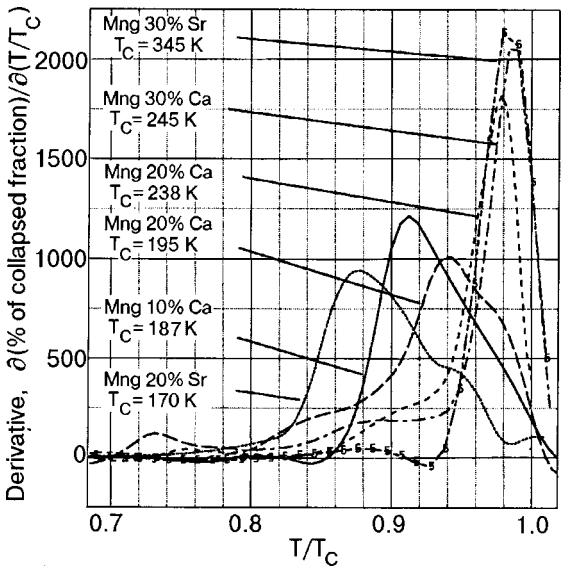

FIG. 5. Derivatives of the results presented in Fig. 4 which reflect the rate of cluster formation from the bulk with temperature as well as the width of the cluster size distribution.

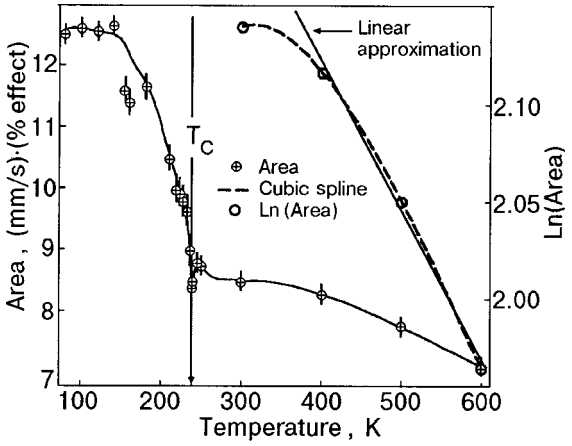

FIG. 6. Plot of normalized total area under the Mössbauer spectra of $La_{0.8}Ca_{0.2}Mn(^{57}Co)O_3$ as a function of temperature. The solid line is a guide for the eye.

that of regular ferromagnets like Fe and Ni, where magnetic correlations are observed only up to $1.1T_C$, and there is no evidence of the formation of spin clusters below T_C. A very revealing observation made by Mössbauer studies was the sharp drop in the total Mössbauer spectral area when approaching T_C from below.[25,35] The magnitude of the Mössbauer area is indicative of how strongly the Mössbauer probe is bound to the Mn–O–Mn network. A sharp decrease below T_C strongly suggests softening of the phonon spectra (Fig. 6). This softening occurs presumably due to the anharmonic stretching of Mn–O bonds and the enhanced amplitude of torsional oscillations of the Mn–O octahedra. The anomalous increase in Mn–O bond lengths, bending of the Mn–O–Mn moiety, and the enhanced Debye–Waller factors for Mn and O atoms below T_C have also been observed by x-ray and neutron diffraction studies.[41–47] These observations have also been attributed to anharmonic oscillations by Dai *et al.*[41] and Rodrigues-Martinex and Attfield.[45] The anomalous increase in thermal expansion near T_C can also be attributed to anharmonicity.[34,41,48,49] The localized distortions resulting from aliovalent substitution, e.g., Ca^{2+} and Sr^{2+}, are presumably responsible for the anomalous anharmonicity. The stretching of bonds and the larger amplitude of torsional oscillations between Mn–O octahedra would decrease the exchange interactions and also the rate of DE electron hopping; the two parameters are intertwined synergistically. For instance, if the amplitude of the torsional oscillations increases with temperature, the rate of electron hopping will decrease, as the neighboring spins will have to wait until thermal fluctuations allow them an appropriate configuration for a double exchange hop (Franck–Condon factor). Therefore, with increasing temperature below T_C the long-range ferromagnetic order breaks down, and nano size ferromagnetic clusters with short range interactions and superparamagnetic-like fluctuations appear. The fluctuations are responsible for strong electron scattering. On application of an external magnetic field, the nano spin clusters (which survive even well above T_C) tend to coalesce and grow in size. If the clusters become large enough to exhibit conductivity by percolation, CMR will be observed.[24–26,30,31] One of the parameters determining the magnitude of CMR depends on the degree of alignment of spin clusters upon application of H_{ext}, which in turn depends on the initial cluster size. Our work seems to suggest that the cluster size increases with decrease in Curie temperature of the material.

Now the question arises whether these magnetic (clusters) polarons are dressed with lattice distortions. The Mössbauer spectra above T_C for all studied manganites show very small quadrupole splitting (about 0.18 mm/s)[22,29] (and which becomes even smaller below T_C), indicating that the distortions imposed on the octahedron containing the Mössbauer probe by the surrounding Mn–O network is quite small. The probe senses distortions in a 10^{-7} s period. Our observation of a single major species above T_C is supported by ESR studies on $La_{1-x}Sr_xMnO_3$ ($x=0.1$, 0.2, and 0.3) by Lofland *et al.*[50] They find that all Mn spins contribute to the spectrum above T_C, indicating the formation of magnetic clusters. Similarly, Kapusta *et al.*[51] report the observation of a single ^{55}Mn NMR line both below and above the Curie temperature for $La_{1-x}A_xMnO_3$ (A=Ca,Sr), providing direct evidence of magnetic correlations on a time scale greater than 10^{-5} s. These results obtained by techniques which operate on a relatively slow time scale are in apparent contradiction with observations made by much faster methods. The x-ray absorption fine structure spectroscopy and pair distribution function studies on CMR manganites show lattice distortions above T_C.[2–5] Neutron scattering investigations also give evidence of distortion in the insulating state above T_C.[41–47] Moreover, the spin stiffness coefficient does not go to zero at T_C, a fact which indicates the existence of short-range magnetic interactions as in magnetic clusters (polarons). Two recent reports which bear directly on our model are worthy of mention. Dai *et al.*[52] and Adams *et al.*[53] using neutron scattering have demonstrated the presence of polarons even below T_C in $La_{1-x}Ca_xMnO_3$ ($x=0.2$ and 0.3). They also observe short- range polaron correlations with a coherence length of $\sim$28 Å just above the Curie temperature. Here the time scale of observations is several orders of magnitude shorter than that for the Mössbauer method. We feel that their results are consistent with our model; they are observing magnetic clusters but with larger distortions than us just because the distortions detected on a time scale of $\sim 10^{-12}$ s would be averaged out on the Mössbauer time scale of $\sim 10^{-7}$ s, if they are of a dynamic nature. Since the frequency of Jahn–Teller oscillations is reduced near T_C due to slowing down of the DE electron transfer, neutron scattering can detect the distortions. However, they are still fast for the Mössbauer time window.

OTHER CMR COMPOUNDS

Recently there have been reports of some non-manganite-based systems which also exhibit magnetoresistivity. Among them are the pyrochlore $Tl_2Mn_2O_7$ and the chalcospinels $Fe_{0.5}Cu_{0.5}Cr_2S_4$ and $FeCr_2S_4$, in which neither DE transfer between aliovalent ions nor Jahn–Teller distortions occur. The pyrochlore $Tl_2Mn_2O_7$ shows CMR without Mn^{3+}/Mn^{4+} DE. Its formal oxidation states as detected by x-ray diffraction are $Tl_2^{3+}Mn_2^{4+}O_7$ (Refs. 13 and 14). Calculations show that the Fermi surface is derived from strongly mixed combinations of Tl, Mn, and O orbitals.[15,16] Our preliminary emission Mössbauer investigations show evidence of the existence of nano-size ferromagnetic clusters in this

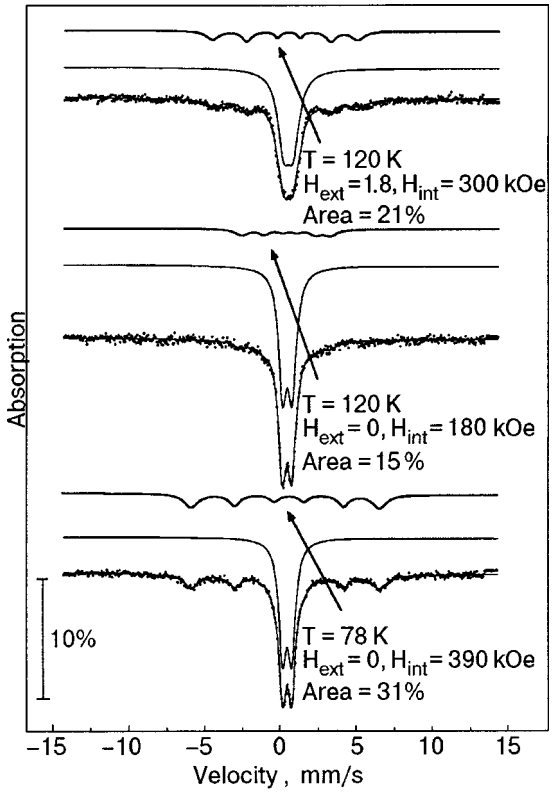

FIG. 7. Mössbauer spectra of the pyrochlore $Tl_2Mn_2(^{57}Co)O_7$ ($T_C = 123$ K) (Ref. 22).

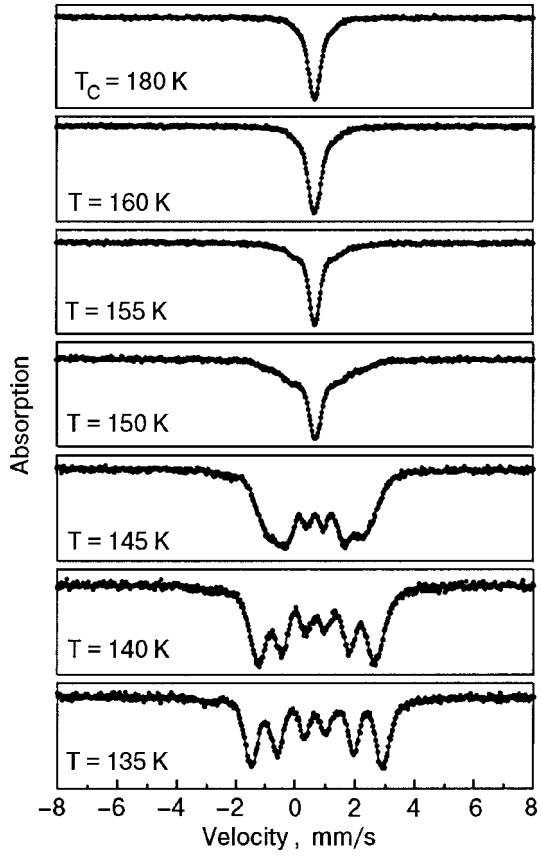

FIG. 8. ^{57}Fe Mössbauer spectra of $FeCr_2S_4$ taken at selected temperatures at and below the magnetic ordering temperature ($T_C = 180$ K) [Ref. 56].

compound at and below the Curie temperature $T_C = 123$ K.[22,54] The Mössbauer spectra of $Tl_2Mn_2(^{57}Co)O_7$ at 78 and 120 K without external magnetic field and at 120 K with $H_{ext} = 1.8$ T are shown in Fig. 7. One can see a coexistence of collapsed and magnetically split components. When the temperature is raised from 78 K to 120 K, the area of the sextet decreases from 31% to 15%, with the corresponding increase of the area of the collapsed component, and the internal hyperfine magnetic field decreases from 390 kOe to 180 kOe. Upon application of $H_{ext} = 1.8$ T at $T = 120$ K, not only does the area of the sextet increase to 21% but, most importantly, H_{int} increases to 300 kOe. We expect that lowering the temperature to $T/T_C \sim 0.15$ would result in a spectrum consisting mainly of the magnetically ordered component. In short, the changes observed in the Mössbauer spectra of $Tl_2Mn_2(^{57}Co)O_7$ as a function of temperature and under the influence of H_{ext} are similar to the case of the manganites, discussed earlier. It allows us to assign with confidence a superparamagnetic nature to the central collapsed component originating from the existence of nano-size magnetic clusters.

Lang *et al.*[55] have reported ^{57}Fe Mössbauer spectra of the CMR chalcospinel $Fe_{0.5}Cu_{0.5}Cr_2S_4$ at temperatures ranging from 4 K to 300 K. From their figures one can observe the coexistence of a central peak and a sextet at all temperatures below 300 K. The central peak increases in intensity at the expense of the sextet as the temperature is increased. The authors do not discuss this behavior. However, we would like to attribute it to superparamagnetic-like behavior of spin clusters which form in increasing amounts from the bulk as one approaches T_C from below.

We have recently studied another chalcospinel $FeCr_2S_4$ using the ^{57}Fe absorption method[56] in the temperature range 78–300 K ($T_C = 180$ K). $FeCr_2S_4$ is a *p*-type semiconducting ferrimagnet with a Curie temperature above 175 K. The formal charges are Fe^{2+}, Cr^{3+}, and S^{2-}, with considerable covalent character. The Fe^{2+} ions occupy tetrahedral sites and Cr^{3+} octahedral ones. They are aligned antiferromagnetically. Double exchange electron transfer in this compound is ruled out. Some representative experimental data are shown in Fig. 8. Features previously discussed can be clearly seen from this figure. At low temperatures one observes only one component—a well defined sextet. As the temperature increases, a central collapsed component emerges, gradually growing at the expense of the sextet. We also found that the total area of the spectrum shows a sharp decrease between 145 and 170 K, indicating softening of the lattice, a feature similar to that observed by us for all CMR manganites. At a temperature of 186 K, i.e., above T_C, application of an external magnetic field of 6 T restores the well-defined sextet typical for the bulk ferromagnet, indicating the coalescence of nano spin clusters.

On the basis the these observations one can infer that in many respects CMR pyrochlore and chalcospinels demonstrate similar behavior, namely: (i) the long-range ferromagnetic order breaks down gradually when approaching T_C from below, with the formation of spin clusters; (ii) nano-size spin clusters survive well above T_C; (iii) application of an external magnetic field at or above T_C causes coalescence of those clusters, with restoration of bulk-like ferromagnetism and lowering of the resistivity. These common fea-

tures among widely different magnetoresistive materials indicate that the existence of nano-size clusters with superparamagnetic-like behavior is a prerequisite for observing bulk negative magnetoresistivity in such systems.

A.N. thanks the donors of the PRF administered by ACS for partial support of this research.

*E-mail: amar.nath@drexel.edu

[1] C. Zener, Phys. Rev. **82**, 403 (1951); P. W. Anderson and H. Hasegawa, Phys. Rev. **100**, 675 (1953).
[2] J. M. D. Coey, M. Viret, and S. von Molnar, Adv. Phys. **48**, 167 (1999).
[3] *Colossal Magnetoresistive Oxides*, Y. Tokura (Ed.), Gordon and Breach Sci. Publ. Amsterdam (2000).
[4] E. L. Nagaev, Phys. Rep. **346**, 387 (2001).
[5] M. B. Salomon and M. Jaime, Rev. Mod. Phys. **73**, 583 (2001).
[6] P. F. Bongers, C. Haas, A. M. J. G. van Run, and G. Zanmarchi, J. Appl. Phys. **40**, 958 (1969).
[7] T. Watanabe, Solid State Commun. **12**, 355 (1973).
[8] K. Ando, Y. Nishihara, T. Okuda, and T. Tsushima, J. Appl. Phys. **50**, 1917 (1979).
[9] A. P. Ramirez, R. J. Cava, and J. Krajewski, Nature (London) **386**, 156 (1997).
[10] Z. Chen, S. Tan, Z. Yang, and Y. Zhang, Phys. Rev. **B59**, 11172 (1999).
[11] Z. Yang, S. Tan, Z. Chen, and Y. Zhang, Phys. Rev. B **62**, 13872 (2000).
[12] E. Z. Kurmaev, A. V. Postnikov *et al.*, J. Phys.: Condens. Matter **12**, 5411 (2000).
[13] M. A. Subramanian, B. H. Toby, A. P. Ramirez, W. J. Marshall, A. W. Sleight, and G. H. Kwei, Science **273**, 81 (1996).
[14] G. H. Kwei, C. H. Booth, F. Bridges, and M. A. Subramanian, Phys. Rev. B **55**, R688 (1997).
[15] D. J. Singh, Phys. Rev. B **55**, 313 (1997).
[16] Y. Shimakawa and Y. Kubo, Mater. Sci. Eng. B **63**, 44 (1999).
[17] M. B. Misrock, C. J. Schramm, and A. Nath, J. Chem. Phys. **65**, 1982 (1976).
[18] A. Nath, Ch. Sauer, and A. Halpern, J. Chem. Phys. **78**, 5125 (1983).
[19] A. Nath, M. Prushan, and J. G. Gilbert, J. Radioanal. Nucl. Chem. **247**, 589 (2001).
[20] I. V. Hertel, H. Steger, J. de Vries, B. Weisser, C. Menzel, B. Kamke, and W. Kamke, Phys. Rev. Lett. **68**, 784 (1992).
[21] S. Hunsche, T. Starczewski, A. l'Huillier, A. Persson, C.-G. Wahström, B. van den Heuvell, and S. Svanberg, Phys. Rev. Lett. **77**, 1966 (1996).
[22] A. Nath, V. Chechersky, and R. L. Greene, J. Solid State Chem. **55**, 116 (2000). *Invited contribution*.
[23] M. Pissas, G. Kallias, E. Devlin, A. Simopolous, and D. Niarchos, J. Appl. Phys. **81**, 5770 (1997).
[24] V. Chechersky, A. Nath, H.-L. Ju, and R. L. Greene, Fiz. Nizk. Temp. **23**, 727 (1997) [Low Temp. Phys. **23**, 545 (1997)].
[25] V. Chechersky, K. Nomura, A. Nath, H.-L. Ju, and R. L. Greene, Fiz. Nizk. Temp. **23**, 732 (1997) [Low Temp. Phys. **23**, 549 (1997)].
[26] V. Chechersky, A. Nath, I. Isaac, J. P. Franck, K. Ghosh, H-L. Ju, and R. L. Greene, Phys. Rev. B **59**, 497 (1999).
[27] V. Chechersky, A. Nath, I. Isaac, J. P. Franck, K. Ghosh, and R. L. Greene, Phys. Rev. B **60**, 3005 (1999).
[28] V. Chechersky, A. Nath, S. E. Lofland, S. Newlander, L. Cerquoni, Y. Mukovskii, A. A. Arsenov, G. Karabshev, D. A. Shulyatev, and R. L. Greene, Phys. Rev. B **63**, 4401 (2001).
[29] V. Chechersky, A. Nath, I. Isaac, J. P. Franck, K. Ghosh, and R. L. Greene, Phys. Rev. B **63**, 052411 (2001).
[30] M. Jaime, P. Lin, S. H. Chun, M. B. Salamon, P. Dorsey, and M. Rubinstein, Phys. Rev. B **60**, 1028 (1999), S. H. Chun, M. B. Salamon, Y. Tomioka, and Y. Tokura, Phys. Rev. B **61**, R9225 (2000).
[31] L. P. Gor'kov and V. Z. Kresin, JETP Lett. **67**, 985 (1998).
[32] H. H. Wickmann, M. P. Klein, and D. A. Shirley, Phys. Rev. **152**, 345 (1966).
[33] S. Morup, Hyperfine Interact. **60**, 959 (1990).
[34] J. M. De Teresa, M. R. Ibarra, P. A. Algarabel, C. Ritter, C. Marquina, J. Blasco, J. Garcia, C. Fermon, A. del Moral, and Z. Arnold, Nature (London) **386**, 256 (1997).
[35] V. Chechersky, A. Nath, I. Isaac, J. P. Franck, K. Ghosh, and R. L. Greene, J. Phys.: Condens. Matter **11**, 8921 (1999).
[36] B. Raquet, A. Anane, S. Wirt, P. Xiang, and S. von Molnar, Phys. Rev. Lett. **84**, 4485 (2000).
[37] V. Podzorov, M. E. Gershenson, M. Uehara, and S.-W. Cheong, Phys. Rev. D **64**, 115113 (2001).
[38] J. Zhang, P. Dai, J. A. Fernandez-Baca, E. W. Plummer, Y. Tomioka, and Y. Tokura, Phys. Rev. Lett. **86**, 3823 (2001).
[39] V. Chechersky, A. Nath, C. Michel, M. Hervieu, K. Ghosh, and R. L. Greene, Phys. Rev. B **62**, 5316 (2000).
[40] M. M. Savosta and P. Novak, Phys. Rev. Lett. **87**, 137204 (2001).
[41] P. Dai, J. Zhang, H. A. Mook, S.-H. Liou, P. A. Dowben, and E. W. Plummer, Phys. Rev. B **54**, R3694 (1996).
[42] P. G. Radaelli, M. Marezio, H. Y. Hwang, S.-W. Cheong, and B. Batlogg, Phys. Rev. B **54**, 8992 (1996).
[43] P. G. Radaelli, G. Iannone, M. Marezio, H. Y. Hwang, S.-W. Cheong, J. D. Jorgensen, and D. N. Argyriou, Phys. Rev. B **56**, 8265 (1997).
[44] Q. Huang, A. Santoro, J. W. Lynn, R. W. Erwin, J. A. Borchers, J. L. Peng, K. Ghosh, and R. L. Greene, Phys. Rev. B **58**, 2684 (1998).
[45] L. M. Rodriguez-Martinez and J. P. Attfield, Chem. Mater. **11**, 1504 (1999).
[46] S. G. Hibble, S. P. Cooper, A. C. Hannon, I. D. Fawcett, and M. Greenblatt, J. Phys.: Condens. Matter **11**, 9221 (1999).
[47] A. Mellergard, R. L. McGreevy, and S. G. Eriksson, J. Phys.: Condens. Matter **12**, 4975 (2000).
[48] V. Caignaert, E. Suard, A. Maignan, C. Simon, and B. Raveau, C. R. Acad. Sci. Paris **321**, 515 (1995).
[49] M. R. Ibarra, P. A. Algarabel, C. Marquina, J. Blasco, and J. Garsia, Phys. Rev. Lett. **75**, 3541 (1995).
[50] S. E. Lofland, P. Kim, P. Dahiroe, S. M. Bhagat, S. D. Tyagi, S. G. Karabshev, D. A. Shulyatev, A. A. Arsenov, and Y. Mukovskii, Phys. Lett. A **233**, 476 (1996).
[51] Cz. Kapusta, P. C. Riedi, W. Kocemba, G. J. Tomka, M. R. Ibarra, J. M. De Teresa, M. Viret, and J. M. D. Coey, J. Phys.: Condens. Matter **11**, 4079 (1999).
[52] P. Dai, J. A. Fernandez-Baca, N. Wakabayashi, E. W. Plummer, Y. Tomioka, and Y. Tokura, Phys. Rev. Lett. **85**, 2553 (2000).
[53] C. P. Adams, J. W. Lynn, Y. M. Mukovskii, A. A. Arsenov, and D. A. Shulyatev, Phys. Rev. Lett. **85**, 3954 (2000).
[54] V. Chechersky, A. Nath, M. A. Subramanian, and R. L. Greene (unpublished).
[55] O. Lang, C. Felser, R. Seshadri, F. Renz, J.-M. Kiat, J. Ensling, P. Gutlich, and W. Tremel, Adv. Mater. **12**, 65 (2000).
[56] A. Nath, Z. Klencsar, E. Kuzmann, Z. Homonnay, A. Vertes, A. Simopoulos, E. Devlin, G. Kallias, A. P. Ramirez, and R. J. Cava (unpublished).

This article was published in English in the original Russian journal. Reproduced here with stylistic changes by the Translation Consultant.

Magnetic phase transitions in the system $La_{1-x}Bi_xMnO_{3+\lambda}$

I. O. Troyanchuk* and O. S. Mantytskaja

Institute of Solid State and Semiconductor Physics of National Academy of Sciences of Belarus, 17 P. Brovki Str., Minsk 220072, Belarus

H. Szymczak

Institute of Physics of Polish Academy of Sciences, 32/46 Al. Lotnikow Str., Warsaw PL-02-668, Poland

M. Yu. Shvedun

B. Verkin Institute for Low Temperature Physics and Engineering of the National Academy of Science of Ukraine, 47 Lenin Ave., Kharkov 61103, Ukraine

(Submitted January 4, 2002)
Fiz. Nizk. Temp. **28**, 790–795 (July 2002)

The crystal structure and magnetic properties of the $La_{1-x}Bi_xMnO_{3+\lambda}$ system ($0 \leqslant x \leqslant 1$; $\lambda \leqslant 0.08$) are studied as functions of the oxygen and bismuth contents. In oxidized samples $La_{1-x}Bi_xMnO_{3+\lambda}$ a phase transition from a ferromagnetic state (rhombohedric phase) to a state of the spin glass type (quasitetragonal phase) is observed with increase of the bismuth concentration. The reduced samples $La_{1-x}Bi_xMnO_3$ are weak ferromagnets down to $x \leqslant 0.6$ and then transform into a ferromagnetic state. It is supposed that the Bi^{3+} ions stabilize the $d_{x^2-y^2}$ orbitals in the nearest Mn^{3+} ions whereas the d_{z^2} orbitals of the La^{3+} ions are stabilized. The orbitally disordered phases and $d_{x^2-y^2}$-orbitally ordered phases are ferromagnetic, the d_{z^2}-orbitally ordered phases show antiferromagnetic ordering, and the state of the orbital glass type corresponds to a state of the spin glass type.
[DOI: 10.1063/1.1496669]

INTRODUCTION

Recently considerable interest has been attracted to strongly correlated systems with perovskite-like structure. The variety of triple perovskites such as RMO_3 (R is a rare-earth metal, M is a transition metal) is quite great, but with variation of the rare-earth element (R=La, Pr, Nd etc.) and the addition of the practically unlimited set of solutions $R_{1-x}A_xMnO_3$, the number of combinations becomes extremely large.

Manganites $R_{1-x}A_xMnO_3$ have interesting and unusual properties. These compounds contain ions with orbital degeneracy or Jahn–Teller (JT) ions (in our case Mn^{3+}).[1] Thus their properties differ appreciably from those of the corresponding substances with the ''ordinary'' ions: the crystal structure turn out to be distorted, structural phase transitions and transitions in a magnetic subsystem[2–6] are frequently observed in them, and in many cases they have anomalously strong magnetic anisotropy and magnetostriction.[7,8] Such phenomena are connected with an interaction of the JT ions and are called the cooperative Jahn–Teller effect (CJTE). Distortions of the crystal lattice are caused by the fact that ion Mn^{3+} is degenerate with respect to the d orbitals: the crystal field splits the atomic d level into two- and threefold degenerate sublevels e_g and t_{2g} (the e_g state is characterized by the real wave functions d_{z^2} and $d_{x^2-y^2}$). The first of them lies above the second one, and consequently the four d electrons of the Mn^{3+} ion occupy the level t_{2g} completely and the level e_g only in part. This also makes CJTE possible, which reduces the energy of such a degenerate system by lowering its symmetry, which lifts the degeneracy of the electronic levels.

Despite the numerous works devoted to research on manganites, many problems remain subject to discussion. The unusual magnetic behavior of bismuth-containing manganites is one such problem. While the lanthanum-based manganites (Ln–La, Y, rare-earth ion) are antiferromagnetic,[9] bismuth manganite is a ferromagnetic insulator.[10,11] Moreover, while substitution of the lanthanoid by an alkaline-earth metal leads to a transition from the antiferromagnetic to a ferromagnetic metallic state,[12] a similar substitution for $BiMnO_3$-based manganites destroys the ferromagnetic order.[13–15]

The aim of the present work is to study phase transitions in a system of manganites where La^{3+} ions are replaced by Bi^{3+} ions. Formally upon such a substitution the valence of the manganese ions should not change.

EXPERIMENT

Samples of the $La_{1-x}Bi_xMnO_{3+\lambda}$ system were obtained by three different methods: in air, under a high pressure, and in vacuum. The initial reagents were oxides of La_2O_3, Bi_2O_3 and Mn_2O_3, mixed in the desired proportion. The manganite of lanthanum was obtained at $T=1500\,^\circ$C in air. Synthesis of Bi-containing samples was carried out in the temperature range of 900–1150 °C with a subsequent slow cooling (100 °C/h). The temperature of synthesis decreased with increasing bismuth content from 1150 °C ($x=0.2$) to 900 °C ($x=0.7$). According to x-ray phase analysis, in a sample with $x=0.7$ there were traces of extraneous phases; therefore

TABLE I. Unit cell parameters of $La_{1-x}Bi_xMnO_{3.07}$ compounds obtained in air.

Composition	Symmetry	*a*, Å	*c*, Å	α, deg	*V*, Å^3
$LaMnO_{3.07}$	R	7.8105	–	90.46	59.55
$La_{0.8}Bi_{0.2}MnO_{3.07}$	R	7.8165	–	90.45	59.69
$La_{0.7}Bi_{0.3}MnO_{3.07}$	R	7.8191	–	90.34	59.75
$La_{0.6}Bi_{0.4}MnO_{3.07}$	R	7.8198	–	90.27	59.7
$La_{0.5}Bi_{0.5}MnO_{3.07}$	T	3.9098	3.9352	–	60.156
$La_{0.4}Bi_{0.6}MnO_{3.07}$	T	3.9048	3.9409	–	60.09

in these states the saturated concentration of bismuth is limited to a value of 65%. A chemical analysis has shown that all compounds obtained in air have an excess of oxygen in comparison with the stoichiometric ratio. Substitution of the La^{3+} ions by Bi^{3+} has only a weak influence on the oxygen content. The chemical formula is $La_{1-x}Bi_xMnO_{3.07\pm0,01}$. The samples prepared by the method described were reduced in quartz vacuum tubes at 900 °C in the presence of tantalum metal for absorption of allocated oxygen. Control of the oxygen maintenance was carried out by mass weighing of the sample before and after the reduction process. The chemical formula was ''squared up'' on loss of the mass. Compounds with $x \geqslant 0.7$ were obtained using a high-pressure technique (pressure 4 GPa, temperature 900 °C, duration of synthesis 20 min). These samples were characterized by the chemical composition $La_{1-x}Bi_xMnO_{3\pm0.01}$.

X-ray structure studies were carried out on a DRON-3 diffractometer in Cr K_α radiation. Single-phase structures were selected for measurement of the magnetic and electric properties. Magnetic measurements were carried out on a commercial vibrating Foner magnetometer. The electroconductivity was measured by a standard four-probe technique. Indium contacts were used. They were applied using ultrasound.

RESULTS AND DISCUSSION

According to the x-ray data, the samples of the $La_{1-x}Bi_xMnO_{3.07}$ series obtained in air were characterized by rhombohedral distortions of the unit cell up to a concentration $x=0.4$. In samples with $x \geqslant 0.5$ the type of distortions changed to tetragonal. The compounds reduced in vacuum and obtained under a high pressure had a monoclinic or orthorhombic deformed unit cell.

Upon substitution of lanthanum by bismuth, the volume of the unit cell varied only slightly, apparently because of the similarity of the ionic radii of La^{3+} and Bi^{3+}. The unit cell parameters of some solid solutions are given in Tables I and II. According to structural studies,[16] the excess over stoichiometric oxygen in the system $LaMnO_{3+\lambda}$ is a consequence of the formation of an equivalent number of vacancies of La^{3+} and Mn^{3+} ions. Apparently this mechanism of nonstoichiometry is pertinent to system $La_{1-x}Bi_xMnO_{3+\lambda}$ also, as the oxygen ions cannot occupy interstitial positions in the close-packed perovskite structure.

Field curves of the magnetization $M(H)$ at liquid helium temperature for several samples prepared in air are shown in Fig. 1. $LaMnO_{3,07}$ is ferromagnetic, as the specific magnetization corresponds to a parallel orientation of the magnetic moments of the manganese ions. With increase of the bismuth content up to $x=0.65$, a gradual decrease of the spontaneous magnetization was observed. In compounds with $x=0.6$ and $x=0.65$ the magnetization remains unsaturated in fields up to 16 kOe, as is typical for magnets with weak cooperative exchange interactions. Ferromagnetic solutions ($x \leqslant 0.4$) are soft magnetic materials whereas in samples with $x \leqslant 0.5$ the coercive force sharply increases. The temperature curves of the magnetization obtained in a rather small external magnetic field of 100 Oe are shown in Fig. 2. The measurements were performed in a mode of heating after cooling in a field (FC) and without a field (ZFC). It follows from the diagrams that the Curie temperature decreases with increase of bismuth content. The ZFC magnetization of a sample with $x=0.6$ has a wide maximum, which is typical for a magnet near the concentration transition from a ferromagnetic state to the state such as a spin glass. On further increase of the bismuth content the magnetic susceptibility sharply decreases. The ZFC magnetization in a sample with $x=0.65$ has a well-defined maximum. Near the temperature of the maximum the ZFC and FC magnetizations diverge. Taking into account the form of $M(H)$ curve we believe that in solutions with $x=0.65$ the long-range magnetic order is apparently destroyed.

The compound $La_{0.5}Bi_{0.5}MnO_{3.07}$ was reduced under various conditions. As a result, two compounds—

TABLE II. Unit cell parameters of $La_{1-x}Bi_xMnO_{3+\lambda}$ compounds obtained in vacuum.

Composition	Symmetry	*a*, Å	*b*, Å	*c*, Å	*V*, Å^3
$La_{0.5}Bi_{0.5}MnO_{3.07}$	T	3.9098	3.9352	–	60.15
$La_{0.5}Bi_{0.5}MnO_{3.04}$	O	5.5456	5.5879	7.7862	61.095
$La_{0.5}Bi_{0.5}MnO_{2.99}$	O′	5.501	5.8266	7.6635	61.41

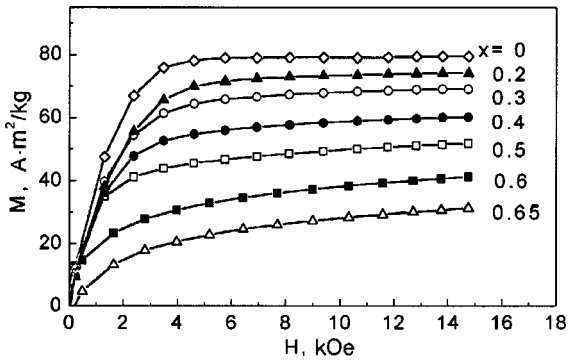

FIG. 1. Magnetic field dependence of the magnetization in the $La_{1-x}Bi_xMnO_{3.07}$ system.

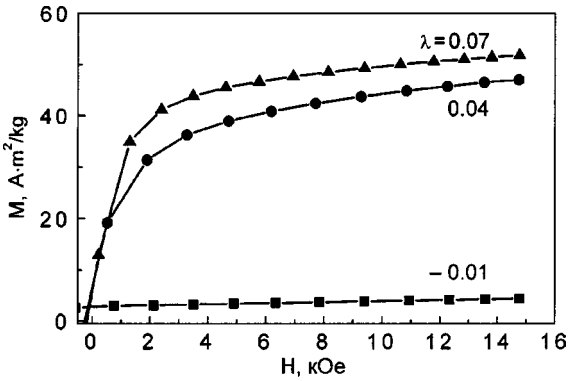

FIG. 3. Magnetic field dependence of the magnetization in the $La_{0.5}Bi_{0.5}MnO_{3+\lambda}$ system.

$La_{0.5}Bi_{0.5}MnO_{3.04}$ and $La_{0.5}Bi_{0.5}MnO_{2.99}$ are obtained. The partially reduced sample had an O-orthorhombically distorted unit cell ($a<c\sqrt{2}<b$), whereas the strongly reduced had O′-orthorhombically deformed unit cell ($c\sqrt{2}<a<b$). It should be noted, that O′-orthorhombic distortions in manganites indicate orbital ordering.[17] The field curves of the magnetization at liquid helium temperature for reduced samples are plotted in Fig. 3. The magnetizations of compounds with $\lambda=0.04$ and $\lambda=0.07$ differ slightly, whereas the composition with $\lambda=-0.01$ has a very small spontaneous magnetization (about 0.2 μ_B in formula units). With loss of oxygen the critical temperature at which a spontaneous magnetization appears at first decreased and then increased again and, moreover, the transition to the paramagnetic state became sharper (Fig. 4).

It should be noted that with decrease of the oxygen content in the reduced manganites the magnetic anisotropy increased sharply. Compounds with stoichiometric oxygen ($x\leqslant 0.65$) are hard, strongly anisotropic magnets. The coercive force H_C at helium temperature reaches 15 kOe, whereas for the ferromagnetic oxidized compositions $H_C=100$ Oe.

As compounds with bismuth content above 65% may not be obtained in air, synthesis of solutions in the range $0.7\leqslant x\leqslant 1$ is performed at high pressures. We have found out that the Curie temperature increases smoothly with increase of bismuth content from 87 K ($x=0.65$) up to 108 K for $BiMnO_3$. The spontaneous magnetization grows sharply on going from a solution with $x=0.8$ to a solution with $x=0.9$. It is necessary to note that the growth of the spontaneous magnetization correlates with a change of the unit cell symmetry type from orthorhombic ($x=0.8$) to monoclinic ($x=0.9$).

Measurements of the electrical conductivity are carried out in a temperature range of 77–350 K. All of the compounds under study had a semiconductor character of the temperature dependence of the electrical resistance. Near the temperature of magnetic ordering for structures with $x\leqslant 0.4$ a maximum of the magnetoresistance was observed (up to 40% in a field 9 kOe), but magnetic ordering did not change the type of the conductivity.

Figure 5 presents the magnetic phase diagram of the $La_{1-x}Bi_xMnO_{3,07}$ system with an excess of oxygen. The ferromagnetic state is gradually destroyed with increase of the bismuth content, until in the solution with $x=0.65$ the state of the cluster-type spin glass is not stabilized.

The magnetic phase diagram of the stoichiometric structures $La_{1-x}Bi_xMnO_3$ is shown in Fig. 6. $LnMnO_3$ is a weak ferromagnet with Néel temperature $T_N=144$ K. With increase of the bismuth content up to $x=0.65$ the stoichiometric structures still show the properties inherent to a weak ferromagnet. The Néel temperature gradually decreases to 87 K ($x=0.65$), apparently is because of a decrease of the Mn–O–Mn bond angles. The lower the Mn–O–Mn angle, the lower are the width of the $3d$ band and the temperature of magnetic ordering.[18–21] It is well known that in $LaMnO_3$ antiferrodistortion ordering of the d_{z^2} orbitals occurs in the

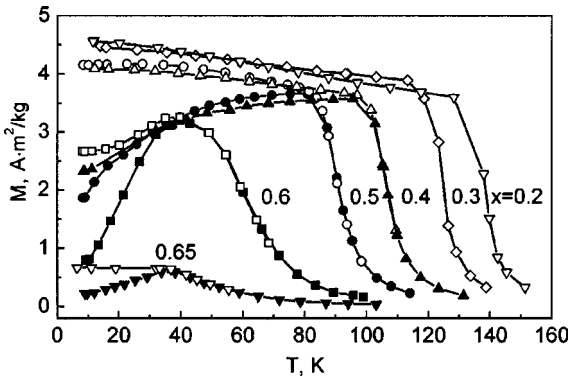

FIG. 2. Temperature dependence of the magnetization in the $La_{1-x}Bi_xMnO_{3.07}$ system (ZFC curve—filled symbols, FC—unfilled symbols).

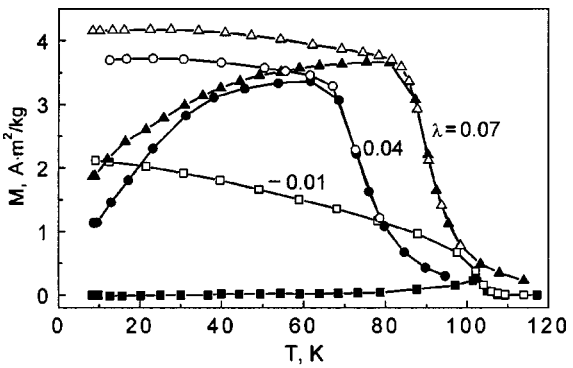

FIG. 4. Temperature dependence of the magnetization in the $La_{0.5}Bi_{0.5}MnO_{3+\lambda}$ system (ZFC curve—filled symbols, FC—unfilled symbols).

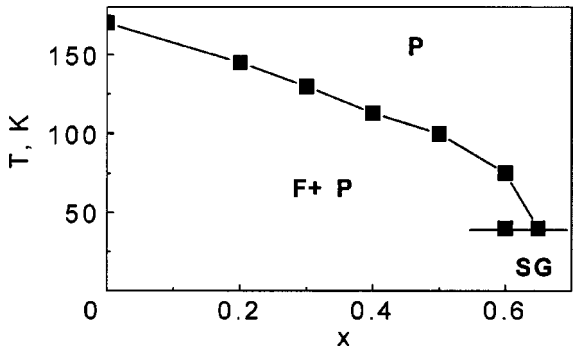

FIG. 5. Magnetic phase diagram of the $La_{1-x}Bi_xMnO_{3.07}$ system. P—paramagnetic state, F—ferromagnetic, SG—spin glass.

ab plane as the exchange interaction becomes ferromagnetic in this plane and antiferromagnetic along the *c* axis.[18] The magnetic moments are oriented along the *b* axis. In Bi-substituted stoichiometric manganites ($x \sim 0.6$) another type of antiferromagnetic and orbital ordering is in principle possible. However, in order to ascertain the features of the magnetic and structural state, neutron diffraction studies are required. In bismuth manganite the orbital state $d_{x^2-y^2}$ is stabilized, leading to an isotropic ferromagnetic state.[14,21] $BiMnO_3$ is a soft magnetic material, despite the orbital ordering.[14,22] In solutions with a high bismuth content the magnetic state is most likely a two-phase one. The sample consists of ferromagnetic and antiferromagnetic areas. We believe that each type of magnetic state is characterized by its own type of orbital state.

It is well known that in manganites the substitution of the rare-earth ions R^{3+} and La^{3+} by an alkaline-earth ion results in orbital disordering and stabilization of the ferromagnetic state. This process is caused by two factors. First, vacancies appear in the orbitally ordered lattice (not Jahn–Teller ions Mn^{4+}), and that destabilizes a cooperative orbital ordering. Second, distortions of the crystal lattice decrease due to optimization of the cation's sizes, whereas the Mn–O–Mn bond angle which describes the width of the $3d$ band, is increased. Under these conditions the static Jahn–Teller distortions transform to dynamic ones, and the exchange interactions of the $Mn^{3+}-O-Mn^{3+}$ and $Mn^{3+}-O-Mn^{4+}$ types become ferromagnetic.[18] The establishment of magnetic order in structures with a large enough width of the $3d$ band leads to transition in metallic state due to overlapping of the bands formed mainly by $3d$ and $2p$ states.

In manganites containing a large quantity of Bi^{3+} ions the appearance of tetravalent ions of manganese does not induce ferromagnetism (Fig. 3). The presence of Mn^{4+} ions promotes the destruction of cooperative orbital ordering and the occurrence of properties inherent to spin glasses. Thus the compounds remain insulators. We believe that in compounds with a large content of Bi^{3+} ions the local static Jahn-Teller distortions are not removed. This is explained by the tendency of Bi^{3+} ions to form strongly anisotropic covalent *ps* bonds. These bonds promote local crystal structure distortions, which is the reason why the local Jahn–Teller orbital ordering is preserved. Indeed, the temperature of the charge and orbital ordering in $Bi_{0.5}Sr_{0.5}MnO_3$ is unusually high, above 500 K[23,24], whereas the characteristic temperature of charge and orbital ordering in the structures $R_{0.5}Sr_{0.5}MnO_3$ is 150 K[25,26]. Due to the local static Jahn–Teller distortions, the anisotropic character of the exchange interactions between the manganese ions persist. On the other hand, in these samples, due to fluctuations of the composition, microareas may exist in which the static Jahn–Teller distortions are removed. These microareas are ferromagnetic. The competition between ferromagnetism and antiferromagnetism results in a spin glass state of a cluster type. It should be noted that orbital and charge ordering in manganites are transitions of the martensitic type.[27,28] Therefore orbitally two-phase states in manganites should be realized at the concentration and temperature boundaries of the orbital order-disorder transitions.

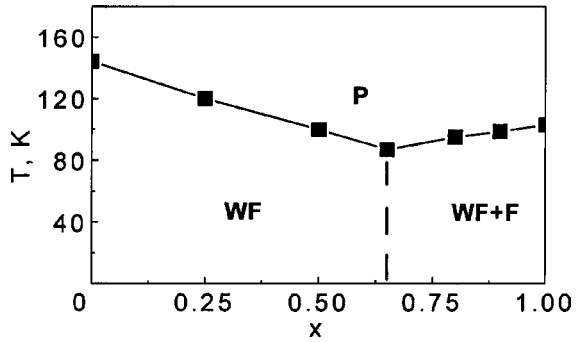

FIG. 6. Magnetic phase diagram of the $La_{1-x}Bi_xMnO_3$ system. WF—weak ferromagnetic state, P—paramagnetic, F—ferromagnetic.

SUMMARY

The crystal structure and magnetic properties of both oxidized $La_{1-x}Bi_xMnO_{3.07}$ and reduced $La_{1-x}Bi_xMnO_3$ perovskites have been studied. It is shown that oxidized $La_{1-x}Bi_xMnO_{3.07}$ series exhibit a concentration transition from ferromagnetic state to spin glass at $x \geqslant 0.65$ whereas reduced $La_{1-x}Bi_xMnO_3$ perovskites transform from weak ferrimagnet state to ferromagnetic one at $x > 0.7$ through a mixed magnetic state. The results obtained are discussed in terms of interplay between orbital ordering and type of magnetic ground state.

This work was supported in part by the Belarus Fund of Basic Research (Project F00-223).

*E-mail: troyan@ifttp.bas-net.by

[1] K. I. Kugel and D. I. Khomskii, Usp. Fiz. Nauk **136**, 621 (1982) [Sov. Phys. Usp. **25**, 231 (1982)].
[2] V. Eremenko, S. Gnatchenko, N. Makedonska, Yu. Shabakayeva, M. Shvedun, V. Sirenko, J. Fink-Finowicki, K. Kamenev, G. Balakrishnan, and P. Mck Paul, Fiz. Nizk. Temp. **27**, 1258 (2001) [Low Temp. Phys. **27**, 930 (2001)].
[3] R. Mahendiran, M. R. Ibarra, F. Maigan, A. Arulraj, R. Mahesh, O. Revcau, and C. N. R. Rao, Phys. Rev. Lett. **82**, 2191 (1999).
[4] P. M. Woodward, D. E. Cox, T. Vogt, C. N. Rao, and A. K. Cheetham, Chem. Mater. **11**, 3528 (1999).
[5] I. O. Shklyarevskiy, M. Yu. Shvedun, S. L. Gnatchenko, P. J. M. van Bentum, P. C. M. Christianen, J. C. Maan, K. V. Kamenev, G. Balakrishnan, P. Mck Paul, and J. Fink-Finowicki, Fiz. Nizk. Temp. **27**, 1250 (2001) [Low Temp. Phys. **27**, 923 (2001)].

[6] I. O. Troyanchuk, D. A. Efimov, V. V. Eremenko, V. A. Sirenko, H. Szymszak, and A. Nabialek, Fiz. Nizk. Temp. **26**, 39 (2000) [Low Temp. Phys. **26**, 28 (2000)].
[7] V. V. Eremenko, V. A. Sirenko, H. Szymszak, and A. Nabialek, Fiz. Nizk. Temp. **25**, 311 (1999) [Low Temp. Phys. **25**, 221 (1999)].
[8] V. M. Loktev and Yu. G. Pogorelov, Fiz. Nizk. Temp. **26**, 231 (2000) [Low Temp. Phys. **26**, 171 (2000)].
[9] M. R. Ibarra, P. A. Alagarabel, C. Marguina, J. Blasco, and J. Garsia, Phys. Rev. Lett. **75**, 3541 (1995).
[10] S. Quezel-Ambrunaz, Bull. Soc. Fr. Mineral. Cristallogr. **91**, 339 (1968).
[11] F. Sugawara, S. Iida, Y. Syono, and S. Akimoto, J. Phys. Soc. Jpn. **20**, 1529 (1965).
[12] V. A. Bokov, N. A. Milnikova, S. A. Kizhaev, M. F. Brizhina, and I. A. Grigoryan, Fiz. Tverd. Tela (Leningrad) **7**, 3695 (1965) [Sov. Phys. Solid State **7**, 2993 (1965)].
[13] G. H. Jonker and J. H. van Santen, Physica (Amsterdam) **16**, 337 (1950).
[14] I. O. Troyanchuk, N. V. Kasper, O. S. Mantytskaya, and S. N. Pastushonok, Zh. Éksp. Teor. Fiz. **105**, 399 (1994) [Sov. Phys. JETP **78**, 212 (1994)].
[15] I. O. Troyanchuk, N. V. Samsonenko, E. F. Shapovalova, I. M. Kolesova, and H. Szymczak, J. Phys.: Condens. Matter **8**, 11205 (1996).
[16] H. Chiba, T. Atou, and Y. Syono, J. Solid State Chem. **132**, 139 (1997).
[17] J. A. M. van Roosmalen and E. H. P. Cordfunke, J. Solidi State Chem. **110**, 109 (1994).
[18] D. Gudenaf, *Magnetizm i himicheskaya svyaz* (in Russian), Metalurgiya, Moskva (1968).
[19] P. G. De Gennes, Phys. Rev. **18**, 1, 141 (1960).
[20] E. E. Havinga, Philips Res. Rep. **21**, 432 (1966).
[21] T. Atou, H. Chiba, K. Ohoyama, Y. Yamagnuchi, and Y. Syono, J. Solid State Chem. **145**, 639 (1999).
[22] I. O. Troyanchuk and V. N. Derkachenko, Fiz. Tverd. Tela (Leningrad) **32**, 2474 (1990) [Sov. Phys. Solid State **32**, 1436 (1990)].
[23] N. V. Kasper, I. O. Troyanchuk, A. N. Chobot, H. Szymczak, and J. Fink-Finowicki, J. Phys.: Condens. Matter **9**, 7455 (1997).
[24] J. L. Carcia-Munos, C. Froutera, M. A. G. Aranda, A. Liobet, and C. Ritter, Phys. Rev. B **63**, 064415 (2001).
[25] F. Millange, S. de Brion, and G. Chouteau, Phys. Rev. B **62**, 9, 5619 (2000).
[26] H. Kuwahara, Y. Tomioka, A. Asamitsu, Y. Moritomo, and Y. Tokura, Science **270**, 961 (1995).
[27] V. Podzorov, B. G. Kim, V. Kiryukhin, M. E. Gershenson, and S-W. Cheong, Phys. Rev. B **64**, 140406 (2001).
[28] I. O. Troyanchuk, A. I. Akimov, L. A. Bliznjuk, and N. V. Kasper, J. Alloys Compd. **228**, 83 (1995).

This article was published in English in the original Russian journal. Reproduced here with stylistic changes by the Translation Consultant.

On the transverse magnetization of the anisotropic superconductor $2H-NbSe_2$

V. A. Sirenko,* N. I. Makedonska, and Yu. A. Shabakayeva

B. Verkin Institute for Low Temperature Physics and Engineering of the National Academy of Sciences of Ukraine, 47 Lenin Ave., Kharkov 61103, Ukraine

R. Schleser

High Magnetic Field Laboratory, Grenoble, France
(Submitted February 1, 2002)
Fiz. Nizk. Temp. **28**, 796–802 (July 2002)

Torque measurements were performed on a high-quality single crystal of the uniaxial superconductor $2H-NbSe_2$ in a tilted magnetic field 0–200 kG, in the temperature range 1.5–4.2 K. The transverse component of the absolute magnetization was derived in a magnetic field directed at an angle of 77° to the axis of anisotropy, and its field dependence was analyzed in a reversible domain of the mixed state. The penetration depth and anisotropy characteristics were obtained for the sample under study. © *2002 American Institute of Physics.*
[DOI: 10.1063/1.1496670]

1. INTRODUCTION

Measurements of the transverse magnetization of magnetically anisotropic media have proved to be an effective tool for the study of spatially inhomogeneous magnetic states. As a result of such investigations V. V. Eremenko and co-authors have discovered intermediate[1] and mixed[2] states in antiferromagnets, like those existing in type-I and type-II superconductors, respectively. Torque measurement is a technique for registration of the transverse magnetization of a crystal in a uniform magnetic field, which has been used successfully in studies of the magnetic anisotropy[3] (cited from[4]) and the Fermi surface[4] for a long time. The torque value τ in Gaussian units is determined by the simple equation

$$\tau = -M_{\perp} HV, \tag{1}$$

where H is the magnetic field, V is the sample volume, $M_{\perp}$ is the transverse (with respect to the applied magnetic field) component of the absolute magnetization, $M_{\perp} = M_x \cos\theta - M_z \sin\theta$, z is the direction along c, x is the direction along the a or b axis in the ab plane, i.e., normal to the c axis, and θ is the angle between the c axis and the external magnetic field direction (insert in Fig. 1).

Observation of a sample's torque suggests a nonzero component of the magnetization off from the magnetic field direction and, consequently, an orientational dependence of the sample's free energy in a magnetic field. Torque measurements on conventional superconductors[5–7] were made in connection with an investigation of magnetic flux pinning by crystal lattice inhomogeneities. Since the discovery of high-temperature superconductivity (HTSC) and the observation of the orientation of fine particles of these anisotropic compounds in a magnetic field,[8–10] the possibility of intrinsic torque in anisotropic superconductors in the region of equilibrium magnetization has been assumed.[11] Experimental evidence for the existence of transverse magnetization and intrinsic torque of anisotropic HTSC was obtained for the first time in Ref. 12. Later on, intrinsic torque measurements were performed on single crystals of HTSCs[13–15] and organic superconductors.[14] In those works the thermodynamic properties of the equilibrium Abrikosov vortex lattice were examined in the framework of London electrodynamics on the basis of angle dependence of the torque (Kogan model[11]) and Ginzburg–Landau phenomenology (Clem model).[16,17] In the present work the field dependences of the equilibrium torque are analyzed for the first time for the uniaxial superconductor $2H-NbSe_2$.

2. EXPERIMENTAL PART

The measurements aimed at observation of transverse magnetization in equilibrium region of superconducting mixed state placed the following specific requirements on the samples and experimental techniques employed. 1) The sample should be an anisotropic superconductor. Our sample under study meets this requirement, as its anisotropy parameters are close to those of the yttrium HTSC, which was the first object used for reversible torque observation (the ratios of effective masses along the c axis and in the superconducting plane are 10 and 25, respectively, which means that both of them are moderately anisotropic superconductors). Moreover, the superconducting compound $2H-NbSe_2$ is characterized by uniaxial anisotropy, and, consequently, one does not need to assume negligibility of the orthorombicity in the crystallographic planes responsible for superconductivity. 2) Pinning effects should be minimal. Actually, the high-quality single crystals of $2H-NbSe_2$ under study are characterized by a ratio of critical currents attributed to pinning and to depairing of $j_c/j_0 \approx 10^{-6}$, which describes them as the cleanest type-II superconductors. Their field dependences of the magnetization have two reversible regions, viz., weak fields $H \ll H_{c2}$ and near the upper critical field H_{c2} (Ref. 18 and the references therein). 3) As the magnitude of equilibrium magnetization is not large compared to the applied field (see, e.g.,[19]), the torque should be amplified by the sample's volume according to (1). This was realized in our case due to the opportunity of obtaining large crystals of $2H-NbSe_2$.

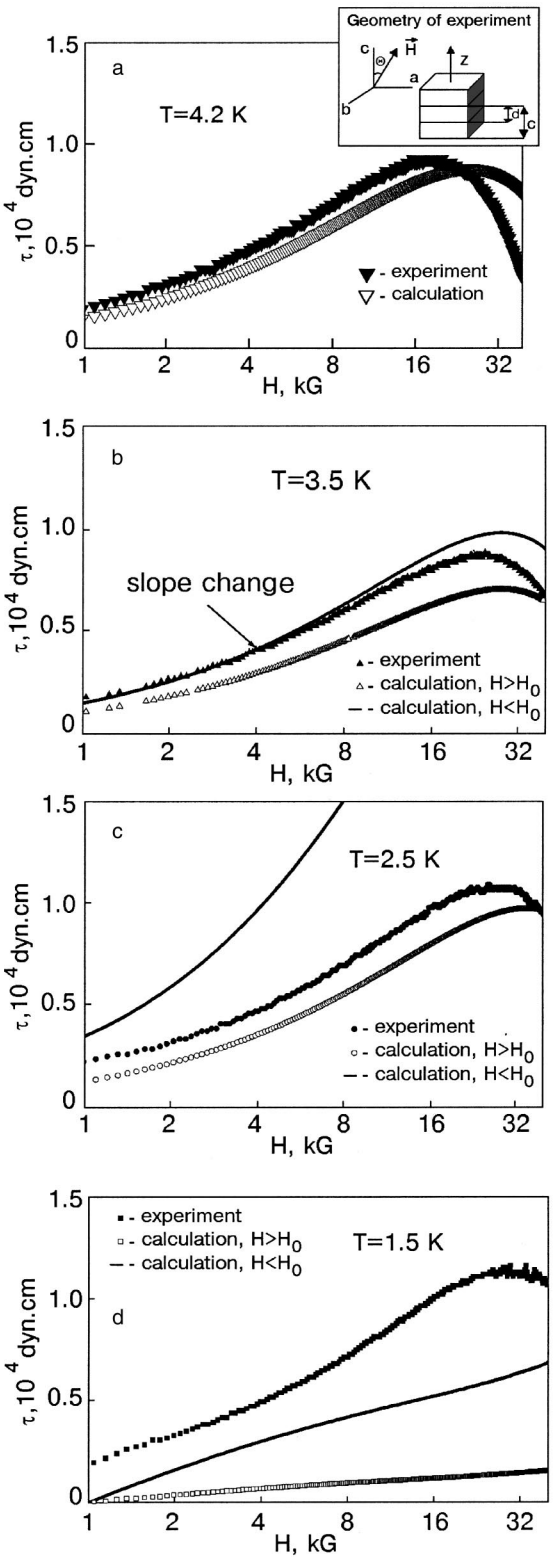

FIG. 1. The measured and calculated dependences $\tau(H)$ for $T=4.2$ (a); 3.5 (b); 2.5 (c); 1.5 (d) K, plotted in semilogarithmic scale. (Insert: c is the crystal lattice spacing and d is the interlayer distance.)

The volume of the crystal under study was 19.7×10^{-9} m^3, which was estimated to an accuracy of better than 1% by weight measurements (127 mg) and using the density value 6.44 g/cm^3, calculated from the atomic distribution in the unit cell of $2H-NbSe_2$, determined from the x-ray measurements. 4) According to the published data on the magnetization of $2H-NbSe_2$, the torque signal near the upper critical field H_{c2} should be of the order of 10^{-3} dyn·cm (10^{-10} N·m), if the transverse magnetization were equal to full magnetization. The available torque measurement technique[20] gave an accuracy of 10^{-5} dyn·cm. It was achieved in the following way. The torque on the sample was transmitted to the registering unit by a Cu–Be spring, the rigidity of which was chosen taking into account weight of the sample. The signal was registered by the capacitance method of Griessen[21] using a bridge scheme. This method allowed us to measure the capacitance with an accuracy of 10^{-4} pF. The large-scale magnet M7 at the High Magnetic Field Laboratory in Grenoble provided a highly uniform field in the sample region. Calibration of the signal was performed using a miniature coil (diameter 4.8 mm, length 1.4 mm, number of turns 20) mounted in the region of the sample in a field of 12 T, to an accuracy of 3%. The out-of-plane angle of the external field direction was 23°, which was estimated with an accuracy of 1°, satisfactory for measurements of the magnetic-field dependence of the torque.

The experimental geometry is presented in Fig. 1a. The measurements presented in this figure (a typical field dependence of the torque, measured at a temperature of 4.2 K) clearly show the occurrence of transverse magnetization of the $2H-NbSe_2$ single crystal in the field range $H_{c1}\ll H\ll H_{c2}$, where H_{c1} is the lower critical field. A thermodynamic data analysis follows below.

3. DISCUSSION OF EXPERIMENTAL RESULTS

The measured field dependences of the torque are presented in Fig. 1 in a comparison with those calculated using the equation:[11]

$$\tau(H)=\frac{\Phi_0 HV}{64\pi^2\lambda_{\alpha\beta}^2}\frac{\gamma^2-1}{\gamma^{2/3}}\frac{\sin^2\theta}{\varepsilon(\theta)}\ln\left[\frac{\gamma\eta H_{c2}(\|c)}{H\varepsilon(\theta)}\right], \qquad (2)$$

where Φ_0 is the magnetic flux quantum, and ε and γ are the anisotropy parameters,

$$\varepsilon(\theta)=(\sin^2\theta+\gamma^2\cos^2\theta)^{1/2}, \qquad (3)$$

and $\eta\sim1$.

Relation (2) was derived on the basis of London electrodynamics. It was already proved by experiments on HTSCs with moderate (Y-Ba-Cu-O) and strong (Ba-Bi-Ca-Cu-O and Tl-superconductors) anisotropy.[12,13] The compound under present study is a classic London superconductor,[22] as the magnetic field penetration depth λ in it sufficiently exceeds its coherence length ξ (for the component of M normal to the ab plane, which is responsible for superconductivity, $\lambda_{ab}\approx1000$ Å and the coherence length $\xi_c\approx10$ Å although it is nevertheless larger than the interlayer distance). A satisfactory agreement between the measured and calculated dependences is observed in a limited low-field range. The field of apparent deviation of the measured curve from the calculated one (the field of the maximum in the field dependence of the torque) is a function of temperature. This may suggest that the field $H_{\rm int}$ is related to the influence of intervortex interactions on the magnetization. It can be calculated taking into account that this interaction becomes considerable when the vortex lattice spacing equals to the penetration depth:

$$a_0 = \sqrt{\frac{\Phi_0}{H_{\rm int}}} = \lambda. \tag{4}$$

3.1. Transverse component of equilibrium magnetization

Though the occurrence of the transverse component of the equilibrium magnetization of uniaxial superconductors was predicted before the discovery of HTSC, and the estimates were made for $2H-NbSe_2$ (Ref. 23) itself, until now the related measurements had been performed on HTSCs only. The satisfactory agreement between the measurements and calculations in this work may be used for estimation of the thermodynamic properties of the compound under study. Initially the transverse magnetization will be determined on the basis of London electrodynamics and the restrictions for its application will be established.

In Gaussian units[19]

$$G_i = F_i(T,B_i) - \frac{B_i H}{4\pi}, \tag{5}$$

where F_i and G_i are the free energy and Gibbs potential for the specific volume of the ith phase (below, the indices i and j correspond, respectively, to the mixed state or Shubnikov phase and to the phase with $B \equiv H$, where the major part of the sample remains in the normal state).

The relation between field and induction in the mixed state follows from the condition of minimum of G at fixed H and T:

$$\frac{\partial}{\partial B_i} F_i(T,B_i) = \frac{H}{4\pi}. \tag{6}$$

The thermodynamic Gibbs potential for the system of interacting vortices is determined by the following equation:

$$G = n_L \mathcal{F} + \sum_{i,j} U_{ij} - \frac{BH}{4\pi}, \tag{7}$$

where $\mathcal{F}$ is the free energy of an individual vortex, n_L is the number of vortices per unit volume, U_{ij} is the potential of repulsive interaction between vortices, and

$$B = n_L \Phi_0. \tag{8}$$

Therefore, the first term in (7) is the sum of the individual vortex energies.

The second term in (7) describes the energy of repulsive interaction between the vortices. It will be examined below for different field ranges, following.[11,23–29]

The third term in (7) considers influence of an applied field H. It tends to favor large values of the induction B. This means that the field H stands for an external pressure which tends to increase the vortex density.

The following analysis of the measurements will use a quantitative estimate of the vortex interaction in the range $H_{c1} \ll H \ll H_{c2}$ or $\xi \ll a_0 \ll \lambda$ (ξ is the superconducting coherence length, $a_0 = \sqrt{\Phi_0/B}$ is the vortex lattice spacing, and λ is the penetration depth), or $1/\lambda^2 \ll n_L \ll 1/\xi^2$. In this range of fields and vortex lattice parameters of a *uniform* superconductor in the London limit ($\lambda \gg \xi$) the free energy is equal to[19]

$$F = \frac{B^2}{8\pi} + \frac{B}{4\pi} H_{c1} \frac{\ln(\beta a_0/\xi)}{\ln(\lambda/\xi)}, \tag{9}$$

where β is a parameter that depends on the vortex lattice symmetry. For a triangular lattice $\beta = 0.381$. Considering this relation, the equation for the magnetization was obtained:[26]

$$-4\pi M = (\Phi_0/8\pi\lambda^2)\ln(H_{c2}\beta/H). \tag{10}$$

In this equation β is determined from experimental data. Actually the field range considered[26] is narrower, as it is restricted below by the field $H' > H_{c1}$ above which the irreversibility effects may be neglected, i.e., relation (10) is fulfilled in a field range of

$$H' < H \ll H_{c2}. \tag{11}$$

The London equations may be generalized to the case of a uniaxial anisotropic superconductor through substitution of the isotropic effective mass by an anisotropic mass tensor.[23] Then Eq. (9) transforms to the free-energy equation for a vortex lattice at an angle θ to the symmetry axis c:[27]

$$8\pi F = B^2 + (\Phi_0/4\pi\lambda^2) \times (m_1 B_x^2 + m_3 B_z^2)^{1/2} \ln(H_{c2}\beta/B), \tag{12}$$

where $m_1 = m_2$ are the components of the mass tensor along the in-plane crystallographic axes ab, m_3 is that along the c axis. Minimization of (12) with respect to B gives[26] the magnetization components:

$$-M_z = M_0 \frac{m_3 \cos\theta}{\sqrt{m(\theta)}}, \quad -M_x = M_0 \frac{m_1 \sin\theta}{\sqrt{m(\theta)}}, \tag{13}$$

where

$$M_0 = \frac{\Phi_0}{32\pi^2\lambda^2} \ln\frac{H_{c2}\beta}{H}, \qquad m(\theta) = m_1 \sin^2\theta + m_3 \cos^2\theta. \tag{14}$$

An expression for the magnetization components measured in a direction perpendicular to the applied field was also derived in:[26]

$$M_\perp = M_x \cos\theta - M_z \sin\theta = M_0 \frac{m_3 - m_1}{\sqrt{m(\theta)}} \sin\theta\cos\theta. \tag{15}$$

3.2. Transverse magnetization of the crystal under study

The measured dependences $M_\perp(H)$ are presented in Fig. 2. The slope $M_\perp(\ln H)$ allows one to find the magnetic-field penetration depth λ, using Eqs. (13) and (14). Applying the following relation, which follows from London theory,

$$\lambda_{ab} = m^* c^2/4\pi n_s e^2, \tag{16}$$

one obtains $m^* \approx 7m_e$. Here m_e is the mass of a free electron, and n_s is the density of superconducting electrons. For the sample with $\lambda = 1200$ Å the value $m^* = 13.5m_e$ (Ref. 30) was obtained. The cyclotron mass obtained from analysis of the high-field oscillation amplitude with the lowest frequency (which corresponds to the in-plane field orientation), following,[31] appeared to be lower by an order of magnitude: $m^* \sim 0.6m_e$.

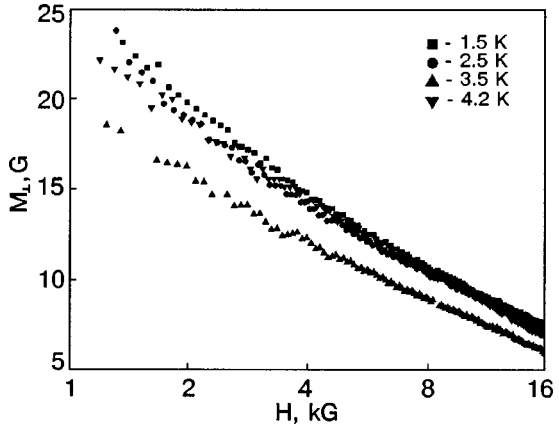

FIG. 2. Field dependences of the transverse component of the magnetization $M_\perp(H)$ in a semilog plot, calculated from experimental data presented in Fig. 1.

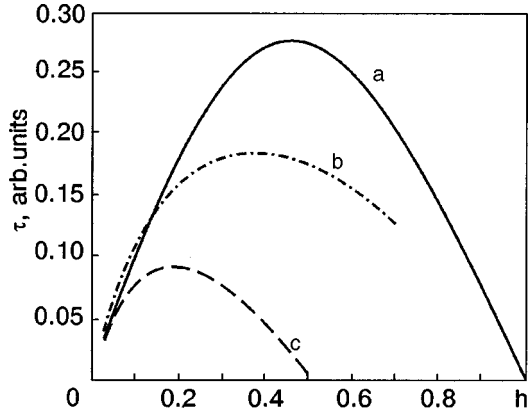

FIG. 3. Calculated torque as a function of $h=H/H_{c2}$: from Ginzburg–Landau model[16] (a); from London model[11] with $\eta=1$ (b); from London model[11] with $\eta=0.5$ (c).

Thus the cyclotron mass m^* at a field orientation $H\perp c$ is close to the lower component of the mass tensor m_1, while the mass derived from the penetration depth of the field normal to the plane of the sample, i.e., $H\|c$, is close to the large component of mass tensor m_3.

3.3. Restrictions of London electrodynamics application

The London model is in reality responsible only for the logarithmic prefactor $-M_0$ and for the linear dependence of M on $\ln H$ in (13). The factor at H_{c2} under the logarithm appears initially as a fitting parameter. In such a form the $M(\ln H)$ dependence allows one to obtain reasonable values of H_{c2} from the field dependences of equilibrium magnetization in a temperature range $T/T_c\approx 0.4-1$ (Ref. 32). The same is true for comparison of our torque measurements with equation (2): a satisfactory agreement is observed down to $T\approx 2.5$ K (for the material under study $T_c=7.2$ K) (see Fig. 1).

The limitation of London electrodynamics is connected with the fact that it does not consider the contribution of the energy of the vortex cores (suppression of the order parameter) to the total energy of the Abrikosov vortex lattice. The situation can be improved at the moment in two ways: 1) using a procedure proposed in Refs. 16 and 17 which is based on the phenomenological Ginzburg–Landau approach and is strictly valid near the upper critical field and in the vicinity of T_c, which is not the case here; 2) taking into account the nonlocal correction after the method described in Ref. 32. That is important for estimation of H_{c2} from magnetization measurements. In the lower limit of the intermediate fields near T_c the calculations of the torque function $\tau(H)$ by techniques based on the Ginzburg–Landau and London models practically coincide (see Fig. 3). That corresponds our data on $\tau(H)$ at $T=4.2$ and 3.5 K (Figs. 1a and 1b). It should be noted that $T\approx 3$ K is the quantum limit temperature for our sample ($T_{ql}=T_c^2/E_F$, where E_F is the Fermi energy), below which the nonlocality radius $\rho(T)$ must be an important parameter in all of the microscopic calculations.[33]

The temperature dependence of the field H_0 at which the nonlocal effects ''switch on'' (Fig. 4), according to Ref. 32 it can have a minimum that is consistent with our data. In Ref. 32 the dependence $H_0(T)=\Phi_0/2\pi^2\sqrt{3}\rho^2$ was derived for materials with a cylindrical Fermi surface, which is the case for $2H-NbSe_2$ (see, e.g.,[31]). Unfortunately in our case an exact estimation of $H_0(T)$ is not possible, because of the lack of reliable data on the electron mean free path in our sample. According to early data on this material,[30] the most optimistic estimates give its value as 250 Å. At the same time, estimation of this characteristic from the oscillatory component of the reversible magnetization M for a sample with all the measured parameters being similar to ours gives ~1000 Å.[31] If these data are true, we are working with an even cleaner ($l\gg\xi$) single crystal than suggested. Then the possible contribution from nonlocal effects should increase.

Taking into account that the magnetostriction follows the same laws as the magnetization and using equations[26] for the magnetization components along the principal crystallographic axes together with our data on magnetostriction along a and c (Fig. 5)[34] one can obtain independently the ratio of the anisotropic mass tensor components:

$$\sqrt{\frac{m_3}{m_1}}=\frac{dM(0)/d\ln H}{dM(\pi/2)/d\ln H}=\frac{d\lambda_{\rm rev}(0)/d\ln H}{c_{11}}\Big/\frac{d\lambda_{\rm rev}(\pi/2)/d\ln H}{c_{33}}\approx 3, \tag{17}$$

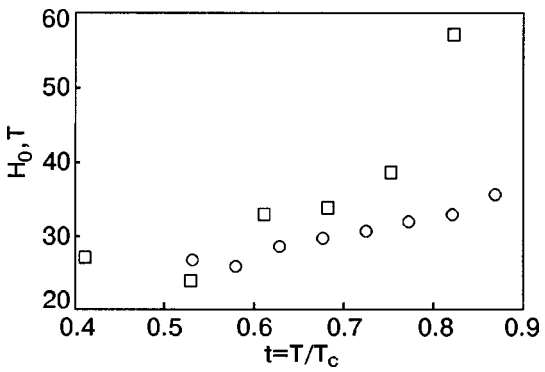

FIG. 4. Temperature dependence of nonlocality parameter $H_0(T/T_c)$ of anisotropic superconductors: Bi-2212 (□), Tl-2212 (○) (Ref. 32).

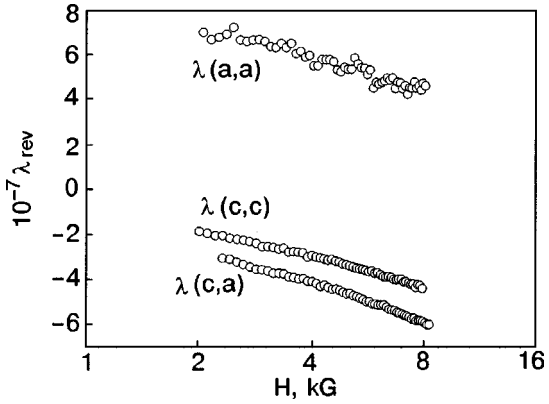

FIG. 5. Field dependence of the reversible magnetostriction $\lambda_{rev}(H)$ in a semilog plot: λ(a,a), λ(c,a)-field applied along *a* axis; λ(c,c)-field applied along hexagonal axis.

where λ_{rev} is the reversible magnetostriction, c_{11} and c_{33} are the components of the elastic modulus. Thus m_3 is an order of magnitude higher than m_1.

4. SUMMARY

1. The torque measurements were performed on single crystal of $2H-NbSe_2$ superconductor with moderate anisotropy. In a limited range of intermediate fields the measurements are well described by Kogan's formula, derived on the basis of London electrodynamics. This torque is connected neither with pinning nor with a form factor, but results from the tendency of Abrikosov vortices (the normal to circular currents, screening vortex cores) in anisotropic superconductor to build up in a preferred crystal direction.

2. The transverse component of magnetization is isolated.

3. The penetration depth λ is calculated and compared with published data. The data obtained for λ are used for estimation of the effective electron masses, which are compared with the data on the cyclotron mass. The latter was determined from analysis of the amplitudes of magnetization oscillations with the lowest frequencies. The cyclotron mass m^* in a field $H\perp c$ is close to the small component m_1 of the mass tensor, and the mass determined from the penetration depth for out-of-plane magnetic field $H\|c$ is close to the large component m_3 of the mass tensor. The magnitudes of the effective electron masses determined from the penetration depths for magnetization oscillations in a field oriented at angle 77° to the crystal axis *c* differ by an order of magnitude. That corresponds to the ratio of the components of the anisotropic mass tensor, derived from magnetostriction measurements.

4. Comparison of the field dependences of the magnetostriction and magnetization allowed us to estimate the anisotropy parameter as $\gamma=3$, i.e., the ratio $m_3/m_1\sim 9$ from magnetostriction measurements in fields directed along the crystal axes.

Finally, the authors express their deepest gratitude to Victor Valentinovich Eremenko for guiding them to the field of low-temperature magnetism. The present work could not have been accomplished without his involvement.

*E-mail: sirenko@ilt.kharkov.ua

[1] K. L. Dudko, V. V. Eremenko, and V. M. Fridman, Sov. Phys. JETP **24**, 362 (1971).
[2] K. L. Dudko, V. V. Eremenko, and V. M. Fridman, Zh. Éksp. Teor. Fiz. **68**, 659 (1975) [Sov. Phys. JETP **41**, 326 (1975)].
[3] K. S. Krishnan and S. Banerjee, Philos. Trans. R. Soc. London **234**, 265 (1935).
[4] D. Shoenberg, *Magnetic Oscillations in Metals* (in Russian), Mir, Moscow (1986).
[5] S. M. Ashimov and I. A. Naskidashvili, Fiz. Nizk. Temp. **10**, 479 (1984) [Sov. J. Low Temp. Phys. **10**, 248 (1984)].
[6] M. Furmans and C. Heiden, Cryogenics **16**, 451 (1976).
[7] G. L. Dorofeev and E. Yu. Klimenko, Fiz. Nizk. Temp. **32**, 175 (1987) [Sov. Phys. Tech. Phys. **57**, 291 (1987)].
[8] J. M. Tranquada, A. J. Goldman, A. R. Moodenbaugh, G. Shirane, S. K. Sinha, D. Vakin, and A. J. Jacobson, Phys. Rev. B **37**, 519 (1988).
[9] S. A. Solin, N. Garsia, S. Vieira, and M. Hortal, Phys. Rev. Lett. **60**, 744 (1988).
[10] V. D. Chechersky, V. V. Eremenko, V. A. Finkel, and N. E. Kaner, Fiz. Nizk. Temp. **15**, 92 (1989) [Sov. J. Low Temp. Phys. **15**, 52 (1989)].
[11] V. G. Kogan, Phys. Rev. B **38**, 7049 (1988).
[12] D. E. Farrell, C. M. Williams, S. A. Wolf, N. P. Bansal, and V. G. Kogan, Phys. Rev. Lett. **61**, 2805 (1988).
[13] D. E. Farrell, S. Bonham, J. Foster, Y. C. Chang, P. Z. Ziang, K. G. Vandervoort, D. J. Lam, and V. G. Kogan, Phys. Rev. Lett. **63**, 782 (1989).
[14] F. Steinmeyer, R. Kleiner, P. Muller, H. Muller, and K. Winzer, Europhys. Lett. **25**, 459 (1994).
[15] O. Waldmann, F. Steinmeyer, P. Muller, J. J. Neumeier, F. X. Regi, H. Savary, and J. Schneck, Phys. Rev. B **53**, 11825 (1996).
[16] Z. Hao and J. R. Clem, Phys. Rev. B **43**, 7622 (1991).
[17] Z. Hao and J. R. Clem, Phys. Rev. Lett. **67**, 2371 (1991).
[18] V. Eremenko, V. Sirenko, Yu. Shabakayeva, R. Schleser, and P. L. Gammel, Fiz. Nizk. Temp. **27**, 952 (2001) [Low Temp. Phys. **27**, 700 (2001)].
[19] P. G. de Gennes, *Superconductivity of Metals and Alloys*, W. A. Benjamin (Ed.), New York, Amsterdam (1966).
[20] P. Christ, W. Biberacher, H. Muller, and K. Andres, Solid State Commun. **91**, 451 (1994).
[21] R. Griessen, Cryogenics **13**, 375 (1973).
[22] L. N. Bulaevskii, M. Ledvij, and V. G. Kogan, Phys. Rev. B **46**, 366 (1992).
[23] V. G. Kogan, Phys. Rev. B **24**, 1572 (1981).
[24] V. G. Kogan, Phys. Rev. B **24**, 2497 (1981).
[25] V. G. Kogan, Phys. Rev. B **37**, 1 (1987).
[26] V. G. Kogan, M. M. Fang, and S. Mitra, Phys. Rev. B **38**, 11958 (1988).
[27] L. J. Campbell, M. M. Doria, and V. G. Kogan, Phys. Rev. B **38**, 2439 (1988).
[28] V. G. Kogan, Phys. Rev. Lett. **63**, 782 (1989).
[29] V. G. Kogan, L. N. Bulaevskii, P. Miranović, and L. Dobrosavljević-Grujić, Phys. Rev. B **51**, 15344 (1995).
[30] L. N. Bulaevskii, Usp. Fiz. Nauk **116**, 449 (1975).
[31] R. Corcoran, P. Meeson, Y. Onuki, P. A. Probst, M. Springford, K. Tokitat, H. Harimot, G. V. Guo, and B. L. Gyoffy, J. Phys.: Condens. Matter **6**, 4479 (1994).
[32] V. G. Kogan, A. Gurevich, J. H. Cho, D. C. Johnston, Ming Xu, J. R. Thompson, and A. Martynovich, Phys. Rev. B **54**, 12386 (1996).
[33] R. I. Miller, R. F. Kiefl, J. H. Brewer, J. Chakhalian, S. Dunsiger, and G. D. Morris, Phys. Rev. Lett. **85**, 1540 (2000).
[34] V. V. Eremenko, V. A. Sirenko, R. Schleser, and P. L. Gammel, Fiz. Nizk. Temp. **27**, 412 (2001) [Low Temp. Phys. **27**, 305 (2001)].

This artical was published in English in the original Russian journal. Reproduced here with stylistic changes by the Translation Consultant.